

**Control of plasma kinetics  
for microelectronics fabrication**

by

Sang-Heon Song

A dissertation submitted in partial fulfillment  
of the requirements for the degree of  
Doctor of Philosophy  
(Nuclear Engineering and Radiological Sciences)  
in The University of Michigan  
2014

Doctoral Committee:

Professor Mark J. Kushner, Chair  
Associate Professor John E. Foster  
Professor Brian E. Gilchrist  
Professor Yue Ying Lau  
Assistant Professor Alexander George Roy Thomas

Copyright © Sang-Heon Song 2014

All rights reserved

## ACKNOWLEDGEMENTS

This thesis would not have been possible without the help, support and patience of my advisor Prof. Mark J. Kushner, not to mention his advice and unsurpassed knowledge of plasma physics and chemistry. I am extremely grateful to him for encouraging and motivating me during difficult times.

I am also grateful to the members of my committee – Prof. Brian E. Gilchrist, Prof. Yue Ying Lau, Prof. John E. Foster, and Prof. Alexander G. R. Thomas for their thoughtful comments and suggestions. I would also like to acknowledge the support of Department of Energy Office of Fusion Energy Sciences, National Science Foundation, and Semiconductor Research Corporation.

I am thankful to the past and present members of the Optical and Discharge Physics Group for their friendship and support – Dr. Natalia Babaeva, Dr. Zhongmin “Andy” Xiong, Dr. Yang Yang, Dr. Mingmei Wang, Dr. Juline Shoeb, Jun-Chieh “Jerry” Wang, Michael Logue, Yiting Zhang, Wei Tian, Peng Tian, and Seth Norberg.

Finally, I would like to thank my parents, grandmother and brother that have supported me long before I began the PhD program and will continue to give support long after. I cannot go this far without them. I would also like to thank my wife Minkyong who is my best friend and greatest source of inspiration. As a new part of my life, our little babies William Tewon

Song and Lily Yerin Song should be mentioned. I thank them for being healthy and cute. With them, my life is full of joy.

## Table of Contents

ACKNOWLEDGEMENTS .....	ii
Table of Contents .....	iv
List of Figures .....	vii
List of Acronyms .....	xvii
ABSTRACT .....	xviii
Chapter 1 INTRODUCTION .....	1
1.1 Plasmas: An Introduction .....	1
1.2 Plasma Material Processing .....	3
1.3 Plasma Etching Systems .....	4
1.4 Control of Plasma Kinetics .....	6
1.5 Computational Modeling of Plasma Kinetics .....	10
1.6 Summary .....	11
1.7 Figures .....	15
1.8 References .....	21
Chapter 2 DESCRIPTION OF THE MODEL .....	26
2.1 Hybrid Plasma Equipment Model (HPEM) .....	26
2.1.1 The Fluid Kinetics-Poisson Module (FKPM) .....	28
2.1.2 The Electromagnetics Module (EMM) .....	35
2.1.3 The Electron Monte Carlo Simulation (eMCS) .....	38
2.1.4 Plasma Chemistry Monte Carlo Module (PCMCM) .....	49
2.2 Monte Carlo Feature Profile Model (MCFPM) .....	50
2.3 Parallel Computing .....	52
2.4 Figures .....	57
2.5 References .....	61
Chapter 3 CONTROL OF ELECTRON DISTRIBUTION USING MAGNETIC FIELD .....	64
3.1 Introduction .....	64
3.2 Description of the Model .....	67
3.3 Plasma Properties in Magnetized ICP .....	69

3.4	Scaling with Pressure and Power .....	73
3.5	Concluding Remarks .....	78
3.6	Figures .....	79
3.7	References .....	95
Chapter 4 BEHAVIOR OF SECONDARY ELECTRONS IN DC-AUGMENTED CAPACITIVELY COUPLED PLASMAS.....		98
4.1	Introduction .....	98
4.2	Description of the Model.....	99
4.3	Behavior of Beam-like Secondary Electrons in the Bulk Plasma.....	101
4.4	Concluding Remarks .....	103
4.5	Figures .....	105
4.6	References .....	109
Chapter 5 CONTROL OF ELECTRON ENERGY DISTRIBUTION FUNCTION USING PULSED POWER .....		110
5.1	Introduction .....	110
5.2	Description of the Model.....	112
5.3	Plasma Properties of Pulse Powered DF-CCP Sustained in Argon .....	114
5.4	Plasma Properties in Ar/CF <sub>4</sub> /O <sub>2</sub> .....	118
5.5	Pulse Repetition Rate and Duty cycle .....	125
5.6	Concluding Remarks .....	127
5.7	Figures .....	129
5.8	References .....	146
Chapter 6 CONTROL OF ION ENERGY DISTRIBUTION USING PULSED POWER .....		148
6.1	Introduction .....	148
6.2	Description of the Model.....	150
6.3	Plasma Properties of Pulse Powered DF-CCP with Constant Voltage .....	152
6.4	Control of the IED in Pulse Powered DF-CCP using Blocking Capacitance .....	155
6.5	Concluding Remarks .....	162
6.6	Figures .....	164
6.7	References .....	180
Chapter 7 CONTROL OF SiO <sub>2</sub> ETCH PROFILE IN PULSED CAPACITIVELY COUPLED PLASMAS SUSTAINED IN Ar/CF <sub>4</sub> /O <sub>2</sub> .....		182
7.1	Introduction .....	182
7.2	Description of the Model.....	185
7.3	Plasma Properties of Pulse-Powered DF-CCP.....	188
7.4	Ion Energies and Etch Properties .....	190
7.5	Concluding Remarks .....	195

7.6	Figures .....	197
7.7	References .....	212
Chapter 8 CONCLUSION AND FUTURE WORK.....		214
8.1	Overview of Research .....	214
8.2	Validation and Impact .....	216
8.3	Future Work .....	217
8.4	References .....	219
AUTHOR'S BIOGRAPHY .....		220

## List of Figures

Fig. 1.1 Different plasma etching systems as a function of plasma density and pressure.[1] Acronyms key: ECR – electron cyclotron resonance, PR – photo resist, HM – hard mask, GP – gate poly, OE – over etch, SL – soft landing, HARC – high aspect ratio contact, STI – shallow trench isolation, ICP – inductively coupled plasma, CCP – capacitively coupled plasma, RIE – reactive ion etching, MERIE – magnetically enhanced RIE.....	15
Fig. 1.2 A number of applications using low-temperature plasma technology.[4].....	16
Fig. 1.3 Plasma classification by its density and temperature. Relativistic effects play a role for $T > 10^9$ K.[6].....	17
Fig. 1.4 Schematic diagram for parallel plate reactors: (a) “PE mode” – wafer on grounded electrode; (b) “RIE mode” – wafer on <i>RF</i> powered electrode.[7].....	18
Fig. 1.5 Schematic diagram of dual frequency CCP in which the <i>RF</i> powers are applied to both of the electrodes.[8].....	19
Fig. 1.6 Illustration of plasma kinetics in the pulse powered system.[9] (a) Ion energy distribution, (b) charge distribution on the feature, and (c) source and loss mechanism of radicals during <i>power-ON</i> and <i>-OFF</i> cycles. ....	20
Fig. 2.1 Example of results from HPEM. (a) Computational geometry for CCP and ICP. (b) Electron energy distributions are compared between CCP, ICP, and mICP. Ion energy distribution is obtained from CCP. (c) Electron energy distribution as a function of time when using pulsed power. ....	57
Fig. 2.2 Percent of CPU time spent in different modules when using the eMCS.....	58
Fig. 2.3 Speedup and efficiency of parallelization as a function of (a) number of eMCS particles and (b) number of threads.....	58
Fig. 2.4 Percent of CPU time spent in different modules when using the electron energy equation. .....	59

Fig. 2.5 The red-black technique is used to parallelize SOR routines. (a) Schematic of the red-black technique. (b) Speedup and efficiency of parallelization of SOR routines using red-black methods. ....	59
Fig. 2.6 Profiling of HPEM when using Scharfetter-Gummel fluxes and sparse matrix techniques for Poisson's equation. ....	60
Fig. 3.1 Properties of the mICP. (a) Geometry of the mICP chamber. The permanent magnet is placed inside the antenna coil which is immersed in the plasma. (b) The magnetic field intensity at height of 6.3 cm as a function of radial position. ....	79
Fig. 3.2 Power deposition and electric fields for the base case conditions (3 mTorr, 100 W, 5 MHz). Power dissipation for (a) unmagnetized and (b) magnetized conditions. (c) Azimuthal electric field for unmagnetized condition. (d) Radial, (e) axial, and (f) azimuthal components of electric field for magnetized condition. The azimuthal electric field is larger with the magnetic field than without in order to compensate for the reduced conductivity. The power absorbing volume in a magnetized discharge is larger than in an unmagnetized discharge.....	80
Fig. 3.3 Electron density and temperature for the base case conditions (3 mTorr, 100 W, 5 MHz). (a) Unmagnetized and (b) magnetized conditions. The peak electron density and temperature increased with magnetic field and the position of the peak shifted toward adjacent to the coil.....	81
Fig. 3.4 Ionization rates for unmagnetized and magnetized conditions. Due to the enhanced tail of the EED adjacent to the coils, the ionization occurs by an orders of magnitude more with the magnetic field than without. ....	82
Fig. 3.5 Electron energy probability functions at different radial positions for unmagnetized condition. (a) Model and (b) experiment. The distribution does not vary much by the radial position. The model and experiment agree well each other. ....	83
Fig. 3.6 Electron energy probability functions at different radial positions for magnetized condition. (a) Model and (b) experiment. The tail of the distribution is rased due to the confinement of hot electrons adjacent to the coil. The result from the model agrees well with the experimental result. ....	84
Fig. 3.7 Comparison of the electron density and temperature between the model and experiment. (a) Unmagnetized and (b) magnetized conditions. By applying the magnetic field, the peak electron density increases by an order of magnitude and the electron temperature far from the coil is reduced by half due to the confinement of the hot electrons. ....	85

- Fig. 3.8 Electron energy distribution functions with various pressures. (a) Unmagnetized and (b) magnetized conditions. The tail component of the distribution is enhanced due to the non-local electron kinetics at the lower pressure and the trend is the same regardless of the magnetic field. .... 86
- Fig. 3.9 Electron temperature as a function of radial position with various pressures for (a) unmagnetized and (b) magnetized conditions. Without magnetic field, the electron temperature is higher at the lower pressure in order to compensate for the larger diffusion loss. With magnetic field, the difference of the electron temperature between adjacent to the coil and away from the coil becomes smaller as pressure increases due to the collisional diffusion across the magnetic field at higher pressure..... 87
- Fig. 3.10 Electron density as a function of radial position with various pressures. (a) Unmagnetized, (b) magnetized conditions for the pressure range 3 – 30 mTorr, and (c) magnetized conditions for the pressure range 30 – 100 mTorr. Without magnetic field, the peak electron density is significantly increased by the pressure increase due to the reduced diffusion loss at the higher pressure. With magnetic field the peak density decreases which is accompanied by the shift towards larger radii as pressure increases from 3 to 30. .... 88
- Fig. 3.11 Ionization rate as a function of radius with various pressures. (a) Unmagnetized, (b) magnetized conditions for the pressure range 3 – 30 mTorr, and (c) magnetized conditions for the pressure range 30 – 100 mTorr. .... 89
- Fig. 3.12 Rate coefficient for energy loss at a function of radius with various pressures. (a) Unmagnetized, (b) magnetized conditions for the pressure range 3 – 30 mTorr, and (c) magnetized conditions for the pressure range 30 – 100 mTorr..... 90
- Fig. 3.13 Electron energy distribution functions with various powers. (a) Unmagnetized and (b) magnetized conditions. The effect of the power on the distribution is relatively small compared to the effect of the pressure but with the magnetic field the distribution is affected by the power change due to more efficient power coupling into the electron heating. .... 91
- Fig. 3.14 Electron temperature as a function of radial position with various powers. (a) Unmagnetized and (b) magnetized conditions. The electron temperature does not vary with power without magnetic field while it increases by power with magnetic field.... 92
- Fig. 3.15 Electron density as a function of radial position with various powers. (a) Unmagnetized and (b) magnetized conditions. The peak electron density increases as the power increases and the trend is the same with and without magnetic field..... 93

- Fig. 3.16 Electron energy distributions with various magnetized. Pulsed condition of the magnetic field is chosen with the repetition frequency of 25 kHz and the duty cycle of 10%..... 94
- Fig. 4.1 Geometry and plasma properties for Ar/N<sub>2</sub> = 80/20, 40 mTorr, V<sub>dc</sub> = -140 V and V<sub>rf</sub> = 100 V at 10 MHz. (a) Geometry for the dc-augmented capacitively coupled plasma. (b) Electron density. (c) Electron temperature. (d) Power density delivered from the beam electrons. Electron temperature is highest adjacent to the electrodes due to the combination of sheath heating and beam electron heating..... 105
- Fig. 4.2 Energy distributions of the bulk electrons with and without beam-bulk interaction at different heights in the reactor (locations indicated in Fig. 4.1). (a) Near the upper electrode and (b) in the middle of the reactor. The heating effect by beam electron is larger near the electrodes due to the reduced speed by the sheath potential. .... 106
- Fig. 4.3 Behavior of secondary electrons in the plasma includes collision, reflection, and slowing down. (a) Fraction of reflected beam electrons at the sheath boundary on the lower electrode. (b) Electron induced secondary emission yield as a function of energy when the incident angle is perpendicular to the lower electrode. (c) Number of collision and reflection of the secondary electrons in the reactor as a function of the amplitude of the negative dc bias on the upper electrode. On the average, beam electrons make one collision per reflection because the mean free path is shorter than the electrode gap and longer than the half of the gap..... 107
- Fig. 4.4 Energy distribution of the bulk electrons with and without e-SEE. The additional energetic electrons from e-SEE contribute to the bulk electron heating..... 108
- Fig. 5.1 Operating conditions for this investigation. (a) Geometry of the dual frequency capacitively coupled plasma chamber. The low frequency (*LF*, 10 MHz) is applied on the lower electrode in continuous wave (*CW*) mode, and the high frequency (*HF*, 40 MHz) is applied on the upper electrode in pulse mode with a few tens of kHz pulse repetition frequency (*PRF*). The dots show where  $f(\varepsilon)$  will be plotted. (b) Pulsed operation is determined by the duty cycle and pulse repetition frequency. The power is turned on during the fraction of the total period designated by the duty cycle (*DC*). Pulse repetition frequency is how many times per second the pulse waveform repeats. .... 129
- Fig. 5.2 Plasma properties for *CW* operation in Ar (40 mTorr, 200 sccm, 500 W at 10 MHz, 500 W at 40 MHz). (a) Electron density, temperature, and electron ionization sources by bulk electron and secondary electrons. (b) Electron energy distribution at selected heights in the reactor (locations indicated in Fig. 5.1). The inset shows an enlargement of the low energy portion of the distribution..... 130

- Fig. 5.3 Electron density and temperature in Ar for the base case conditions (40 mTorr, 200 sccm, 500 W at 10 MHz CW, 500 W at 40 MHz in pulse mode – 50 kHz PRF with 25% duty cycle) at different times during the pulsed cycle (as indicated in the lower figure). The electron density does not change significantly over the pulse period, whereas the electron temperature shows instantaneous changes as the power toggles on and off, especially near the sheaths due to enhanced stochastic heating. .... 131
- Fig. 5.4 Ionization source by (left) bulk electrons and (right) secondary electrons in Ar for the base case conditions (40 mTorr, 500 W at 10 MHz CW, 500 W at 40 MHz in pulse mode – 50 kHz PRF with 25% duty cycle) at different times during the pulsed cycle (as indicated in the lower figure). .... 132
- Fig. 5.5 Electron energy distribution functions in Ar for the base case conditions (40 mTorr, 500 W at 10 MHz CW, 500 W at 40 MHz in pulse mode – 50 kHz PRF with 25% duty cycle) at different times during the pulse cycle (as indicated in the lower figure) for (a) near the *HF* sheath, (b) in the bulk plasma and (c) near the *LF* sheath (locations indicated in Fig. 5.1). Comparisons of  $f(\varepsilon)$  averaged over the pulse period and with CW excitation are in the right column. The enhanced tail of  $f(\varepsilon)$  is most prominent at the leading edge of the *power-ON* period. .... 133
- Fig. 5.6 Electron density, temperature, and electron ionization sources by bulk electron and secondary electrons in Ar/CF<sub>4</sub>/O<sub>2</sub>=75/20/5 for CW excitation with different secondary electron emission coefficients,  $\gamma$ . (a) 0.02, (b) 0.10, (c) 0.15, and (d) 0.25. .... 134
- Fig. 5.7 Electron energy distributions in Ar/CF<sub>4</sub>/O<sub>2</sub>=75/20/5 with CW excitation for different secondary electron emission coefficients,  $\gamma$  for base case conditions. (a) Near the *HF* sheath and (b) at the center of the plasma. With increasing rates of ionization by secondary electrons with increasing  $\gamma$ , the tail of the  $f(\varepsilon)$  decreases. .... 135
- Fig. 5.8 Plasma properties with pulsed excitation in Ar/CF<sub>4</sub>/O<sub>2</sub>=75/20/5 – (left) Electron density and (right) electron temperature for the base case conditions (40 mTorr, 500 W at 10 MHz CW, and 500 W at 40 MHz in pulse mode – 50 kHz PRF with 25% duty cycle) at different times during the pulsed cycle (as indicated in the lower figure). .... 136
- Fig. 5.9  $E/N$  over the pulsed cycle with Ar and Ar/CF<sub>4</sub>/O<sub>2</sub>=75/20/5 for base case conditions (40 mTorr, 500 W at 10 MHz CW, and 500 W at 40 MHz in pulse mode – 50 kHz PRF with 25% duty cycle). The overshoot is more severe in the Ar/CF<sub>4</sub>/O<sub>2</sub> mixture due to the lower electron density at the beginning of the pulse. .... 137
- Fig. 5.10 Ionization source by (left) bulk electrons and (right) secondary electrons in Ar/CF<sub>4</sub>/O<sub>2</sub>=75/20/5 for the base case conditions (40 mTorr, 500 W at 10 MHz CW, and 500 W at 40 MHz in pulse mode – 50 kHz PRF with 25% duty cycle) at different times

during the pulsed cycle (as indicated in the lower figure). The ionization source by bulk electrons is largest at the beginning of the *power-ON* stage due to the expansion of the sheath with the application of voltage. .... 138

Fig. 5.11 Electron energy distribution functions in Ar/CF<sub>4</sub>/O<sub>2</sub>=75/20/5 for the base case conditions (40 mTorr, 500 W at 10 MHz CW, and 500 W at 40 MHz in pulse mode – 50 kHz PRF with 25% duty cycle) at different times during the pulsed cycle (as indicated in the lower figure). (a) Near the *HF* sheath, (b) in the bulk plasma and (c) near the *LF* sheath (locations indicated in Fig. 5.1). Comparisons of  $f(\varepsilon)$  averaged over the pulse period and with CW excitation are in the right column. .... 139

Fig. 5.12 Mole fraction weighted rate coefficients for electron impact ionization sources and electron impact loss reactions during the pulsed cycle for the base case conditions. (a) Ar and (b) Ar/CF<sub>4</sub>/O<sub>2</sub>=75/20/5. In Ar, the electron loss rate coefficient is negligible. Whereas in Ar/CF<sub>4</sub>/O<sub>2</sub> the loss rate coefficient is finite through the pulsed cycle. .... 140

Fig. 5.13 Mole fraction weighted rate coefficients for the electron impact ionization sources and electron impact loss reactions during the pulsed cycle at different heights in the reactor for the base case conditions. (a) Ar ionization, sources, (b) Ar/CF<sub>4</sub>/O<sub>2</sub> ionization sources and (c) Ar/CF<sub>4</sub>/O<sub>2</sub> losses. The loss rate coefficients respond to the overshoot in *E/N* due to the resonant cross sections for attachment. The locations for heights are shown in Fig. 5.1. .... 141

Fig. 5.14 Electron energy distribution functions near the *HF* sheath for the base case conditions (40 mTorr, 500 W at 10 MHz CW, 500 W at 40 MHz in pulse mode, 25% duty cycle) for different PRF. (a) Argon and (b) Ar/CF<sub>4</sub>/O<sub>2</sub>. Insets show enlargements of the low energy portion of  $f(\varepsilon)$ . .... 142

Fig. 5.15 Mole fraction weighted electron impact ionization rate coefficients in the middle of the gap with different PRFs (40 mTorr, 500 W at 10 MHz in CW mode, and 500 W at 40 MHz in pulse mode with 25% duty cycle). (a) Ar and (b) Ar/CF<sub>4</sub>/O<sub>2</sub>=75/20/5. The relative overshoot of the electron impact ionization rate coefficient is larger with smaller PRF. .... 143

Fig. 5.16 Electron energy distribution functions near the *HF* sheath for the base case conditions (40 mTorr, 500 W at 10 MHz CW, 500 W at 40 MHz in pulse mode, 50 kHz) for different duty cycles. (a) Argon and (b) Ar/CF<sub>4</sub>/O<sub>2</sub>. Insets show enlargements of the low energy portion of  $f(\varepsilon)$ . .... 144

Fig. 5.17 Mole fraction weighted electron impact ionization rate coefficients in the middle of the gap with different duty cycles (40 mTorr, 500 W at 10 MHz in CW mode, and 500 W at 40 MHz in pulse mode, 50 kHz). (a) Ar and (b) Ar/CF<sub>4</sub>/O<sub>2</sub>=75/20/5. The relative

overshoot of the electron impact ionization rate coefficient scales inversely with duty cycle..... 145

Fig. 6.1 Operating system for this investigation. (a) Geometry of the DF-CCP chamber. The *LF* (10 MHz) is applied on the lower electrode, and the *HF* (40 MHz) is applied on the upper electrode. One of the two frequencies is operated in pulse mode with a few tens of kHz PRF. (b) Electrical schematic for the DF-CCP system. The blocking capacitor (BC) is connected in series with the lower electrode. .... 164

Fig. 6.2 Electron density (left) and temperature (right) when pulsing the *HF* power at different times during the pulsed cycle (as indicated in the lower figure). ( $\text{Ar}/\text{CF}_4/\text{O}_2 = 75/20/5$ , 40 mTorr, 200 sccm, *LF* = 250 V at 10 MHz CW, *HF* = 250 V at 40 MHz in pulse mode with BC = 1  $\mu\text{F}$ , PRF = 50 kHz and duty-cycle = 25%) The electron density is modulated by about 30% during the pulse cycle while the electron temperature shows nearly instantaneous changes as the *HF* power toggles on and off, especially near the sheaths due to enhanced stochastic heating..... 165

Fig. 6.3 Electron density and temperature when pulsing the *LF* power at different times during the pulsed cycle (as indicated in the lower figure). ( $\text{Ar}/\text{CF}_4/\text{O}_2 = 75/20/5$ , 40 mTorr, 200 sccm, *LF* = 250 V at 10 MHz in pulse mode with BC = 1  $\mu\text{F}$ , PRF = 50 kHz and duty-cycle = 25%, *HF* = 250 V at 40 MHz CW). Pulsing the *LF* power produces nominal inter-cycle changes in electron density and temperature over the pulse period as the majority of the *LF* power is dissipated in ion acceleration..... 166

Fig. 6.4 Plasma potential,  $V_P$ , and dc-bias,  $V_{dc}$ , during one pulse period when pulsing the *HF* power (PRF = 50 kHz, 25% duty-cycle). (a) BC = 10 nF and (b) BC = 1  $\mu\text{F}$ . The sheath potential is  $V_S = V_P - V_{dc}$ . The *LF* power is always on and the *HF* power is on only during the pulse window of 25%. Due to the smaller RC time constant with the small BC, the dc-bias responds more quickly. Since the voltage amplitude of the *LF* power rides on the dc-bias, the maximum envelope of the plasma potential has the same shape as the dc-bias. .... 167

Fig. 6.5 Plasma potential,  $V_P$ , and dc-bias,  $V_{dc}$ , during one period when pulsing the *LF* power (PRF = 50 kHz, duty-cycle = 25%). (a) BC = 10 nF and (b) BC = 1  $\mu\text{F}$ . The sheath potential is  $V_S = V_P - V_{dc}$ . The *HF* power is always on and the *LF* power is on only during the pulse window of 25%. The plasma potential is mainly determined throughout the pulse period by the voltage amplitude of the CW *HF* power. The dynamic range of dc-bias is larger with the smaller BC. .... 168

Fig. 6.6 Total IEDs for all ions with different sizes of the BC for the base case (40 mTorr, 250 V at 10 MHz, 250 V at 40 MHz). (a) CW operation, (b) pulsing *HF* power and (c) pulsing *LF* power. Pulsing has a PRF of 50 kHz and duty-cycle of 25%. The IED is insensitive

to the size of BC with *CW* operation while its shape depends on the size of BC with pulsed operation..... 169

Fig. 6.7 Total IEDs for all ions for different PRFs when pulsing the *HF* power with duty-cycle of 25%. (a) BC = 10 nF and (b) BC = 1  $\mu$ F. The IED becomes single-peaked in appearance with the smaller BC while the IED maintains a multiple-peaked shape with the larger BC. The IEDs with larger PRFs extend to the higher energies..... 170

Fig. 6.8 The dc-bias as a function of normalized time (which is time divided by the length of each pulse period) with different PRFs when pulsing the *HF* power with a 25% duty-cycle. (a) BC = 10 nF and (b) BC = 1  $\mu$ F. The *LF* power is *CW*. During *power-ON* period, the dc-bias becomes less negative with some overshoot with smaller PRFs... 171

Fig. 6.9 Ion energy distributions for  $O^+$ ,  $Ar^+$  and  $CF_3^+$  when pulsing the *HF* power. (a) BC = 10 nF and (b) BC = 1  $\mu$ F. .... 172

Fig. 6.10 Total IEDs for all ions for different PRFs when pulsing the *LF* power with duty-cycle of 25%. (a) BC = 10 nF and (b) BC = 1  $\mu$ F. The IED extends to higher energies with the smaller BC. .... 173

Fig. 6.11 The dc-bias as a function of the normalized time (which is time divided by the length of each pulse period) with different PRFs when pulsing the *LF* power with a 25% duty-cycle. (a) BC = 10 nF and (b) BC = 1  $\mu$ F. The *HF* power is *CW*. If the size of BC is small enough for the dc-bias to respond to the voltage on the electrode, the temporal behavior of dc-bias is similar for different PRFs. .... 174

Fig. 6.12 IEDs for  $O^+$ ,  $Ar^+$  and  $CF_3^+$  when pulsing the *LF* power. (a) BC = 10 nF and (b) BC = 1  $\mu$ F..... 175

Fig. 6.13 Total IEDs for all ions for different duty-cycles when pulsing the *HF* power with a PRF of 50 kHz. (a) BC = 10 nF and (b) BC = 1  $\mu$ F. The *LF* power is *CW*. The smaller duty-cycle tends to produce an extended energy range in the IED. .... 176

Fig. 6.14 The temporal behavior of dc-bias with different duty-cycles when pulsing the *HF* power with a PRF of 50 kHz. (a) BC = 10 nF and (b) BC = 1  $\mu$ F. The *LF* power is *CW*. The dynamic range of the dc-bias is from 0 V to -200 V with the smaller BC while the range is only from -60 to -90 V with larger BC. .... 177

Fig. 6.15 Total IEDs for all ions for different duty-cycles when pulsing the *LF* power with a PRF of 50 kHz. (a) BC = 10 nF and (b) BC = 1  $\mu$ F. The *HF* power is *CW*. The amplitude of the low energy peak diminishes while the amplitude of the high energy peak increases

as the duty-cycle increases. The IED becomes similar to that of the *CW* case with further increase of the duty-cycle. .... 178

Fig. 6.16 The temporal behavior of dc-bias with different duty-cycles when pulsing the *LF* power with a 50 kHz PRF. (a)  $BC = 10$  nF and (b)  $BC = 1$   $\mu$ F. The *HF* power is *CW*. The dynamic range is from -40 to +80 V with the smaller BC while the range is at most  $\pm 15$  V at 25% duty-cycle with larger BC. Note that the range of oscillation the dc-bias is similar for different duty-cycles with the smaller BC while the range is shifted by duty-cycle with the larger BC. .... 179

Fig. 7.1 Operating conditions for this investigation. (a) Geometry of the DF-CCP chamber. The *LF* (10 MHz) is applied on the lower electrode, and the *HF* (40 MHz) is applied on the upper electrode. One or both of the two frequencies are operated in pulse mode with 5 and 10 kHz PRF. Electron density ( $n_e$ ) and temperature ( $T_e$ ) are traced at the reference point indicated in the chamber. .... 197

Fig. 7.2 Electron density, temperature, and source rates for the conditions of pulsing the *LF* power (the *HF* in *CW*). The *LF power-ON* period is from 10  $\mu$ s to 35  $\mu$ s. (a)  $n_e$  and  $T_e$  as a function of time at the reference point (indicated in Fig. 7.1). (b) The spatial distribution of  $n_e$ ,  $T_e$ , and electron sources in the chamber at 25  $\mu$ s (15  $\mu$ s after the *LF* power ON). (c) The spatial distribution of  $n_e$ ,  $T_e$ , and electron sources in the chamber at 85  $\mu$ s (50  $\mu$ s after the *LF* power OFF). .... 198

Fig. 7.3 Electron density, temperature, and source rates for the conditions of pulsing the *HF* power (the *LF* in *CW*). The *HF power-ON* period is from 10  $\mu$ s to 35  $\mu$ s. (a)  $n_e$  and  $T_e$  as a function of time at the reference point (indicated in Fig. 7.1). (b) The spatial distributions of  $n_e$ ,  $T_e$ , and electron sources in the chamber at 25  $\mu$ s (15  $\mu$ s after the *HF* power ON). (c) The spatial distributions of  $n_e$ ,  $T_e$ , and electron sources in the chamber at 85  $\mu$ s (50  $\mu$ s after the *HF* power OFF). .... 199

Fig. 7.4 Electron density, temperature, and source rates for the conditions of pulsing the *LF* and *HF* power. The *power-ON* period is from 10  $\mu$ s to 35  $\mu$ s. (a)  $n_e$  and  $T_e$  as a function of time at the reference point (indicated in Fig. 7.1). (b) The spatial distributions of  $n_e$ ,  $T_e$ , and electron sources in the chamber at 25  $\mu$ s (15  $\mu$ s after the powers ON). (c) The spatial distributions of  $n_e$ ,  $T_e$ , and electron sources in the chamber at 85  $\mu$ s (50  $\mu$ s after the powers OFF). .... 200

Fig. 7.5 Energy flux with various duty cycles. (a) Average energy flux during ON-cycle. (b) Average energy flux over the total pulse period. .... 201

Fig. 7.6 Ion energy and angular distribution when pulsing the *LF* with a 25% of duty cycle and a 10 kHz of PRF. (a) IEAD for the ON and OFF periods compared to *CW*. (b) IED... 202

Fig. 7.7 Ion energy and angular distribution when pulsing the *HF* with a 25% of duty cycle and a 10 kHz of PRF. (a) IEAD for the ON and OFF periods compared to *CW*. (b) IED... 203

Fig. 7.8 Ion energy and angular distribution when pulsing the *LF* & *HF* with 25% duty and 10 kHz PRF. (a) IEAD for the ON and OFF periods compared to *CW*. (b) IED. The ion energy during the OFF cycle appears only at about zero because the sheath collapses during the afterglow. .... 204

Fig. 7.9 IEDs when pulsing the *LF* power. (a) IEDs with different duty cycles at 10 kHz of PRF. (b) IEDs with different PRFs at 25% of duty cycle..... 205

Fig. 7.10 IEDs when pulsing the *HF* power. (a) IEDs with different duty cycles at 10 kHz of PRF. (b) IEDs with different PRFs at 25% of duty cycle. .... 206

Fig. 7.11 IEDs when pulsing the *LF* & *HF* powers. (a) IEDs with different duty cycles at 10 kHz of PRF. (b) IEDs with different PRFs at 25% of duty cycle. .... 207

Fig. 7.12 Etch profile when pulsing the *LF* power at 10 kHz. (a) Etch profile after overetch 100%. (b) Profile width as a function of height with 100% of overetching. At 100% over etching, the sidewall bowing with *CW* mode started at about 100 nm in the depth but this is suppressed by pulsed operation. .... 208

Fig. 7.13 Etch profile when pulsing the *HF* power at 10 kHz. (a) Etch profile after Overetch 100%. (b) Profile width as a function of height with 100% of overetching..... 209

Fig. 7.14 Etch profile when pulsing the *LF* & *HF* powers at 10 kHz. (a) Etch profile after overetch 100%. (b) Profile width as a function of height with 100% of overetching. 210

Fig. 7.15 Etch rate and CD ratio as a function of duty cycle for different configurations of pulsing. (a) Power normalized etch rate. (b) CD ratio of middle to top. The normalized etch rate is higher with pulsed operation than *CW* mode except for the *LF* pulsed. An intermediate duty cycle produces a better sidewall profile. .... 211

Fig. 8.1 Number of ions into the feature as a function of the feature size with the ion current of 0.5 mA/cm<sup>2</sup> and duty cycle of 50%. For 20 nm feature size, only one single ion gets into the feature during the *power-ON* period with 5 kHz of PRF. .... 218

## List of Acronyms

BC	Blocking Capacitor
CCP	Capacitively Coupled Plasma
CD	Critical Dimension
CW	Continuous Wave
dc	Direct Current
DC	Duty Cycle
DF-CCP	Dual Frequency Capacitively Coupled Plasma
eMCS	Electron Monte-Carlo Simulation
e-e	electron-electron
EED	Electron Energy Distribution
EETM	Electron Energy Transport Module
EMM	Electromagnetic Module
FKPM	Fluid Kinetics-Poisson Module
HAR	High Aspect Ratio
HF	High Frequency
HPEM	Hybrid Plasma Equipment Model
ICP	Inductively Coupled Plasma
IED	Ion Energy Distribution
IEAD	Ion Energy and Angular Distribution
LF	Low Frequency
MCS	Monte-Carlo Simulation
MCFPM	Monte-Carlo Feature Profile Model
mICP	Magnetized Inductively Coupled Plasma
PCMCM	Plasma Chemistry Monte-Carlo Module
PIC	Particle in Cell
PR	Photoresist
PRF	Pulse Repetition Frequency
RF	Radio Frequency
SOR	Successive over Relaxation

## ABSTRACT

The fluxes of radicals and ions to the wafer during plasma processing of microelectronics devices determine the quality of the etch or deposition. These fluxes are largely controlled by controlling the electron energy distribution (EED) which determines the dissociation patterns of feedstock gases. Also, the quality of the process is in large part determined by the ability to control the ion energy distribution (IED) onto the wafer. In this thesis, the possibilities of controlling EED and IED are modeled using a two-dimensional plasma equipment model.

The techniques to control the EED include a magnetic field, beam electrons and a pulsed power source. Due to the magnetic confinement, the EED varies with position of the chamber depending on the pressure and power. Using beam electrons also provides a possibility to customize EED by delivering the energy to the bulk electrons through the  $e-e$  collisions.

In dual frequency capacitively coupled plasmas (DF-CCP), the pulsed power is one technique being investigated to provide additional degrees of freedom to control the EED and IED. By using pulsed power, electron sources and sinks do not need to instantaneously balance – they only need to balance over the longer pulse period. This provides additional leverage to customize EED and IED. As an application, the etching properties were also investigated in the DF-CCP using pulsed power. In the pulsed operation, there are typically two phases; deposition and etching. As a result, using pulse power provides one with the ability to control the balance

between the etching and deposition, which enables us to manipulate the etching profile. It was found that sidewall bowing can be suppressed by pulsing.

## Chapter 1 INTRODUCTION

Plasmas are used in many industrial applications, especially for microelectronics fabrication, as shown in Fig. 1.1.[1] Understanding the fundamental physics behind the applications is essential to improve the efficiency and to find an optimum design. Computational modeling often helps us greatly to develop plasma based technologies and understand details of the phenomena. Investigating the plasma kinetics, such as energy distributions of plasma species, is one of the most important challenges. In this thesis, I discuss results from computational investigations to optimize the distribution of electron and ion energies produced in low pressure plasmas for material process using pulsed power and other techniques. In this chapter, an overview of plasma technologies will be provided in the parameter space of interest for these investigations.

### 1.1 Plasmas: An Introduction

Plasmas are gases that give off light. These glowing gases are electrically conductive and chemically reactive. Plasma is often referred to as the 4<sup>th</sup> state of matter after solids, liquids, and gases.[2] Water exists on Earth as a solid, liquid, or gas. However, if more energy is supplied to the water vapor, the vapor will be ionized as the electron is detached from the atom or molecule. This ionized gas is the plasma. Although plasmas already exist in nature—for example, in the Sun, aurorae, and lightning—plasma state was first discovered by Sir William Crookes in 1879,

using a “Crookes tube” – an experimental electrical discharge tube in which air is ionized by the application of a high voltage through a voltage coil.[3] Man-made plasmas are usually generated by electric discharge because the discharge is more efficient than heating up the gas. The plasma technology is used in a wide range of applications from semiconductor manufacturing to rocket propulsion, as illustrated in Fig 1.2.[4] The discovery and control of plasmas has innovatively changed our lifestyle in the same way that the control of fire by early humans 400,000 years ago brought about an important change in human history. In fact, plasma has the same governing equations as combustion, except for Maxwell’s equations.[5] Imagine our life without fluorescent lamps, smartphones, computers, and flat-panel displays. Furthermore, the windows in buildings, the cylinders in car engines, artificial bones, potato chips bags, diapers, and any plastic material in our life are all being treated by plasma to modify the surface properties. These devices and products would not have been realized without plasma technology.

Since plasmas are often generated by electric discharge, the temperature unit for plasma is often expressed as eV (electron volt), and 1 eV is equivalent to 11594.2 K. Plasma temperature for thermonuclear fusion is above 10 keV, and the electron temperature of a fluorescent lamp is about 1 eV. Due to the wide dynamic range of the density and temperature, plasmas can be categorized in various different ways, as shown in Fig 1.3.[6] First, by temperature—plasmas with a temperature above 1 keV are considered “hot,” and plasmas between 1 and 10 eV are placed in the “low” temperature regime. Plasmas are also classified as “thermal” or “non-thermal” based on the relative temperatures of the electrons, ions, and neutrals. Thermal plasmas have all of the species in the same temperature, which is thermodynamic equilibrium. Non-thermal plasmas have the ions and neutrals at a much lower temperature than that of electrons, which is a non-equilibrium state. Another classification is based on the fraction

of ionization. If all atoms and molecules are ionized, the plasma is “fully” ionized; but if not, the plasma is “partially” ionized. For example, the plasmas considered for thermonuclear fusion can be categorized as fully ionized and hot plasmas. The plasmas we are going to discuss in this thesis are partially ionized, non-equilibrium, and low-temperature plasmas, the combination of which makes for a plasma that is typically used in the fabrication of microelectronics.

## **1.2 Plasma Material Processing**

Plasma material processing is essential in the semiconductor manufacturing industry. Typically, nanoelectronic chips (e.g., Intel® Core™ i7 Processor) have over 20 layers forming complex circuitry. Multiple metal layers are created to interconnect the millions of transistors in the chip. These metal layers are then appropriately insulated or isolated by the dielectric materials between them. The narrowest width in the layer is often called the critical dimension (CD) for the semiconductor industry. This important quantity has become as small as a few dozen nanometers, recently exceeding the expectation of Moore’s law. For example, the Samsung Galaxy S4 (released in April 2013) uses the quad-core 1.6GHz cortex-A15 MPCore, which was designed by ARM using technology based on a CD of 25 nm. In the manufacturing of nanoelectronic computer chips, there are typically 4 steps in making 1 layer: deposition, lithography, etching, and cleaning. Among these processes, deposition, etching, and cleaning all employ advanced plasma process equipment. For example, the deposition of a metal layer is carried out using a sputtering process whereby the metal atoms are ejected from a solid target material due to energetic particles from the plasma bombarding the target. The deposition of dielectric materials is done by plasma-enhanced chemical vapor deposition (PECVD), in which the energetic electrons in the plasma induce many processes that would otherwise be very improbable at low temperatures, such as the dissociation of precursor molecules and the creation

of large quantities of free radicals that can then be attached to make thin films on a substrate. Plasma etching is accomplished by the chemically reactive species such as fluorine or chlorine containing radicals and energetic ions generated in the plasmas. Finally, the cleaning, as the last step of the layer patterning, is also conducted by a plasma cleaning system in which the residue and photoresist used in the lithography step are cleaned by energetic particles produced in the plasma. In other words, the plasma material processing is responsible for roughly 75% of the entire manufacturing processes in the field of semiconductor fabrication.

### **1.3 Plasma Etching Systems**

There are typically two types of plasmas for microelectronic fabrication. One is capacitively coupled plasma (CCP), which is operated with two parallel electrodes; the other is inductively coupled plasma (ICP), which is generated by the antenna coil. Electrons in an ICP are accelerated back and forth by the oscillating electric field in the azimuthal direction induced from the loop coil antenna around the cylindrical chamber. Since the direction of the electron acceleration in an ICP is parallel to the chamber wall, the electron loss to the wall can be reduced. Moreover, as the acceleration path is circular, electrons are accelerated until the collision or phase change of the electric field. On the other hand, electrons in CCP are accelerated back and forth between two electrodes by the oscillating electric field that is perpendicular to the electrode, such that the electron loss to the electrodes is inevitable. By the different discharge configurations for each system, ICP is called a current-driven discharge while CCP is referred to as a voltage-driven discharge. As a result of the different electron loss mechanisms in these two systems, the electron density is typically higher in ICP than in CCP, but the plasma potential is higher with CCP due to the applied voltage on the electrodes. The higher electron density in ICP

is attractive for the metal etching due to the higher flux of radicals and ions, whereas the higher potential of CCP is more attractive for the dielectric etching due to the higher ion energy.

CCP can be operated in two modes depending on which electrode is powered, as shown in Fig. 1.4.[7] The plasma enhanced (PE) mode is achieved when the radio frequency (*RF*) power is applied to the upper electrode that also serves as the showerhead. The reactive ion etching (RIE) mode is obtained when the *RF* power is applied to the lower electrode on which the wafer sits. With *RF* power on the lower electrode to which a blocking capacitor is connected in series, a direct current self-bias is often naturally generated in order to produce equal currents flowing into both sides of a series capacitance in the circuit. As a result, the RIE mode can produce higher ion energy than the PE mode can due to the larger sheath potential on the lower electrode.

In order to improve the performance by controlling electron and ion kinetics separately, an attempt was made to use both PE and RIE modes, the combination of which is known as the dual frequency CCP (DF-CCP), as shown in Fig. 1.5.[8] For example, two *RF* powers are applied to electrodes at different frequencies. The lower-frequency power (a few MHz to 10 MHz) is applied to the lower electrode and is intended to control the ion energy on the wafer. The higher-frequency power (tens of MHz to hundreds of MHz) is applied to the upper electrode and is meant to control the electron energy. The electrons gain energy from the oscillating sheath boundary, which is called sheath heating. Since the sheath heating is larger at a higher frequency, a more efficient electron heating is acquired with a higher-frequency power. On the other hand, since the blocking capacitor is connected in series to the substrate where the lower-frequency power is applied, the dc self-bias is naturally generated on the electrode, which ultimately determines ion energies on the wafer. Therefore, the lower-frequency power is

responsible for the ion energy on the wafer. By using pulse power in DF-CCP, it is possible to selectively control electron heating and ion energy with more flexibility, as shown in Fig. 1.6.[9]

#### 1.4 Control of Plasma Kinetics

The reactive species in the plasma are generated by electron impact processes, as electrons are very energetic in the non-equilibrium plasmas. The rate coefficient for the electron impact processes are determined by the electron energy distribution as follows,

$$k = \int_0^{\infty} f(\varepsilon) \left( \frac{2\varepsilon}{m_e} \right)^{1/2} \sigma(\varepsilon) d\varepsilon, \quad (1.1)$$

where  $k$  is the reaction rate constant,  $f(\varepsilon)$  is electron energy distribution,  $m_e$  is electron mass,  $\varepsilon$  is electron energy, and  $\sigma(\varepsilon)$  is the cross section as a function of electron energy. In the microelectronic device fabrication using a plasma process, for example, the radical flux incident onto the wafer is important for determining the quality of the device. Since the electrons in the plasma collide with neutral atoms and molecules to create ions and radicals, the radical fluxes are ultimately determined by the EED. As a result, controlling the electron energy distribution (EED) is important for controlling the flux of radicals and ions to the substrate.[10] EED in plasmas as typically used in materials processing has been extensively investigated [11,12] and, given electric fields and gas mixtures, is generally predictable. However, there is an emerging need for a way to better control EED in order to, for example, optimize the production of a particular radical. There have been several attempts at controlling EED, including tuning the gas pressure [13], adding external ionization sources such as an electron beam [14], using magnetic fields [15], using an augmented  $dc$  bias on an  $RF$  electrode [16], and varying the frequency [17].

On the other hand, anisotropic (vertical) etching is obtained when the surface reaction is induced by the energetic ion bombardment due to the vertical incidence on the wafer. Therefore,

the ion energy distribution (IED) is also an important control variable in plasma materials processing, especially for high aspect ratio (HAR) etching during microelectronics fabrication.[7] Maintaining the critical dimension (CD)—such as a specified angle of the side wall—during etching without reducing the etch rate requires optimizing the IED. A number of strategies have been developed to achieve this goal, including manipulating the shape of the bias voltage waveform [18], applying multiple frequencies [19], and pulsing either or both of the power supplies when using multiple frequencies.[20–24].

As integrated circuit features continue to shrink, the HAR dielectric etching in microelectronics fabrication using DF-CCP continues to offer a challenge in optimizing the feature profile. Feature scale etch or deposition properties in the plasma processing of microelectronic devices are determined by the energies and fluxes of radicals and ions to the wafer. These fluxes are ultimately managed by controlling and customizing the EED that determines the dissociation patterns of feedstock gases. In quasi steady state operation, an equilibrium condition for EED results from a real-time balance between electron sources and sinks. As such, for a given geometry, pressure, and frequency of operation, there is not much latitude in controlling EED. By using pulse power, electron sources and sinks do not need to instantaneously balance—they need to balance only over the longer pulse period. This provides additional leverage for controlling EED. Using a pulsed power in CCPs is attractive for controlling EED and plasma properties, as it provides a means for producing combinations of fluxes (e.g., magnitude, identity, and energy) not otherwise attainable using continuous wave (CW) excitation. For example, with CW operation, the rate coefficient is

$$k_{CW} = \int_0^{\infty} f_{CW}(\varepsilon, t) \left( \frac{2\varepsilon}{m_e} \right)^{1/2} \sigma(\varepsilon) d\varepsilon, \quad (1.2)$$

whereas, in the pulse powered systems, the cycle average rate coefficient is

$$k_{ave-pulsed} = \int_0^{\infty} \left[ \frac{1}{\tau} \int_0^{\tau} f_{pulsed}(\varepsilon, t) dt \right] \left( \frac{2\varepsilon}{m_e} \right)^{1/2} \sigma(\varepsilon) d\varepsilon. \quad (1.3)$$

As a result, the customization of  $f_{pulsed}(\varepsilon, t)$  can provide the controlled generation of reactive species in the plasma processing chamber. In these systems, the choice of duty cycle is important in determining the cycle average value of EED due to the role of the thermalization of electrons during the afterglow. Also, the IED determines the anisotropic profile in HAR etching as the ions are hitting the wafer surface in the perpendicular direction, which can be customized by the relationship between applied power and sheath potential. In pulse-powered DF-CCP, the blocking capacitor is connected in series to the substrate, which determines the IED. With pulse mode operation, the control of IED can be achieved due to the RC time constant. The ability to control EED and IED may have both clear and subtle effects on the critical dimensions (CD) of etch features. For example, charge accumulation in the feature and the angular spread of ions may be controlled by the choice of duty cycle, both of which affect the etch profile. This gives process engineers some ability to control, for example, the sidewall slope of HAR features by pulse-power formats.

Controlling EED is important not only in the HAR etching, but also in any plasma application. Since EED is the fundamental parameter in understanding the physics behind plasma properties, it often needs to be controlled for the desired application. Employing a magnetic field can be an option for manipulating the EED. A magnetic field has been used in a variety of plasma applications in order to manipulate not only the spatial distribution but also the peak value of plasma parameters. The plasma sources using magnetic fields include electron cyclotron resonance (ECR) discharge [25,26], the magnetically enhanced reactive ion etching

(MERIE) system [27], helicon discharge [28], a hollow cathode magnetron [29], and a hall thruster [30–32]. Computational investigations have been attempted to better understand magnetized plasmas.[33–35] Although these plasmas are developed for different applications—such as etching, deposition, ion source, and propulsion—the fundamental physics behind using magnetic fields is controlling the energy distributions of electrons, ions, and neutrals.[36–38] Although the magnetic field cannot do work, the spatial distribution of particle’s energy is modified due to the magnetic confinement of charged species and this indirectly affects neutral species distribution as well. In particular, electron kinetics in the magnetized plasma has been intensively studied both experimentally [39–43] and computationally [44–50]. Computational investigation into the electron kinetics in magnetized plasmas includes using analytic models [44–47], a fluid method [48], and particle simulation [49,50].

Using an energetic electron beam can be another option for controlling EED. In the dc-augmented CCP, the secondary electron emitted from the biased electrode has enough energy to heat up the plasma. The electrons are characterized into two groups: one is secondary electrons and the other is bulk electrons. The secondary electrons have a high energy due to the acceleration in the sheath after being emitted from the surface. The high-energy secondary electrons are also called beam electrons because of their ballistic characteristics. The bulk electrons represent the electrons in the bulk plasma that have relatively low energy compared to the secondary electrons. Although the cross section of the beam electrons for the Coulomb collision is inversely proportional to their energy, the bulk electrons can interact with the beam electrons through electron-electron ( $e-e$ ) Coulomb collisions to gain some energy from the interaction. Also, some of the beam electrons can be trapped between the electrodes by the sheath potential, and have more opportunity to interact with bulk electrons to deliver their energy

into the bulk plasma. Historically, the electron beam has been used to sustain the plasma or to manipulate the EED properly to efficiently create particular radicals.[51] In the *RF* discharge, the secondary electrons are important for sustaining the plasma.[52] Hass *et al.* [53] has theoretically studied the effect of the secondary electrons on the energy distribution of the bulk electrons. By considering the *e-e* collision, the electron beam effect on the EED was investigated by Bretagne *et al.* [54].

## 1.5 Computational Modeling of Plasma Kinetics

As the number of control parameters increases in the plasma equipment for the semiconductor manufacturing, the design and process optimizations for the plasma equipment are limited by the time and cost. It therefore cannot be emphasized enough that understanding plasma physics and predicting the plasma parameters using appropriate computational tools is essential for the microelectronics manufacturing industry. Advanced computational simulation software has become essential to helping tool manufacturers and process recipe designers select the design parameters of the plasma devices better. As a result, the prediction, assessment, and understanding of the physics behind the plasma technology using a computational method leads directly to the improved quality and production yields of microelectronic chips.

For plasma simulation, there are three approaches: fluid, kinetic, and hybrid. The fluid approach solves continuity, momentum, and energy equations, and is the fastest approach among these. However, many kinetic phenomena in plasmas result from the individual motion and collective behavior of charge particles, especially in a low pressure environment. The kinetic simulations include Particle-in-cell with Monte Carlo Collisions (PIC-MCC) [55] or Direct Simulation Monte Carlo (DSMC) [56]. Since the kinetic approaches yield the particle distributions as an output, they are often used for investigating EED and IED. However, the

Monte Carlo method is computationally expensive because it typically uses a number of pseudoparticles (on the order of  $10^6$ ) that represent a large number of real particles (electrons, ions, and neutrals). The hybrid method becomes attractive for preserving the accuracy of kinetic simulations and at the same time reducing the computational burden by combining particle and fluid approaches.[57] In the hybrid approach, the electrons are treated as a particle since they are very mobile compared to the other species, while the heavy particles (ions and neutrals) are treated as a fluid. For some other applications—such as a thruster where the ion kinetics are important—the ions are simulated as a particle while electrons and neutrals are handled as a fluid. In any combination of the particle and fluid technique, the hybrid simulation greatly improves the computational performance without sacrificing accuracy. Parallel computing is another option for compensating for the computational burden, and has become popular due to multicore processors.

## **1.6 Summary**

This thesis is about my journey, starting from the fundamental physics of plasma and stretching towards application. The organization of this thesis is as follows.

In Chapter 2, a detailed description of models used in this work is presented. The models include the two-dimensional (2d) Hybrid Plasma Equipment Model (HPEM) for the reactor scale investigation and the Monte Carlo Feature Profile Model (MCFPM) for the feature scale simulation. The fluxes of reactant species incident on the wafer and their energy and angular distributions obtained from HPEM are used as inputs to the MCFPM. The algorithms developed in this work were incorporated into HPEM and MCFPM.

In Chapter 3, EEDs in a magnetized inductively coupled plasma (mICP) sustained in Ar are discussed with results from a two-dimensional plasma hydrodynamics model. Results are

compared with experimental measurements by others. We found that the character of the EED indeed changes from non-local to local depending on the magnitude of the magnetic field, pressure and power. Since the electrons are confined within the magnetic field line, ambipolar diffusion across the magnetic field is greatly diminished. For example, if the magnetic field is applied across the plasma that is generated by the *RF* power applied through the antenna coil, the hot electrons generated adjacent to the dielectric wall cannot move across the magnetic field line. Thus, EEDs are differentiated by the positions in the chamber.

In Chapter 4, the kinetic role of beam-like secondary electrons emitted from the biased electrode in the CCP is discussed. The secondary electrons are emitted from the chamber walls including electrodes due to the bombardment of particles such as ions, electrons, neutrals, and photons produced in the plasma. Once emitted from the surface, the secondary electrons are accelerated into the plasma by the large electric field in the sheath. In one configuration, one of the electrodes is negatively biased with direct current (dc) voltage in order to enlarge the sheath potential on the electrode. These fast electrons may interact with electrons in the bulk plasma through electron-electron (*e-e*) collisions to transfer energy to the bulk electrons. If the fast electrons do not lose enough energy through collisions, they can reach the other electrode and return by the potential barrier at the sheath boundary. Thus, the fast electrons can bounce back and forth between two electrodes until they finally lose most of their energy through collisions. This way the beam-like secondary electrons deliver their energy to the bulk electrons, such that the EED in the bulk plasma can be modified by the secondary electrons.

In Chapter 5, the properties of EED in the *HF*-pulsed DF-CCP sustained in Ar and Ar/CF<sub>4</sub>/O<sub>2</sub> are discussed with the same average power applied. The oscillating sheath boundary adjacent to the electrodes accelerates the electrons and is often called stochastic heating or

collisionless heating. Thus, as the *HF* power is turned on and off, the EED is drastically manipulated. High-energy electrons are instantaneously generated at the leading edge of the *power-ON* stage, but these hot electrons immediately disappear through the diffusion and collisions as soon as the pulsed power is turned off. The population change of the hot electrons over the pulse period is larger in Ar/CF<sub>4</sub>/O<sub>2</sub> than in Ar due to an increased collisional thermalization of electrons with CF<sub>4</sub> and O<sub>2</sub>.

In Chapter 6, the properties of IED in pulse-powered DF-CCP sustained in Ar/CF<sub>4</sub>/O<sub>2</sub> are discussed by pulsing either the *LF* or *HF* power. In order to do side-by-side comparisons of IEDs when varying other parameters, the power is specified by the voltage amplitude. The plasma typically has a higher potential than the chamber wall including electrodes because electrons diffuse faster than ions but the plasma stays in quasi-neutral state through the naturally generated ambipolar potential. The ions are accelerated by the potential difference between the plasma and the substrate. Thus, the IEDs show different shapes and energy ranges depending on which power is operated in pulse mode. Also, the blocking capacitor provides additional leverage for customizing the IED in the pulse mode operation due to the different charging times of the capacitors; this is not attainable in the *CW* operation.

In Chapter 7, the properties of etching SiO<sub>2</sub> in pulse-powered DF-CCP sustained in Ar/CF<sub>4</sub>/O<sub>2</sub> are discussed using results from HPEM and MCFPM. The anisotropic etching is accomplished by combining the chemical and physical reactions. The incident radicals (O, F, CF, CF<sub>2</sub>, and CF<sub>3</sub>) on the wafer are responsible for the chemical reactions with SiO<sub>2</sub>, and the ions bombarding the wafer surface are responsible for the anisotropic physical reaction and the directional enhancement of the chemical reactions. Since the ions are directionally accelerated to hit perpendicular to the substrate as opposed to the neutral species, the ions enable the

anisotropic vertical etching. The ability to control EED is ultimately the means to control the generation of reactive species, and to control IED is directly related to the etching profile, selectivity, and damage. Based on the controllability of EED and IED using pulsed power, the etch properties are investigated with different configurations of a pulse-power system.

In Chapter 8, an overview of research is presented for each topic discussed in the previous chapters with general conclusions. Possible future works are also suggested.

## 1.7 Figures

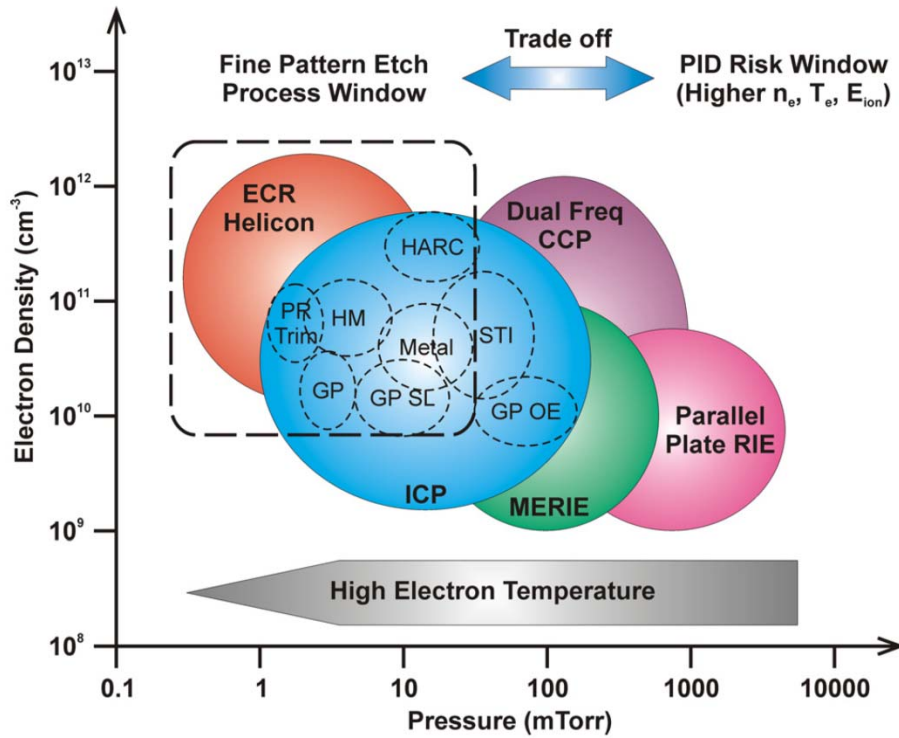


Fig. 1.1 Different plasma etching systems as a function of plasma density and pressure.[1]  
 Acronyms key: ECR – electron cyclotron resonance, PR – photo resist, HM – hard mask, GP – gate poly, OE – over etch, SL – soft landing, HARC – high aspect ratio contact, STI – shallow trench isolation, ICP – inductively coupled plasma, CCP – capacitively coupled plasma, RIE – reactive ion etching, MERIE – magnetically enhanced RIE.

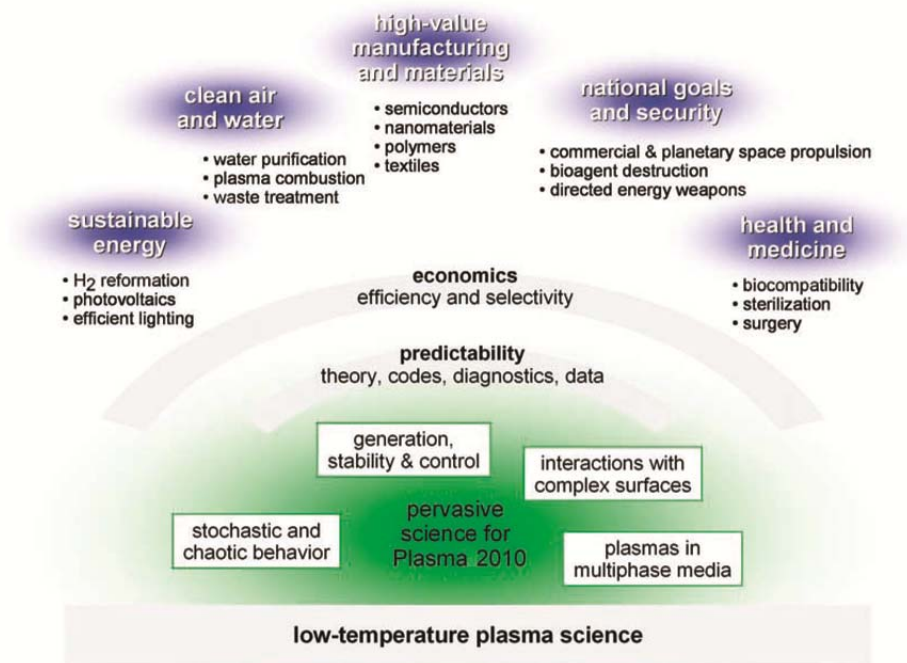


Fig. 1.2 A number of applications using low-temperature plasma technology.[4]

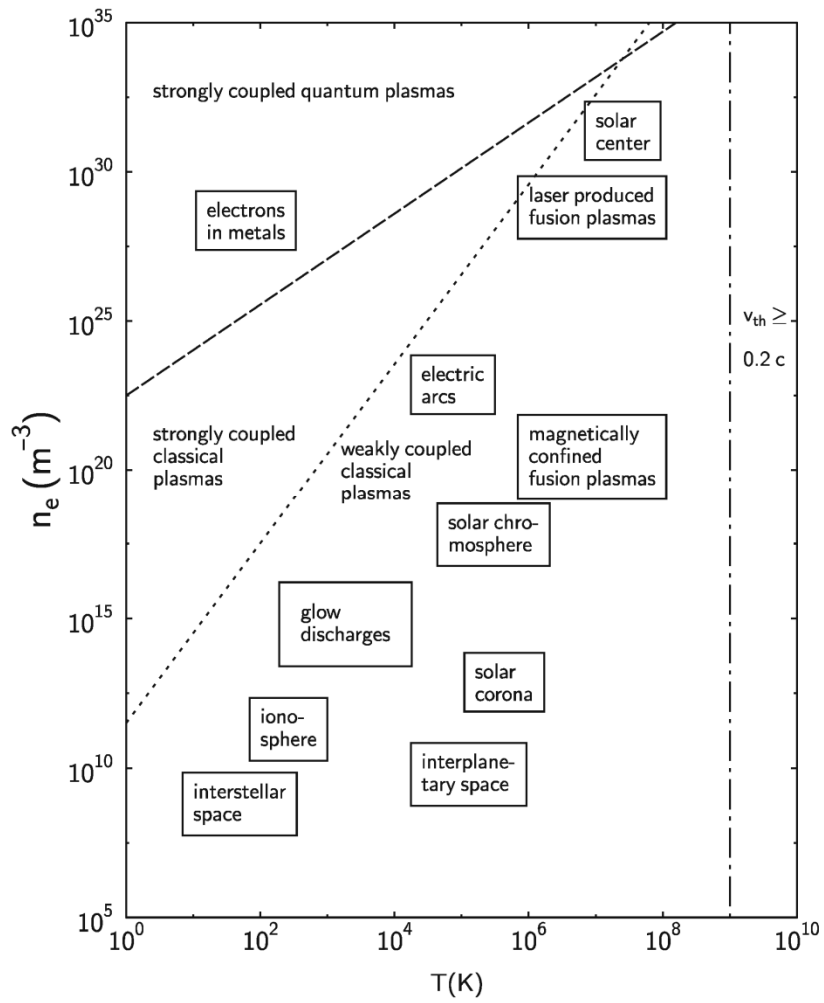


Fig. 1.3 Plasma classification by its density and temperature. Relativistic effects play a role for  $T > 10^9$  K.[6]

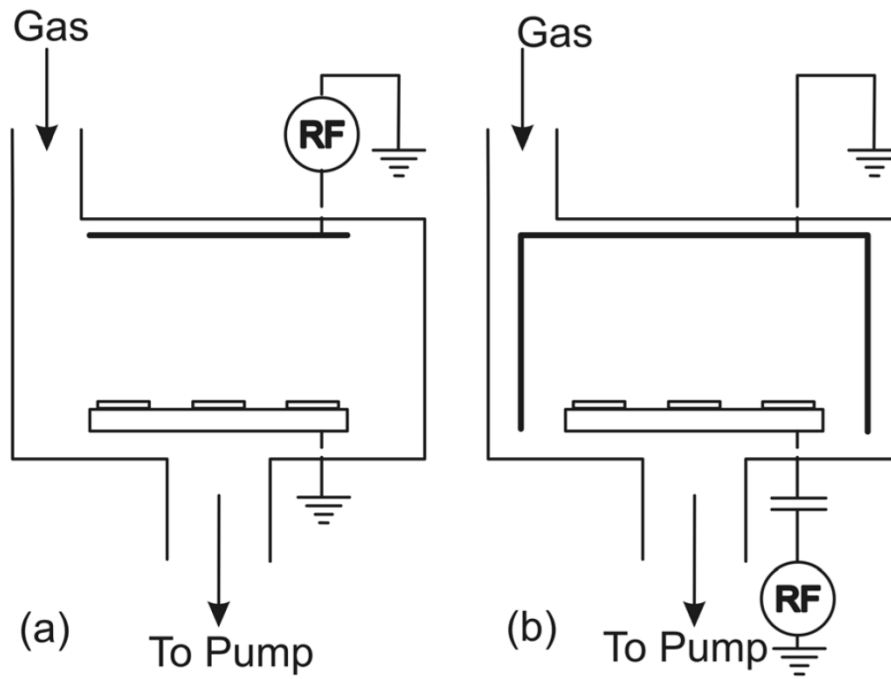


Fig. 1.4 Schematic diagram for parallel plate reactors: (a) “PE mode” – wafer on grounded electrode; (b) “RIE mode” – wafer on *RF* powered electrode.[7]

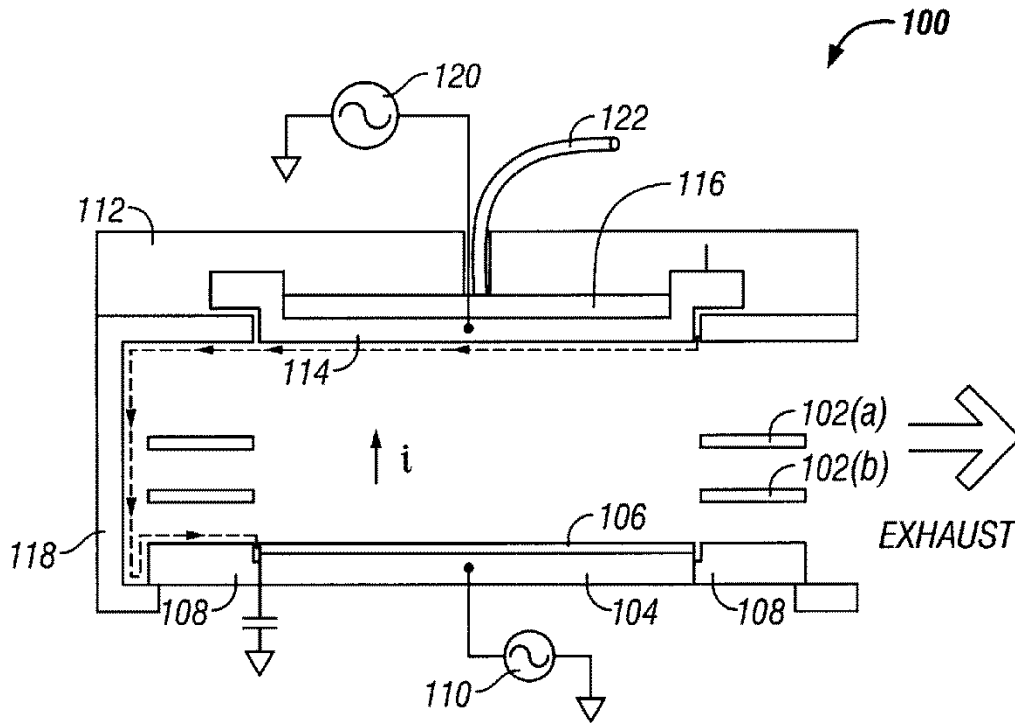


Fig. 1.5 Schematic diagram of dual frequency CCP in which the *RF* powers are applied to both of the electrodes.[8]

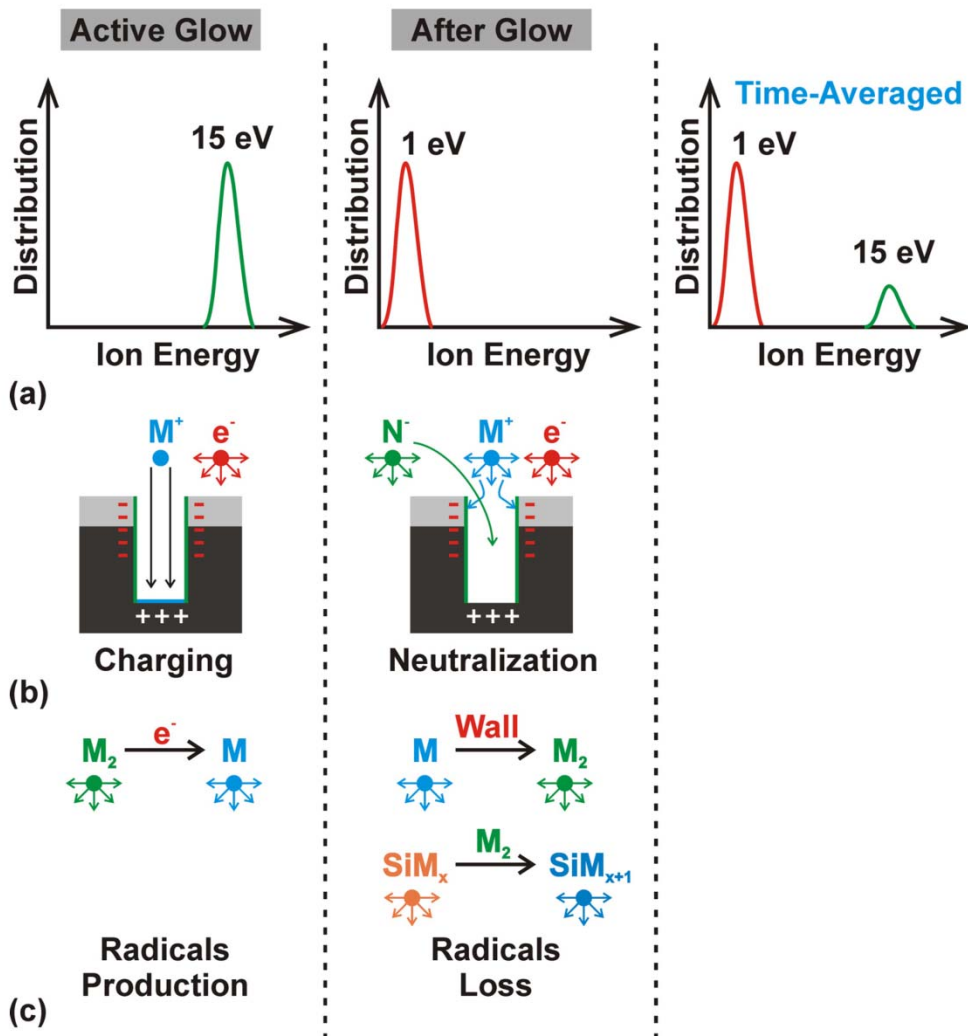


Fig. 1.6 Illustration of plasma kinetics in the pulse powered system.[9] (a) Ion energy distribution, (b) charge distribution on the feature, and (c) source and loss mechanism of radicals during *power-ON* and *-OFF* cycles.

## 1.8 References

1. K. Tokashiki, H. Cho, S. Banna, J.-Y. Lee, K. Shin, V. Todorow, W.-S. Kim, K. Bai, S. Joo, J.-D. Choe, K. Ramaswamy, A. Agarwal, S. Rauf, K. Collins, S. J. Choi, H. Cho, H. J. Kim, C. Lee, D. Lymberopoulos, J. Yoon, W. Han, and J.-T. Moon, "Synchronous pulse operation upon source and bias radio frequencies for inductively coupled plasma for highly reliable gate etching technology", *Jpn. J. Appl. Phys.* **48**, 08HD01 (2009).
2. D. P. Mishra, *Fundamentals of Combustion* (Prentice-Hall of India Pvt. Ltd, New Delhi, 2008), p. 2.
3. W. Crookes, "On the Illumination of Lines of Molecular Pressure, and the Trajectory of Molecules", *Phil. Trans.* **170**, 135 (1879).
4. National Research Council, *Plasma Science: Advancing Knowledge in the National Interest* (National Academies Press, Washington, D.C., 2007), p. 39.
5. P. L. Fauchais, J. V. R. Heberlein, and M. I. Boulos, *Thermal Spray Fundamentals* (Springer, New York, 2014), p. 100.
6. Alexander Piel, *Plasma Physics – An introduction to Laboratory, Space, and Fusion Plasmas* (Springer, New York, 2010), p. 41.
7. V. M. Donnelly and A. Kornblit, "Plasma etching: Yesterday, today, and tomorrow", *J. Vac. Sci. Technol. A* **31**, 050825 (2013).
8. E. H. Lenz, "Plasma confinement by use of preferred RF return path", US Patent No. 6,602,381 (5 Aug. 2003).
9. S. Banna, A. Agarwal, G. Cunge, M. Darnon, E. Pargon, and O. Joubert, "Pulsed high-density plasmas for advanced dry etching processes", *J. Vac. Sci. Technol. A* **30**, 040801 (2012).
10. H. Sugai, I. Ghanashev, M. Hosokawa, K. Mizuno, K. Nakamura, H. Toyoda, and K. Yamauchi, "Electron energy distribution functions and the influence on fluorocarbon plasma chemistry", *Plasma Sources Sci. Technol.* **10**, 378 (2001).
11. V. A. Godyak, R. B. Piejak, and B. M. Alexandrovich, "Measurement of the electron energy distribution in low pressure RF discharges", *Plasma Sources Sci. Technol.* **1**, 36 (1992).
12. D. D. Blackwell and F. F. Chen, "Time-resolved measurements of the electron energy distribution function in a helicon plasma", *Plasma Sources Sci. Technol.* **10**, 226 (2001).
13. V. A. Godyak and R. B. Piejak, "Abnormally low electron energy and heating-mode transition in a low-pressure argon RF discharge at 13.56 MHz", *Phys. Rev. Lett.* **65**, 996 (1990).
14. D. J. Heason and J. W. Bradley, "Modifying the IEDFs at a plasma boundary in a low-

- pressure RF discharge using electron beam injection”, *Plasma Sources Sci. Technol.* **10**, 627 (2001).
15. C. W. Chung, S. S. Kim, and H. Y. Chang, “Experimental measurement of the electron energy distribution function in the radio frequency electron cyclotron resonance inductive discharge”, *Phys. Rev. E* **69**, 016406 (2004).
  16. J. I. Hong, S. H. Seo, S. S. Kim, N. S. Yoon, C. S. Chang, and H. Y. Chang, “Electron temperature control with grid bias in inductively coupled argon plasma”, *Phys. Plasmas* **6**, 1017 (1999).
  17. H. Akashi, S. Samukawa, N. Takahashi, and T. Sasaki, “Dependence of frequency and pressure on electron energy distribution functions in low pressure plasma”, *Jpn. J. Appl. Phys.* **36**, 877 (1997).
  18. X. V. Qin, Y.-H. Ting, and A. E. Wendt, “Tailored Ion Energy Distributions at an rf-biased plasma electrode”, *Plasma Sources Sci. Technol.* **19**, 065014 (2010).
  19. S. H. Lee, P. K. Tiwari, and J. K. Lee, “Control of ion energy distribution in low-pressure and triple-frequency capacitive discharge”, *Plasma Sources Sci. Technol.* **18**, 025024 (2009).
  20. A. Agarwal, S. Rauf, and K. Collins, “Extraction of negative ions from pulsed electronegative capacitively coupled plasmas”, *J. Appl. Phys.* **112**, 033303 (2012).
  21. A. Agarwal, P. J. Stout, S. Banna, S. Rauf, K. Tokashiki, J.-Y. Lee, and K. Collins, “Effect of simultaneous source and bias pulsing in inductively coupled plasma etching”, *J. Appl. Phys.* **106**, 103305 (2009).
  22. S. Samukawa, “Pulse-time-modulated Electron Cyclotron Resonance Plasma Etching for Highly Selective, Highly Anisotropic, and Notch-free Polycrystalline Silicon Patterning”, *Appl. Phys. Lett.* **64**, 3398 (1994).
  23. S. Banna, A. Agarwal, K. Tokashiki, H. Cho, S. Rauf, V. Todorow, K. Ramaswamy, K. Collins, P. Stout, J.-Y. Lee, J. Yoon, K. Shin, S.-J. Choi, H.-S. Cho, H.-J. Kim, C. Lee, and D. Lymberopoulos, “Inductively coupled pulsed plasmas in the presence of synchronous pulsed substrate bias for robust, reliable, and fine conductor etching”, *IEEE Trans. Plasma Sci.* **37**, 1730 (2009).
  24. P. Diomedede, D. J. Economou, and V. M. Donnelly, “Particle-in-cell simulation of ion energy distributions on an electrode by applying tailored bias waveforms in the afterglow of a pulsed plasma”, *J. Appl. Phys.* **109**, 083302 (2011).
  25. J. Asmussen, “Electron cyclotron resonance microwave discharges for etching and thin-film deposition”, *J. Vac. Sci. Technol. A* **7**, 883 (1989).
  26. P. Roychowdhury, H. Kewlani, L. Mishra, D. S. Patil, and K. C. Mittal, “Langmuir probe diagnostics of plasma in high current electron cyclotron resonance proton ion source”, *Rev. Sci. Instrum.* **84**, 073303 (2013).

27. R. A. Lindley, C. H. Bjorkman, H. Shan, K.-H. Ke, K. Doan, R. R. Mett, and M. Welch, "Magnetic field optimization in a dielectric magnetically enhanced reactive ion etch reactor to produce an instantaneously uniform plasma", *J. Vac. Sci. Technol. A* **16**, 1600 (1998).
28. T. Harle, S. J. Pottinger, and V. J. Lappas, "Helicon double layer thruster operation in a low magnetic field mode", *Plasma Sources Sci. Technol.* **22**, 015015 (2013).
29. L. Wu, E. Ko, A. Dulkan, K. J. Park, S. Fields, K. Leeser, L. Meng, and D. N. Ruzic, "Flux and energy analysis of species in hollow cathode magnetron ionized physical vapor deposition of copper", *Rev. Sci. Instrum.* **81**, 123502 (2010).
30. J. A. Linnell and A. D. Gallimore, "Efficiency analysis of a Hall thruster operating with krypton and xenon", *J. Propul. Power* **22**, 1402 (2006).
31. Y. Raitses, E. Merino, and N. J. Fisch, "Cylindrical Hall thrusters with permanent magnets", *J. Appl. Phys.* **108**, 093307 (2010).
32. N. A. MacDonald, C. V. young, M. A. Cappelli, and W. A. Hargus, Jr., "Ion velocity and plasma potential measurements of a cylindrical cusped field thruster", *J. Appl. Phys.* **111**, 093303 (2012).
33. K. G. Kostov and J. J. Barroso, "Numerical simulation of magnetic-field-enhanced plasma immersion ion implantation in cylindrical geometry", *IEEE Tans. Plasma Sci.* **34**, 1127 (2006).
34. D. Benyoucef, M. Yousfi, and B. Belmadani, "Self-consistent particle modeling of radio frequency discharge in Ar/O<sub>2</sub> mixtures: Effects of crossed electric and magnetic fields and partial pressure", *J. Appl. Phys.* **109**, 083304 (2011).
35. I. D. Boyd and J. T. Yim, "Modeling of the near field plume of a Hall thruster", *J. Appl. Phys.* **95**, 4575 (2004).
36. W. Cronrath, N. Mayumi, M. D. Bowden, K. Uchino, M. Yoshida, and K. Muraoka, "A study of ion velocity distribution functions in processing plasmas produced by electron cyclotron discharges", *J. Appl. Phys.* **82**, 1036 (1997).
37. Z. Wang, S. A. Cohen, D. N. Ruzic, and M. J. Goeckner, "Nitrogen atom energy distributions in a hollow-cathode planar sputtering magnetron", *Phys. Rev. E* **61**, 1904 (2000).
38. Y. Hayakawa, K. Miyazaki, and S. Kitamura, "Measurements of electron energy distributions in an ion thruster", *J. Propul. Power* **8**, 118 (1992).
39. N. Hershkowitz and T. Intrator, "Improved source of cold plasma electrons and negative ions", *Rev. Sci. Instrum.* **52**, 1629 (1981).
40. J. Bretagne, W. G. Graham, and M. B. Hopkins, "A comparison of experimental and theoretical electron energy distribution functions in a multicusp ion source", *J. Phys. D* **24**, 668 (1991).

41. G.-H. Kim, N. Hershkowitz, D. A. Diebold, and M.-H. Cho, “Magnetic and collisional effects on presheaths”, *Phys. Plasmas* **2**, 3222 (1995).
42. A. Aanesland, J. Bredin, P. Chabert, and V. Godyak, “Electron energy distribution function and plasma parameters across magnetic filters”, *Appl. Phys. Lett.* **100**, 044102 (2012).
43. J. A. Monreal, P. Chabert, and V. Godyak, “Reduced electron temperature in a magnetized inductively-coupled plasma with internal coil”, *Phys. Plasmas* **20**, 103504 (2013).
44. V. Yu. Fedotov, A. A. Ivanov, G. Guerrini, A. N. Vesselovzorov, and M. Bacal, “On the electron energy distribution function in a Hall-type thruster”, *Phys. Plasmas* **6**, 4360 (1999).
45. S. S. Kim, C. S. Chang, N. S. Yoon, and K. W. Whang, “Inductively coupled plasma heating in a weakly magnetized plasma”, *Phys. Plasmas* **6**, 2926 (1999).
46. O. V. Polomarov, C. E. Theodosiou, I. D. Kaganovich, B. N. Ramamurthi, and D. J. Economou, “Effectiveness of electron-cyclotron and transmission resonance heating in inductively coupled plasmas”, *Phys. Plasmas* **12**, 104505 (2005).
47. A. Rehman and Y. K. Pu, “Effect of electron thermal motion on plasma heating in a magnetized inductively coupled plasma”, *Phys. Plasmas* **14**, 063503 (2007).
48. A. Rehman and J. K. Lee, “Effective viscosity model for electron heating in warm magnetized inductively coupled plasma discharges”, *Phys. Plasmas* **16**, 083504 (2009).
49. D. H. Kim and C.-M. Ryu, “Particle simulation of a magnetically enhanced dual-frequency capacitively coupled plasma”, *J. Phys. D: Appl. Phys.* **41**, 015207 (2008).
50. F. Taccogna, R. Schneider, S. Longo, and M. Capitelli, “Kinetic simulations of a plasma thruster”, *Plasma Sources Sci. Technol.* **17**, 024003 (2008).
51. N. P. Vagin, A. A. Ionin, Yu. M. Klimachev, A. A. Kotkov, I. V. Kochetov, A. P. Napartovich, Yu. P. Podmar’kov, L. V. Seleznev, D. V. Sinitsyn, M. P. Frolov, G. D. Hager, and N. N. Yuryshv, “Pulsed electron-beam-sustained discharge in oxygen-containing gas mixtures: electrical characteristics, spectroscopy, and singlet oxygen yield”, *Quantum Electronics* **34**, 865 (2004).
52. V. A. Godyak and A. S. Khanneh, “Ion bombardment secondary electron maintenance of steady RF discharge”, *IEEE Trans. on Plasma Sci.* **PS-14**, 112 (1986).
53. F. A. Haas, A. Goodyear, and N. St. J. Braithwaite, “Tailoring of electron energy distributions in low temperature plasmas”, *Plasma Sources Sci. Technol.* **7**, 471 (1998).
54. J. Bretagne, G. Delouya, C. Gorse, M. Capitelli, and M. Bacal, “Electron energy distribution functions in electron-beam-sustained discharges: application to magnetic multicusp hydrogen discharges”, *J. Phys. D: Appl. Phys.* **18**, 811 (1985).
55. Y. Takao, N. Kusaba, K. Eriguchi, and K. Ono, “Two-dimensional particle-in-cell Monte

Carlo simulation of a miniature inductively coupled plasma source”, J. Appl. Phys. **108**, 093309 (2010).

56. J. Johannes, T. Bartel, G. A. Hebner, J. Woodworth, and D. J. Economou, “Direct Simulation Monte Carlo of Inductively Coupled Plasma and Comparison with Experiments”, J. Electrochem. Soc. **144**, 2448 (1997).
57. A. Bogaerts, R. Gijbels, and W. Goedheer, “Hybrid Modeling of a Capacitively Coupled Radio Frequency Glow Discharge in Argon: Combined Monte Carlo and Fluid Model”, Jpn. J. Appl. Phys. **38**, 4404 (1999).

## Chapter 2 DESCRIPTION OF THE MODEL

### 2.1 Hybrid Plasma Equipment Model (HPEM)

The model used in this thesis is a two-dimensional fluid hydrodynamics simulation, the Hybrid Plasma Equipment Model (HPEM), which combines separate modules that address different physical phenomena.[1-18] The HPEM is a plasma equipment model developed to simulate low-pressure ( $< 10$ 's Torr) plasma sources. For example, the HPEM is capable of modeling a broad range of types of plasma processing reactors, such as inductively coupled plasma (ICP) sources, reactive ion etching (RIE) tools, electron cyclotron resonance (ECR) plasmas, ionized metal physical vapor deposition (IMPVD) tools, and plasma enhanced chemical vapor deposition (PECVD) systems. For the specific application, not all modules in the HPEM will necessarily be called. For example, electron density and collision frequency are functions of the electron energy distribution,  $f(\varepsilon, \vec{r}, \phi)$ , which are dependent on the electric field and gas density. The electrostatic field is obtained by either directly solving Poisson's equation or using an ambipolar approximation. The  $f(\varepsilon, \vec{r}, \phi)$  can be obtained either by solving an electron energy equation or using a Monte-Carlo technique. In this study, Poisson's equation is directly solved and the electron transport is obtained from using Monte-Carlo technique. An example of results from HPEM is illustrated in Fig. 2.1.

The modules used in this study include a fluid kinetics-Poisson module (FKPM), an

electromagnetic module (EMM), an electron energy transport module (EETM), a Plasma chemistry Monte Carlo module (PCMCM). In FKPM, continuity, momentum, and energy equations for neutrals and ions; continuity equations for electrons and Poisson's equation for the electric potential are integrated in time to obtain a periodic steady state. The EMM calculates inductively coupled electric (from  $RF$  coils) and magnetic fields as well as static magnetic fields produced by dc magnetic fields produced by magnetic coils or permanent magnet. The EETM calculates electron kinetics properties such as an electron energy distribution, electron temperature, and electron impact coefficients. For this investigation, the trajectories of electron pseudoparticles are calculated using Monte-Carlo technique based on the electrostatic fields computed in FKPM, electromagnetic and magnetostatic fields computed in EMM. The resulting electric fields and ion fluxes to surfaces obtained from the FKPM are periodically transferred to the electron Monte-Carlo simulation (eMCS) where the electron energy transport of bulk and secondary electrons emitted from surfaces is addressed. Electron impact source functions and sources of secondary electron current are derived from these distribution functions and are returned to the FKPM. The process is iterated to convergence. The electric fields binned as a function of  $RF$  phase produced by the FKPM are interpolated for position and time in the EETM. Two sets of calculations are performed in the eMCS – for bulk electrons and for secondary electrons emitted from electrodes in response to ion bombardment.

The FKPM and EETM are sequentially and iteratively called during execution of the model. The time spent in the FKPM is chosen to be a small fraction of the pulsed period so that the electron transport and rate coefficients are frequently updated. The source functions for generation of the ions from all sources (electron impact and heavy particle collisions) and electric fields computed in the FKPM are exported to the PCMCM. Pseudoparticles,

representing ions in PCMCM, are launched during the  $RF$  period at locations weighted by their source functions throughout the plasma volume. The trajectories of the pseudoparticles are integrated by interpolating electric fields in space and time in the same manner as in the eMCS. The gas phase collisional processes of the pseudoparticles are computed based on the same reaction mechanism as in the FKPM. The trajectories of the pseudoparticles are followed until they strike the surface at which time their energy and angular distributions are recorded.

### 2.1.1 The Fluid Kinetics-Poisson Module (FKPM)

In the FKPM, continuity, momentum and energy equations are solved for all neutral particles and ions. The plasma conductivity produced in the FKPM is passed to the EMM, and the species densities and time dependent electrostatic potential are passed to the eMCS. The equations solved for neutral and ion transport (continuity, momentum and energy) are

$$\frac{\partial N_i}{\partial t} = -\nabla \cdot \vec{\phi}_i + S_i - \left[ \sum_j \gamma_{ij} (\nabla \cdot \vec{\phi}_j) \right]_S, \quad (2.1)$$

$$\begin{aligned} \frac{\partial \vec{\phi}_i}{\partial t} = \frac{\partial(N_i \vec{v}_i)}{\partial t} = & -\frac{1}{m_i} \nabla(kN_i T_i) - \nabla \cdot (N_i \vec{v}_i \vec{v}_i) + \frac{q_i N_i}{m_i} \times (\vec{E}_S + \vec{v}_i \times \vec{B}) \\ & - \nabla \cdot \vec{\tau}_i - \sum_j \frac{m_j}{m_i + m_j} N_i N_j k_{ij} (\vec{v}_i - \vec{v}_j) + S_{mi}, \end{aligned} \quad (2.2)$$

$$\begin{aligned} \frac{\partial(N_i c_i T_i)}{\partial t} = & \nabla \cdot \kappa_i \nabla T_i - P_i \nabla \cdot \vec{v}_i - \nabla \cdot (N_i \vec{v}_i \varepsilon_i) \\ & + \frac{N_i q_i^2}{m_i v_i} E_S^2 + \frac{N_i q_i^2 v_i}{m_i (v_i^2 + \omega^2)} E_\Theta^2 \\ & + \sum_j 3 \frac{m_{ij}}{m_i + m_j} N_i N_j k_{ij} k_B (T_j - T_i) \pm \sum_j 3 N_i N_j R_{ij} k_B T_j. \end{aligned} \quad (2.3)$$

In Eq. (2.1),  $N_i$  is density of species  $i$ ,  $\vec{\phi}_i$  is the flux of species,  $S_i$  is the source due to gas phase collision processes,  $\gamma_{ij}$  is the coefficient for production of species  $i$  by reactions of species  $j$  on a surface. In Eq. (2.2),  $\vec{v}_i$  is velocity,  $m_i$  is the mass,  $T_i$  is temperature,  $E_s$  is the electrostatic field,  $\bar{\tau}_i$  is viscosity tensor,  $k_{ij}$  is the rate coefficient for momentum transfer collisions between heavy species  $i$  and  $j$ . The last term  $S_{mi}$  is the rate of generation and loss of momentum for species  $i$  resulting from collisions which change the identity of the reactant. The viscosity term is included for only neutrals because viscous forces are negligible for ions for our conditions. The transport properties are either taken from a database or calculated from Lenard-Jones parameters. Slip boundary conditions are employed for the momentum equation using the method described by Thompson.[19] In Eq. (2.3),  $c_i$  is the heat capacity in a relation of  $\varepsilon_i = c_i T_i$ ,  $\kappa_i$  is the thermal conductivity,  $P_i$  is the pressure,  $\nu_i$  is the momentum transfer collision frequency,  $E_\ominus$  is the  $RF$  electric field,  $\omega$  is the  $RF$  frequency,  $m_{ij} \equiv m_i m_j / (m_i + m_j)$  is the reduced mass,  $k_B$  is Boltzmann's constant, and  $R_{ij}$  is the rate coefficient for formation of the species by collisions between heavy particles. The first three terms on the RHS of Eq. (2.3) are power transfer by thermal conductivity, compressive heating, and advective transport. The following two terms are additional heating contributions for ions from both the electrostatic and electromagnetic fields. The last two sums are heating contributions from elastic collisions and charge exchange collisions (either positive or negative contribution). The thermal conductivity was obtained from

$$\kappa_i = k_B N_i \left( \frac{8k_B T_i}{\pi m_i} \right)^{1/2} \left[ \sum_j 2N_j \sigma_{ij} (m_{ij}/m_i)^{1/2} \right]^{-1}, \quad (2.4)$$

where  $\sigma_{ij}$  is the Lennard-Jones collision cross section for species  $i$  and  $j$ . The rate constants for elastic collisions are

$$k_{ij} = \left( \frac{8k_B T_{eff}}{\pi m_{ij}} \right)^{1/2} \sigma_{ij}, \quad (2.5)$$

where  $T_{eff} = T_i + m_{ij}(\vec{v}_i - \vec{v}_j)^2 / 3k_B$  is the effective temperature which takes account of the directed motion of the particles. Lennard-Jones parameters were used to compute the cross section.[20,21] A temperature jump at reactor walls is accounted for using the method developed by Kennard.[22] The difference between the wall temperature  $T_w$  and the gas temperature  $T_g$  at the wall is given by

$$T_w - T_g = \frac{(2-\alpha)(9\gamma-5)\lambda}{2\alpha(\gamma+1)} \frac{\partial T_g}{\partial x}, \quad (2.6)$$

where  $\alpha$ ,  $\lambda$ , and  $\gamma$  are the thermal accommodation coefficient, ratio of specific heats, and the mean free path, respectively. The accommodation coefficient determines how well the gas is thermally coupled to the surface and its value varies from 0 (no coupling) to 1 (perfect coupling). In this study, a thermal accommodation coefficient ranges from 0.75 to 1.

For electrons, only the continuity equation is solved and the flux is obtained assuming either drift-diffusion approximation or Scharfetter-Gummel [23] instead of solving the momentum equation. Also, the electron energy is obtained from the eMCS instead of solving the energy equation. Consequently, rate coefficients for electron impact processes are derived from electron energy distribution,  $f(\varepsilon, \vec{r}, \phi)$ , obtained in eMCS. The electron fluxes can be computed by various methods. The first method is using the conventional drift-diffusion approximation which calculated electron fluxes by

$$\vec{\phi}_e = n_e \overline{\overline{\mu}}_e \cdot \vec{E} - \overline{\overline{D}}_e \cdot \nabla n_e, \quad (2.7)$$

where  $n_e$  is density of electrons moving in the electric field  $\vec{E}$  and having tensor mobility  $\overline{\overline{\mu}}_e$ , and tensor diffusivity  $\overline{\overline{D}}_e$ . In the presence of static magnetic field, the transport coefficients (mobility and diffusivity) for electron (or ion) transport are of tensor forms  $\overline{\overline{A}}$  that are derived from their isotropic values,  $A_0$ , by

$$\overline{\overline{A}} = \frac{A_0}{\alpha^2 + |B|^2} \times \begin{pmatrix} \alpha^2 + B_r^2 & \alpha B_z + B_r B_\theta & -\alpha B_\theta + B_r B_z \\ -\alpha B_z + B_r B_\theta & \alpha^2 + B_\theta^2 & \alpha B_r + B_\theta B_z \\ \alpha B_\theta + B_r B_z & -\alpha B_r + B_\theta B_z & \alpha^2 + B_z^2 \end{pmatrix}, \quad (2.8)$$

where  $\alpha = m_e(v_m + i\omega)/q$ .

Alternatively, the electron flux can be computed by the Scharfetter-Gummel discretization.[23] Combining upwind and downwind techniques, the flux  $\vec{\phi}_{i+\frac{1}{2}}$  between node  $i$  and neighbor  $i+1$  separated by  $\Delta x$  is given by

$$\vec{\phi}_{i+\frac{1}{2}} = \frac{\alpha \overline{D} (n_{i+1} - n_i \exp(\alpha \Delta x))}{(1 - \exp(\alpha \Delta x))}, \quad (2.9)$$

where  $\alpha$  is given by

$$\alpha = \frac{\left(\frac{q}{|q|}\right) \overline{\mu} \left(\frac{\Phi_{i+1} - \Phi_i}{\Delta x}\right)}{\overline{D}}, \quad (2.10)$$

and  $\overline{D} = 0.5 \times (D_{i+1} + D_i)$  is the average diffusion coefficient, and  $\overline{\mu} = 0.5 \times (\mu_{i+1} + \mu_i)$  is the average mobility in the interval.

The ion and neutral flux calculation can be done using the drift diffusion equation or by including the effects of momentum by the replacement of the diffusional term with terms for

pressure, advection, and collision, as shown in Eq. (2.2). Determination of the time-dependent electrostatic fields is accomplished either by solution of Poisson's equation or based on quasi-neutrality allowing an ambipolar approximation. For the investigation in this thesis, the ion and neutral fluxes are obtained by solving the momentum equation and the electrostatic fields are obtained from the solution of Poisson's equation.

Due to the tight coupling of electrostatic fields to the densities of charged particles, Poisson's equation is solved within the FKPM. The semi-implicit Poisson's equation is given by

$$-\nabla \cdot \varepsilon \nabla \Phi^{t+\Delta t} = \rho^{t+\Delta t} \quad (2.11)$$

where  $\varepsilon$  is the permittivity,  $\Phi^{t+\Delta t}$  is the electric potential at time  $t + \Delta t$ , and  $\rho^{t+\Delta t}$  is the net charge density at time  $t + \Delta t$ . The potential is solved for at a future time. Charged densities are provided by their present values plus an incremental prediction of their values at the future time based on the divergence of their fluxes provided by drift-diffusion expressions. Since the solution technique is semi-implicit, there is typically not a constraint on the dielectric relaxation time,  $\Delta t = \varepsilon_0 / \sigma$ , which is the ratio of the permittivity of free space ( $\varepsilon_0$ ) to the plasma conductivity ( $\sigma$ ). In practice, the explicit Poisson's equation is rarely used due to the limitation on the time step presented by the dielectric relaxation time that can be as small as a few picoseconds. Poisson's equation is calculated semi-implicitly by approximating the charge density linearly as

$$\rho^{t+\Delta t} = \rho^t + \Delta t \left. \frac{\partial \rho}{\partial t} \right|^{t+\Delta t} \quad (2.12)$$

where  $\rho^{t+\Delta t}$  is the charge density at time  $t + \Delta t$ , and  $\rho^t$  is the charge density at time  $t$ . The evolution rate of the charge density is determined by the gradient of the total current  $\vec{j}$ :

$$\frac{\partial \rho}{\partial t} = -\nabla \cdot \vec{j} + S. \quad (2.13)$$

When the  $\vec{j}$  is obtained using drift-diffusion approximation, the form of Eq. (2.11) is then

$$\begin{aligned} -\nabla \cdot (\varepsilon \nabla \Phi^{t+\Delta t}) = & \rho_m^t + \sum_i q_i N_i^t + \Delta t \cdot \left[ \frac{\partial \rho_m(t')}{\partial t} - q_e \nabla \cdot \vec{\phi}_e(t') \right. \\ & \left. - \sum_j q_j \nabla \cdot \left( \vec{\phi}_j(t) + \frac{\Delta t}{2} \frac{\partial \vec{\phi}_j(t)}{\partial t} \right) \right], \end{aligned} \quad (2.14)$$

where  $\varepsilon$  is the local permittivity,  $\rho_m$  is the charge density in or on non-plasma materials,  $q_i$  is the electrical charge of species  $i$ , and  $N_i$  is the density. The species density and charge density are evaluated at  $t$ , while  $t'$  denotes that the densities are evaluated at  $t$  but the potentials are evaluated at  $t + \Delta t$ . The appearance of the potential in the fluxes provides a degree of implicitness. When the  $\vec{j}$  is obtained using Scharfetter-Gummel fluxes, the form of Eq. (2.11) is then

$$\begin{aligned} -\nabla \cdot (\varepsilon \nabla \Phi^{t+\Delta t}) = & \rho_m^t + \sum_i q_i N_i^t + \Delta t \cdot \left[ \frac{\partial \rho_m(t')}{\partial t} \right. \\ & \left. - q_e \nabla \cdot \left( \vec{\phi}_e(t) + \frac{\partial \vec{\phi}_e}{\partial \Phi} [\Phi^{t+\Delta t} - \Phi^t] \right) \right. \\ & \left. - \sum_j q_j \nabla \cdot \left( \vec{\phi}_j(t) + \frac{\Delta t}{2} \frac{\partial \vec{\phi}_j(t)}{\partial t} \right) \right], \end{aligned} \quad (2.15)$$

where  $\rho_m$  is the charge density on surfaces and in materials,  $\varepsilon$  is the local permittivity either in the plasma, non-plasma gases or materials,  $\vec{\phi}_e$  and  $\vec{\phi}_j$  are the fluxes of electrons and ions.  $\rho_m$  and  $N_i$  are evaluated at  $t$ , while potentials are evaluated at  $t + \Delta t$ , thereby providing implicitness. Jacobian elements  $\frac{\partial \vec{\phi}_e}{\partial \Phi}$  in Eq. (2.15) are the first-order partial derivatives of the

function  $\vec{\phi}_e$  with respect to  $\Phi$ . Here, Jacobian elements are numerically evaluated by perturbing  $\Phi$  a small fractional value and computing the change in  $\vec{\phi}_e$ . For example, due to the finite differencing method used the radial electron flux  $\phi_{i,j}$  at a location  $(i, j)$  in the numerical mesh is a function of the electrostatic potentials at that mesh point and all adjacent mesh points. In the absence of magnetostatic field, the numerical molecule contains contributions only from nearest neighbors which is five-point numerical molecule. In this case, an iterative method such as successive-over-relaxation (SOR) is a favorable method of solving Eqs. (2.14) and (2.15).[24] In this study, the typical SOR parameter was chosen to be 1.8. However, in the presence of the static magnetic field, all adjacent mesh points produce a 9-point numerical molecule and 9 terms in the sum over Jacobian elements in Eq. (2.15). In this case, a direct sparse matrix technique for solving Poisson's equation is preferred and the Jacobian element for  $\Phi_{i+1,j}$  is derived from

$$\frac{\partial \vec{\phi}_{i,j}}{\partial \Phi_{i+1,j}} = \frac{\vec{\phi}_{i,j}(\Phi_{i+1,j} + \Delta\Phi_{i+1,j}) - \vec{\phi}_{i,j}(\Phi_{i+1,j})}{\Delta\Phi_{i+1,j}}, \quad (2.16)$$

where  $\Delta\Phi_{i+1,j}$  is a predefined perturbation. A typical perturbation is 5% of the current value,  $\Delta\Phi_{i,j} = 0.05 \times \Phi_{i,j}$ . The sparse matrix solvers such as *dslucs* and *dslugm* is obtained from SLAP Sparse Matrix Library.[25] These solvers use bi-conjugate gradient matrix solution methods with incomplete *LU* factorization for preconditioning.

Acceleration techniques are used to speed the rate convergence of computed quantities. During execution of the FKPM, the cycle averaged time rate of change of densities is recorded over a period of many *RF* cycles. The integration is then paused and the densities of species are increased (or decreased) proportional to these average rates and the integration restarted. As different rates of acceleration are applied to different species depending on their derivatives, it is

difficult to assign a precise time interval for which the densities are projected into the future. For example, a well converged case will consist of approximately 100-200 iterations through the modules with 0.5-1  $\mu\text{s}$  of actual integration time (5-10 cycles at 10 MHz) occurring in the FKPM (or up to 2,000 cycles). For 10 cycles of actual time integration, acceleration will typically be applied after 2-3 cycles of the first 6 cycles, with no acceleration for the last cycles of the iteration. Based on convergence rates, this is effectively the equivalent of 50-100 times as many cycles. Since different species are accelerated at different rates, it is possible that the net charge density is not conserved through the acceleration process. To prevent unphysical transients in plasma potential and charging of surfaces, the charge density in each cell in the volume and on surfaces is recorded before acceleration. After the acceleration, the electron density is adjusted so that the charge density in each cell is the same as before the acceleration.

### **2.1.2 The Electromagnetics Module (EMM)**

The EMM calculates the electric and magnetic fields in the reactor as a function of position and phase during the *RF* cycle by solving Maxwell's equation under time harmonic conditions. The EMM also calculates the static magnetic fields generated by permanent magnets or by solenoid coils. When using fluid techniques to model plasma transport in the presence of static magnetic fields from a permanent magnet, tensor forms of the transport coefficients (e.g., conductivity, mobility, diffusion coefficient) should be used.

In the absence of the static magnetic field in cylindrical coordinates, an azimuthally symmetric antenna driven at *RF* frequencies will produce only an azimuthal ( $\theta$ ) component of the *RF* electric field, and radial ( $r$ ) and axial ( $z$ ) components of the *RF* magnetic field. The amplitude of the *RF* electric field is obtained solving the following form of the wave equation:

$$-\nabla\left(\frac{1}{\mu}\nabla\cdot\vec{E}\right)+\nabla\cdot\left(\frac{1}{\mu}\nabla\vec{E}\right)=\frac{\partial^2(\epsilon\vec{E})}{\partial t^2}+\frac{\partial(\vec{J}_{plasma}+\vec{J}_{antenna})}{\partial t}, \quad (2.17)$$

where  $\mu$  is the permeability,  $\vec{E}$  is the electric field,  $\epsilon$  is the permittivity,  $\vec{E}(r,t)=E_\theta(r)\exp(i\omega t)$  is the electric field from azimuthally symmetric antenna excited at frequency  $\omega$ ,  $\vec{J}_{antenna}(r,t)=J_\theta(r,\phi)$  is the antenna current density in the phase  $\phi$  during the *RF* cycle, and  $\vec{J}_{plasma}(r,\phi)=\overline{\overline{\sigma}}\cdot E_\theta(r,\phi)$  is the plasma current density by electrons with tensor conductivity  $\overline{\overline{\sigma}}$ . The ion current is ignored due to the low mobility of ions. Once the electric field is obtained, the *RF* magnetic field is computed from  $B(r,z)=(i/\omega)\nabla\times\vec{E}$ . The boundary conditions imposed upon the equation are that  $E_\theta=0$  on metal surfaces in the reactor and on the axis ( $r=0$ ).

In the presence of the static magnetic field, the tensor form of the conductivity is derived from its isotropic value,  $\sigma_0$  by

$$\overline{\overline{\sigma}}=\frac{\sigma_0}{\alpha^2+|B|^2}\times\begin{pmatrix} \alpha^2+B_r^2 & \alpha B_z+B_r B_\theta & -\alpha B_\theta+B_r B_z \\ -\alpha B_z+B_r B_\theta & \alpha^2+B_\theta^2 & \alpha B_r+B_\theta B_z \\ \alpha B_\theta+B_r B_z & -\alpha B_r+B_\theta B_z & \alpha^2+B_z^2 \end{pmatrix}, \quad (2.18)$$

$$\alpha=\frac{m_e(\nu_m+i\omega)}{q_e}, \quad (2.19)$$

$$\sigma_0=\frac{q_e^2 n_e}{m_e} \frac{1}{\nu_m(1+(\omega/\nu_m)^2)}, \quad (2.20)$$

where  $B$  is the static applied magnetic field,  $q_e$  is the unit electron charge,  $n_e$  represents electron density,  $m_e$  denotes electron mass,  $\nu_m$  is the electron momentum transfer collision frequency. With tensor transport coefficients, an azimuthally symmetric antenna in the presence

of a static magnetic field having  $(r, z)$  components will produce  $(r, z, \theta)$  components of both the  $RF$  electric and magnetic fields. The electromagnetic fields,  $E(r, z, \theta)$  and  $B(r, z, \theta)$ , in the entire volume of the reactor, are solved by conjugate gradient method using sparse matrix technique.

The leading divergence term in Eq. (2.17) can be either ignored or included based on the plasma conditions. The  $\nabla \cdot \vec{E}$  is typically needed to resolve the Trivelpiece-Gould (TG) wave which is an electrostatic wave identified by Trivelpiece and Gould as the cavity eigenmode of a cold plasma, space charge wave in a cylinder.[26] This term can be taken into account by using a perturbation form of Poisson's equation. For a quasi-neutral plasma, neglecting ion mobility over the  $RF$  cycle, the divergence of the electric field is equal to the perturbation in the electron density from neutrality, defined as,

$$\nabla \cdot \vec{E} = \frac{\Delta\rho}{\varepsilon} = \frac{q_e \Delta n_e}{\varepsilon}, \quad (2.21)$$

where  $\Delta\rho$  is a harmonically driven perturbation and  $\Delta n_e$  is perturbation to the electron density. On the time scale of the electromagnetic period, the total electron density,  $n_e(t)$ , is the sum of the steady state electron density  $n_e$ , and the perturbed electron density  $\Delta n_e \exp(i\omega t)$ ,

$$\frac{\partial n_e(t)}{\partial t} = \frac{\partial}{\partial t} [n_e + \Delta n_e \exp(i\omega t)] = i\omega \Delta n_e \exp(i\omega t). \quad (2.22)$$

The magnitude of the perturbed electron density is obtained by solving the continuity equation for the electron density, with an appropriate damping term,

$$\Delta n_e = \frac{-\nabla \cdot \left( \frac{\vec{\sigma} \cdot \vec{E}}{q} \right)}{\left( \frac{1}{\tau} + i\omega \right)}, \quad (2.23)$$

where the damping term factor  $\tau$  takes into account the average time it takes a perturbed electron to return the steady state. At high magnetic field ( $> 150$  G), the electrostatic waves deposit power primarily at the periphery of the plasma column. In this plasma condition, by setting  $\nabla \cdot \vec{E} = 0$ , we ignore the consequences of the electrostatic TG mode on plasma heating.

The static magnetic field,  $\vec{B}$ , is obtained from the vector potential  $\vec{A}$  expressed by

$$\nabla \times \frac{1}{\mu} \nabla \times \vec{A} = \vec{j}_c, \quad \vec{B} = \nabla \times \vec{A}, \quad (2.24)$$

where  $\vec{j}_c$  is the current density in reactor surrounding solenoids and  $\mu$  is the local permeability.

The current loops, which provide source terms when solving for vector potential  $\vec{A}$ , by differentiation, yields the static magnetic fields. The vector potential is solved using SOR method with an SOR parameter of 1.4, with the same convergence criteria as the electric field.[24] For the boundary conditions,  $\vec{A}$  is made zero on the extended boundaries and on the axis ( $r = 0$ ).

### 2.1.3 The Electron Monte Carlo Simulation (eMCS)

The Monte Carlo method is a fully kinetic treatment, which resolves the transport of electrons in electric and magnetic fields using a semi-implicit technique. The eMCS is a 3v-3d (3 velocity components, 3 dimensions) model which integrates electron trajectories in electric fields obtained from the fluid modules of the model, and employs Monte Carlo techniques for collisions with heavy particles and with other electrons. In the fluid portion of the model, charge densities and Poisson's equation are integrated as a function of time over many *RF* cycles. Over the last cycle of integration prior to calling the eMCS, the vector components of the electric field are recorded as a function of position and phase during the *RF* cycle,  $\vec{E}(\vec{r}, \phi)$ . These recordings

typically contain 200 phase points during the lower frequency  $RF$  cycle and are recorded on the same spatial mesh as the fluid portion of the model is performed. The cycle averaged densities of all charged and neutral species,  $N_i(\vec{r})$ , are also recorded. These electric fields and densities are transferred to the eMCS. In the eMCS, two simulations are performed – for bulk and for secondary beam electrons.

For the computation of the distribution function of bulk electrons,  $f_b(\varepsilon, \vec{r})$ , at the beginning of the first call to the eMCS, electrons are initially given a Maxwellian velocity distribution and placed in the reactor using a distribution weighted by the local electron density obtained from the fluid simulation. On subsequent calls to the eMCS, the trajectories are restarted from their coordinates at the end of the previous call to the eMCS. Particle trajectories are computed using the Lorentz equation,

$$\frac{d\vec{v}}{dt} = \frac{q_e}{m_e} (\vec{E} + \vec{v} \times \vec{B}) \quad (2.25)$$

and

$$\frac{d\vec{r}}{dt} = \vec{v} \quad (2.26)$$

where  $\vec{v}$ ,  $\vec{E}$  and  $\vec{B}$  are the electron velocity, local electric field, and magnetic field, respectively.

The trajectories of pseudoparticles are advanced using a second order Euler method. For integration of the trajectory (location  $\vec{r}$  and velocity  $\vec{v}$ ) of a pseudoparticle from  $t$  to  $t + \Delta t$ ,

$$\begin{aligned} \vec{r}'(t + \Delta t) &= \vec{r}(t) + \vec{v}(t)\Delta t, & \vec{v}'(t + \Delta t) &= \vec{v}(t) + \frac{q\vec{E}(\vec{r}(t), \phi(t))}{m_e} \Delta t, \\ \vec{r}(t + \Delta t) &= \vec{r}(t) + \frac{\Delta t}{2} (\vec{v}(t) + \vec{v}'(t + \Delta t)), \\ \vec{v}(t + \Delta t) &= \vec{v}(t) + \frac{q\Delta t}{2m_e} (\vec{E}(\vec{r}(t), \phi(t)) + \vec{E}(\vec{r}'(t + \Delta t), \phi(t + \Delta t))) \end{aligned} \quad (2.27)$$

where  $\vec{E}(\vec{r}(t), \phi(t))$  at an arbitrary position and time is obtained from a second order interpolation of the record of  $\vec{E}(\vec{r}, \phi)$  on the numerical mesh at fixed phase points. In this thesis, the calculation of densities and solution of Poisson's equation in the fluid portion of the model are performed in cylindrical coordinates with azimuthal symmetry,  $(r, z)$ . For computational convenience to more easily facilitate the collision operator, the integration of trajectories in the eMCS is performed in 3-d Cartesian coordinates. The cylindrical vector components of  $\vec{E}(r, z, \phi)$  are transformed to Cartesian vector components  $\vec{E}(x, y, z, \phi)$  based on the instantaneous position of each particle.

Since Poisson's equation is not being solved in the eMCS, the particles do not need to be at the same time unless statistics are being collected. Therefore, the time step  $\Delta t$  for each particle is independently chosen as the minimum of the following: a specified fraction of the *RF* cycle, the time to cross half of the computational mesh in any direction, the time to the next collision, the time for the particle to be decelerated to zero speed, or the time to when statistics are being collected when all particles should be at the same time,  $T_f$ . Once a particle has reached  $T_f$ , its trajectory is no longer integrated until other particles reach  $T_f$ . This is done in a computational efficient manner by stenciling out particles having already reached  $T_f$  and shuffling the arrays containing particle information so that there is a (nearly) continuous array of particles whose trajectories are being integrated. This enables more efficient pipelining of the numerical operations. After recording statistics, the trajectories are restarted. (In the case of two frequency excitation with the lower frequency being 10 MHz and the higher frequency being 40 MHz, the time-step is limited to be no greater than 0.5% of the low frequency cycle and 2% of the high frequency cycle.)

Statistics and collision frequencies are discretely collected or calculated on an energy grid.

Energy bins have constant widths over a specified energy range to simplify gathering statistical data while resolving the structure in electron impact cross sections. In this work, 500 total bins were used with energy ranges (100 bins/range) of 0-5, 5-12, 12-50, 50-300, and 300-1000 eV. (The extended range in energy is used to cover the energy of sheath accelerated secondary electrons.) Within energy bin  $i$ , the total collision frequency,  $\nu_i$ , is computed by summing all the possible collisions with heavy particles,

$$\nu_i = \left( \frac{2\varepsilon_i}{m_e} \right)^{1/2} \sum_{j,k} \sigma_{ijk} N_j, \quad (2.28)$$

where  $\varepsilon_i$  is the average energy within the bin,  $\sigma_{ijk}$  is the cross section at energy  $i$ , for species  $j$  and collision process  $k$ , and  $N_j$  is the number density of species  $j$ . As this point,  $\nu_i$  does not account for the frequency of electron-electron ( $e-e$ ) collisions since this frequency depends on the relative velocity of the collision partners and, therefore, depends on the dynamics of these trajectories during the simulation.

Separate null collision cross sections are used in each energy range to provide a constant collision frequency. This is accomplished by adding an additional fictitious process referred to as a null collision such that all electrons within a given energy range appear to have the same collision frequency.[27] The null collisional frequency at energy  $\varepsilon_i$  in energy range  $j$  is  $\nu_{nij} = \nu_{mj} - \nu_i$ , where  $\nu_{mj}$  is the maximum collision frequency in energy range  $j$  based on both electron energy and density of collision partners. The separate null collision frequency in each energy range is used to minimize the occurrence of null collisions since over the range of expected electron energies, the total collision frequency can vary by more than an order of magnitude. The time between collisions is obtained from  $\Delta t = -\ln(r_1)/\nu_{mj}$ , where  $r_1$  is a

random number distributed on (0,1). There is an inconsistency in choosing  $\Delta t$  if between collisions the particle crosses the boundary between energy ranges and  $\nu_{mj}$  varies between ranges. However, the frequency of these occurrences is small. The type of collision is determined by generating a series of random numbers. If  $r_2 \leq \nu_{nij} / \nu_{mj}$ , then the collision is null and the electron trajectory continues unhindered. For a real collision, we find the particular electron collision  $j$  which satisfies

$$\frac{1}{\nu_{mj}} \sum_{k=1}^{n-1} \nu_k < r_3 \leq \frac{1}{\nu_{mj}} \sum_{k=1}^n \nu_k, \quad (2.29)$$

where all collision frequencies are computed based on the maximum density of the collision partner in the entire reactor for process  $n$ ,  $N_{mn}$ . A second level of null collision is then used to determine if based on the local density of the collision partner a real or null collision has occurred. If  $r_4 \leq N_n(\vec{r}) / N_{mn}$ , where  $N_n(\vec{r})$  is the actual local density of the collision partner, then a real collision occurs. Otherwise, the collision is considered null and the trajectory proceeds unhindered.

After determining the final type of collision, the electron energy is reduced according to the inelastic or elastic nature of the collision (or increased in the case of a super-elastic collision), and the trajectory is scattered. The final velocity following a collision is determined by applying the scattering matrix,

$$\begin{aligned} v_x &= v \cdot (\cos \beta \cdot \cos \alpha \cdot \sin \theta \cdot \cos \phi + \cos \beta \cdot \sin \alpha \cdot \cos \theta - \sin \beta \cdot \sin \theta \cdot \sin \phi) \\ v_y &= v \cdot (\sin \beta \cdot \cos \alpha \cdot \sin \theta \cdot \cos \phi + \sin \beta \cdot \sin \alpha \cdot \cos \theta + \cos \beta \cdot \sin \theta \cdot \sin \phi) \\ v_z &= v \cdot (-\sin \alpha \cdot \sin \theta \cdot \cos \phi + \cos \alpha \cdot \cos \theta) \end{aligned} \quad (2.30)$$

where  $\alpha$  and  $\beta$  are the polar and azimuthal Eulerian angles of the electron velocity prior to the collision;  $\theta$  and  $\phi$  are the polar and azimuthal scattering angles, and  $v$  is the electron speed after

the collision. Assuming azimuthal symmetry for the collision,  $\phi$  is randomly chosen from the interval  $(0, 2\pi)$ . Unless experimental data is available,  $\theta$  is chosen by specifying a scattering parameter  $\chi$  where the polar scattering probability is proportional to  $\cos^\chi(\theta/2)$ .  $\chi = 0$  provides for isotropic scattering and  $\chi \gg 1$  provides for forward scattering. The randomly selected scattering angle is then

$$\theta = 2 \left[ \cos^{-1} (1 - r_5) \right]^{\left( \frac{1}{2+\chi} \right)}. \quad (2.31)$$

In the absence of experimental data, we used  $\chi = 0 - 0.1$  for elastic collisions derived from momentum transfer collision cross sections. For inelastic collisions,  $\chi = 2 - 3$ .

Following an ionizing collision, a secondary electron is added to the simulation at the same location as the primary particle and with a randomly chosen isotropic angular distribution. The distribution of secondary energies,  $f_{\text{sec}}(\varepsilon)$ , produced by an ionizing collision with species  $j$  by primary electron with energy  $\varepsilon_p$  is randomly chosen from [28]

$$f_{\text{sec}}(\varepsilon) \sim \left( 1 + \left( \frac{\varepsilon}{\bar{\varepsilon}_j} \right)^2 \right)^{-1}, \quad \varepsilon = \bar{\varepsilon}_j \tan \left( r_6 \cdot \tan \left( \frac{\varepsilon_p - E_j}{\bar{\varepsilon}_j} \right)^{-1} \right), \quad (2.32)$$

where  $\bar{\varepsilon}_j$  is a semi-empirical parameter for species  $j$  having ionization potential  $E_j$ .

Statistics for  $f_b(\varepsilon)$  are collected for every particle on every time step. The particles are binned by energy and location with a weighting proportional to the product of the number of electrons each pseudoparticle represents,  $w$ , and the time spent in the spatial mesh cell,  $\Delta t$ . Finite particle size techniques are used to distribute the particle weighting to its own cell and to neighboring cells in proportion to the fraction of the volume of the finite particle size that resides in the neighboring cell,  $\eta$ . The particle size and volume are equal to that of the numerical mesh.

So for a particle in spatial bin  $j$  and energy bin  $i$ , the running sum of statistics is

$$\sum_{j'=j, \text{neighbors}} [F_{ij'} \rightarrow F_{ij'} + w\Delta t \eta_{ij'}]. \quad (2.33)$$

When modeling transients, the time spent in the FKPM between calls to the eMCS is relatively short so that there is frequent feedback from the eMCS to the fluid modules and vice-versa. The relative change in voltage or power should be small between calls to the eMCS. To maintain the eMCS in lockstep with the fluid simulations, in this study trajectories are computed for 5  $RF$  low frequency cycles for each call of the eMCS (which at 10 MHz is 0.5  $\mu\text{s}$ ). Statistics are typically gathered for only the latter two or three of those cycles to allow for artificial transients which may occur at the beginning of each iteration to dampen out. An average of 50,000 pseudo-particles are used, with particles added for ionizations and removed for losses by attachment, recombination or leaving the volume. If the particle number exceeds a maximum value (typically 150,000), then the particle number is reduced by randomly removing particles. If the particle number is reduced below a minimum value (typically 40,000), particles are randomly seeded in the plasma. When a particle is removed from the simulation, its index and velocity is stenciled out – the location is termed empty. A record is kept of the empty locations and new particles are first placed into the empty locations while keeping track of the highest index in the array that is occupied. If the fraction of empty locations exceeds a specified value (which may be computer dependent), the empties are removed by compressing the stack of arrays so that pipelining can be more efficiently performed.

At the end of a given call to the eMCS, the  $f_b(\mathcal{E}, \vec{r})$  at each spatial location is obtained by normalizing the statistics such that

$$\sum_i F_{ij} = \sum_i f_{bij} \mathcal{E}_i^{1/2} \Delta \mathcal{E}_i = 1, \quad (2.34)$$

where  $f_{bij}$  ( $\text{eV}^{-3/2}$ ) is the  $f_b(\varepsilon_i, \vec{r})$  at  $\vec{r}$ , and  $\Delta\varepsilon_i$  is the width of the energy bin.

$e$ - $e$  collisions are accounted for using a particle mesh technique where the electrons collide with an energy resolved electron fluid. This is accomplished by using spatially dependent  $f_b(\varepsilon, \vec{r})$  recorded during the previous call to the eMCS. The incident pseudoparticle in the  $e$ - $e$  collision begins with a velocity  $\vec{v}_0$ . The velocity of an electron collision partner for the incident pseudoparticle is randomly chosen from the distribution function at that location,  $f_b(\varepsilon, \vec{r})$ , that was computed on the previous call to the eMCS. As only the energy distribution  $f_b(\varepsilon, \vec{r})$  is retained from the previous iteration, as opposed to the electron velocity distribution, we assume that the chosen target electron has an isotropic angular distribution. The probability of selecting a collision partner having an energy  $\varepsilon'$  for a pseudoparticle in the  $j^{\text{th}}$  spatial bin is determined with a cumulative probability. With,

$$P_j(\varepsilon') = f_j(\varepsilon')\varepsilon'^{1/2}\Delta\varepsilon' / \left( \sum_i f_j(\varepsilon_i)\varepsilon_i^{1/2}\Delta\varepsilon' \right), \quad (2.35)$$

where  $f_j(\varepsilon')$  is the  $f_b(\varepsilon, \vec{r})$  in the  $j^{\text{th}}$  spatial bin, and the summation is over the entire energy range, the cumulative probability is,

$$\Pi_j(\varepsilon'_i) = \sum_{k=1}^i P_j(\varepsilon'_k) / \sum_k P_j(\varepsilon'_k), \quad (2.36)$$

where the summation in the numerator is over lower energies, so that  $\sum_i \Pi_j(\varepsilon'_i) = 1$ . The energy of the target electron  $\varepsilon'_i$  is that which satisfies

$$\Pi_j(\varepsilon'_{i-1}) < r_7 \leq \Pi_j(\varepsilon'_i). \quad (2.37)$$

Once the velocity of the collision partner,  $\vec{v}'$ , is chosen, the impact parameter for a  $90^\circ$  scattering,  $b_0$  is determined as [29],

$$b_0 = e^2 / (2\pi\epsilon_0 m_e g^2), \quad (2.38)$$

where  $m_e$  is the mass of electron,  $\vec{g} = \vec{v}_0 - \vec{v}'$  is the velocity between the collision partners,  $g$  is the speed and  $\epsilon_0$  is the vacuum permittivity. If  $\cos(\theta) < b_0 / \lambda_D$ , where  $\theta$  is the angle between velocity of the pseudo-electron and its collision partner and  $\lambda_D$  is the local Debye length, the collision event is ignored. Although scattering through very small angles may not be well represented by this approach, such scattering does not appreciably affect the  $f_b(\epsilon)$  at energies which determine inelastic rate coefficients. Otherwise, the probability of an  $e$ - $e$  collision during the current time step  $\Delta t$  is determined from

$$P_{ee}(g, \Delta t) = n_j \sigma_{ee}(g) g \Delta t, \quad (2.39)$$

where  $n_j$  is the density of electrons in the  $j^{\text{th}}$  spatial bin obtained from the FKPM, and the momentum transfer Coulomb cross section,  $\sigma_{ee}(g)$ , is [30]

$$\sigma_{ee}(g) = 4\pi b_0^2 \left[ 1 + \ln(\lambda_D / b_0) \right]^{1/2}, \quad (2.40)$$

where  $\lambda_D$  is the Debye length. This procedure is justified if, for the conditions of interest,  $P_{ee}(g, \Delta t) \ll 1$ , which is the case for virtually all conditions of this study. The collision event takes place if  $P_{ee}(g, \Delta t) \geq r_8$ . If a collision occurs, then a post collision relative velocity,  $\vec{g}'$ , is randomly determined such that [31]

$$g'_z = \pm |\vec{g}| r_9, \quad g'_x = |\vec{g}| \sqrt{1-r_9^2} \cos(2\pi r_{10}), \quad g'_y = |\vec{g}| \sqrt{1-r_9^2} \sin(2\pi r_{10}), \quad (2.41)$$

where  $g'_z$  is positive or negative if  $g_z$  is positive or negative. The final velocity of the incident pseudoparticle,  $\vec{v}_f$ , is updated with,

$$\vec{v}_f = \vec{v}_R + 0.5\vec{g}, \quad \vec{v}_R = 0.5(\vec{v}' + \vec{v}_0) \quad (2.42)$$

At the end of a call to the eMCS, the  $f_b(\varepsilon, \vec{r})$  are used to compute electron impact rate coefficients  $k_j(\vec{r})$  for collision process  $j$ ,

$$k_j(\vec{r})[cm^3 s^{-1}] = \sum_{i=1} f_{bi}(\vec{r}) \sigma_j(\varepsilon_i) \left( \frac{2\varepsilon_i}{m_e} \right)^{1/2} \Delta\varepsilon_i. \quad (2.43)$$

The values of  $k_j(\vec{r})$  are held constant in the FKPM until the next call to the eMCS. The source function resulting from the rate coefficient in the fluid modules is then  $S_j(\vec{r})[cm^{-3} s^{-1}] = n_e(\vec{r})k_j(\vec{r})N_j(\vec{r})$ , for electron density  $n_e$  and heavy particle collision partner  $N_j$ .

A similar process is followed to obtain the electron energy distributions of secondary electrons that are first emitted from surfaces and accelerated by sheaths,  $f_s(\varepsilon, \vec{r})$ . Instead of seeding electrons in the bulk plasma, the flux of energetic particles (ions, photons, excited states) of type  $j$  striking surfaces,  $\vec{\phi}_j(\vec{r})$  is obtained from the FKPM. The total rate of secondary electron emission,  $R_s$ , (1/s) is obtain from

$$R_s = \sum_k R_{sk}, \quad R_{sk} = \sum_j \gamma_j \vec{\phi}_j(\vec{r}_k) A_k, \quad (2.44)$$

where the summation is over species  $j$  having secondary electron emission coefficient  $\gamma_j$  and surface locations  $k$  having surface area  $A_k$ . A preselected number of secondary electrons, typically 25,000-50,000 per call to the eMCS, are then randomly launched perpendicularly to the surface with an energy of 4 eV from spatial location  $k$  in proportion to  $R_{sk} / R_s$  with initial times randomly distributed in the low frequency *RF* cycle. The statistical weighting of the particle,  $w$ , has units of current or particles/s. Particle trajectories are then tracked and statistics collected to produce  $f_s(\varepsilon, \vec{r})$  in the same manner as for the bulk  $f_b(\varepsilon, \vec{r})$ . Since the weightings  $w$  of the secondary electron pseudoparticles are particles/s, the distribution functions  $f_s(\varepsilon, \vec{r})$  are

normalized,

$$\sum_j F_{ij} = \sum_{i,j} f_{sij} \varepsilon_i^{1/2} \Delta \varepsilon_i \Delta V_j, \quad (2.45)$$

where  $\Delta V_j$  is the volume of the cell at location  $j$  and  $f_{sij} = f_s(\varepsilon_i)$ . With this normalization,  $f_s(\varepsilon, \vec{r})$  has units of electrons/cm<sup>3</sup>-eV-s.

The trajectories of pseudoparticles are followed until the particle strikes a surface or falls below a specified energy, which is typically the lowest electronic excitation threshold,  $\varepsilon_T$ . At that time, the pseudoparticle is removed from the simulation. The weighting of originally emitted pseudoparticles falling below  $\varepsilon_T$  are summed into a current source,  $Q_e(\vec{r})$  (C/cm<sup>3</sup>-s),

$$\sum_{j'=j, \text{neighbors}} \left[ Q_{j'} \rightarrow Q_{j'} + \frac{qw\eta_{jj'}}{\Delta V_{j'}} \right], \quad (2.46)$$

where  $Q_j$  is the current source for location  $j$  having volume  $\Delta V_j$ . Secondary electrons emitted from surfaces represent a source of electrons for the electron continuity equation in the fluid simulation. This source is provided by  $Q_e(\vec{r})$ . Since this source does not also appear in a positive ion continuity equation, it appears as net charge injection in solution of Poisson's equation through the change in electron density. Secondary electrons striking surfaces are similarly summed into a rate of surface charging  $Q_{se}(\vec{r})$  (C/cm<sup>2</sup>-s) which is then included in the continuity equation for surface charging in the fluid modules.

Since  $f_s(\varepsilon, \vec{r})$  is ultimately normalized to the magnitude of the secondary electron current,  $R_S$ , instead of rate coefficients being transferred back to the fluid modules, electron impact source functions due to secondary electrons, are returned to the FKPM,

$$S_{ej}(\vec{r}) [cm^{-3} s^{-1}] = N_j(\vec{r}) \sum_{i=1} f_{si}(\vec{r}) \sigma_j(\varepsilon_i) \left( \frac{2\varepsilon_i}{m_e} \right)^{1/2} \Delta \varepsilon_i. \quad (2.47)$$

The values of  $S_{e_j}(\vec{r})$  are held constant until the next call to the eMCS.

#### 2.1.4 Plasma Chemistry Monte Carlo Module (PCMCM)

The PCMCM is a 3v-3d (three velocity components, three dimensions) simulation which integrates ion trajectories in electric fields obtained from the FKPM. The source functions for generation of the ions from all sources (electron impact and heavy particle collisions) and electric fields computed in the FKPM are exported to the PCMCM. Pseudoparticles, representing ions and neutral species in PCMCM, are launched at times randomly chosen in the *RF* period at locations weighted by their source functions throughout the plasma volume. The initial velocities are randomly chosen from a Maxwell-Boltzmann distribution having the temperature of that species as computed by the FKPM. Trajectories of the pseudoparticles are integrated by interpolating electric fields in space and time in the same manner as in the eMCS. Null collision techniques are used to simplify the random selection of collision times and mean free paths for individual particles.[32] The maximum collision frequency for each PCMCM species,  $i$ , over the entire computational domain is determined

$$v_{im} = \sum_j v_{ij}, \quad v_{ij} = \max\left((v\sigma_j(v))_m N_{jm}\right), \quad (2.48)$$

where the sum is over collisions  $j$ ,  $(v\sigma_j(v))_m$  is the maximum product of speed and cross section, and  $N_{jm}$  is the maximum value of the collision partner in the computational domain.

The randomly chosen time to the next collision is then given by

$$t_c = t_0 - \frac{1}{v_{im}} \ln(1-r), \quad (2.49)$$

where,  $t_0$  is the current time and  $r$  is a random number distributed on (0,1). The use of maximum collision frequency is then corrected later by through of a null-cross section technique.

If a null collision happens, the particle is simply not collided. Another time to the next collision is chosen, and the integration of the trajectory is continued. The gas phase collisional processes of the pseudoparticles are computed based on the same reaction mechanism as in the FKPM. The trajectories of the pseudoparticles are followed until they strike the surface at which time their energy and angular distributions (EADs) are recorded. The angles are recorded relative to the local normal. Time steps in the PCMCM are dynamically chosen to resolve ion transport in the time varying sheath. The time step is chosen to be no larger than a fraction of the *RF* cycle (typically 0.01) or the time to cross a fraction of a computational mesh cell (typically 0.5 far from the sheath and 0.02 in the sheath).

## **2.2 Monte Carlo Feature Profile Model (MCFPM)**

The fluxes of the reactant species and their EADs from the PCMCM are used as inputs to the MCFPM that is an off-line module of the HPEM. This module is used to determine and predict topographical feature evolution for nanometer-scale processing in plasma reactors. In this thesis, the MCFPM has been used for predicting profile evolution for SiO<sub>2</sub> in the CCP etching reactor incorporated with pulsed powers. The MCFPM resolves features on the wafer using a two-dimensional rectilinear mesh. Each cell in the mesh has a material property. Typical mesh dimension for this study is 1.5 nm × 1.5 nm. Pseudoparticles representing the incident plasma species are launched towards the surface with energy and angle randomly chosen from the EADs obtained from the PCMCM. The trajectories of the pseudoparticles are tracked until they hit a surface, where a generalized surface reaction mechanism controls the interaction. The reaction mechanism is ultimately expressed as a probability array encompassing all possible reactions between the pseudoparticle plasma species and the surface species. When a pseudoparticle strikes a material cell, an outcome is chosen based on probabilities from a

surface reaction mechanism using Monte-Carlo techniques. The identity of the material mesh cell is changed (representing a surface chemical reaction), removed (etching), or a cell is added (deposition) as dictated by the reaction mechanism. Gas phase pseudoparticles are reflected or emitted from the surface consistent with the mechanism. The returning plasma species from the surface are tracked as new pseudoparticles.

The pseudoparticles are launched with a frequency computed from the total flux of radicals or ions incident onto the substrate so that each pseudoparticle represents a fraction of the number of atoms in a mesh cell based on the gas-to-material weighting ratio:

$$W_g = \frac{1}{\gamma} W_s, \quad (2.50)$$

where  $W_g$  is the gas particle weighting,  $W_s$  is the mesh or surface cell weighting, and  $\gamma$  is the gas-to-material ratio that is chosen to be unity for this study. The time between the launched particles (i.e. launching frequency) can be computed based on the total flux and computational bin size by

$$\Delta t_p = \frac{\Delta x \cdot \Delta y \cdot \rho}{\Gamma \cdot D}, \quad (2.51)$$

where  $\Delta x$  and  $\Delta y$  are the dimensions of a mesh cell,  $\rho$  is the density of the surface material,  $\Gamma$  is total flux of plasma species, and  $D$  is the width of total computational domain. For this investigation with SiO<sub>2</sub> etching,  $\rho$  is  $2.5 \times 10^{22} \text{ cm}^{-3}$ ,  $D$  is 67.5 nm, both  $\Delta x$  and  $\Delta y$  are 1.5 nm, and the total flux of plasma species,  $\Gamma$ , is around the order of  $1 \times 10^{16} \text{ cm}^{-2}\text{s}^{-1}$ . Using these numbers in the Eq. (2.51), the time between the launched particles is turned out to be in the order of  $1 \times 10^{-3} \text{ s}$ . The typical residence time of a particle in a feature is at best a nanosecond. As a result, only a single gas phase pseudoparticle is tracked at a time.

Due to the statistical randomness inherent to Monte-Carlo based simulators, it is necessary to smooth the data. This smoothing was accomplished by running many cases with different random number seeds. Typically 80 identical trenches were simulated with different random number seeds for each process starting condition. The use of different random number seeds in the calculation provides a different sequence of particles randomly selected from the same EADs provided by the HPEM. This also produces a different sequence of randomly chosen reactions of gas phase particles with the surface. This procedure emulates a set of adjacent side-to-side features which randomly receive different fluxes.

For the conditions using a pulsed power, the plasma properties are greatly changed by the modulation of the power. As a result, the fluxes and EADs of ions and radicals bombarding the wafer are considerably different between the *power-ON* and *-OFF* cycles. In order not to average out these changes between the pulsed cycles, the fluxes and EADs are recorded separately for both ON and OFF cycles. The MCFPM is then modified to read in multiple input files and to alternate them accordingly between the ON and OFF phases based on the duty cycle.

### **2.3 Parallel Computing**

The very nature of the HPEM makes it difficult to efficiently make the code parallel. The ideal code for parallelization consists of a single *do-loop* that is executed many, many times and which contains simple functions without any logical operations. In such a code, the vast majority of the computer time is consumed by this single loop, so parallelizing the loop gains large increases in computational efficiency. These types of codes are highly specialized since there is little flexibility in the coding. In contrast, the intent of the HPEM is to be extremely flexible to address a broad range of conditions, timescales, processes and types of plasma sources using many different types of computational techniques. As a result, its structure is poorly

matched to those structures which efficiently parallelize. The code consists of many modules and loops, none of which consume a large fraction of the computer time. So even if the CPU time of a single module is driven to zero by parallelization, the improvement in execution time of the overall code is only a few tens of percent (and not factors of 10).

Another issue has to do with computational overhead charges. When a computer program “goes parallel”, there is an overhead time-charge incurred during which commands are given and data is distributed to the multiple cores (or processors). This overhead charge is a penalty since no computations are being done. In the ideal parallel code, the length of the *do-loops* (or the number of times that those loops are sequentially executed without interruption) is great enough that the improved efficiency of the parallel operations is greater than the overhead charge incurred in setting up the parallel operations. The net result is an improvement in performance. If the *do-loops* are not long enough (or not executed sequentially enough times), the improved efficiency of the parallel operations may not make up for the overhead charges, and the code could actually slow down. Due to the highly modular and algorithmically diverse nature of the HPEM, if one simply blindly inserts parallelization commands into the code, the code may actually run slower since the *do-loops* are not long enough to recoup the overhead charges.

The test case for initial parallelization activities was a two-frequency, capacitively coupled plasma sustained in argon using the electron Monte Carlo Simulation (eMCS). Other options were selected so that the amount of CPU time spent in other modules was minimized. The result of profiling the code (i.e., how much CPU time is used in various modules) is shown in Fig. 2.2. Roughly 50% of the computer time is spent in the eMCS split between 2 major subroutines (RATES, MCS\_STATS), each of which have multiple loops. We implemented

OpenMP directives in the eMCS modules which consume the majority of the CPU time. (Note that the term “threads” is synonymous with the number of cores.) The results are shown in Fig.

2.3. The parameters are:

- $T_s$  = Clock time taken to run the parallel algorithm with 1 thread. (serial execution)
- $T_p$  = Clock time taken to run the parallel algorithm with N threads
- SN (speed-up) =  $T_s / T_p$
- EN (efficiency) =  $SN / N$
- S = serial calculation portion
- P = parallel calculation portion
- $T_s = S + P$
- $T_p = S + P / N$
- F (serial fraction) =  $S / T_s$
- SN (speed-up) =  $1 / (F + (1 - F) / N)$

The parallel speedup and efficiency increase with the number of particles used in the eMCS since we are amortizing the overhead charges to launch the parallel loops over longer loops. This scaling saturates at about 10,000-20,000 particles. By increasing the number of cores (or threads), there is additional parallel speed up, however this improvement saturates at about 8 cores. This result may be prejudiced by the fact that the particular machine we used for this study had only 8 cores, and so may have been bandwidth limited at 8 cores. Since the parallel speedup is sub-linear with the increase in the number of cores, the parallel efficiency decreases with increase in the number of cores.

Choice of which modules are used within the HPEM determines where the majority of CPU time is spent. For example, we used the same two-frequency, capacitively coupled plasma

as in the first example, but instead of using the eMCS, we solved the electron energy equation instead. The profile of the resulting performance is shown in Fig. 2.4. The distribution of the major sources of CPU time shifts to SOR (solution of Poisson's equation), TE\_UPDATE (electron energy equation) and TGAS\_UPDATE (gas temperature equations). None of the modules consume more than 30% of the CPU time. In each of these modules, a mathematical technique, successive-over-relaxation (SOR), is used to solve an elliptic type of equation. The basic SOR technique is not parallelizable because of some recursive indices dependencies. These SOR routines for the Poisson, electron energy equation and gas temperature equations were rewritten using the "red-black" SOR technique. (See Fig. 2.5.) In the 2-d red-black technique (like on a checkerboard) the indices calls are on (odd, odd), (even, even), (odd, even) and (even, odd) groupings of neighboring cells, which is parallelizable. The results are shown in Fig. 2.5. Using the red-black SOR algorithms, we obtain a 50% speedup of the code, however the method saturates at 4 threads/cores with a concurrent decrease in efficiency. Due to the structure within each of these modules, the speed up in TE\_UPDATE was only 30% whereas the speedup in TGAS\_UPDATE was 150%.

One of the challenges in parallelizing the HPEM is that by virtue of the breadth and diversity of the code, the computational load is spread over many modules. For example, profiling of the HPEM when using Scharfetter-Gummel fluxes (IPETER=2) and sparse matrix techniques for solving Poisson's equation (IPOISSON\_SPARSE=1) is shown in Fig. 2.6. Under these conditions, no single set of routines consumes more than 10% of the CPU time. The routines SDLUI2, DSMV and QS2I1D are parts of the sparse-matrix solver. SG\_ZFLUX, SG\_RFLUX and EIMPLICIT\_SG are routines used to calculate the Scharfetter-Gummel fluxes and Jacobian elements for the matrix solution of Poisson's equation (which in turn call

SG\_ZFLUX and SG\_RFLUX). Driving any of these routines to zero CPU time gains only 10% improvement in performance.

It is clear that getting highly efficient parallel performance while still retaining the broad flexibility of the HPEM will be difficult. However, for highly specialized conditions where only a known subset of modules is being used, the code can be optimized by creating specialty modules within the HPEM. For example, if the simulation is addressing purely capacitive coupling, then only a subset of options in the eMCS are used. These conditions are checked for and a specialty subroutine is called to integrate the electron trajectories. Similarly, if purely drift diffusion is used for both electrons and ions, then a specialty subroutine can be used to combine their transport updates.

## 2.4 Figures

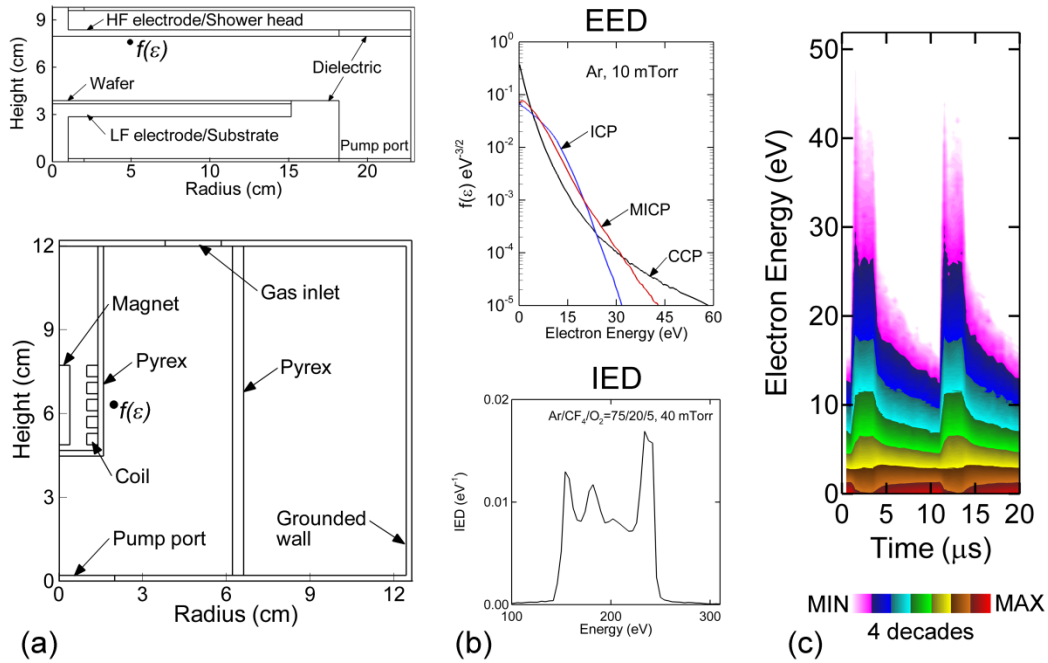


Fig. 2.1 Example of results from HPEM. (a) Computational geometry for CCP and ICP. (b) Electron energy distributions are compared between CCP, ICP, and mICP. Ion energy distribution is obtained from CCP. (c) Electron energy distribution as a function of time when using pulsed power.

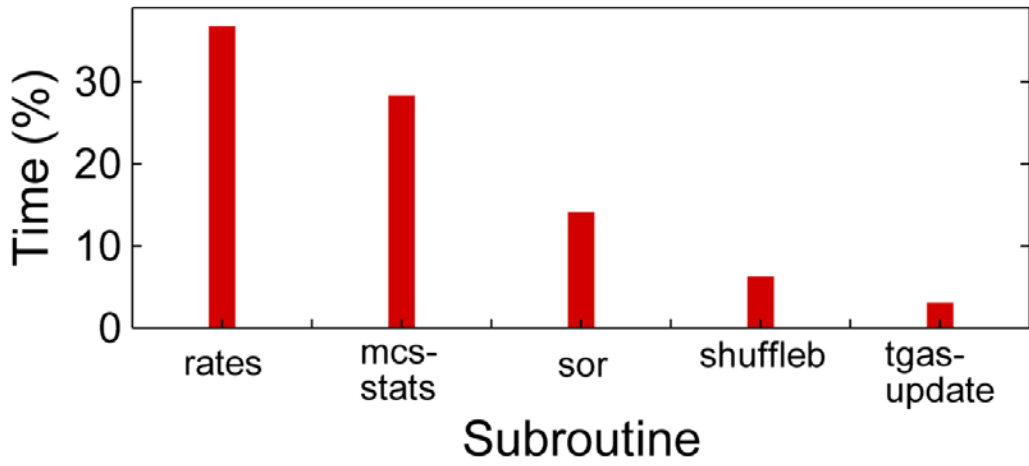


Fig. 2.2 Percent of CPU time spent in different modules when using the eMCS.

rates= particle trajectory integration in eMCS  
 mcs-stats= statistics collection in eMCS  
 sor= Poisson's equations solution

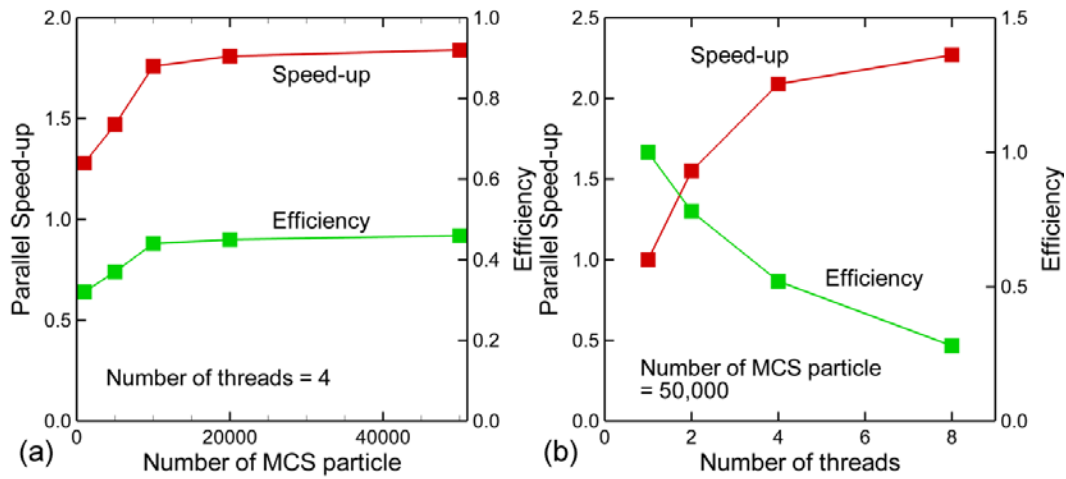


Fig. 2.3 Speedup and efficiency of parallelization as a function of (a) number of eMCS particles and (b) number of threads.

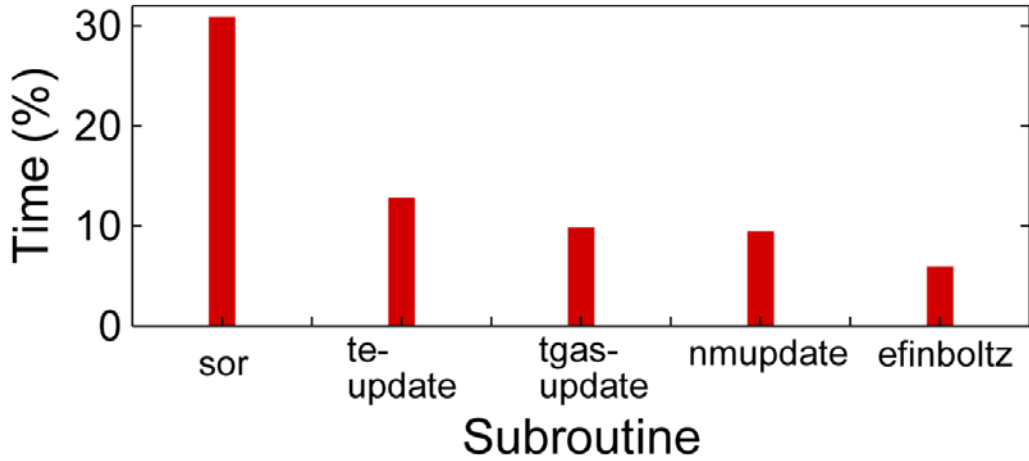


Fig. 2.4 Percent of CPU time spent in different modules when using the electron energy equation.

sor= Poisson equation solution  
 te\_update= Solution of electron energy equation  
 tgasupdate= Solution of gas temperature equations  
 nmupdate= Solution of ion momentum equations.

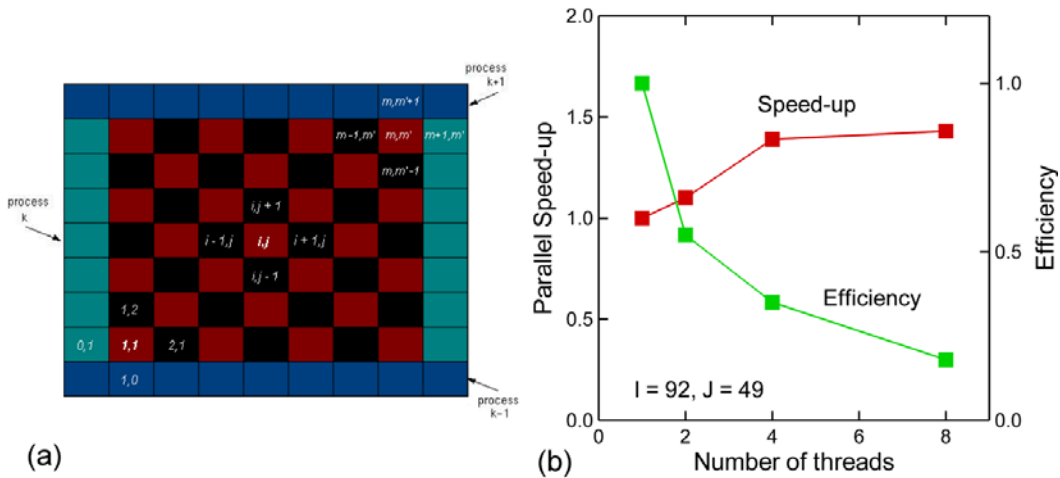


Fig. 2.5 The red-black technique is used to parallelize SOR routines. (a) Schematic of the red-black technique. (b) Speedup and efficiency of parallelization of SOR routines using red-black methods.

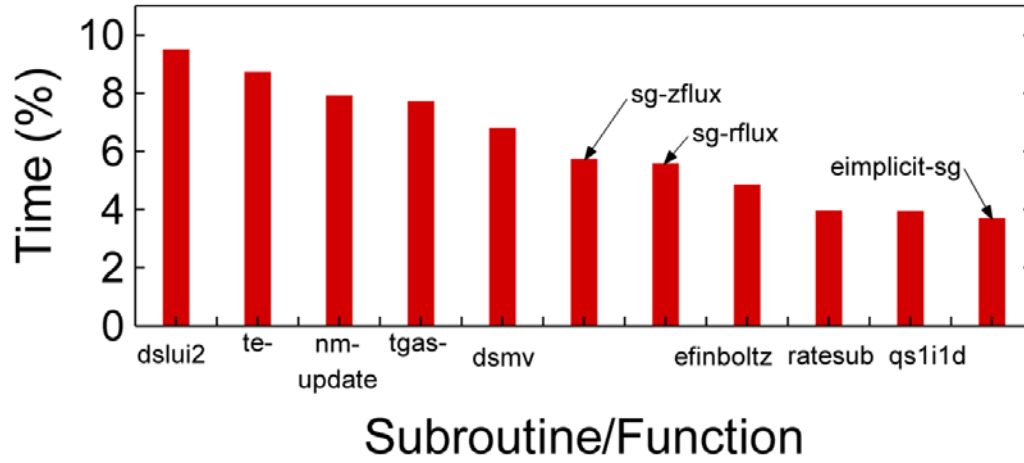


Fig. 2.6 Profiling of HPEM when using Scharfetter-Gummel fluxes and sparse matrix techniques for Poisson's equation.

## 2.5 References

1. P. L. G. Ventzek, M. Grapperhaus and M. J. Kushner, "Investigation of Electron Source and Ion Flux Uniformity in High Plasma Density Inductively Plasma Tools Using 2-dimensional Modeling", *J. Vac. Science Tech. B* **12**, 3118 (1994).
2. M. J. Kushner, W. Z. Collison and D. N. Ruzic, "Electron-Beam Sustained Radio Frequency Discharges for Plasma Processing", *J. Vac. Sci. Technol. A* **14**, 2094 (1996).
3. M. J. Kushner, W. Z. Collison, M. J. Grapperhaus, J. P. Holland and M. S. Barnes, "A 3-dimensional Model for Inductively Coupled Plasma Etching Reactors: Azimuthal Symmetry and Coil Properties", *J. Appl. Phys.* **80**, 1337 (1996).
4. M. J. Grapperhaus and M. J. Kushner, "A Semi-Analytic Sheath Model Integrated into a 2-dimensional Model for Radio Frequency Biased, Inductively Coupled Plasma Etching Reactors", *J. Appl. Phys.* **81**, 569 (1997).
5. S. Rauf and M. J. Kushner, "A Model for Non-Collisional Heating in Inductively Coupled Plasma Processing Sources", *J. Appl. Phys.* **81**, 5966 (1997).
6. M. J. Kushner, "Consequences of Asymmetric Pumping in Low Pressure Plasma Processing Reactors: A 3-dimensional Modeling Study", *J. Appl. Phys.* **82**, 5312 (1997).
7. J. Lu and M. J. Kushner, "Effect of Sputter Heating in Ionized Metal Physical Vapor Deposition Reactors", *J. Appl. Phys.* **87**, 7198 (2000).
8. D. Zhang and M. J. Kushner, "Mechanisms for CF<sub>2</sub> Radical Generation and Loss on Surfaces in Fluorocarbon Plasmas", *J. Vac. Sci. Technol. A* **18**, 2661 (2000).
9. R. Kinder and M. J. Kushner, "Wave Propagation and Power Deposition in Magnetically Enhanced Inductively Coupled and Helicon Plasma Sources", *J. Vac. Sci. Technol. A* **19**, 76 (2001).
10. A. Sankaran and M. J. Kushner, "Harmonic content of electron-impact source functions in inductively coupled plasmas using an "on-the-fly" Monte Carlo technique", *J. Appl. Phys.* **92**, 736 (2002).
11. M. J. Kushner, "Modeling of magnetically enhanced capacitively coupled plasma sources: Ar discharges", *J. Appl. Phys.* **94**, 1436 (2003).
12. A. V. Vasenkov, X. Li, G. S. Oehrlein, and M. J. Kushner, "Properties of c-C<sub>4</sub>F<sub>8</sub> inductively coupled plasma. II. Plasma chemistry and reaction mechanism for modeling of Ar/c-C<sub>4</sub>F<sub>8</sub>/O<sub>2</sub> discharges", *J. Vac. Sci. Technol. A* **22**, 511 (2004).
13. K. Rajaraman and M. J. Kushner, "A Monte Carlo simulation of radiation trapping in electrodeless gas discharge lamp", *J. Phys. D: Appl. Phys.* **37**, 1780 (2004).
14. A. Sankaran and M. J. Kushner, "Etching of porous and solid SiO<sub>2</sub> in Ar/c-C<sub>4</sub>F<sub>8</sub>, O<sub>2</sub>/c-C<sub>4</sub>F<sub>8</sub>

- and Ar/O<sub>2</sub>/c-C<sub>4</sub>F<sub>8</sub> plasmas”, J. Appl. Phys. **97**, 023307 (2005).
15. Y. Yang and M. J. Kushner, “Modeling of magnetically enhanced capacitively coupled plasma sources: Two frequency discharges”, J. Vac. Sci. Technol. A **25**, 1420 (2007).
  16. A. Agarwal and M. J. Kushner, “Plasma atomic layer etching using conventional plasma equipment”, J. Vac. Sci. Technol. A **27**, 37 (2009).
  17. M. J. Kushner, “Hybrid modeling of low temperature plasmas for fundamental investigations and equipment design”, J. Phys. D: Appl. Phys. **42**, 194013 (2009).
  18. Y. Yang, M. Strobel, S. Kirk and M. J. Kushner “Fluorine Plasma Treatments of Polypropylene Films: II. Modeling Reaction Mechanisms and Scaling”, Plasma Proc. Polymers **7**, 123 (2010).
  19. P. A. Thompson, *Compressible Fluid Dynamics* (McGraw-Hill, New York, 1994), Chapter 2.
  20. R. A. Svehla, “Estimated viscosities and thermal conductivities of gases at high temperatures”, NASA technical Report R-132, 1962.
  21. J. O. Hirschfelder, C. F. Curtiss, and R. B. Bird, *Molecular theory of gases and liquids* (Wiley, New York, 1964), p. 1126.
  22. E. H. Kennard, *Kinetic Theory of Gases* (McGraw-Hill, New York, 1938), pp. 311-315.
  23. D. L. Scharfetter and H. K. Gummel, “Large-signal analysis of a silicon read diode oscillator”, IEEE Trans. Electronic Devices **ED-16**, 64 (1969).
  24. W. H. Press, B. P. Flannery, S. A. Teukolsky and W. T. Vetterling, *Numerical Recipes: The Art of Scientific Computing* (Cambridge University Press, Cambridge, 1987).
  25. SLAP Sparse Matrix Library, <http://www.netlib.org>
  26. A. W. Trivelpiece and R. W. Gould, “Space charge waves in cylindrical plasma columns”, J. Appl. Phys. **30**, 1784 (1959).
  27. S. L. Lin and J. N. Bardsley, “Monte Carlo simulation of ion motion in drift tubes”, J. Chem. Phys. **66**, 435 (1977).
  28. C. P. Opal, W. K. Peterson and E. C. Beaty, “Measurements of Secondary-Electron Spectra Produced by Electron Impact Ionization of a Number of Simple Gases”, J. Chem. Phys. **55**, 4100 (1971).
  29. M. Mitchner, C. H. Kruger, *Partially Ionized Gases* (Wiley, New York, 1973), p. 265.
  30. V. Vahedi, M. A. Lieberman, G. DiPeso, T. D. Rognlien and D. Hewett, “Analytic model of power deposition in inductively coupled plasma sources”, J. Appl. Phys. **78**, 1446 (1995).
  31. G. A. Bird, *Molecular Gas Dynamics and the Direct Simulation of Gas Flows* (Oxford

University Press, New York, 1994).

32. H. R. Skullerud, "The stochastic computer simulation of ion motion in a gas subjected to a constant electric field", *J. Phys. D* **1**, 1567 (1968).

## Chapter 3 CONTROL OF ELECTRON DISTRIBUTION USING MAGNETIC FIELD

### 3.1 Introduction

Magnetic fields have been used in a variety of low pressure plasma applications in order to manipulate not only the spatial distribution but also the peak values of electron temperature and density. In the context of plasma materials processing, the plasma sources using magnetic fields include electron cyclotron resonance (ECR) discharges [1,2], magnetically enhanced reactive ion etching (MERIE) systems [3], helicon discharges [4] and hollow cathode magnetrons [5]. Computational investigations have been attempted to offer a better understanding of the magnetized plasmas.[6,7] Although these plasmas are developed for different applications—such as etching, deposition, ion source, and propulsion—the fundamental physics behind using magnetic fields is controlling the energy distributions of electrons, ions, and neutrals.[8-10] In particular, electron kinetics in the magnetized plasma has been intensively studied both experimentally [11-16] and numerically [17-21]. Computational investigation on the electron kinetics in magnetized plasmas includes using an analytic model [17-19], a fluid method [20] and particle simulation [21].

Electron kinetics is often described as being *local* or *nonlocal*. Local electron kinetics are typically observed in high pressure where the electron energy relaxation length ( $\lambda_e$ ) is smaller than the chamber size (L).[22] In non-local kinetics,  $\lambda_e$  is sufficiently large that the electron

energy distribution (EED) based on total energy (kinetics plus potential) is uniform across the chamber. In some sense, the electron acceleration and energy loss processes appear to be volume averaged. In magnetized plasmas, there are additional constraints based on the frequency of the electric field and electron cyclotron frequency. If the driving frequency ( $\omega$ ) in an inductively coupled plasma (ICP) is greater than the electron cyclotron frequency ( $\Omega_e$ ), the plasma is similar to an unmagnetized plasma because the incident electromagnetic wave decays within the skin depth as it does in an unmagnetized plasma due to the skin effect. However, if the  $\omega < \Omega_e$ , the wave penetrates into the plasma along the magnetic field line, and this is often referred to as the wave effect dominant regime.[23]

Rehman *et al.* [20] calculated power absorption in a magnetized inductively coupled plasma (mICP) using a fluid method. They demonstrated the propagation of electromagnetic wave along the direction of the external magnetic field. They also observed negative power deposition which originates from opposing phases of current and electric field due to the thermal motion of the electrons, it has been typically observed only by extensive kinetic approaches. Although the fluid method is computationally efficient, it cannot capture the detailed electron kinetics such as EEDs. To resolve EED, particle-in-cell/Monte-Carlo collision (PIC/MCC) simulation code has been used for the magnetized plasmas.[21] Kim *et al.* [21] computationally obtained EEDs in dual-frequency capacitively coupled plasma with a magnetic field. They showed the heating of low-energy electrons due to the confinement by the magnetic field using a one-dimensional PIC/MCC simulation code. An alternate method includes hybrid methods by combining merits of each of the fluid and kinetic methods.[24]

In low pressure ICPs, electron energy transport is largely non-local. Although power deposition and ionization rates are, in fact, larger in the skin depth of the incident

electromagnetic wave [25], these differences result from relatively small changes in the tail of the EEDs. Pulsing of ICPs [26] and changing the frequency of the  $RF$  power [27] can be used to customize EEDs. However, even with these techniques it is still difficult to control the spatial distribution of the EEDs in the absence of increasing gas pressure so that  $\lambda_e \ll L$ . Local control of the EEDs in ICPs using static magnetic fields was demonstrated Monreal *et al.* [16]. In these experiments, the plasma was generated by a re-entrant antenna excited at 5 MHz. A coaxial bar magnetic produced a static dipole magnetic field having a decay length commensurate with the electromagnetic skin depth. They found that the magnetic field created non-local electron transport conditions which enabled manipulation of the local EEDs. For a constant power with a magnetic field, there were increased populations of hot electrons in the vicinity of the antenna (larger magnetic fields) and decreased populations in the remote from the coil (smaller magnetic fields).

In this chapter we discuss results from a computational investigation of EEDs in magnetically confined ICPs (mICPs) for the experimental conditions of Monreal *et al.* [16]. The model used in this investigation is a kinetic-fluid hybrid simulation described in Chapter 2. EEDs are produced with the kinetic portion of the model whereas plasma densities are produced in the fluid portion of the model. To address the magnetized plasmas in this study, we developed a fully implicit solution for the electron continuity equation combined with a semi-implicit solution for Poisson's equation. To speed the calculation, the electron transport algorithms in the kinetics portions of the model were made computationally parallel. Other portions of the model that were computationally taxing, such as successive-over-relaxation routines, were also made parallel.

The computed trends for EEDs with and without the magnetic field for ICPs sustained in

3 mTorr of Ar shows a quantitative agreement between the model and the experiment. The distribution of the plasma is also affected by combinations of the magnetic field and pressure, in part due to the plasma being sustained at constant power as opposed to constant coil current. For a given magnetic field and pressure, the applied power had little influence on the EEDs.

The model used in this study is described in Sec. 3.2. The typical plasma properties in magnetized ICP are discussed in Sec. 3.3, and scaling with pressure and power are in Sec. 3.4. Our concluding remarks are in Sec. 3.5.

### **3.2 Description of the Model**

The model used in this investigation is a two-dimensional kinetic-fluid hydrodynamics simulation that combines separate modules that address different physical phenomena in an iterative manner.[28] The modules used in this study include the electromagnetic module (EMM), the fluid kinetics-Poisson module (FKPM), the electron energy transport module (EETM), the electron Monte Carlo simulation (eMCS), and the Monte Carlo radiation transport module (MCRTM). The EMM calculates inductively coupled electric and magnetic fields (from antenna coils) as well as static magnetic fields produced by dc magnetic coils or permanent magnets. In the FKPM, separate continuity, momentum, and energy equations are simultaneously integrated in time for all heavy particle species (neutral and charged). All electron transport coefficients and rate coefficients for electron impact collisions are provided by the EETM using the eMCS which also provides EEDs as a function of position. The eMCS including electron-electron collision is described in Ref. [29]. The method used here is essentially the same with the exception that the Lorentz equation is used to advance the trajectories of the pseudoparticles. For particle  $i$  at location  $\vec{r}$ ,

$$\frac{d\vec{v}_i(\vec{r},t)}{dt} = q(\vec{E}_s(\vec{r}) + \vec{E}_\omega(\vec{r},t)) + q\vec{v}_i(\vec{r},t) \times (\vec{B}_s(\vec{r}) + \vec{B}_\omega(\vec{r},t)), \quad (3.1)$$

where  $\vec{E}_s(\vec{r})$  is the two-dimensional  $(r, z)$  electrostatic field produced in the FKPM and  $\vec{B}_s(\vec{r})$  is the 2D externally applied magnetostatic field.  $\vec{E}_\omega(\vec{r},t)$  and  $\vec{B}_\omega(\vec{r},t)$  are the 3D  $(r, z, \theta)$  harmonic electromagnetic fields produced by the EMM. In practice  $\vec{E}_\omega(\vec{r},t)$  and  $\vec{B}_\omega(\vec{r},t)$  are transferred to the eMCS as spatially dependent amplitudes and phases. The phase of each pseudoparticle in the  $RF$  cycle is then used to obtain the local electromagnetic fields. Although these fields are computed in cylindrical coordinates, they are converted to Cartesian form to advance the trajectories of the pseudoparticles, which are tracked in 3D Cartesian space.

The discharge system modeled in this investigation is an mICP sustained in argon at 3 mTorr. The species in the simulation are Ar,  $\text{Ar}^+$ ,  $\text{Ar}_2^+$ ,  $\text{Ar}(1s_2)$ ,  $\text{Ar}(1s_3)$ ,  $\text{Ar}(1s_4)$ ,  $\text{Ar}(1s_5)$ ,  $\text{Ar}(3p^5 4p)$ ,  $\text{Ar}(3p^5 4d)$ , and excited state of  $\text{Ar}_2$ . The reaction mechanism includes radiation transport, photoionization, electron impact excitation and ionization, electron ion recombination, heavy particle mixing of  $1s_n$  levels, penning ionization, associative and dissociative penning ionization, symmetric charge exchange, and 3-body dimer formation. Photon transport is calculated in the MCRTM where the rates of photon absorption and re-emission are recorded for each optical transition, and are used to calculate radiation trapping factors that lengthen the natural lifetime of the emitting species.[30,31] The detail description of MCRTM is found in Ref. [32]. The radiation trapping factors are adequately chosen based on initiative calculations for different pressures. Photoionization due to VUV at 106.66 nm (transition from  $\text{Ar}(1s_4)$  to Ar) and 104.82 nm (transition from  $\text{Ar}(1s_2)$  to Ar) is included.[33] The rate coefficients for heavy particle mixing and penning ionization are obtained from Ref. [34]. The  $\text{Ar}_2^+$  ions are mainly created by Hornbeck-Molnar and associative penning ionization.[35] When using fluid techniques to

model plasma transport in the presence of static magnetic fields from a permanent magnet, tensor forms of the transport coefficients (e.g., conductivity, mobility, diffusion coefficient) should be used. In the absence of the static magnetic field in cylindrical coordinates, an azimuthally symmetric antenna driven at  $RF$  frequencies will produce only an azimuthal component of the  $RF$  electric field, and radial and axial components of the  $RF$  magnetic field. With tensor transport coefficients, an azimuthally symmetric antenna in the presence of a static magnetic field having  $(r,z)$  components will produce  $(r,z,\theta)$  components of both the  $RF$  electric and magnetic fields.

### 3.3 Plasma Properties in Magnetized ICP

The two-dimensional, cylindrically symmetric reactor used in this investigation is schematically shown in Fig. 3.1a and is patterned after the reactor described in Ref. [16]. A permanent magnet is placed coaxially inside the antenna coil that is housed in a Pyrex reentrant cavity (30 mm inner diameter and 1 mm thick) immersed into the plasma. To increase coupling efficiency between the coil and the plasma, the thickness of the Pyrex is chosen to be very thin. The radius and height of the chamber are 6 cm and 12 cm, respectively. The mid-height of the coil is at about 6.3 cm. A specially designed coil was employed in the experiment to minimize the capacitive coupling. In the model, we generate the plasma purely inductively through the coil excited at 5 MHz with 100 W. We extended our computational domain to the outside (up to 12 cm of radius) of the plasma chamber in order to implement the boundary conditions properly at the Pyrex wall (6 cm of radius). The base case operating conditions are 3 mTorr of Ar with the flow rate of 1 sccm. Gas was injected annularly at the top and pumped on axis at the bottom. The flow rate is slow to isolate the neutral gas flow in the plasma. The strength of the magnet is chosen to produce a field of 100 Gauss at a radius of 2.4 cm, shown in Fig. 3.1b. At mid-height

of the coil, the applied magnetic field is in the axial direction.

The power densities and  $RF$  cycle-averaged inductively coupled electric fields for the base cases with and without the magnetic field are shown in Fig. 3.2. Based on Figs. 3.2b and 3.2d, it should be noted that the radial electric field plays an important role in the power deposition in addition to the power absorption from the azimuthal electric field. Consequently, the power absorbing volume in a magnetized discharge is larger than in an unmagnetized discharge. By applying the static magnetic field in the axial direction to the plasma, the conductivity in azimuthal direction is significantly reduced due to the reduction of azimuthal transport of electrons. Therefore, the  $\vec{E}_\theta$  is larger with the magnetic field than without in order to keep the power constant and it is shown in Figs. 3.2c and 3.2f. Also, in the presence of the static magnetic field, the electromagnetic wave penetrates into the plasma deeper than the conventional skin depth. Three-dimensional components of the inductively coupled electric field are generated within the plasma due to the full tensor conductivity and these three components are coupled in the form of electromagnetic wave. One of the previous examples for the wave penetration into the ICP with the external magnetic field includes the demonstration by H.-J. Lee *et al.*[36].

The electron density,  $n_e$ , and electron temperature,  $T_e$  for the base case with and without the magnetic field are shown in Fig. 3.3.  $T_e$  is calculated from the EED as an effective temperature. With the magnetic field, the peak  $n_e$  increases by nearly a factor of 20 (from  $2.5 \times 10^{10} \text{ cm}^{-3}$  to  $5.3 \times 10^{11} \text{ cm}^{-3}$ ) and shifts to a smaller radius (from 3.3 cm to 2.3 cm). This shift is accompanied by an increase in the peak  $T_e$  from 5.9 to 8.1 eV, and a shift in the peak from a radius of 3.8 cm to 2.1 cm. In the experiment, the peak electron density increases by nearly a factor of 30 (from  $3 \times 10^{10} \text{ cm}^{-3}$  to  $9 \times 10^{11} \text{ cm}^{-3}$ ) and shifts from 3 cm to 2.3 cm. This is

accompanied by an increase in the peak  $T_e$  from 6.3 eV to 17 eV, and a change in the spatial distribution from uniform to peak adjacent to the coil. The ionization rates with and without the magnetic field calculated from the model are shown in Fig. 3.4. With the magnetic field, the peak ionization rate increases by a factor of 60 (from  $0.5 \times 10^{16} \text{ cm}^{-3}\text{s}^{-1}$  to  $3.0 \times 10^{17} \text{ cm}^{-3}\text{s}^{-1}$ ) and shifts to a smaller radius (from 3.3 cm to 1.85 cm) due to the confinement of hot electrons at the smaller radius. The increase in peak electron density with the magnetic field is potentially misleading. With the total power deposition constant, if the ionization efficiency is not changed by the magnetic field, then the total inventory of electrons should not appreciably change. However, it turned out that the total inventories of electrons with and without the magnetic field are  $1.67 \times 10^{14}$  and  $1.46 \times 10^{13}$ , respectively. This indicates that the ionization efficiency is better with the magnetic field than without for a given power. The electron motion is in large part along the azimuthal electric field line without the magnetic field, while it has additional circular motions with the magnetic field which gives rise to the increased chance to encounter the neutral species and to ionize them.

The electron energy probability functions (EEPF) at different radial positions are compared with experimental results in Figs. 3.5 and 3.6. The  $n_e$  and  $T_e$  for these cases are in Fig. 3.7. For the unmagnetized case (Fig. 3.5), the computed  $f(\varepsilon)$  is a weak function of radius and this is consistent with the experimental results. For the magnetized case (Fig. 3.6),  $f(\varepsilon)$  is a strong function of radius. Due to the confinement of hot electrons adjacent to the coil, the population of high-energy electrons significantly reduces at the outer region. Since electrons encounter more collisions with other electrons within the magnetic field line, the distribution tends to be Maxwellian.

In the absence of the magnetic field, the mean-free-path for energy loss,  $\lambda_e$ , is  $\approx 17$  cm,

and electron transport is non-local. Although the majority of the electron heating occurs within the skin depth ( $\approx 1$  cm) from the *RF* antenna coil, momentum transfer collision scattering,  $\lambda_m = 12.5$  cm (gas density  $8 \times 10^{13}$  cm $^{-3}$  and cross section  $1 \times 10^{-15}$  cm $^2$ ), distribute these hot electrons well beyond the skin depth. This non-local distribution is aided by a Lorentzian force due to the *RF*-induced magnetic field that, on the average, produces a  $\vec{v} \times \vec{B}$  force that points radially outward from the skin depth. The  $f(\varepsilon)$  is therefore fairly uniform across the radius, appearing Maxwellian due to the influence of electron-electron collisions.

The electron Larmor radius is about 0.66 mm at 100 Gauss, at a radius of about 2.4 cm. At this location, the electron cyclotron frequency is about  $2.8 \times 10^8$  Hz, the plasma frequency is about  $6.6 \times 10^9$  Hz (the electron density is  $5.4 \times 10^{11}$  cm $^{-3}$ ), and the electron-neutral collision frequency is  $6.1 \times 10^6$  Hz. These conditions produce well magnetized electrons. The ambipolar diffusion coefficient parallel to the magnetic field is  $3.2 \times 10^6$  cm $^2$ s $^{-1}$ , while the diffusion coefficient perpendicular to the magnetic field is  $2.6 \times 10^4$  cm $^2$ s $^{-1}$ . Electrons therefore have their energy loss collisions in close proximity to where they were accelerated, and so are confined to the skin depth. The tail of  $f(\varepsilon)$  is therefore highest in the skin depth closest to the coil and monotonically drops with increasing radius.

The radial electron density and temperature profiles are compared with experimental results in Fig. 3.7 at the mid-height of the coil. In general, without the magnetic field, the electron density peaks near the center of the chamber with a small shift towards the coils due to isotropic ambipolar diffusion dominating charged particle loss. The computed and experimental electron densities agree to within 20%.  $T_e$  does not significantly vary with radial position due to the dominance of nonlocal transport, and the agreement with experiment is within about 10%. For the magnetized case, agreement is within 20% at large radius and 40-50% at small radius.

This difference is largely a consequence of there being more depletion of low energy electrons at high magnetic field (small radius) in the experiment than predicted by the model. In the computed results, we have a small depletion of electrons only at the smallest radius. The large deviations at the smaller radius for the magnetized plasma may also be in part due to the large electromagnetic field that may cause uncertainties in the model and experiments, especially in the presence of the large static magnetic field.[16] The uncertainties may include the hall effect and the fluctuation of the plasma potential.

### 3.4 Scaling with Pressure and Power

The electron energy distribution functions  $f(\varepsilon)$  for unmagnetized and magnetized plasmas at the reference position (radius = 3 cm at height of the mid-coil as noted in Fig. 3.1a where  $B = 57$  Gauss) are shown in Fig. 3.8 for pressures of 3 – 100 mTorr. Since the plasma shape changes as pressure increases, the  $f(\varepsilon)$  at a fixed radius may represent combinatorial results of the pressure effect and the plasma shape change. However, as shown in Fig. 3.9, although the peak electron temperature shifts to the smaller radius as pressure increases, the variation of electron temperature at the radius of 3 cm where the  $f(\varepsilon)$  is obtained is mainly determined by the pressure. Nevertheless, it is worth noting that if the  $f(\varepsilon)$  had been obtained at the larger radius, it could have been exaggerated because it could reflect both effects of the peak shift and the pressure dependence. Without the magnetic field, as the pressure increases, the tail of  $f(\varepsilon)$  progressively becomes more cut-off at the threshold energy for excitation of the Ar(4s) manifold, approximately 12 eV. With the magnetic field, the tail of  $f(\varepsilon)$  is more enhanced due to the confinement of the hot electrons and the reduction in diffusion cooling that naturally depletes the tail. As the pressure increases, the confinement effect diminishes due to the increase in collision

frequency. At 100 mTorr, the electron-neutral collision frequency,  $1.9 \times 10^8$  Hz, is commensurate to the cyclotron frequency,  $1.6 \times 10^8$  Hz, at the reference position.

The electron temperature and density as a function of radius at the middle of the coil are shown in Figs, 3.9 and 3.10 for pressures of 3 – 100 mTorr. Without the magnetic field,  $T_e$  decreases while  $n_e$  increases as pressure increases due to a lower rate of loss by diffusion. The electron energy relaxation length ( $\lambda_e$ ) is 17 cm at 3 mTorr and decreases to 0.5 cm at 100 mTorr, which is commensurate with the chamber radius. Therefore,  $T_e$  is fairly uniform across the chamber at 3 mTorr while there is significant radial variation at 100 mTorr. The radial shape of  $n_e$  does not significantly change as the pressure increases, which indicates that the electron ionization source peaks at approximately the same position over this range of pressure. The

ionization rate  $n_e(\vec{r})N_g \int_0^\infty f(\varepsilon, \vec{r}) \left(\frac{2\varepsilon}{m_e}\right)^{1/2} \sigma_{ion}(\varepsilon) d\varepsilon$  is determined by  $f(\varepsilon, \vec{r})$ , electron density ( $n_e$ ) and neutral density ( $N_g$ ). In unmagnetized condition, the increase in  $n_e$  and  $N_g$  with increasing pressure is faster than the lowering of the tail of  $f(\varepsilon)$ . Therefore, the ionization rate increases as pressure increases, as shown in Fig. 3.11a. For the total power deposition remaining constant at 100 W, the volume integral  $\int n_e(\vec{r})K_\varepsilon(\vec{r})N_g d^3r$  should remain constant, where  $K_\varepsilon$  is the rate coefficient for energy loss (eV-cm<sup>3</sup>/s) and  $N_g$  is the gas density. The lowering of the tail of  $f(\varepsilon)$  decreases  $K_\varepsilon$  with increasing pressure faster than the increase in  $N_g$ , as shown in Fig. 3.12a. Therefore,  $n_e$  must increase to deposit the same total power.

With the magnetic field, there is a change in the shape of the plasma, peaking at smaller radius at lower pressure. The peak plasma density is constant within less than a factor of two from 3 – 100 mTorr. In the low pressure regime (3 – 30 mTorr), as pressure increases, the electron transport transits from nonlocal to local, and consequently the peak electron density

shifts to a larger radius (from 2.1 cm to 3.1 cm) where the volume is larger. Although the peak electron density decreases a little bit from  $4.98 \times 10^{11} \text{ cm}^{-3}$  at 2.1 cm to  $3.72 \times 10^{11} \text{ cm}^{-3}$  at 3.1 cm, the volume integral of  $n_e$  is increased as pressure increases from 3 to 30 mTorr to compensate for the decrease in  $K_e$ . In the high pressure regime (30 – 100 mTorr), as the pressure increases, the peak electron density stays at the same radius and so the peak value must increase in order to compensate for the decrease of  $K_e$ . At the lower pressure, the collision frequency is smaller than the cyclotron frequency which results in electron transport being local in spite of the low pressure. The plasma is skewed towards small radius where the ionization source,  $S_e$ , is maximum. At 100 mTorr, the plasma is magnetized at small radii ( $< 3$  cm) and unmagnetized at large radius ( $> 4$  cm), while based on pressure alone, electron transport is transitioning to being non-local. The shape of the plasma closely resembles that without the magnetic field. This demonstrates that the electron kinetics is in the local regime due to the electron confinement within the magnetic field at lower pressures, while it transits to the nonlocal regime due to the collisions at the higher pressure. As with the unmagnetized case,  $\int n_e(\vec{r})K_e(\vec{r})N_g d^3r$  must remain constant. Since  $K_e$  is maximum at small radius (with smaller incremental volume) at low pressure, then  $n_e$  must increase to deliver the desired power. The decrease in peak electron density from 3 to 30 mTorr is in part a consequence of  $K_e$  becoming more uniform radially as  $v_m/\omega_c$  increases and the plasma becomes less magnetized. The larger incremental volume at larger radius results in a lower  $n_e$  to deliver the same power.

The EEDs are relatively insensitive changes in power from 5-200 W in the unmagnetized case, as shown in Fig. 3.13a for a pressure of 3 mTorr. The  $f(\varepsilon)$  have only minor differences in the tail between various powers. In quasi-steady state operation,  $f(\varepsilon)$  is determined by results from a real-time balance between electron sources and sinks. Since diffusion dominates in all

cases, the electron loss rate by the diffusion is balanced by the source rate by the ionization but the diffusion is determined by the pressure (not by the power). Since the source rate is determined by the EED, the EED does not need to change for a fixed diffusion loss (fixed pressure). As increasing the power from 5 W to 200 W, the gas temperature increased from 327 K to 397 K. Consequently, the gas density decreased from  $8.8 \times 10^{13} \text{ cm}^{-3}$  with 5 W to  $7.2 \times 10^{13} \text{ cm}^{-3}$  with 200 W. As a result,  $T_e$  and  $n_e$  shown in Figs. 3.14 and 3.15, have shapes that vary little with power deposition. Since  $f(\varepsilon)$  and  $T_e$  are weak functions of power,  $K_\varepsilon$  is a weak function of power and  $n_e$  increases to keep  $\int n_e(\vec{r})K_\varepsilon(\vec{r})N_g d^3r$  constant.

However, for the magnetized plasma, the  $f(\varepsilon)$  is somewhat sensitive to power. The tail of  $f(\varepsilon)$  is raised with increasing power, which increases  $T_e$  (Fig. 3.14) and changes the shape of  $n_e$  (Fig. 3.15), shifting the maximum in  $n_e$  to smaller radius. In the magnetized plasma, the electrons exchange energies with other electrons in the same magnetic field line as they move along the magnetic field lines. Thus, as the power increases, the confined electrons can gain more energy without losing much energy through the inelastic collision because the collision frequency at 3 mTorr is an order of magnitude smaller than the cyclotron frequency with 100 Gauss. Furthermore, as increasing the power from 5 W to 200 W, the gas temperature increased significantly from 353 K to 782 K. Consequently, the gas density decreased by factor of 3 (from  $8.2 \times 10^{13} \text{ cm}^{-3}$  to  $2.7 \times 10^{13} \text{ cm}^{-3}$ ). Due to the reduced gas density at the higher power, the diffusion loss is enhanced which requires a raised tail in the EED in order to balance the electron source and sink.

As the power increases, the maximum value of the electron density increases while the position of the maximum value remains about the same. This trend is true regardless of the presence of the magnetic field, as shown in Fig. 3.10. However, the electron temperature is

independent of the power for the unmagnetized case while it is proportional to the power because the temperature of confined electrons adjacent to the coils is enhanced by the increased power, but the electrons away from the coils remain cold. The gradient of the electron temperatures between different radial positions is independent of the applied power because it is determined by the thermal diffusivity that is affected by the ratio of the electron-neutral collision frequency to the cyclotron frequency rather than by the applied power. This reflects how the electron kinetics is independent of the applied power. This is because the applied power affects neither the electron energy relaxation length nor the electron-neutral collision frequency.

Although the pressure and power can provide the controllability of the EED to some extent as shown in Figs. 3.8 and 3.13, they also change the other plasma conditions simultaneously, which makes it difficult to predict the end result. In order to control the EED independently, we also studied the time-modulated magnetic field. If the magnetic field is operated in pulse mode, the EED may vary as a function of time at a given location without much change in the other plasma conditions. It has been reported that the ion density increased but the electron temperature decreased with the time-modulated external magnetic field compared to the continuous application of the magnetic field.[37,38] Our preliminary results of the EED with pulsed magnetic field are shown in Fig. 3.16. In order to briefly demonstrate the possibility of using pulsed magnetic fields as a means to control the EED, the comparison between different magnetized conditions is plotted in Fig. 3.16. For this comparison, the magnetic field is applied in pulsed mode with a repetition frequency of 25 kHz, and a duty cycle of 1%. It was found that using pulsed magnetic field provides another controllability to customize the tail component of the EED without much change in the low energy component. Also this result suggests that a further control in the tail of the EED can be achieved by adjusting

the duty cycle of the pulsed magnetic field. However, understanding further details on physics behind the pulsed magnetic fields relies upon more calculations on the temporal behavior of power deposition and fundamental plasma parameters.

### **3.5 Concluding Remarks**

The properties of ICP with and without the magnetic field have been computationally investigated using results from a 2D plasma hydrodynamic model having an electron Monte Carlo simulation including electron-electron collisions. Results are compared with the experimental measurements of plasma properties and EEDs. The static magnetic field prevents hot electrons generated adjacent to the antenna coils from diffusing outward, so that the EEDs show wide variations between different radial positions. In the presence of the magnetic field, the tail component of the distribution is enhanced due to the trapping of hot electrons, but this effect diminishes at the higher pressure due to the larger collision frequency being commensurate to the cyclotron frequency. The power change typically has a nominal effect on the EED without magnetic field but it turned out that in the presence of the magnetic field the gas temperature increased significantly by the power which resulted in the raised tail of the EED due to the reduced gas density. However, the applied power does not have a significant influence on the transition between local and nonlocal regimes of the electron kinetics, while the electron kinetics changes from the local to the nonlocal regime with increased pressure in the presence of the magnetic field. It was also found that the pulsed magnetic field can provide additional maneuverability for EED.

### 3.6 Figures

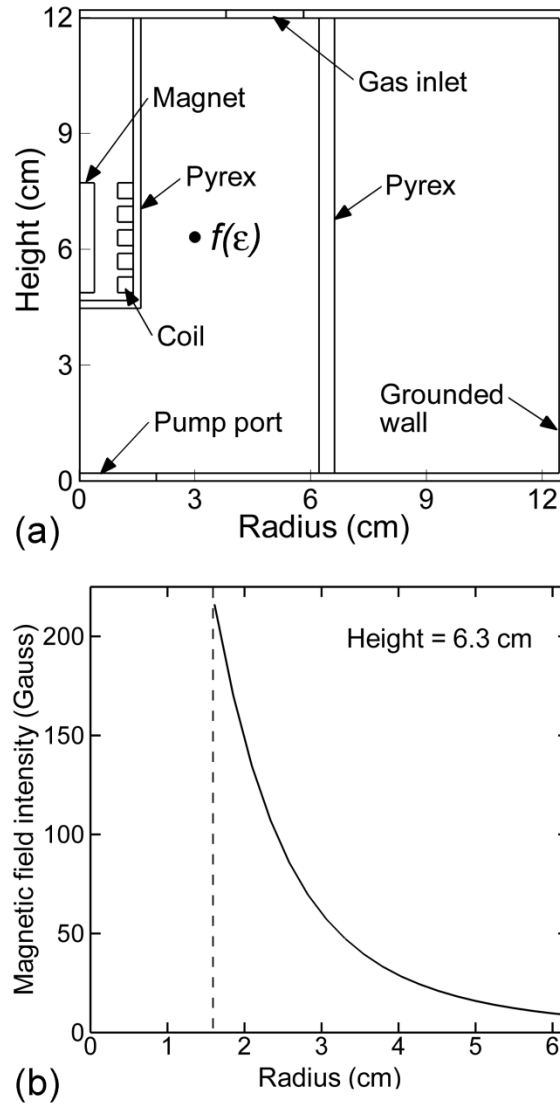


Fig. 3.1 Properties of the mICP. (a) Geometry of the mICP chamber. The permanent magnet is placed inside the antenna coil which is immersed in the plasma. (b) The magnetic field intensity at height of 6.3 cm as a function of radial position.

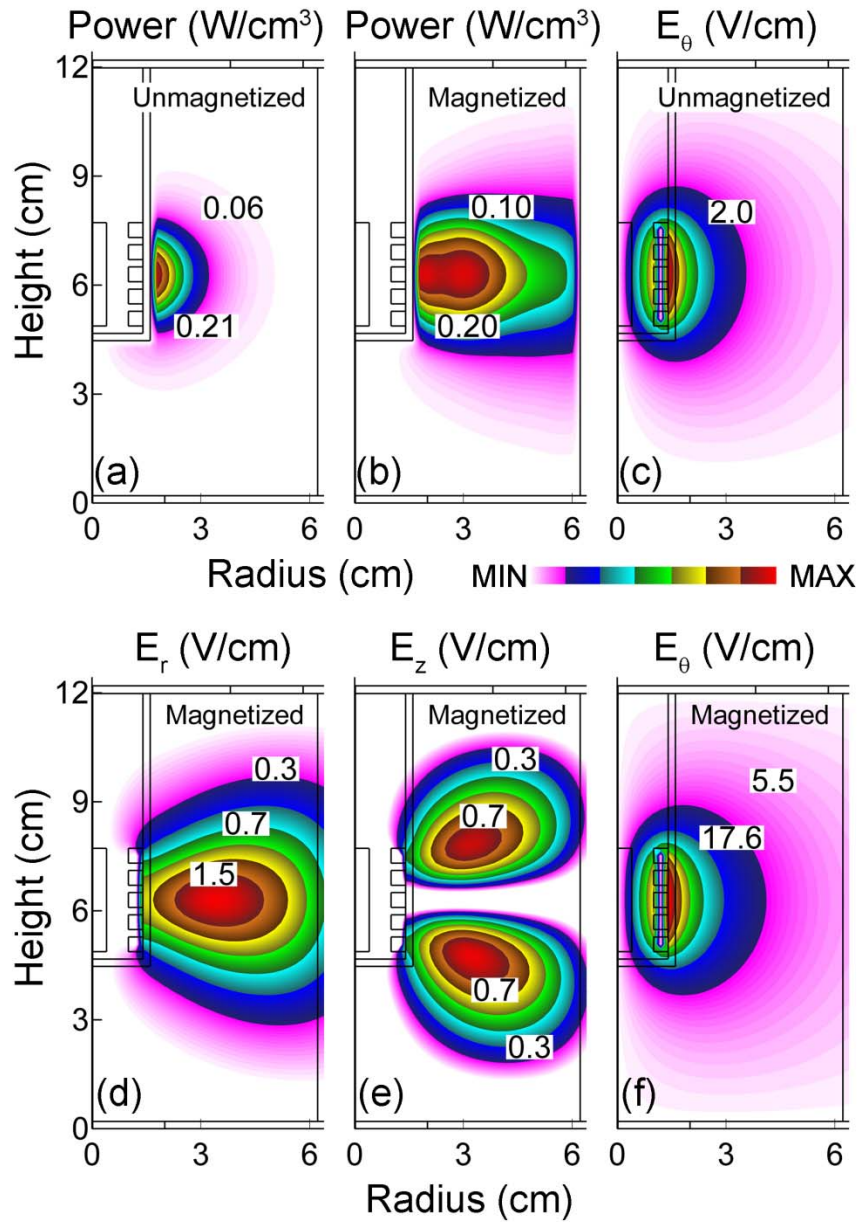


Fig. 3.2 Power deposition and electric fields for the base case conditions (3 mTorr, 100 W, 5 MHz). Power dissipation for (a) unmagnetized and (b) magnetized conditions. (c) Azimuthal electric field for unmagnetized condition. (d) Radial, (e) axial, and (f) azimuthal components of electric field for magnetized condition. The azimuthal electric field is larger with the magnetic field than without in order to compensate for the reduced conductivity. The power absorbing volume in a magnetized discharge is larger than in an unmagnetized discharge.

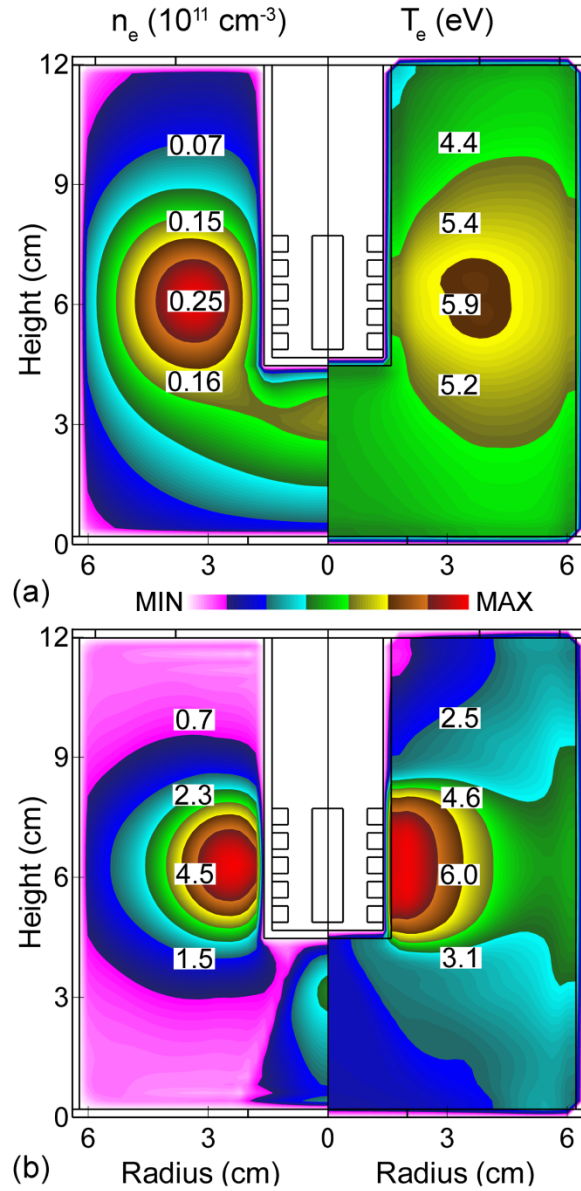


Fig. 3.3 Electron density and temperature for the base case conditions (3 mTorr, 100 W, 5 MHz). (a) Unmagnetized and (b) magnetized conditions. The peak electron density and temperature increased with magnetic field and the position of the peak shifted toward adjacent to the coil.

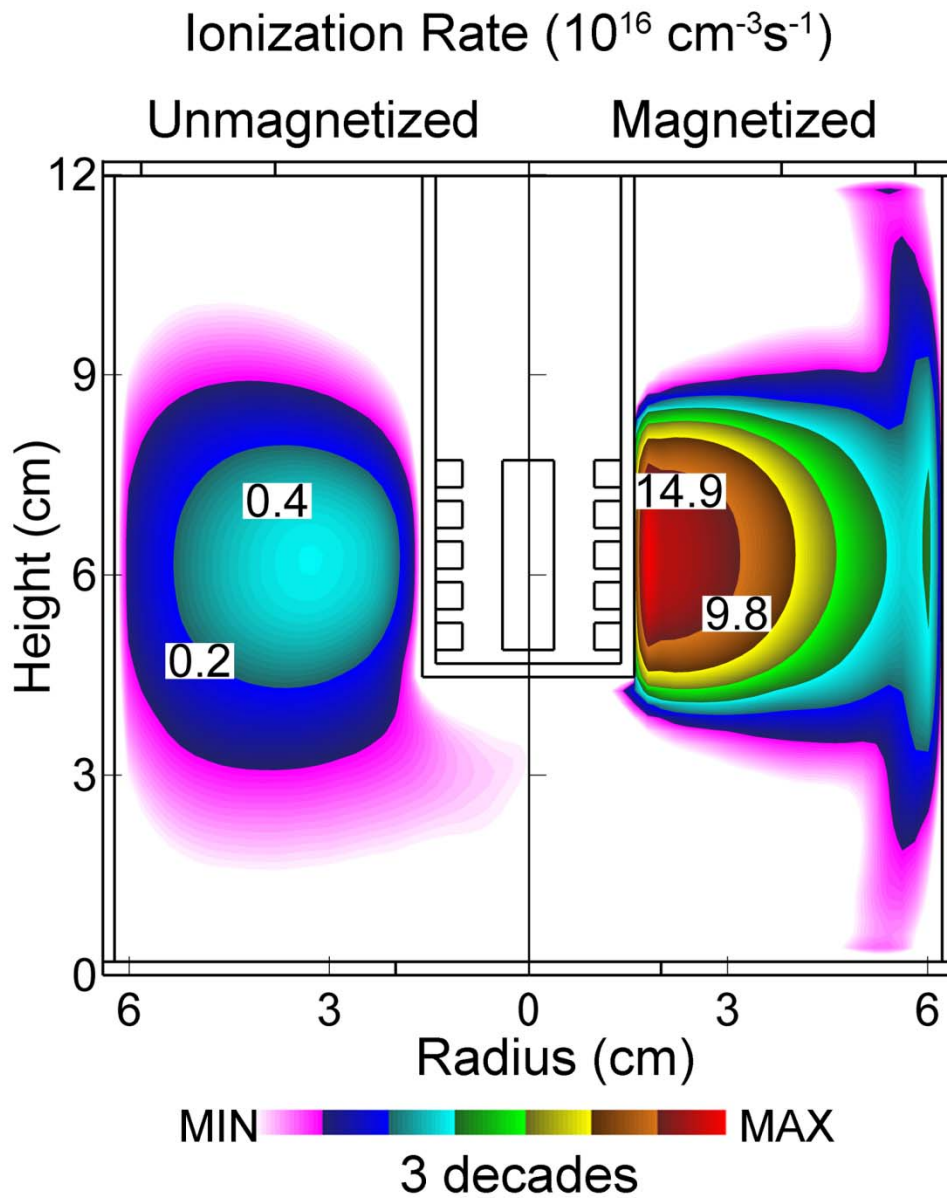


Fig. 3.4 Ionization rates for unmagnetized and magnetized conditions. Due to the enhanced tail of the EED adjacent to the coils, the ionization occurs by an orders of magnitude more with the magnetic field than without.

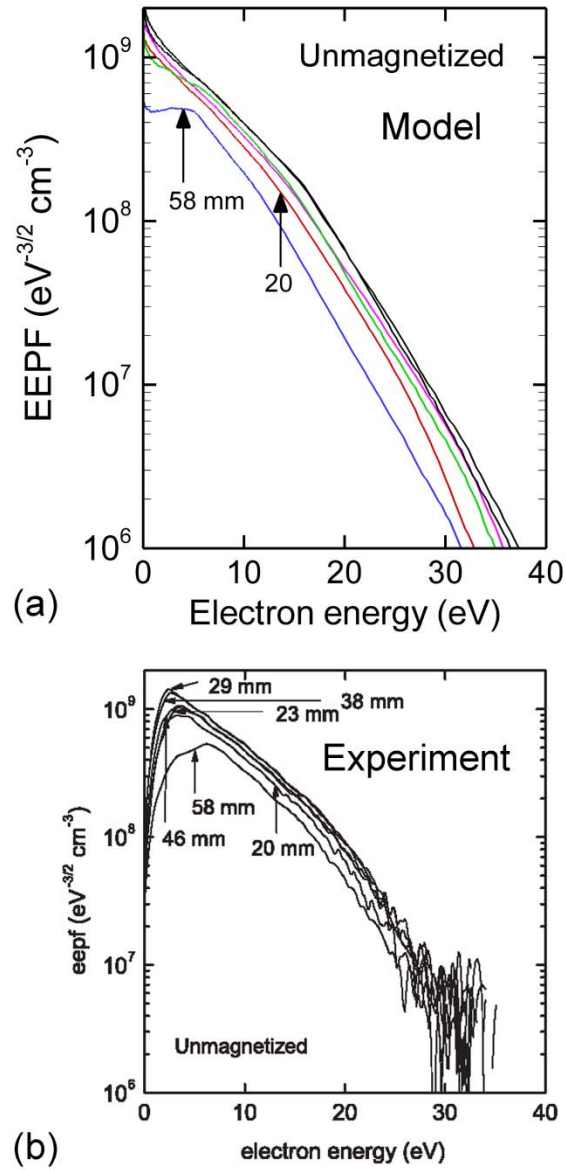


Fig. 3.5 Electron energy probability functions at different radial positions for unmagnetized condition. (a) Model and (b) experiment. The distribution does not vary much by the radial position. The model and experiment agree well each other.

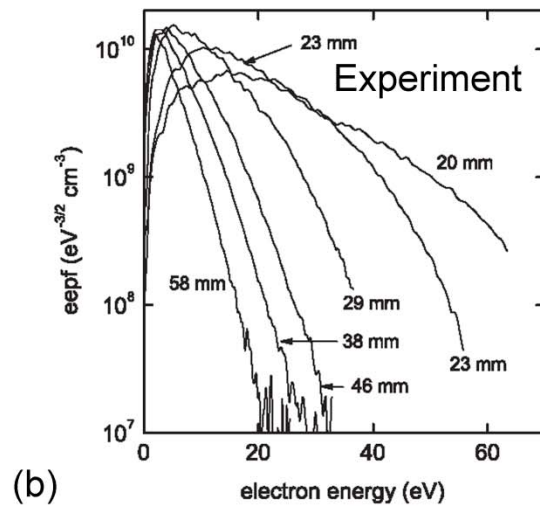
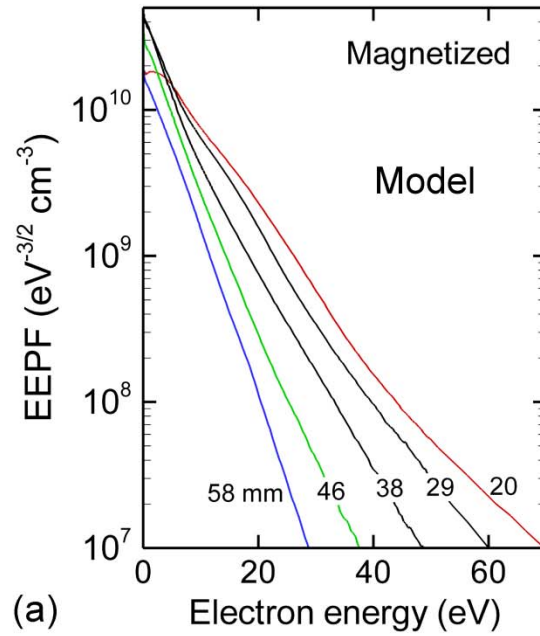


Fig. 3.6 Electron energy probability functions at different radial positions for magnetized condition. (a) Model and (b) experiment. The tail of the distribution is rased due to the confinement of hot electrons adjacent to the coil. The result from the model agrees well with the experimental result.

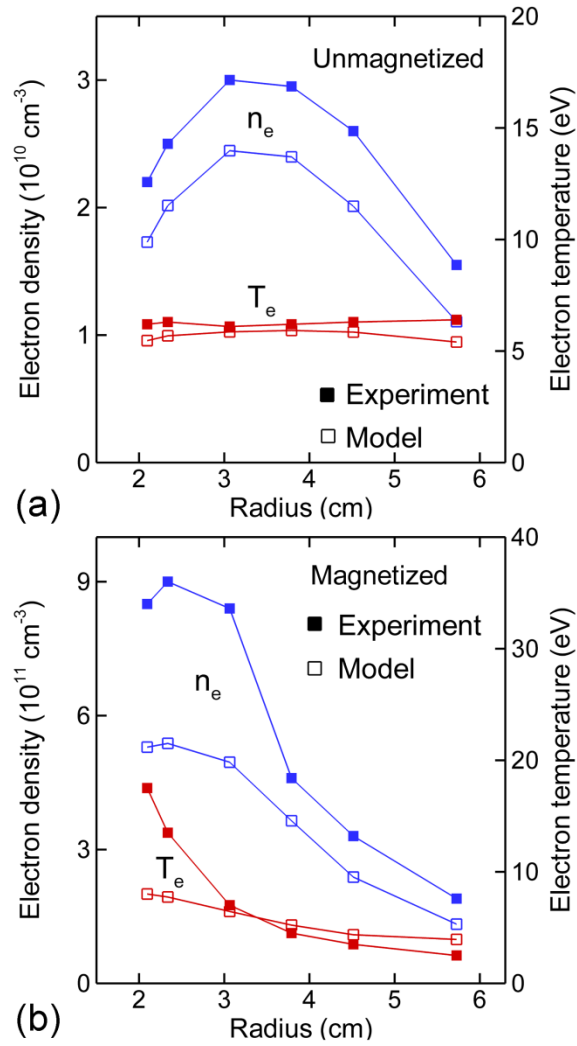


Fig. 3.7 Comparison of the electron density and temperature between the model and experiment. (a) Unmagnetized and (b) magnetized conditions. By applying the magnetic field, the peak electron density increases by an order of magnitude and the electron temperature far from the coil is reduced by half due to the confinement of the hot electrons.

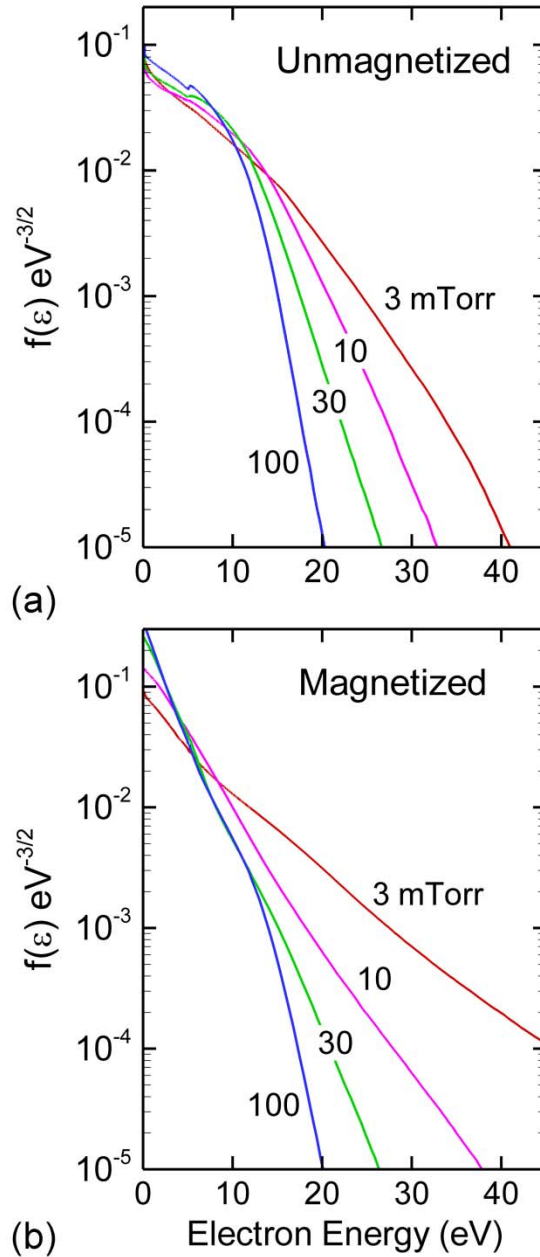


Fig. 3.8 Electron energy distribution functions with various pressures. (a) Unmagnetized and (b) magnetized conditions. The tail component of the distribution is enhanced due to the non-local electron kinetics at the lower pressure and the trend is the same regardless of the magnetic field.

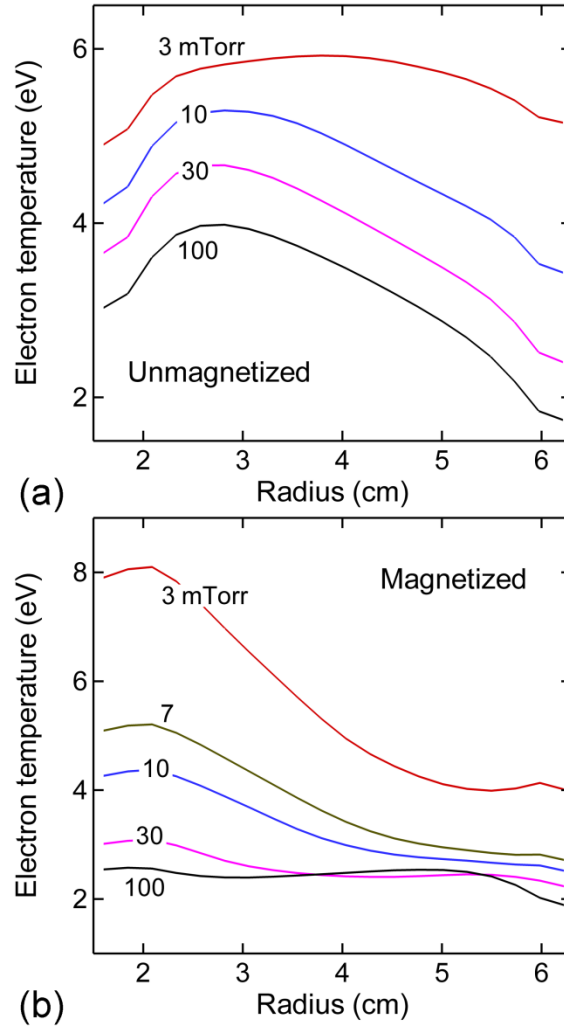


Fig. 3.9 Electron temperature as a function of radial position with various pressures for (a) unmagnetized and (b) magnetized conditions. Without magnetic field, the electron temperature is higher at the lower pressure in order to compensate for the larger diffusion loss. With magnetic field, the difference of the electron temperature between adjacent to the coil and away from the coil becomes smaller as pressure increases due to the collisional diffusion across the magnetic field at higher pressure.

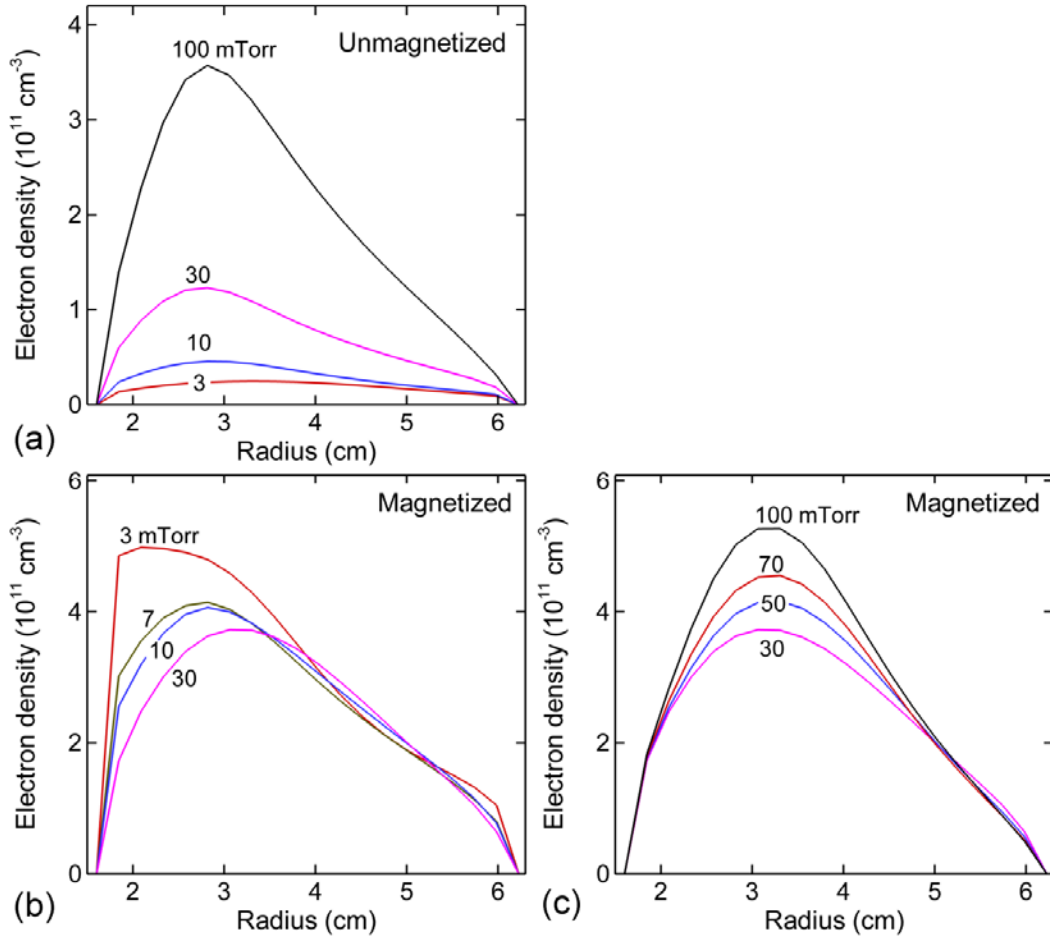


Fig. 3.10 Electron density as a function of radial position with various pressures. (a) Unmagnetized, (b) magnetized conditions for the pressure range 3 – 30 mTorr, and (c) magnetized conditions for the pressure range 30 – 100 mTorr. Without magnetic field, the peak electron density is significantly increased by the pressure increase due to the reduced diffusion loss at the higher pressure. With magnetic field the peak density decreases which is accompanied by the shift towards larger radii as pressure increases from 3 to 30.

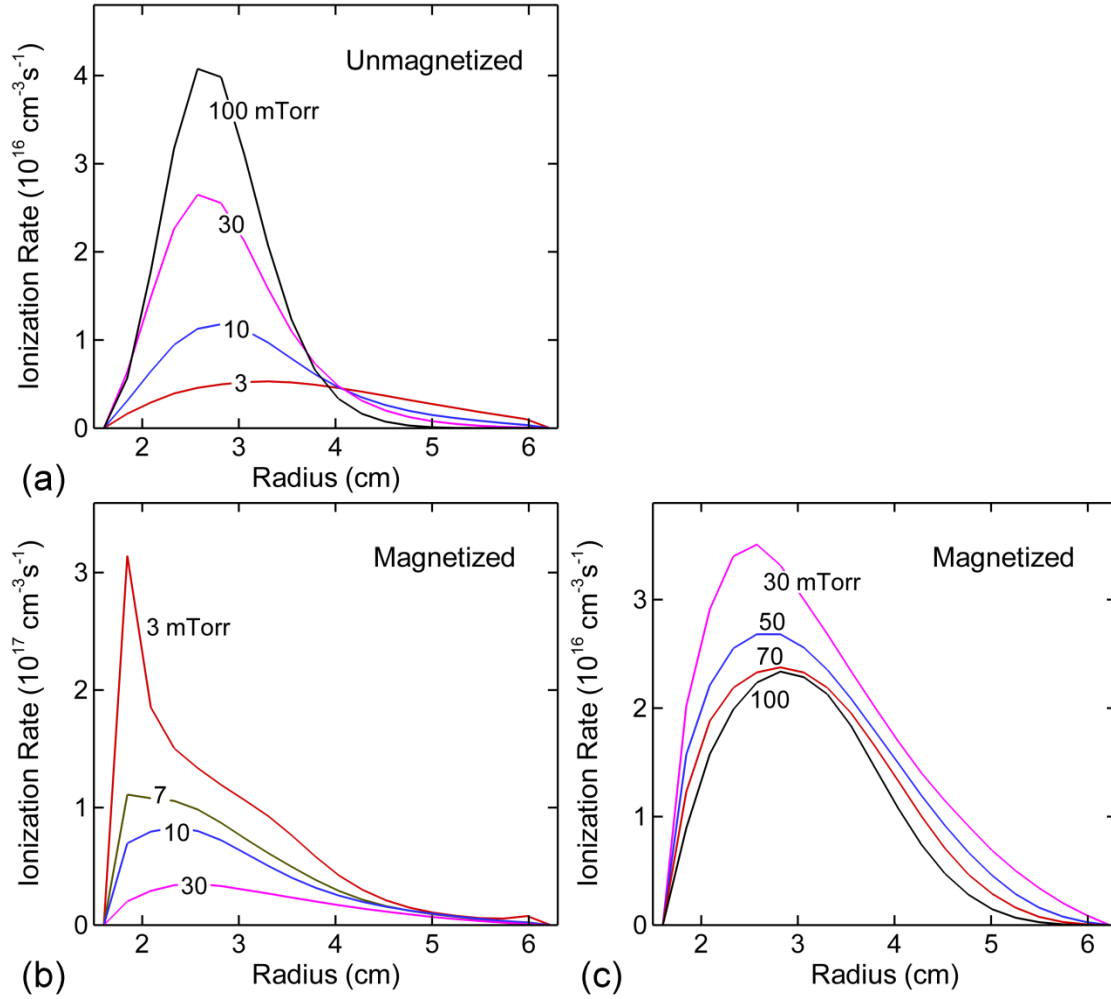


Fig. 3.11 Ionization rate as a function of radius with various pressures. (a) Unmagnetized, (b) magnetized conditions for the pressure range 3 – 30 mTorr, and (c) magnetized conditions for the pressure range 30 – 100 mTorr.

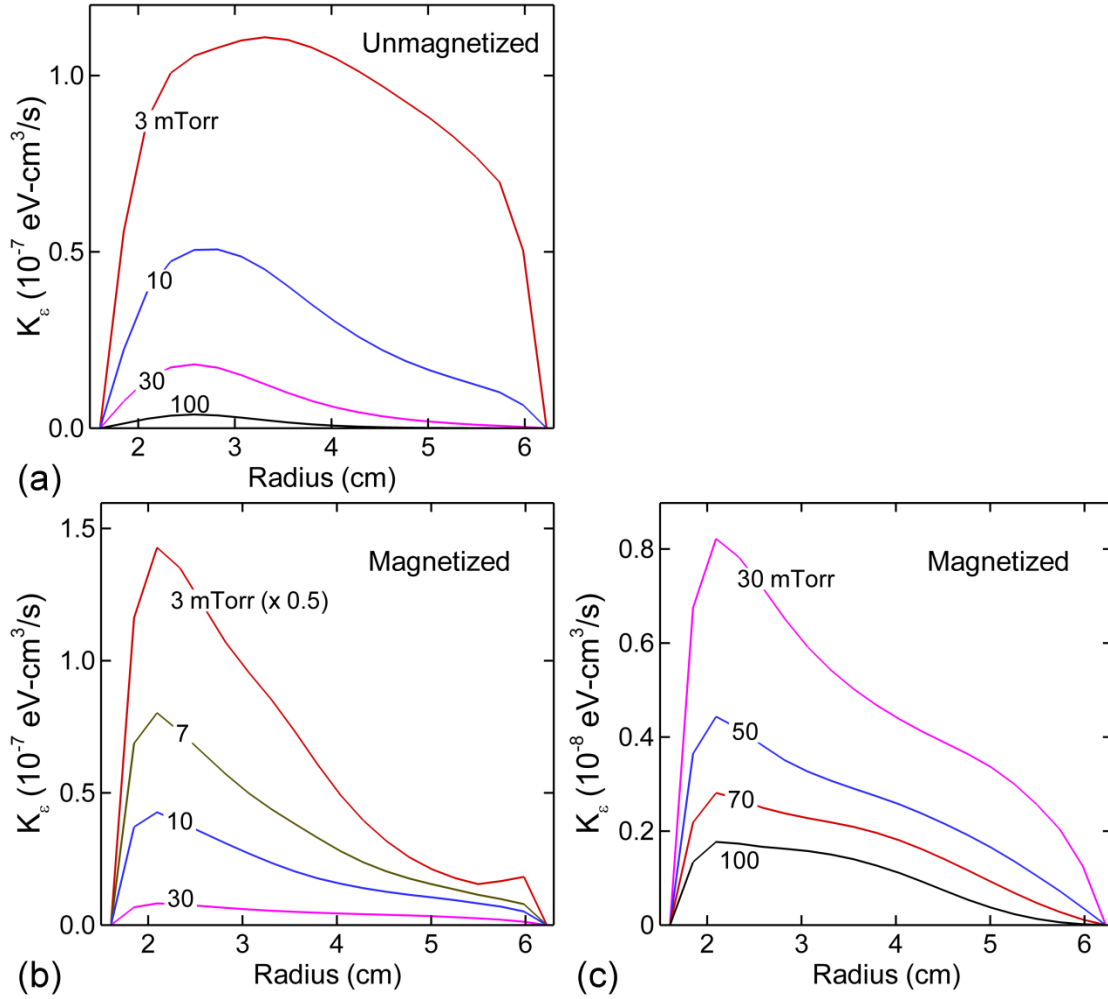


Fig. 3.12 Rate coefficient for energy loss at a function of radius with various pressures. (a) Unmagnetized, (b) magnetized conditions for the pressure range 3 – 30 mTorr, and (c) magnetized conditions for the pressure range 30 – 100 mTorr.

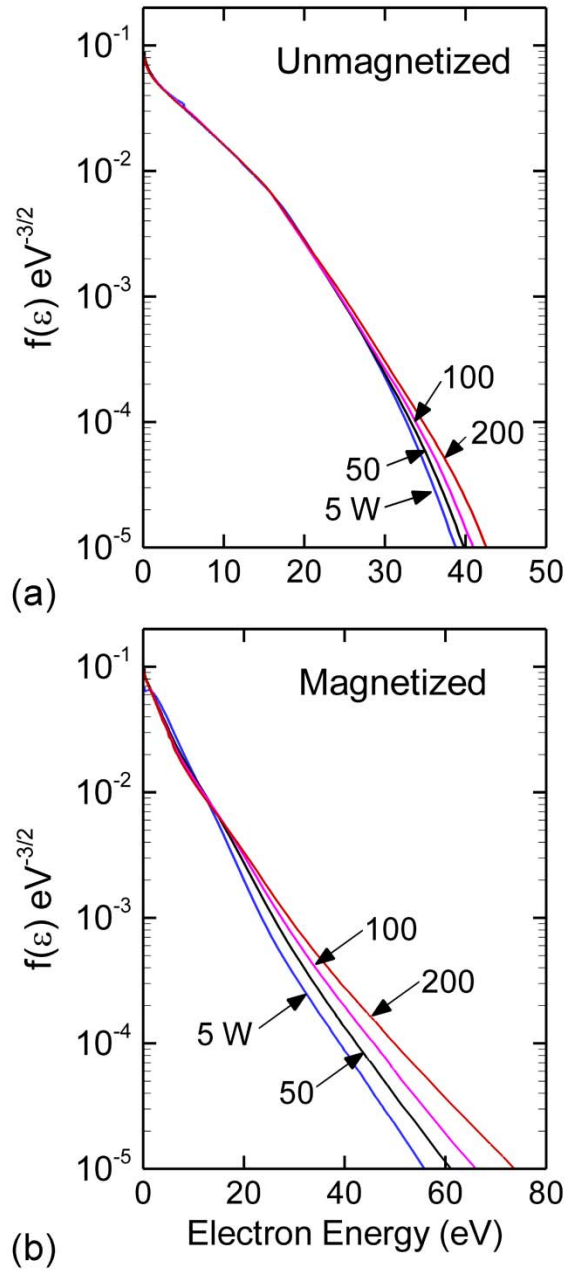


Fig. 3.13 Electron energy distribution functions with various powers. (a) Unmagnetized and (b) magnetized conditions. The effect of the power on the distribution is relatively small compared to the effect of the pressure but with the magnetic field the distribution is affected by the power change due to more efficient power coupling into the electron heating.

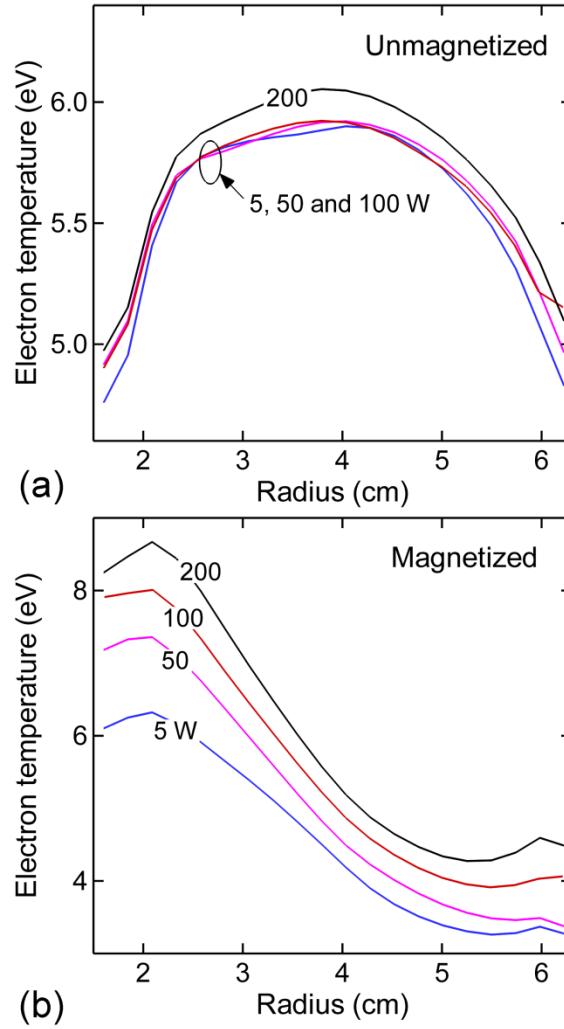


Fig. 3.14 Electron temperature as a function of radial position with various powers. (a) Unmagnetized and (b) magnetized conditions. The electron temperature does not vary with power without magnetic field while it increases by power with magnetic field.

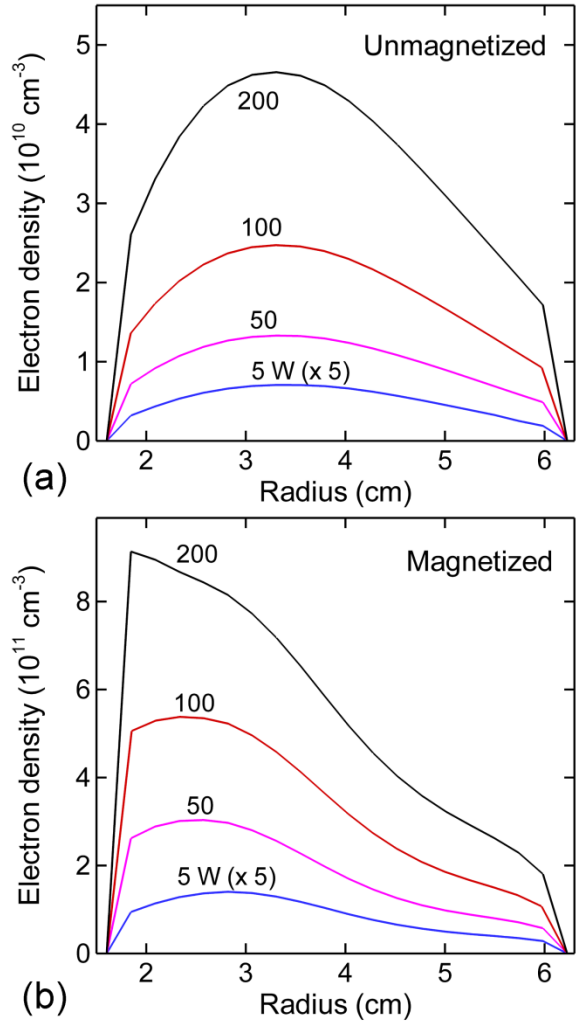


Fig. 3.15 Electron density as a function of radial position with various powers. (a) Unmagnetized and (b) magnetized conditions. The peak electron density increases as the power increases and the trend is the same with and without magnetic field.

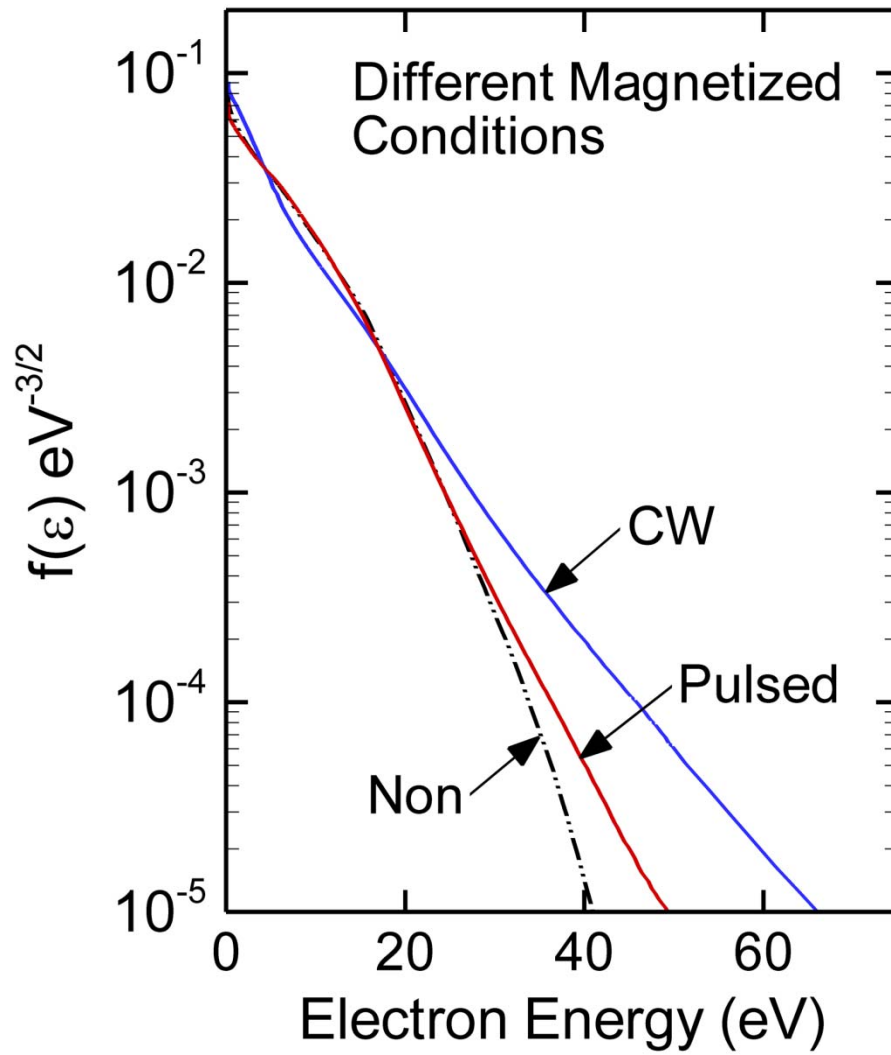


Fig. 3.16 Electron energy distributions with various magnetized. Pulsed condition of the magnetic field is chosen with the repetition frequency of 25 kHz and the duty cycle of 10%.

### 3.7 References

1. J. Asmussen, "Electron cyclotron resonance microwave discharges for etching and thin-film deposition", *J. Vac. Sci. Technol. A* **7**, 883 (1989).
2. O. J. Glembocki, J. A. Tuchman, K. K. Ko, S. W. Pang, A. Giordana, R. Kaplan, and C. E. Stutz, "Effects of electron cyclotron resonance etching on the ambient (100) GaAs surface", *Appl. Phys. Lett.* **66**, 3054 (1995).
3. R. A. Lindley, C. H. Bjorkman, H. Shan, K.-H. Ke, K. Doan, R. R. Mett, and M. Welch, "Magnetic field optimization in a dielectric magnetically enhanced reactive ion etch reactor to produce an instantaneously uniform plasma", *J. Vac. Sci. Technol. A* **16**, 1600 (1998).
4. A. Herrick, A. J. Perry, and R. W. Boswell, "Etching silicon by SF<sub>6</sub> in a continuous and pulsed power helicon reactor", *J. Vac. Sci. Technol. A* **21**, 955 (2003).
5. L. Wu, E. Ko, A. Dulkan, K. J. Park, S. Fields, K. Leeser, L. Meng, and D. N. Ruzic, "Flux and energy analysis of species in hollow cathode magnetron ionized physical vapor deposition of copper", *Rev. Sci. Instrum* **81**, 123502 (2010).
6. K. G. Kostov and J. J. Barroso, "Numerical simulation of magnetic-field-enhanced plasma immersion ion implantation in cylindrical geometry", *IEEE Tans. Plasma Sci.* **34**, 1127 (2006).
7. D. Benyoucef, M. Yousfi, and B. Belmadani, "Self-consistent particle modeling of radio frequency discharge in Ar/O<sub>2</sub> mixtures: Effects of crossed electric and magnetic fields and partial pressure", *J. Appl. Phys.* **109**, 083304 (2011).
8. W. Cronrath, N. Mayumi, M. D. Bowden, K. Uchino, M. Yoshida, and K. Muraoka, "A study of ion velocity distribution functions in processing plasmas produced by electron cyclotron discharges", *J. Appl. Phys.* **82**, 1036 (1997).
9. D. D. Blackwell and F. F. Chen, "Time-resolved measurements of the electron energy distribution function in a helicon plasma", *Plasma Sources Sci. Technol.* **10**, 226 (2001).
10. Z. Wang, S. A. Cohen, D. N. Ruzic, and M. J. Goekner, "Nitrogen atom energy distributions in a hollow-cathode planar sputtering magnetron", *Phys. Rev. E* **61**, 1904 (2000).
11. N. Hershkowitz and T. Intrator, "Improved source of cold plasma electrons and negative ions", *Rev. Sci. Instrum.* **52**, 1629 (1981).
12. J. Bretagne, W. G. Graham, and M. B. Hopkins, "A comparison of experimental and theoretical electron energy distribution functions in a multicusp ion source", *J. Phys. D* **24**, 668 (1991).
13. G.-H. Kim, N. Hershkowitz, D. A. Diebold, and M.-H. Cho, "Magnetic and collisional effects on presheaths", *Phys. Plasmas* **2**, 3222 (1995).

14. C. W. Chung, S. S. Kim, and H. Y. Chang, "Experimental measurement of the electron energy distribution function in the radio frequency electron cyclotron resonance inductive discharge", *Phys. Rev. E* **69**, 016406 (2004).
15. A. Aanesland, J. Bredin, P. Chabert, and V. Godyak, "Electron energy distribution function and plasma parameters across magnetic filters", *Appl. Phys. Lett.* **100**, 044102 (2012).
16. J. A. Monreal, P. Chabert, and V. Godyak, "Reduced electron temperature in a magnetized inductively-coupled plasma with internal coil", *Phys. Plasmas* **20**, 103504 (2013).
17. S. S. Kim, C. S. Chang, N. S. Yoon, and K. W. Whang, "Inductively coupled plasma heating in a weakly magnetized plasma", *Phys. Plasmas* **6**, 2926 (1999).
18. O. V. Polomarov, C. E. Theodosiou, I. D. Kaganovich, B. N. Ramamurthi, and D. J. Economou, "Effectiveness of electron-cyclotron and transmission resonance heating in inductively coupled plasmas", *Phys. Plasmas* **12**, 104505 (2005).
19. A. Rehman and Y. K. Pu, "Effect of electron thermal motion on plasma heating in a magnetized inductively coupled plasma", *Phys. Plasmas* **14**, 063503 (2007).
20. A. Rehman and J. K. Lee, "Effective viscosity model for electron heating in warm magnetized inductively coupled plasma discharges", *Phys. Plasmas* **16**, 083504 (2009).
21. D. H. Kim and C.-M. Ryu, "Particle simulation of a magnetically enhanced dual-frequency capacitively coupled plasma", *J. Phys. D: Appl. Phys.* **41**, 015207 (2008).
22. L. D. Tsendin, "Current trends in electron kinetics of gas discharges", *Plasma Sources Sci. Technol.* **12**, S51 (2003).
23. H.-J. Lee, I. D. Yang, and K. W. Whang, "The effects of magnetic fields on a planar inductively coupled argon plasma", *Plasma Sources Sci. Technol.* **5**, 383 (1996).
24. B. E. R. Williams and R. J. Kingham, "Hybrid simulations of fast electron propagation including magnetized transport and non-local effects in the background plasma", *Plasma Phys. Control. Fusion* **55**, 124009 (2013).
25. I. D. Kaganovich, O. V. Polomarov, and C. E. Theodosiou, "Revisiting the anomalous RF field penetration into a warm plasma", *IEEE Trans. Plasma Sci.* **34**, 696 (2006).
26. A. Maresca, K. Orlov, and Uwe Kortshagen, "Experimental study of diffusive cooling of electrons in a pulsed inductively coupled plasma", *Phys. Rev. E* **65**, 056405 (2002).
27. H. S. Jun and H. Y. Chang, "Development of 40 MHz inductively coupled plasma source and frequency effects on plasma parameters", *Appl. Phys. Lett.* **92**, 041501 (2008).
28. Mark J. Kushner, "Hybrid modelling of low temperature plasmas for fundamental investigations and equipment design", *J. Phys. D: Appl. Phys.* **42**, 194013 (2009).

29. S. H. Song and M. J. Kushner, "Control of electron energy distributions and plasma characteristics of dual frequency, pulsed capacitively coupled plasmas sustained in Ar and Ar/CF<sub>4</sub>/O<sub>2</sub>", *Plasma Sources Sci. Technol.* **21**, 055028 (2012).
30. T. Holstein, "Imprisonment of resonance radiation in gases", *Phys. Rev.* **72**, 1212 (1947).
31. T. Holstein, "Imprisonment of resonance radiation in gases. II", *Phys. Rev.* **83**, 1159 (1951).
32. K. Rajaraman and M. J. Kushner, "A Monte Carlo simulation of radiation trapping in electrodeless gas discharge lamps", *J. Phys. D: Appl. Phys.* **37**, 1780 (2004).
33. K. J. McCann and M. R. Flannery, "Photoionization of metastable rare-gas atoms (He<sup>\*</sup>, Ne<sup>\*</sup>, Ar<sup>\*</sup>, Kr<sup>\*</sup>, Xe<sup>\*</sup>)", *Appl. Phys. Lett.* **31**, 599 (1977).
34. N. A. Dyatko, Y. Z. Ionikh, I. V. Kochetov, D. L. Marinov, A. V. Meshchanov, A. P. Napartovich, F. B. Petrov, and S. A. Starostin, "Experimental and theoretical study of the transition between diffuse and contracted forms of the glow discharge in argon", *J. Phys. D: Appl. Phys.* **41**, 055204 (2008).
35. A. Bogaerts and R. Gijbels, "Role of Ar<sup>2+</sup> and Ar<sub>2</sub><sup>+</sup> ions in a direct current argon glow discharge: A numerical description", *J. Appl. Phys.* **86**, 4124 (1999).
36. H.-J. Lee, H.-S. Tae, Y. T. Kim, and K.-W. Whang, "Electric field in magnetized inductively coupled plasma", *IEEE Trans. Plasma Sci.* **27**, 52 (1999).
37. B.-H. O, J.-S. Jeong, and S.-G. Park, "Improvement of ICP plasma with periodic control of axial magnetic field", *Surf. Coat. Tech.* **120-121**, 752 (1999).
38. R. Doron, R. Arad, K. Tsigutkin, D. Osin, A. Weingarten, A. Starobinets, V. A. Bernshtam, E. Stambulchik, Yu. V. Ralchenko, Y. Maron, A. Fruchtman, A. Fisher, J. D. Huba, and M. Roth, "Plasma dynamics in pulsed strong magnetic fields", *Phys. Plasmas* **11**, 2411 (2004).

## Chapter 4 BEHAVIOR OF SECONDARY ELECTRONS IN DC-AUGMENTED CAPACITIVELY COUPLED PLASMAS

### 4.1 Introduction

There have been many computational studies on the instabilities induced by the electron beam such as two stream instability and bump on tail instability. When the electron beam is injected into the plasma, it excites the Langmuir electron plasma wave which then undergoes the Landau damping to transfer the energy to the bulk electrons making raised tail of the  $f(\varepsilon)$ . Silin *et al.* solved the Poisson equation for the electric field by a Fourier method and the Vlasov equation for the  $f(\varepsilon)$  using Eulerian-type flux balanced method.[1] They found that the coherent Langmuir wave packets can be generated only in the presence of very weak electron beam with  $n_b/n_e \approx 10^{-3}$ , where  $n_b$  is beam electron density and  $n_e$  is bulk electron density. For higher beam densities,  $n_b/n_e > 0.5$ , the interaction leads to strong nonlinearity and formation of solitary structures. Other than solving Vlasov equation [2], there are also several works on the electron beam-plasma interaction using particle in cell (PIC) method [3-6], Monte-Carlo simulation (MCS) [7-9], or molecular dynamics (MD) method [10,11]. MD method is particularly used to capture the relaxation of the electron and ion kinetic energies in strongly coupled plasmas. Since the typical beam electron density ( $n_b$ ) from secondary emission with  $\gamma_i$  of 0.15 is about  $4 \times 10^5 \text{ cm}^{-3}$ , the stream instability does not occur due to  $n_b/n_e < 10^{-4}$ . Thus, we consider only the

Coulomb interaction between the beam and bulk electrons.

In this chapter, we discuss the bulk electron heating by the high energy secondary electrons using results from a two-dimensional (2D) fluid hydrodynamic simulation dealing with the electron transport by Monte-Carlo method. The  $f(\varepsilon)$  of the bulk electrons changes drastically by the secondary (beam) electrons, especially in the high energy tail component of  $f(\varepsilon)$ . We found that the enhancement of tail component is more significant adjacent to the electrodes and the e-SEE plays an important role in the bulk electron heating.

## 4.2 Description of the Model

The model used in this investigation is 2D fluid hydrodynamic simulation in which the energy distribution of bulk and secondary electrons are obtained using an electron Monte-Carlo simulation (eMCS). The collisions between electrons are implemented by the particle mesh technique where the electrons collide with an energy resolved electron fluid with Coulomb collision parameters. Since the  $e-e$  collision is elastic, the relative speed does not change but it changes only in the direction randomly. In the center of mass system, the velocity of the beam electron is

$$\vec{V}_C^F = \vec{V}_F - \vec{V}_C = \vec{V}_F - \frac{\vec{V}_F + \vec{V}_T}{2} = \frac{\vec{V}_F - \vec{V}_T}{2} = \frac{\vec{V}_R}{2}, \quad (4.1)$$

and the velocity of the bulk electron is

$$\vec{V}_C^T = \vec{V}_T - \vec{V}_C = \vec{V}_T - \frac{\vec{V}_F + \vec{V}_T}{2} = -\frac{\vec{V}_F - \vec{V}_T}{2} = -\frac{\vec{V}_R}{2}, \quad (4.2)$$

where  $\vec{V}_C^F$  is the beam electron velocity in the center of mass (COM) system,  $\vec{V}_C^T$  is the bulk electron velocity in the COM system,  $\vec{V}_F$  is the beam electron velocity in the laboratory (LAB) system,  $\vec{V}_T$  is the bulk electron velocity in LAB system,  $\vec{V}_C$  is the velocity of the COM system,

and  $\vec{V}_R$  is the relative velocity. After the collision, the magnitude of  $\vec{V}_R$  does not change, but its direction changes randomly according to the random collision angle. Thus, the new velocities of the electrons after collision are going to be

$$\vec{V}_{C\_new}^F = \frac{\vec{V}_R^{new}}{2}, \quad \vec{V}_{C\_new}^T = -\frac{\vec{V}_R^{new}}{2}, \quad (4.3)$$

$$\vec{V}_F^{new} = \vec{V}_C + \frac{\vec{V}_R^{new}}{2}, \quad \vec{V}_T^{new} = \vec{V}_C - \frac{\vec{V}_R^{new}}{2}. \quad (4.4)$$

When the secondary electrons lose their energy by colliding with bulk electrons, the energy loss is stored at the position of the collision. The energy loss of the beam electron is

$$E_{ij}^k = \frac{1}{2} m_e \left( |\vec{V}_F^{new}|^2 - |\vec{V}_F|^2 \right), \quad (4.5)$$

where  $E_{ij}^k$  is the energy loss of the beam electron (k) at the location of (i, j) and  $m_e$  is the electron mass. The bulk electrons gain the energy from the beam electron energy loss stored at the position. The beam electron energy loss is delivered to bulk electrons in a random fashion with randomly chosen azimuthal and polar angles. Total beam electron energy loss can be expressed as a beam electron heating power density,

$$P_{eb} = \frac{1}{\Delta t} \times n_e \times \sum_k E_{ij}^k, \quad (4.6)$$

where  $\Delta t$  is the integration time and  $n_e$  is the bulk electron density. In this investigation, we take into account not only ion-induced secondary electron emission but also electron-induced. The ion-induced secondary electron emission coefficient,  $\gamma_i$  is provided as a constant value, whereas, the electron-induced secondary electron emission coefficient,  $\gamma_e$  is calculated by accounting for the incident beam electron energy and angle.[12]

### 4.3 Behavior of Beam-like Secondary Electrons in the Bulk Plasma

The 2D cylindrically symmetric reactor used in this investigation is schematically shown in Fig. 4.1a. The reactor has two electrodes: the lower electrode is excited by  $RF$  power, and the upper electrode is biased with negative dc voltage. The lower electrode serves as the substrate that is powered at 10 MHz, through blocking capacitor (10 nF). A conductive Si wafer ( $\epsilon/\epsilon_0 = 12.0$ ,  $\sigma = 0.01 \Omega^{-1} \text{ cm}^{-1}$ ), 30 cm in diameter, sits in electrical contact with the lower electrode. The upper electrode, 36 cm in diameter, is powered by the negative dc voltage. The negative dc bias electrode serves as the shower head through which gas is injected at 200 sccm. Both of the electrodes are surrounded by the dielectric ( $\epsilon/\epsilon_0 = 8.0$ ,  $\sigma = 10^{-6} \Omega^{-1} \text{ cm}^{-1}$ ). The gap between the two electrodes is 4 cm. There are two kinds of secondary electron emissions (SEE): ion-induced (i-SEE) and electron-induced (e-SEE). All of the surfaces facing the plasma have the same secondary emission coefficient,  $\gamma_{ie} = 0.35$ , for the ion bombardment. For the electron bombardment, the secondary emission coefficient is dependent on the surface material and the incident energy and angle of the beam electron. The dc and  $RF$  electrodes are applied at constant voltage to maintain the energy of the electrons and ions incident on the electrodes. The operating conditions are 40 mTorr of  $\text{Ar}/\text{N}_2 = 80/20$  with negative 140 V (dc) on the upper electrode and 100 V (10 MHz) on the lower electrode.

As a consequence of the negative dc bias on the upper electrode, the ion-induced secondary electrons are emitted from the upper electrode and accelerated by the large sheath potential to have sufficient energy to heat up the bulk electrons. These high-energy beam electrons interact with the bulk electrons to transfer energy through an electron-electron ( $e-e$ ) Coulomb collision. If there is no interaction between the beam and bulk electrons, the peak electron density is only  $1.5 \times 10^{10} \text{ cm}^{-3}$  and the electron temperature is 2.6 eV in the bulk plasma.

Whereas, with the Coulomb interaction, the electron density increases by a factor of 3 and the electron temperature slightly decreases in the bulk region, as shown in Figs. 4.1b and 4.1c. However, the electron temperature adjacent to electrodes increases significantly due to the secondary (beam) electron heating effect. The heating power density is maximized adjacent to the electrodes, as shown in Fig. 4.1d. At the center of the reactor, the power deposition due to the secondary electrons is about  $20 \text{ mW/cm}^3$ . The heating power density adjacent to the electrodes is an order of magnitude larger than the value in the middle of the reactor. The beam electrons are reflected back and forth between electrodes and slow down at the sheath. Once they slow down, the Coulomb collision cross section becomes larger, so that the beam electrons have more interactions with the bulk, thereby delivering the energy at the sheath boundary. This is why a higher electron beam heating power density is observed adjacent to the electrodes. Since the electron temperature reflects only the distribution of the low-energy component, the high-energy tail component of the distribution is not captured by the electron temperature.

The high-energy tail component of the distribution is affected by the secondary beam electron energy transfer, as shown in Fig. 4.2. With Coulomb interactions between beam and bulk electrons, the energy distribution changes more significantly near the electrode due to the larger beam electron heating power density. The high-energy beam electrons collide with the low-energy electrons in the bulk plasma – delivering energy to the bulk, and depleting beam electrons. Since the negative dc voltage is applied on the upper electrode, most of i-SEE occurs on the upper electrode. The beam-like secondary electrons from i-SEE then strike the lower electrode to produce e-SEE if the energy is large enough to overcome the sheath potential on the lower electrode. If the energy of the secondary electron is lower than the  $RF$  sheath potential, the electron is reflected. For example, roughly half of the electrons from i-SEE are reflected at

the sheath edge on the lower electrode. The fraction of the reflection is inversely proportional to the absolute value of the negative dc voltage on the upper electrode, since the higher-energy beam electrons are more likely to penetrate the *RF* sheath potential. If the beam electron penetrates the sheath barriers, the energetic beam electrons produce e-SEE by hitting the surface. The secondary emission yield due to electron bombardment is a function of beam energy and incident angle. If the beam electron strikes the lower electrode vertically, the emission yield is within the range of 1 to 2 with hundreds of electron volt beam energies, as shown in Fig. 4.3b. The average mean free path of the secondary electrons ranging between 50 eV and 300 eV is about 1.2 cm to 2.5 cm, both of which are shorter than the electrode gap distance, which means that the secondary electrons make at least one collision before arriving at the sheath edge. On average, the secondary electrons experience one collision per reflection, as shown in Fig. 4.3c. We found that the e-SEE produces additional heating on the energy distribution of the bulk electrons, as shown in Fig. 4.4. The additional electrons from e-SEE on the substrate are accelerated by the self dc-bias on the lower electrode. Since the self dc-bias on the lower electrode is about -50 V, the secondary electron from e-SEE has around 50 eV.

#### **4.4 Concluding Remarks**

The behavior of secondary electrons in the dc-augmented CCP has been computationally investigated using results from a two-dimensional plasma hydrodynamic model by solving the electron transport explicitly by a Monte-Carlo method. With a purely kinetic approach, we observed the bulk electron heating from the energetic electron beam. We found that the intensive secondary electrons from the negative-biased electrode produce a significant electron heating in the bulk plasma through the *e-e* collisions. If the beam electron energy is large enough to overcome the sheath potential in the opposite electrode, then the beam electron hits the

surface to produce additional secondary electrons. These additional electrons from e-SEE also contribute to the bulk electron heating.

## 4.5 Figures

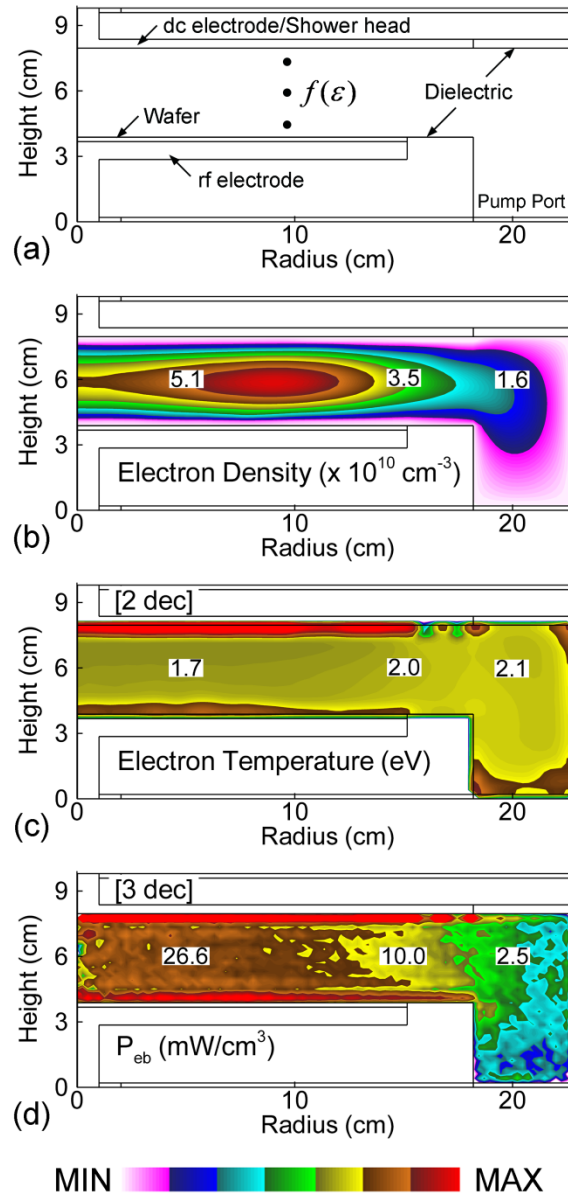


Fig. 4.1 Geometry and plasma properties for  $\text{Ar}/\text{N}_2 = 80/20$ , 40 mTorr,  $V_{dc} = -140 \text{ V}$  and  $V_{rf} = 100 \text{ V}$  at 10 MHz. (a) Geometry for the dc-augmented capacitively coupled plasma. (b) Electron density. (c) Electron temperature. (d) Power density delivered from the beam electrons. Electron temperature is highest adjacent to the electrodes due to the combination of sheath heating and beam electron heating.

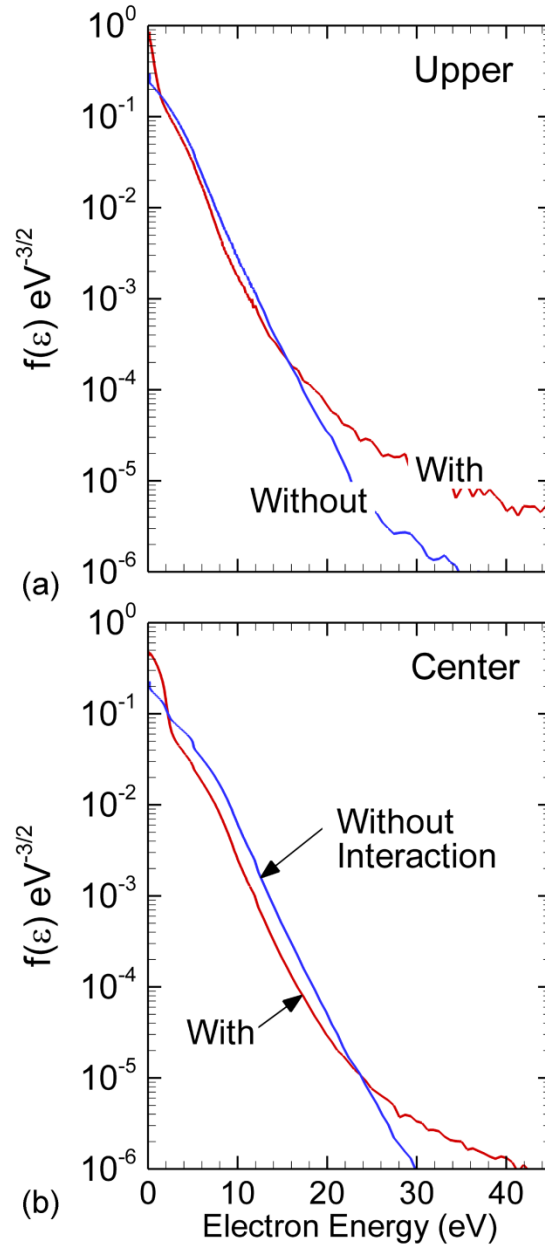


Fig. 4.2 Energy distributions of the bulk electrons with and without beam-bulk interaction at different heights in the reactor (locations indicated in Fig. 4.1). (a) Near the upper electrode and (b) in the middle of the reactor. The heating effect by beam electron is larger near the electrodes due to the reduced speed by the sheath potential.

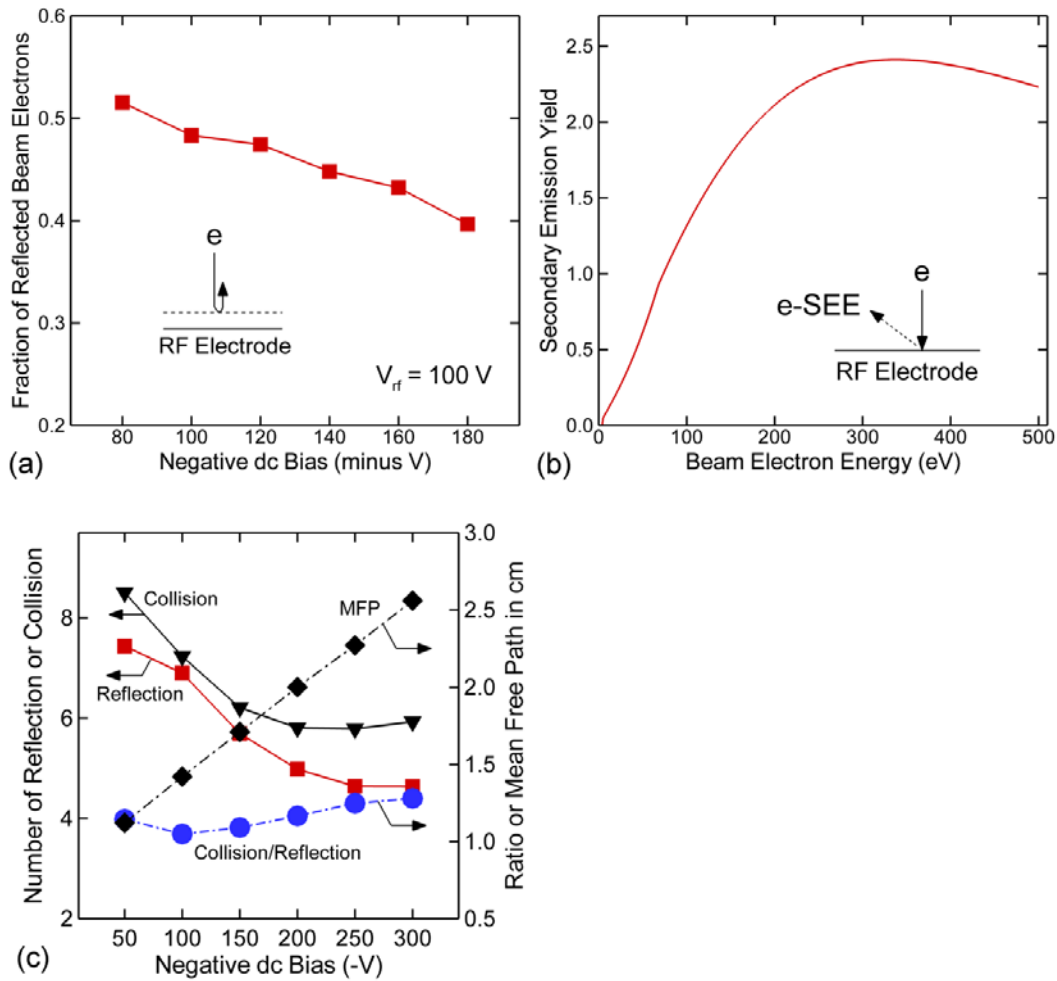


Fig. 4.3 Behavior of secondary electrons in the plasma includes collision, reflection, and slowing down. (a) Fraction of reflected beam electrons at the sheath boundary on the lower electrode. (b) Electron induced secondary emission yield as a function of energy when the incident angle is perpendicular to the lower electrode. (c) Number of collision and reflection of the secondary electrons in the reactor as a function of the amplitude of the negative dc bias on the upper electrode. On the average, beam electrons make one collision per reflection because the mean free path is shorter than the electrode gap and longer than the half of the gap.

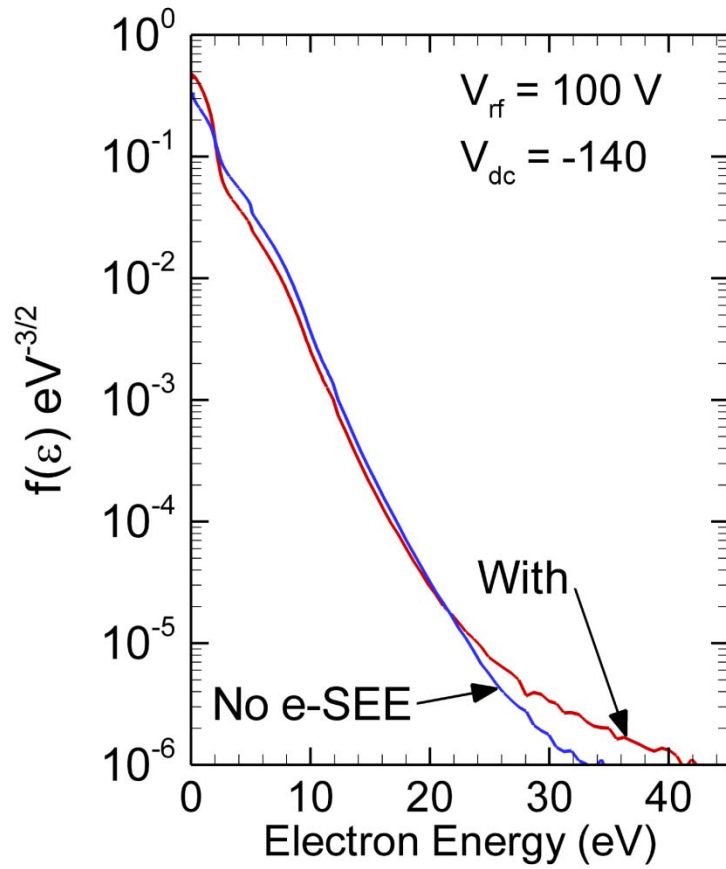


Fig. 4.4 Energy distribution of the bulk electrons with and without e-SEE. The additional energetic electrons from e-SEE contribute to the bulk electron heating.

## 4.6 References

1. I. Silin, R. Sydora, and K. Sauer, "Electron beam-plasma interaction: Linear theory and Vlasov-Poisson simulations", *Phys. Plasmas* **14**, 012106 (2007).
2. Y. S. Sigov and V. D. Levchenko, "Beam-plasma interaction and correlation phenomena in open Vlasov systems", *Plasma Phys. Control. Fusion* **38**, A49 (1996).
3. Y. Omura, H. Matsumoto, T. Miyake, and H. Kojima, "Electron beam instabilities as generation mechanism of electrostatic solitary waves in the magnetotail", *J. Geophys. Res.* **101**, 2685 (1996).
4. K. Akimoto, Y. Omura, and H. Matsumoto, "Rapid generation of Langmuir wave packets during electron beam-plasma instabilities", *Phys. Plasmas* **3**, 2559 (1996).
5. D. V. Rose, J. U. Guillory, and J. H. Beall, "Comparison of particle-in-cell simulations and a wave-population model of electron-beam-plasma interactions", *Phys. Plasma* **9**, 1000 (2002).
6. V. P. Tarakanov and E. G. Shustin, "Dynamics of beam instability in a finite plasma volume: numerical experiment", *Plasma Physics Reports* **33**, 130 (2007).
7. J. Schulze, B. G. Heil, D. Luggenholscher, T. Mussenbrock, R. P. Brinkmann, and U Czarnetzki, "Electron beams in asymmetric capacitively coupled radio frequency discharges at low pressures", *J. Phys. D: Appl. Phys.* **41**, 042003 (2008).
8. M. A. Tas, E. M. van Veldhuizen, and W. R. Rutgers, "Plasma excitation processes in flue gas simulated with Monte Carlo electron dynamics", *J. Phys. D: Appl. Phys.* **30**, 1636 (1997).
9. A. V. Vasenkov, "Monte Carlo simulation of electron beam plasma in a silane-argon mixture", *J. Phys. D: Appl. Phys.* **32**, 240 (1999).
10. I. V. Morozov, G. E. Norman, A. A. Valuev, and I. A. Valuev, "Nonideal plasmas an non-equilibrium media", *J. Phys. A: Math. Gen.* **36**, 8723 (2003).
11. M. Rosenberg, G. J. Kalman, S. Kyrkos, and Z. Donko, "Beam-plasma interaction in strongly coupled plasmas", *J. Phys. A: Math. Gen.* **39**, 4613 (2006).
12. C. K. Purvis, "Effects of secondary yield parameter variation on predicted equilibrium potential of an object in a charging environment", NASA Technical Memorandum 79299, 1979.

## Chapter 5 CONTROL OF ELECTRON ENERGY DISTRIBUTION FUNCTION USING PULSED POWER

### 5.1 Introduction

Using pulsed power can provide an additional leverage to customize the electron energy distribution function,  $f(\varepsilon)$ . [1] In quasi-steady state operation, an equilibrium condition for  $f(\varepsilon)$  requires an instantaneous (or  $RF$  cycle average) balance between electron sources and sinks. As such, for a given geometry, pressure and frequency of operation, there is little latitude in customizing  $f(\varepsilon)$ . By using pulsed power, electron sources and sinks do not need to instantaneously balance – they only need to balance when averaged over the longer pulsed period. This provides additional leverage to control  $f(\varepsilon)$ . By pulsing, one may be able to modulate  $f(\varepsilon)$  to produce shapes or access energies that are not otherwise (or easily) attainable using  $CW$  excitation. For example,  $f(\varepsilon)$  may be produced that has both a high energy tail and a large thermal component. These  $f(\varepsilon)$  will produce different dissociation patterns of the feedstock gases and so produce different ratios of fluxes to the substrate for a given time average power. This strategy of customizing fluxes using pulsed power has been applied in inductively coupled plasmas ( $ICPs$ ). [2]

For example, during the *power-OFF* period of a pulsed cycle, high energy electrons may quickly thermalize due to inelastic collisions and be lost by rapid diffusion to the wall. At the

beginning of the *power-ON* portion of the pulsed cycle, high energy electrons are generated due to an overshoot of  $E/N$  (electric field/gas number density) above the value that can be sustained in the steady state. This overshoot is due to the initially lower conductivity of the plasma following electron losses during the *power-OFF* period. In such systems,  $f(\varepsilon)$  can be controlled through choice of the pulse repetition frequency (PRF) and duty cycle (DC). (DC is the fraction of the pulsed period that power is applied.) These determine the relative roles of both electron acceleration during the *power-ON* portion of the cycle and thermalization during the *power-OFF* portion. These concepts have been demonstrated in pulsed *ICPs* to produce ion-ion plasmas during the *power-OFF* period, and so provide a means for negative ion acceleration into trenches to remediate charge damage.[3] Pulsed *CCPs* are a more recent development.[4]

In this chapter, we build on these prior works by using results from a computational investigations to discuss strategies for controlling  $f(\varepsilon)$  of electrons by varying the PRF and DC in *CCPs*. We found that the tail of  $f(\varepsilon)$  is more enhanced when operating with a lower PRF in order to compensate for the losses of electrons incurred during the longer afterglow period. For this reason, the overshoot of the tail of  $f(\varepsilon)$  at the beginning of the *power-ON* period is particularly prominent in Ar/CF<sub>4</sub>/O<sub>2</sub> gas mixtures compared to Ar mixtures due to the larger electron losses during the *power-OFF* period. Due to the transient nature of pulsed *CCPs* in which the electron temperature cycles from above the steady state value to below, the relative rate of attachment is particularly high in these mixtures during the *power-OFF* period. Secondary electrons emitted from surfaces and accelerated in the sheath provide the additional ionization required to sustain the plasma in electronegative gas mixtures where electron attachment and dissociative recombination dominate at low energy. Varying the rate of secondary electron emission then provides an additional means for controlling  $f(\varepsilon)$ .

The model used in this study is described in Sec. 5.2 with emphasis on the computation of  $f(\varepsilon)$ . The  $f(\varepsilon)$  in pulsed dual frequency capacitively coupled plasma (*DF-CCP*) sustained in Ar are discussed in Sec 5.3, and sustained in Ar/CF<sub>4</sub>/O<sub>2</sub> are discussed in Sec. 5.4. A comparison of ionization and loss rates between Ar and Ar/CF<sub>4</sub>/O<sub>2</sub> is presented in Sec. 5.5. Our concluding remarks are in Sec. 5.6.

## 5.2 Description of the Model

In HPEM, electron energy distributions of bulk and secondary electrons are obtained using an electron Monte Carlo simulation (eMCS). The model is described in detail in Ref. [5]. The electron energy distributions as a function of position,  $f(\varepsilon, r)$ , are obtained using the eMCS, which is a statistical, kinetic solution of Boltzmann's equation. The eMCS, including our algorithms for electron-electrons collisions, is described in detail in Ref. [6].

This hybrid method of obtaining and utilizing  $f_b(\varepsilon, \vec{r})$  and  $f_s(\varepsilon, \vec{r})$  is sometimes referred to as *time slicing*, as a slice of time is separately addressed by each module. For any given call to the eMCS or FKPM, the time integration within that module does capture transient behavior. For example, the time step in the FKPM for update of species densities and between solutions of Poisson's equation is about  $10^{-11}$  s with consideration of the Courant limit and resolution of the *RF* cycles. The time step within the eMCS is similarly as small. However, the ability to represent transients truly consistently with changes in  $f(\varepsilon, \vec{r})$  in the FKPM, and with changes in densities within the eMCS, is determined by the frequency with which there is information exchange between the FKPM and the eMCS. In this work, the eMCS is called every 0.5  $\mu$ s, which is also the time of integration of pseudoparticle trajectories in the eMCS. With a PRF of 50 kHz (20  $\mu$ s), there are 40 updates of  $f(\varepsilon)$  during one pulse period, which might be considered

a lower limit of time resolution. The effective time resolution of transients is finer than that due to the finer integration within each module.

The reaction mechanisms for the Ar and Ar/CF<sub>4</sub>/O<sub>2</sub> mixtures used in this investigation are discussed in Ref. [7]. For Ar, the species included in the model are metastable and radiative states of Ar(4s), Ar(4p), and Ar<sup>+</sup>. For Ar/CF<sub>4</sub>/O<sub>2</sub>, the additional species are CF<sub>4</sub>, C<sub>2</sub>F<sub>6</sub>, C<sub>2</sub>F<sub>4</sub>, CF<sub>3</sub>, CF<sub>2</sub>, CF, C, F, F<sub>2</sub>, CF<sub>3</sub><sup>+</sup>, CF<sub>2</sub><sup>+</sup>, CF<sup>+</sup>, C<sup>+</sup>, F<sub>2</sub><sup>+</sup>, F<sup>+</sup>, CF<sub>3</sub><sup>-</sup>, F<sup>-</sup>, O<sub>2</sub>, O<sub>2</sub>(<sup>1</sup>Δ), O<sub>2</sub><sup>+</sup>, O, O(<sup>1</sup>D), O<sup>+</sup>, O<sup>-</sup>, COF, COF<sub>2</sub>, CO<sub>2</sub>, FO, SiF<sub>4</sub>, SiF<sub>3</sub>, and SiF<sub>2</sub>. For the operating conditions in this work, the dominant ions and neutral radicals are CF<sub>3</sub><sup>+</sup>, CF<sub>3</sub>, CF<sub>2</sub>, CF, C, F and O. Vibrational excitation collisions of all molecular species are included in solving for  $f(\varepsilon)$ . In particular for the feedstock gases, we include CF<sub>4</sub>(v1,3), CF<sub>4</sub>(v2,4) and O<sub>2</sub>(v1 to v6). Threshold energies for these processes are listed in Ref. [7]. Although electron energy losses for exciting these vibrational states are included in the eMCS, the vibrational states are not explicitly included in the continuity equations. The consequence of this approach is that superelastic relaxation and gas heating resulting from electron and heavy particle V-T collisions with these states are not captured. The secondary electron emission coefficient for all ions is  $\gamma = 0.15$ . The voltage is specified for each frequency and applied to the electrode. A blocking capacitor is in series with the low frequency electrode and a time dependent dc bias is computed based on the value of the blocking capacitor and integral of collected current. The voltages on the electrodes are adjusted to provide a specified pulsed-cycle averaged power,  $\bar{P}$ . This is accomplished by computing for each electrode

$$\bar{P} = v_{rf} \iint \left( V(t) \left( j(\vec{r}, t) + \varepsilon \frac{dE(\vec{r}, t)}{dt} \right) dt dA \right), \quad (5.1)$$

where  $V$  is the voltage on the electrode,  $j$  is the conduction current density to the electrode,  $\varepsilon$  is the permittivity,  $E$  is the electric field at the surface of the electrode and the integral is over the

area of the electrode and the  $RF$  cycle having frequency  $\nu_{rf}$ .

### 5.3 Plasma Properties of Pulse Powered DF-CCP Sustained in Argon

The 2-dimensional, cylindrically symmetric reactor used in the model is schematically shown in Fig. 5.1. The lower electrode serves as the substrate which is powered at a low frequency ( $LF$ ), 10 MHz, through a blocking capacitor (1  $\mu$ F). A conductive Si wafer ( $\epsilon/\epsilon_0 = 12.0$ ,  $\sigma = 0.01 \Omega^{-1} \text{ cm}^{-1}$ ), 30 cm in diameter, sits in electrical contact with the substrate which is surrounded by a dielectric ( $\epsilon/\epsilon_0 = 8.0$ ,  $\sigma = 10^{-6} \Omega^{-1} \text{ cm}^{-1}$ ). The upper electrode, 36 cm in diameter, is powered at a high frequency ( $HF$ ), 40 MHz. The  $HF$  electrode also serves as the shower head through which gas is injected at 200 sccm. The  $HF$  electrode is surrounded by the same dielectric as the  $LF$  electrode. The gap between the two electrodes is 4 cm. All other surfaces in the reactor are grounded metal including the annular pump port.  $LF$  power is delivered in  $CW$  operation and  $HF$  power is delivered in either  $CW$  or pulsed format. The pulse operation was characterized by the pulse repetition frequency (PRF) which is how many times per second the waveform is repeated and the duty cycle (DC), which is the fraction of the total time of *power-ON* stage, as shown in Fig. 5.1b. The rise (or decay) time of the power on (or off) period is 500 ns. The voltage on the electrodes is periodically adjusted so that the power through each electrode averaged over the pulse period is the specified amount.

The base case operating conditions are 40 mTorr of Ar with the  $LF$  (10 MHz) delivering 500 W on a  $CW$  basis and the  $HF$  (40 MHz) delivering an average of 500 W in a pulse power format. The PRF is 50 kHz (pulse period 20  $\mu$ s) and DC is 25%. The PRF was varied from 50 kHz to 250 kHz and the duty cycle was varied from 25% to 50%. As a point of reference, the electron density ( $n_e$ ), electron temperature ( $T_e$ ), and electron impact ionization sources are shown

in Fig. 5.2a for *CW* operation of both the *LF* and *HF*. The adjusted voltage amplitude is 112 V for *LF* and 95 V for *HF* for both to deliver 500 W. The resulting dc bias is  $-50$  V. The peak electron density is  $9.7 \times 10^{11} \text{ cm}^{-3}$  and the bulk electron temperature is  $T_e \approx 1.7$  eV.  $T_e$  adjacent to the electrodes is higher (2.0 eV) than in the bulk due to the stochastic heating produced by the oscillating sheath boundary. The electron impact ionization sources by bulk,  $S_b$ , and secondary e-beam  $S_s$ , have maximum values of  $3.1 \times 10^{16} \text{ cm}^3\text{s}^{-1}$  and  $6.5 \times 10^{15} \text{ cm}^3\text{s}^{-1}$ , respectively.  $S_b$  is a factor of ten larger than  $S_s$  due to the continuous electron heating at the *LF* and *HF* sheath boundaries.

The electron energy distributions,  $f(\varepsilon)$ , at different heights in the reactor (heights are noted in Fig. 5.1) are shown in Fig. 5.2b. Due to the relatively high electron density and so high thermal conductivity, the  $f(\varepsilon)$  are essentially Maxwellian at low energies and nearly indistinguishable as a function of height. However, as expected from the trends of  $T_e$ , the tails of  $f(\varepsilon)$  are raised adjacent to electrodes and more so near the *HF* electrode due to the more efficient stochastic heating at the higher frequency.[8] To compensate for the increased the tail portion of  $f(\varepsilon)$ , the low energy portion decreases.

$n_e$  and  $T_e$  are shown in Fig. 5.3 and electron impact ionization sources are shown in Fig. 5.4 at different times during the pulse period for a pulsed discharge in Ar for the base case conditions. The *CW* amplitude of the *LF* to deliver 500 W is 206 V. Due to the varying amount of current that is collected during the pulsed period and the finite size of the blocking capacitor (1  $\mu\text{F}$ ) the dc bias oscillates during the pulse period, here between  $-124$  and  $-157$  V. This variation in dc bias during a pulse period has been noted in Ref. [9]. The pulsed *HF* voltage amplitude to deliver 500 W averaged over the pulsed cycle is 251 V. At the beginning of the pulse period, the maximum value of  $n_e$  is  $2.5 \times 10^{11} \text{ cm}^{-3}$  and the bulk  $T_e \approx 2.0$  eV. There is

some heating of the bulk electrons by the *LF* bias (to about 1.0 eV), however at this high electron density, the heating by the *LF* is nominal. When the power is turned on, the maximum electron density increases to  $3.2 \times 10^{11} \text{ cm}^{-3}$ . The more efficient stochastic electron heating by the *HF* raises  $T_e$  to 2.0 eV in the bulk and to 4.2 eV in the sheaths.  $E/N$  (electric field/gas number density,  $1 \text{ Td} = 10^{-17} \text{ V-cm}^2$ ) near the *HF* sheath increases from 500 Td to 2000 Td during the pulse power rise time before settling to 1400 Td during the remainder of the *power-ON* stage. With  $T_e = (2/3)\langle \varepsilon \rangle$  being proportional to the distribution average energy, its value is heavily weighted towards the more numerous low energy bulk electrons. Due to the non-Maxwellian nature of  $f_b(\vec{r})$  at high energies, the dynamics of  $T_e$  are a poor measure of ionization rates. (See discussion below.) When the *HF* power is turned off after a 25% duty cycle (5  $\mu\text{s}$  in this case),  $T_e$  falls to the off-period value of 1.2 eV in about 8.5  $\mu\text{s}$ . The PRF (50 kHz) is high enough that the plasma density does not significantly change over the pulse period.

The electron impact ionization sources by bulk electrons,  $S_b$ , and secondary beam electrons  $S_s$ , are shown in Fig. 5.4.  $S_s$  has a continuous background value of  $5 \times 10^{14} \text{ cm}^3\text{s}^{-1}$  due to continuous secondary electron emission from the *LF* electrode. As the pulse power is toggled on-and-off, the ion density and so ion flux to surfaces do not significantly change, so this source of ionization is fairly constant. With an inelastic mean-free-path of  $\approx 4 \text{ cm}$  at 300 eV, the secondary electrons accelerated in the sheath cross the gap and produce a fairly spatially uniform ionization source. The delay in the peak of the ionization source is due, in part, to a time lag in increasing secondary electron yield due to transport of ions across the sheath from the bulk plasma.

Note that  $S_s$  increases during the *power-ON* period. This is due to a small decrease in the dc bias (becoming less negative) which reduces the energy of the secondary electrons which also

decreases the energy relaxation length. More ionization occurs in the gap with there being less likelihood for secondary electrons to be collected by the opposite electrode. (Since during the *power-OFF* period, the *HF* electrode is held at ground and there is approximately a  $-150$  V dc bias on the substrate, the majority of secondary electrons that cross the gap are collected by the *HF* electrode.) At the other extreme, there are also increasing contributions to  $S_s$  by secondary electrons emitted from the now powered *HF* electrode.

During the *power-OFF* period  $S_b$  is not important. Prior to turning the *HF* power on, there are statistically only a few electrons produced by stochastic heating by the *LF* sheath that have high enough energy to produce significant ionization. During the *power-ON* portion of the cycle the additional ionization by sheath accelerated secondary electrons from the *HF* electrode increases  $S_s$  to  $5 \times 10^{15} \text{ cm}^3\text{s}^{-1}$ , a factor of nearly ten greater than that from the *LF* alone. Coincident to the increase in  $T_e$  during the *power-ON* period is an increase in  $S_b$ , to  $10^{17} \text{ cm}^3\text{s}^{-1}$ , so that bulk electrons dominate ionization. The decrease in  $S_b$ , to background levels occurs in about  $8.5 \mu\text{s}$  after the *HF* power is terminated.

$f(\varepsilon)$  has dynamic behavior during the pulse period. For example,  $f(\varepsilon)$  is shown in Fig. 5.5 adjacent to the *HF* sheath, mid-gap and adjacent to the *LF* sheath at different times during the pulse period. (See Fig. 5.1 for these locations.) The low energy component ( $\varepsilon < 2\text{-}3$  eV) varies little during the pulse period and appears Maxwellian-like, which explains the small variation in  $T_e$  during the pulse period. (This small variation in  $T_e$  cannot explain the large change in ionization rates.) This nearly invariant part of  $f(\varepsilon)$  is largely due to the thermalizing influence of electron-electron collisions. The tail of the  $f(\varepsilon)$  raises and lowers nearly coincidentally with the application and termination of the *HF* power. At its maximum extent, the tail of  $f(\varepsilon)$  reaches to energies in excess of  $60$  eV with only a nominal change in the low energy portion of  $f(\varepsilon)$ .

Although there is a *HF* component oscillation at the *LF* sheath, the amplitude of this oscillation is smaller than at the *HF* sheath, and the tail of  $f(\varepsilon)$  extends to only 50 eV. In the middle of the gap, the extension is to 40 eV.

The 20  $\mu$ s, pulsed period averaged (*PPA*)  $\underline{f(\varepsilon)}$  compared to *CW* operation for the same average powers at different heights in the reactor are also shown in Fig. 5.5. The *PPA*  $f(\varepsilon)$  adjacent to the *HF* electrode appears more bi-Maxwellian than with *CW* power due to the rapid and enhanced electron heating from the *HF* power during the *power-ON* stage and the rapid cooling during the *power-OFF* stage. Although the *PPA* and *CW*  $f(\varepsilon)$  do not show dramatic differences, the temporal dynamics of  $f(\varepsilon)$  have the tail of the distribution extending to significantly higher energies than the *CW* case. This extension produces instantaneous sources for inelastic collision processes with high threshold energies that are significantly greater than either the *PPA* or *CW* distribution functions.

#### 5.4 Plasma Properties in Ar/CF<sub>4</sub>/O<sub>2</sub>

There is an interest in plasma materials processing, and plasma etching in particular, to have additional control over the production of radicals and ions to the substrate. In this section we discuss results from the model for a *DF-CCP* sustained in a Ar/CF<sub>4</sub>/O<sub>2</sub> = 75/20/5 gas mixture at 40 mTorr to explore such control strategies. With this plasma being sustained in a molecular and electronegative gas mixture, there are additional volumetric electron loss processes – dissociative attachment and dissociative recombination. Although the rate coefficient for dissociative recombination scales with  $T_e^{-0.5}$  and so increases with decreasing  $E/N$  and average energy, the dissociative attachment cross sections for CF<sub>4</sub> and O<sub>2</sub> have threshold energies of 3.0 and 5.0 eV respectively [10,11]. As a result, the rate coefficient for attachment processes *increase* with increasing  $E/N$  up to about 100 Td. This markedly differs from thermal attaching

gases with as  $\text{Cl}_2$  and  $\text{F}_2$  whose cross sections for dissociative attachment peak at energies of  $< 0.1$  eV and so their rate coefficients for electron loss generally *decrease* with increasing  $E/N$  in the same manner as dissociative recombination.

As a point of reference,  $n_e$ ,  $T_e$ ,  $S_b$  and  $S_s$  are shown in Fig. 5.6 for *CW* operation for both *LF* and *HF*. Results are shown for secondary electron emission coefficients by ion impact of  $\gamma = 0.02, 0.10, 0.15$  and  $0.25$ . With  $\gamma = 0.02$ , the voltage amplitudes are  $LF = 256$  V and  $HF = 155$  V with a dc bias of  $-71$  V. With  $\gamma = 0.15$ ,  $LF = 259$  V,  $HF = 149$  V and  $V_{dc} = -75$  V. The peak electron densities are  $1.0 \times 10^{11} \text{ cm}^{-3}$  for  $\gamma = 0.02$  and  $0.15$ , and  $T_e \approx 0.9$  eV and  $0.6$  eV for  $\gamma = 0.02$  and  $0.15$ .  $T_e$  is significantly higher adjacent to the electrodes ( $2.3$  eV) than in the bulk due to the stochastic heating by the oscillating sheath boundary. The larger disparity between  $T_e$  near the sheath and in the bulk compared with Ar discharge results from the shorter energy relaxation length in the molecular gas mixture. The estimated energy relaxation length in  $\text{Ar}/\text{CF}_4/\text{O}_2 = 75/20/5$  at a few eV is only 10% that in pure argon due to low threshold energy vibrational and electronic excitation collisions with  $\text{CF}_4$  and  $\text{O}_2$ . Note that the larger bulk electron impact ionization occurs adjacent to the *HF* electrode due to the more efficient heating by the high frequency sheath. The maximum secondary electron impact ionization source leans toward the *LF* electrode due to the dc bias on the substrate which provides a higher average secondary energy.

While varying the secondary emission coefficient  $\gamma$ , the power delivered by the *LF* and *HF* remains constant. Since only a small fraction of the power deposition is by acceleration of secondary electrons, the electron (and ion) densities do not significantly change, moderately increasing with increasing  $\gamma$ . (Other methods of power deposition – Joule heating, stochastic and ion acceleration – are proportional to the electron or ion density.) The small increase in electron

density with increasing  $\gamma$  reflects the decrease in voltage amplitudes. What does change with the variation of  $\gamma$ , is the apportioning of ionization between bulk electrons,  $S_b$  and secondary electrons,  $S_s$ . With increasing  $\gamma$ ,  $S_s$  increases due to the larger flux of secondary electrons (in spite of the small decrease in sheath voltages.)  $S_b$  decreases with increasing  $\gamma$  to net negative values (more attachment and recombination than ionization) with  $\gamma = 0.25$ .

The values of  $n_e$ ,  $T_e$ ,  $S_b$  and  $S_s$  are ultimately determined by a balance between electron sources by ionization (or injection) and losses (by attachment, recombination and diffusion) that provides the current that delivers the desired power. Since  $S_s$  increases by virtue of the larger  $\gamma$ , the plasma responds by allowing more electron loss, which is achieved by lowering  $T_e$  and  $S_b$ . This is, in fact, the principle behind externally sustained plasmas, such as electron beam sustained discharges (*EBS*D).[12] In these devices,  $T_e$  in the bulk plasma is controlled by the power deposition from the electron beam. If the externally supplied ionization provides the majority of the ionization, the applied electric fields which heat electrons and determines  $T_e$  can be lower. For example, in *EBS*D excited CO(v) and CO<sub>2</sub>(v) lasers,  $T_e$  is lowered so that rates of vibrational excitation are optimized.[13,14] In our system, with  $\gamma = 0.02$ , the ionization sources from  $S_s$  are insufficient to offset electron losses, and so  $S_b$  must be positive to deliver the desired power. With  $\gamma = 0.25$ , the ionization sources  $S_s$  exceeds that which is required to deliver the desired power, and so  $S_b$  is negative to compensate. So similar to an *EBS*D, varying  $\gamma$  provides a means to control the bulk plasma properties. As an aside, another feature of relying on  $S_s$  for ionization is that the plasma is more uniform since the energy relaxation distance of the higher energy electrons is greater than for bulk electrons.

The  $f(\varepsilon)$  near the *HF* sheath and in the center of the gap for  $\gamma = 0.02, 0.10, 0.15$  and  $0.25$  are shown in Fig. 5.7. Near the *HF* sheath where electron transport is dominated by stochastic

heating and which is little affected by changes in  $\gamma$ ,  $f(\varepsilon)$  is essentially unchanged with  $\gamma$ . In the center of the plasma where collisional Joule heating is more important in determining  $f(\varepsilon)$ , the tail of the distribution rises with decreasing  $\gamma$  and the low energy portion of the distribution increases with increasing  $\gamma$ .

In the steady state and in the absence of external ionization sources, the self-sustaining  $E/N$  or  $T_e$  (that is, shape of  $f(\varepsilon)$ ) occurs where the volume averaged ionization sources are balanced by losses by diffusion, attachment and recombination. In gases where volumetric losses uniformly decrease with increasing  $E/N$  or  $T_e$  while ionization sources uniformly increase with increasing  $E/N$  or  $T_e$ , the self sustaining value is well defined – it is the value of  $E/N$  or  $T_e$  where these two curves having slopes of different sign intersect. In the case where both volumetric losses and ionization increase over a range of increasing  $E/N$  or  $T_e$ , the self sustaining values are less clear and may, in fact, have multiple values.

In *EBSDs*, an external source (the injected electron beam) provides a source of ionization which is independent of the local  $E/N$  or  $T_e$  (shape of  $f(\varepsilon)$ ). [15] By varying the magnitude of the external ionization provided by the electron beam by changing the beam voltage or current, the value of  $E/N$  or  $T_e$  that balances ionization and losses can be tuned. This is the effect that we see in the Ar/CF<sub>4</sub>/O<sub>2</sub> gas mixture. If  $\gamma$  is large, the “external” source of ionization provided by ionization by secondary electrons is large enough to sustain the plasma and, in fact, may be larger than what is required to deliver the desired power. In those cases, the net ionization by bulk electrons is negative, and the tail of  $f(\varepsilon)$  is depressed. (That is, the impedance of the plasma is small, producing a small  $E/N$  and so reduced collisional heating.) If  $\gamma$  is small, the “external” source of ionization provided by secondary electrons cannot sustain the plasma, and so the tail of  $f(\varepsilon)$  is raised to provide the required ionization. (That is, the impedance of the plasma is large,

producing a large  $E/N$  and increased collisional heating.) To some degree, the bulk  $f(\varepsilon)$  can be tuned by varying the amount of external ionization provided by the secondary electrons by varying the secondary electron emission coefficient.

The conditions for pulsed operation of the Ar/CF<sub>4</sub>/O<sub>2</sub> mixture are the same as for the base case in argon (40 mTorr, 200 sccm, *LF* delivering 500 W at 10 MHz, *HF* delivering 500 W at 40 MHz, PRF = 50 kHz, DC = 25%). The amplitude of the *LF* to deliver 500 W is 202 V with a dc bias varying between -54 and -93 V during the pulse period.  $n_e$  and  $T_e$  at selected times over the pulse period are shown in Fig. 5.8 with  $\gamma = 0.15$ .  $E/N$  near the *HF* sheath is shown in Fig. 5.9. Electron impact ionization sources by bulk and secondary electrons are shown in Fig. 5.10. The dynamic range of change in these properties is greater than for the pure argon case due to the higher collisionality and higher rate of volumetric electron loss due to recombination and attachment. Prior to the application of the pulse power,  $T_e$  in the bulk plasma is as low as 0.4 eV and only 0.8 eV adjacent to the sheaths. This value of  $T_e$  is enabled, in part, by the continuous background value of  $S_s$  due to the *LF* bias. When the *HF* power is turned on,  $T_e$  increases within 0.5  $\mu$ s from 0.8 eV to 4.7 eV adjacent to the *HF* sheath, and to 1.9 eV in the bulk plasma. This is accompanied by an increase in the maximum  $n_e$  from  $1.3 \times 10^{11} \text{ cm}^{-3}$  to  $1.7 \times 10^{11} \text{ cm}^{-3}$ . These values of  $T_e$  relax during the *power-ON* period, to 2.1 eV adjacent to the sheaths and 0.8 eV in the bulk, before returning to their pre-pulse value at the termination of the *HF* power. The increase in  $T_e$  at the beginning of the *power-ON* stage is due to an overshoot of  $E/N$  above the quasi-steady state during the pulse. Although not as severe, such overshoot is common in pulsed *ICPs*. [16]. In pulsed *ICPs*, the overshoot is due to the larger power dissipation into a smaller density of surviving electrons at the end of the afterglow. At the boundary of *HF* sheath, the  $E/N$  changes from 200 Td to 2500 Td during the pulse rise before settling down to 1400 Td for the

*power-ON* stage, as shown in Fig. 5.9.

As in the *CW* cases for high values of  $\gamma$ , the net ionization by bulk electrons,  $S_b$ , averaged over the pulse period is negative. During the *power-OFF* period,  $S_b$  is as large (negative) as  $-3.5 \times 10^{15} \text{ cm}^3\text{s}^{-1}$ , which is primarily due to attachment (as opposed to recombination). Although the cross section for dissociative electron attachment to  $\text{CF}_4$  and  $\text{O}_2$  with few eV electrons is 3 orders of magnitude smaller than the cross section for the recombination of  $\text{CF}_3^+$  and  $\text{O}_2^+$ , the number density of  $\text{CF}_4$  and  $\text{O}_2$  is 4 to 6 orders larger than the  $\text{CF}_3^+$  and  $\text{O}_2^+$ . At the leading edge of the pulsed power, an increase in  $T_e$  produces a momentary positive increase in  $S_b$  to  $9 \times 10^{16} \text{ cm}^3\text{s}^{-1}$  during the overshoot in  $E/N$  and remains net positive during the remainder of the *power-ON* cycle. During the *power-OFF* period,  $S_b$  is negative. The ionization balance is provided by the secondary electrons. As with the Ar discharge, there is a background  $S_s$  due to the *LF* bias of  $3 \times 10^{14} \text{ cm}^3\text{s}^{-1}$ . This ionization source is not large enough to balance attachment on a *CW* basis – the increase in  $S_s$  during the *power-ON* period to  $2 \times 10^{15} \text{ cm}^3\text{s}^{-1}$  coupled with the momentary increase in  $S_b$  provides the pulse averaged ionization balance. Due to the resonant dissociative attachment cross sections, there is essentially no volumetric electron loss for energies greater than 15-20 eV. Since the majority of the secondary electron energies greatly exceed 15-20 eV, they make a negligible contribution to volumetric losses.

$f(\varepsilon)$  near the sheaths and in the bulk plasmas (locations shown in Fig. 5.1a) at different times during the pulse period are shown in Fig. 5.11 for the base case conditions. As the pulsed power is toggled on-and-off, the high energy electron population in the tail of the  $f(\varepsilon)$  is modulated to high and low values. This modulation is more extreme in this gas mixture compared to the pure argon case. The tail of  $f(\varepsilon)$  at the *HF* sheath extends to over 120 eV at the leading edge of the *power-ON* period due to the overshoot of  $E/N$  at the leading edge of the

*power-ON* period above the steady state value. The  $f(\varepsilon)$  then adjusts quickly to the *power-ON* value after the local enhancement in  $E/N$  diminishes. The enhancement in the tail of  $f(\varepsilon)$  at the *LF* sheath is to 60 eV, and in the bulk plasma to 50 eV. The rate at which the high energy tail  $f(\varepsilon)$  collisionally relaxes is greater than in the argon case due to the lower energy inelastic thresholds in this gas mixture. The *PPA*  $f(\varepsilon)$  are also compared to the *CW*  $f(\varepsilon)$  in Fig. 5.11. The disparity between the *PPA* and *CW* distributions is most acute near the *HF* sheath where the *PPA*  $f(\varepsilon)$  is both more thermal (larger low energy component) and has a more extensive high energy tail. This results from thermalization during the *power-OFF* period (enhancing the low energy component) and stochastic heating at the leading edge of the *power-ON* period (enhancing the high energy tail).

The distribution and mole fraction averaged rate coefficient for all electron impact ionization processes and for all electron loss processes due to bulk electrons in the middle of the reactor are shown in Fig. 5.12 for the base case conditions in pure argon and Ar/CF<sub>4</sub>/O<sub>2</sub>. In Ar, the only measurable volumetric loss is radiative recombination ( $k \approx 10^{-13}/Te(\text{eV})^{0.5} \text{ cm}^3/\text{s}$ ), and whose contribution is negligible for these conditions. The modulation in ionization rate coefficient is a factor of 40 during the pulse cycle (nearly 140 when considering the overshoot at the beginning of the *power-ON*). The finite ionization rate coefficient during the *power-OFF* period results from the continuous heating from *LF* power on the substrate. Although the super-elastic relaxation of Ar metastable states produces some amount of electron heating, the contribution of the super-elastic relaxation during the *power-OFF* period is small and equivalent to  $E/N = 0.65 \text{ Td}$ . In Ar/CF<sub>4</sub>/O<sub>2</sub> mixtures, the average bulk rate coefficient for ionization increases by  $\approx 100$  during the pulse period (nearly 2000 when considering the overshoot at the beginning of the *power-ON*). In this mixture, there is significant collisional loss of electrons,

which results in a net collisional loss during the *power-OFF* period which exceeds ionization. The rapid quenching of Ar metastable states reduces significant sources of superelastic heating during the *power-OFF* period. Note that the electron loss rate coefficient increases during the *power-ON* period due to the resonant cross sections for attachment which increase with increasing  $E/N$  (at low  $E/N$ ).

The source and loss rate coefficients at different heights in the reactor are shown in Fig. 5.13. The electron source rate coefficient is dependent on the tail of  $f(\varepsilon)$  and so is most sensitive to local sources of electron heating. The ionization rate coefficient is largest near the *HF* electrode due to the higher efficiency of stochastic heating, next highest near the *LF* electrode and lowest in the bulk plasma. The absolute value of the source rate coefficients are larger in Ar/CF<sub>4</sub>/O<sub>2</sub> than in Ar in order to compensate for the volumetric electron losses.

There are two electron heating mechanisms – stochastic heating due to the oscillating sheath boundary and Ohmic heating due to the resistivity of the plasma in the bulk. The relative overshoot of the ionization rate coefficient at the beginning of the *power-ON* period is largest in the center of the plasma. This is a consequence of long-mean-free path transport of electrons which were accelerated by stochastic heating in the sheaths but which have ionizing collisions in the middle of the plasma – the local value of  $E/N$  is not high enough to support the local increase in ionization by Ohmic heating. The electron loss rate coefficients for Ar/CF<sub>4</sub>/O<sub>2</sub> behave similarly to the ionization rates, through over a smaller dynamic range. Due to the resonant cross sections for attachment having non-zero threshold energies, the electron loss rates increase during the *power-ON* period – more so near the *HF* and *LF* sheaths.

## 5.5 Pulse Repetition Rate and Duty cycle

The  $f(\varepsilon)$  at the beginning of the *power-ON* stage near the *HF* sheath for different PRFs of

50 and 250 kHz, and for *CW* excitation sustained in argon and Ar/CF<sub>4</sub>/O<sub>2</sub> are shown in Fig. 5.14. In both argon and Ar/CF<sub>4</sub>/O<sub>2</sub> mixtures, the tail of  $f(\varepsilon)$  reaches higher energies with lower PRF. With the lower PRF and longer interpulse period, electron losses are larger and so the conductivity of the plasma is lower at the time the pulse power is applied. This affects collisional heating by there being a larger  $E/N$  in the bulk plasma and affects stochastic heating by increasing the sheath width and so sheath speed. The  $f(\varepsilon)$  in Ar/CF<sub>4</sub>/O<sub>2</sub> is more distinctly bi-Maxwellian compared to Ar due to the generation of high energy electrons during the enhanced overshoot in  $E/N$  and the more rapid rate of collisional energy loss (and attachment) in the molecular gas mixture at energies  $< 12$  eV (inelastic threshold for ground state Ar). As the tail is enhanced, the low energy portion of  $f(\varepsilon)$  is more depleted with smaller PRF.

The overshoot of the average electron source rate coefficient at the beginning of the *power-ON* stage is observed in both argon and Ar/CF<sub>4</sub>/O<sub>2</sub>. However, the relative amount of overshoot decreases with increasing PRF, approaching *CW*, as shown in Fig. 5.15. For a given duty cycle, with increasing PRF, there is less electron loss during the *power-OFF* period and so a higher conductivity at the start of the next *power-ON* period. The higher conductivity results in a lower  $E/N$ .

The same logic produces a dependence of  $f(\varepsilon)$  on duty cycle. The  $f(\varepsilon)$  at the leading edge of the pulse power near the *HF* sheath for duty cycles of 25%, 50% and *CW* (PRF = 50 kHz) for argon and Ar/CF<sub>4</sub>/O<sub>2</sub> are shown in Fig. 5.16. Corresponding ionization coefficients are in Fig. 5.17. With increasing DC and longer inter-pulse period, there is greater loss of electrons and so smaller conductivity at the start of the *power-ON* period. As a result, the overshoot in  $E/N$  is greater and so the tail of  $f(\varepsilon)$  extends to higher energy. For a PRF of 50 kHz in argon, the overshoot effect already diminishes with a 50% DC, whereas, for Ar/CF<sub>4</sub>/O<sub>2</sub>, the overshoot

effect starts to diminish with a duty cycle of 90%, since the electron density is still small compared to argon discharge. The low energy portion of  $f(\varepsilon)$  is enhanced with decreasing DC, as shown in the insets of Fig. 5.16, as the tail of  $f(\varepsilon)$  decreases. The ionization source rate coefficients reflect two trends with decreasing DC- increasing overshoot in  $E/N$  and the increase in power during the *power-ON* portion of the cycle to keep the cycle-averaged *HF* power constant at 500 W. Note that the ionization rate coefficient increases during the *power-ON* period with argon, but is constant or slightly decreasing with Ar/CF<sub>4</sub>/O<sub>2</sub>. This is due in part to the accumulation of Ar metastable states during the *power-ON* cycle that provides more efficient ionization by multistep processes, a process that is of less importance in Ar/CF<sub>4</sub>/O<sub>2</sub>.

## 5.6 Concluding Remarks

The properties of  $f(\varepsilon)$  in pulse powered DF-CCP sources sustained in Ar and Ar/CF<sub>4</sub>/O<sub>2</sub> mixtures have been computationally investigated using results from a 2D plasma hydrodynamic model having an electron Monte-Carlo simulation including electron-electron collisions. The pulse-period-averaged  $f(\varepsilon)$  obtained when pulsing the *HF* power differs from that obtained with *CW* excitation and has a shape that arguably would be difficult to replicate under *CW* conditions. The *PPA*  $f(\varepsilon)$  poorly represents the dynamics of  $f(\varepsilon)$  during the pulsed period, where the tail of  $f(\varepsilon)$  can extend to energies in excess of 100 eV at the leading edge of the *power-ON* period. The properties of  $f(\varepsilon)$  are differentiated between the *HF* and *LF* sheaths, and the bulk plasma. When the power is turned on, the electrons are quickly heated due to the increase in sheath voltage which provides an impulsive acceleration through stochastic heating. The heating is also more prominent at the leading edge of the pulse due to an overshoot of  $E/N$  above the quasi-steady state during the *power-ON* period. The overshoot is more prominent in Ar/CF<sub>4</sub>/O<sub>2</sub> mixtures due

to the greater fractional decrease in electron density during the *power-OFF* stage. Also, the shorter energy relaxation length in Ar/CF<sub>4</sub>/O<sub>2</sub> mixture produces more dynamic changes in the plasma properties near the sheath as the pulse power is toggled on and off. We found that the plasma properties including  $f(\varepsilon)$  can be controlled with different PRFs and DCs. Lower PRF and smaller DC produce larger excursions of the tail of  $f(\varepsilon)$  and so larger ionization sources in both Ar and Ar/CF<sub>4</sub>/O<sub>2</sub> mixtures. These results are sensitive to the electron emitting boundary conditions. With lower values of  $\gamma$ , more ionization must be provided by bulk electron collisions and so the tail of the  $f(\varepsilon)$  is raised. This gives some opportunity to customize  $f(\varepsilon)$  in CCPs by varying the electron emitting boundary condition.

## 5.7 Figures

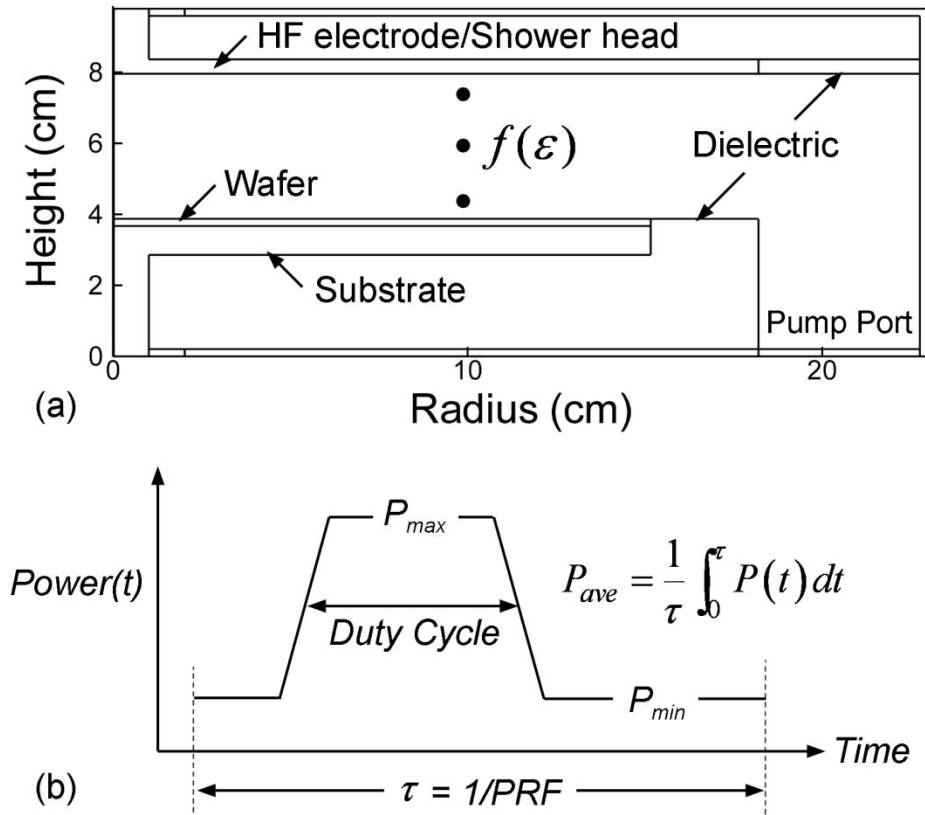


Fig. 5.1 Operating conditions for this investigation. (a) Geometry of the dual frequency capacitively coupled plasma chamber. The low frequency (*LF*, 10 MHz) is applied on the lower electrode in continuous wave (*CW*) mode, and the high frequency (*HF*, 40 MHz) is applied on the upper electrode in pulse mode with a few tens of kHz pulse repetition frequency (*PRF*). The dots show where  $f(\epsilon)$  will be plotted. (b) Pulsed operation is determined by the duty cycle and pulse repetition frequency. The power is turned on during the fraction of the total period designated by the duty cycle (*DC*). Pulse repetition frequency is how many times per second the pulse waveform repeats.

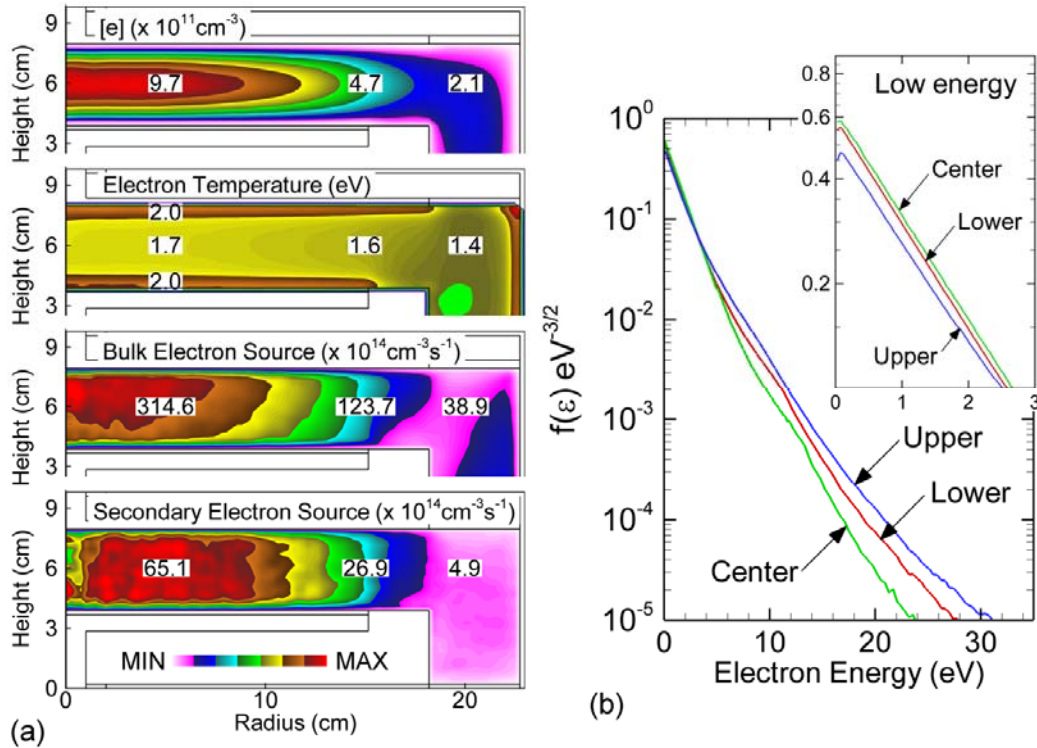


Fig. 5.2 Plasma properties for *CW* operation in Ar (40 mTorr, 200 sccm, 500 W at 10 MHz, 500 W at 40 MHz). (a) Electron density, temperature, and electron ionization sources by bulk electron and secondary electrons. (b) Electron energy distribution at selected heights in the reactor (locations indicated in Fig. 5.1). The inset shows an enlargement of the low energy portion of the distribution.

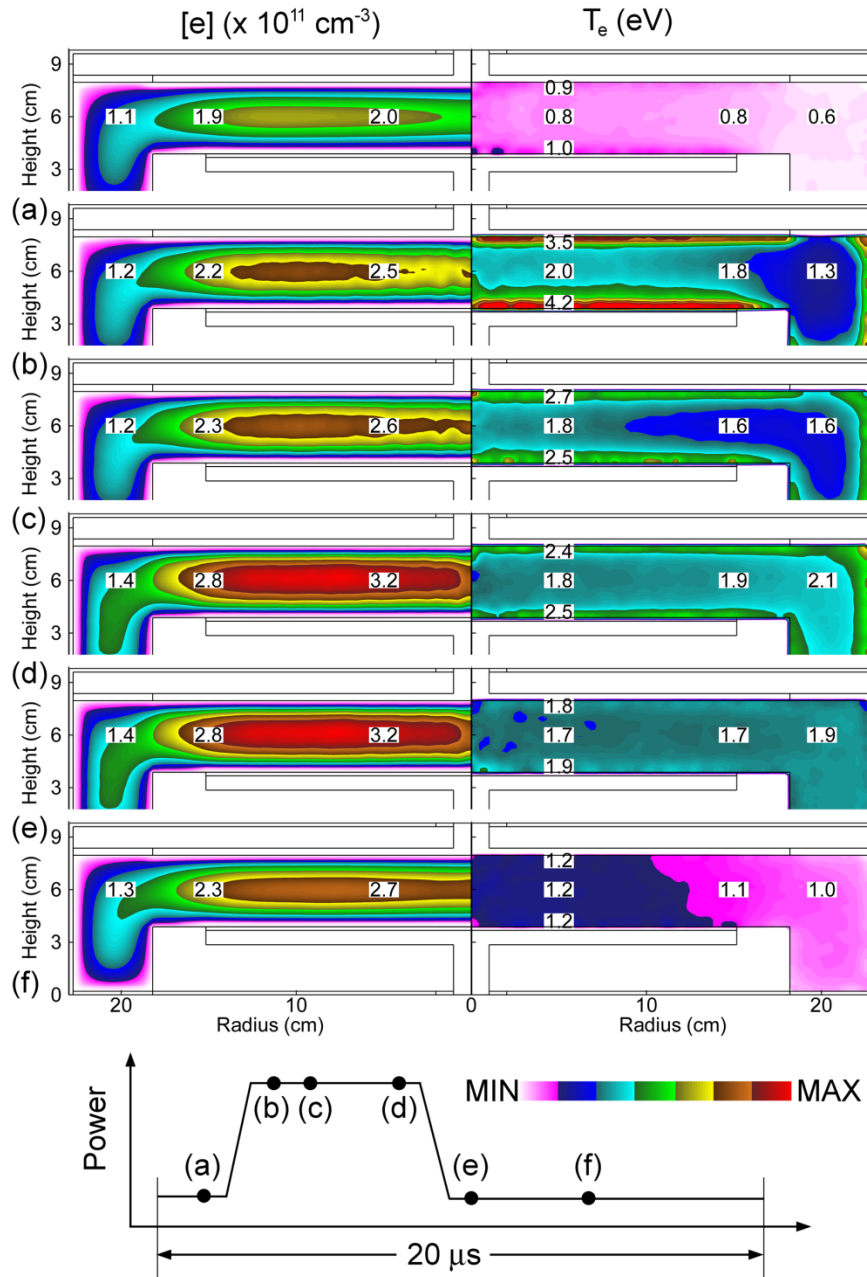


Fig. 5.3 Electron density and temperature in Ar for the base case conditions (40 mTorr, 200 scm, 500 W at 10 MHz CW, 500 W at 40 MHz in pulse mode – 50 kHz PRF with 25% duty cycle) at different times during the pulsed cycle (as indicated in the lower figure). The electron density does not change significantly over the pulse period, whereas the electron temperature shows instantaneous changes as the power toggles on and off, especially near the sheaths due to enhanced stochastic heating.

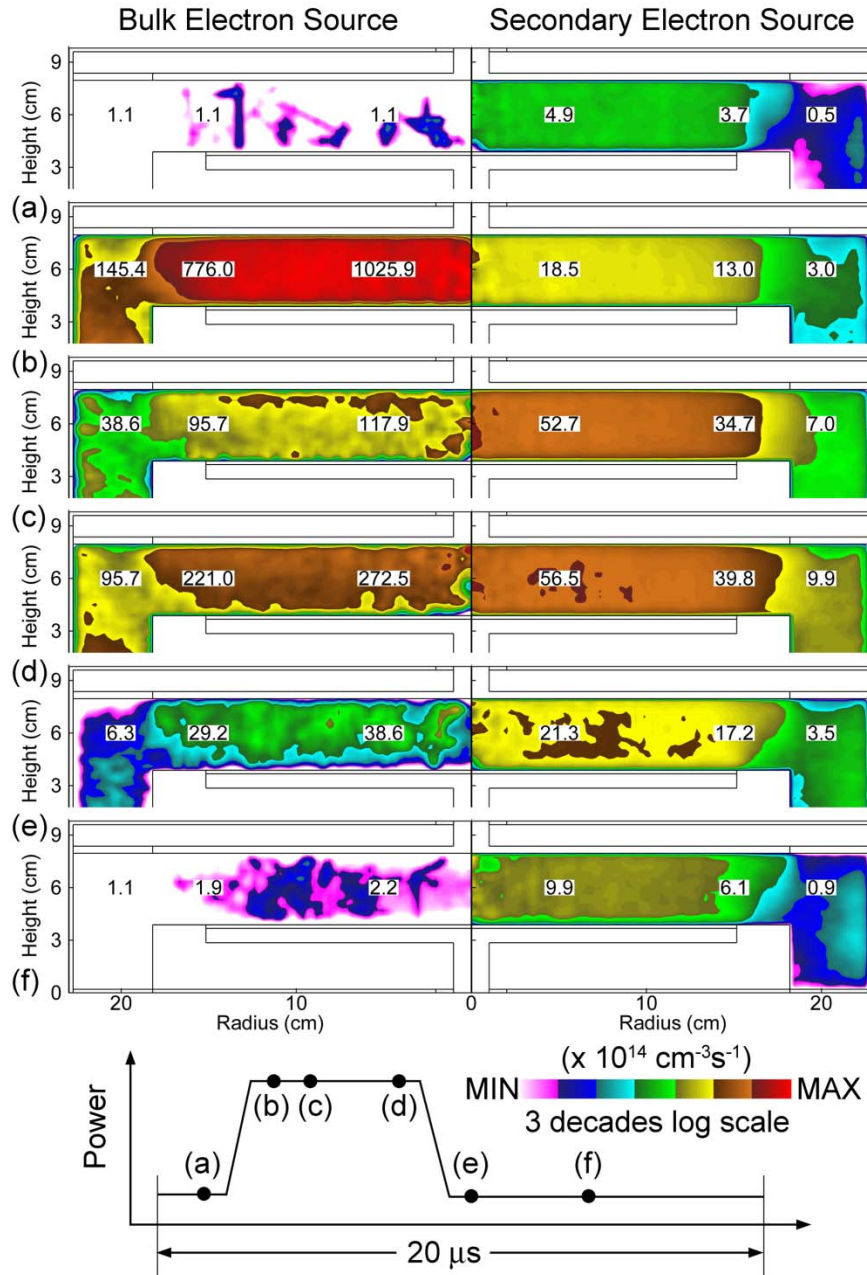


Fig. 5.4 Ionization source by (left) bulk electrons and (right) secondary electrons in Ar for the base case conditions (40 mTorr, 500 W at 10 MHz CW, 500 W at 40 MHz in pulse mode – 50 kHz PRF with 25% duty cycle) at different times during the pulsed cycle (as indicated in the lower figure).

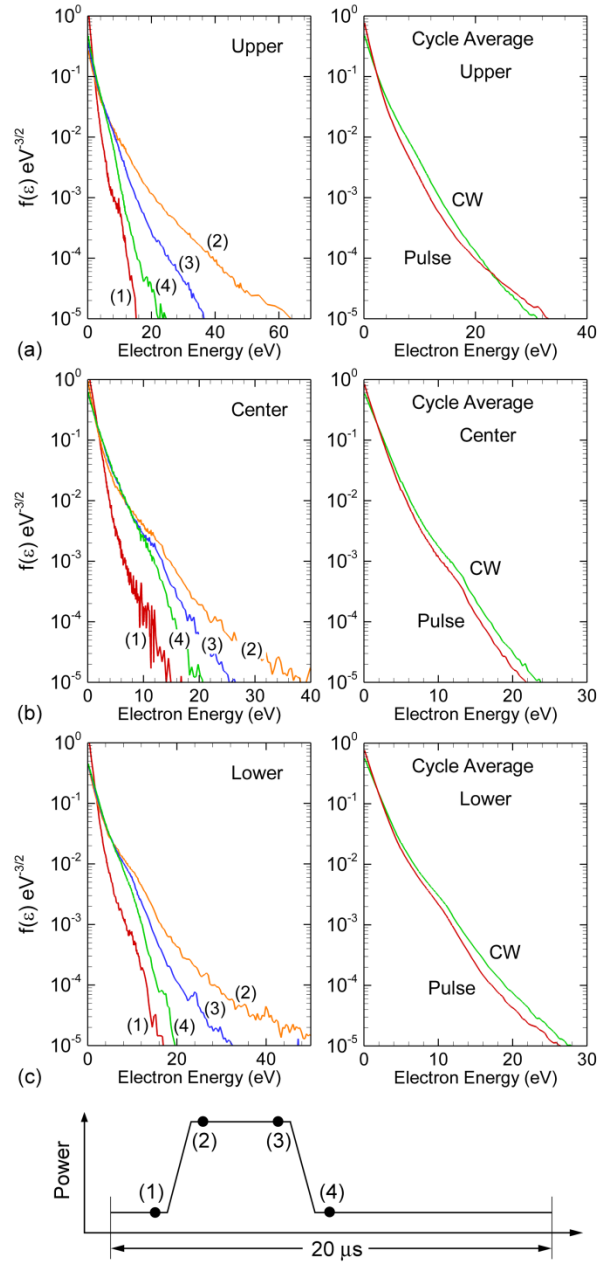


Fig. 5.5 Electron energy distribution functions in Ar for the base case conditions (40 mTorr, 500 W at 10 MHz CW, 500 W at 40 MHz in pulse mode – 50 kHz PRF with 25% duty cycle) at different times during the pulse cycle (as indicated in the lower figure) for (a) near the *HF* sheath, (b) in the bulk plasma and (c) near the *LF* sheath (locations indicated in Fig. 5.1). Comparisons of  $f(\varepsilon)$  averaged over the pulse period and with *CW* excitation are in the right column. The enhanced tail of  $f(\varepsilon)$  is most prominent at the leading edge of the *power-ON* period.

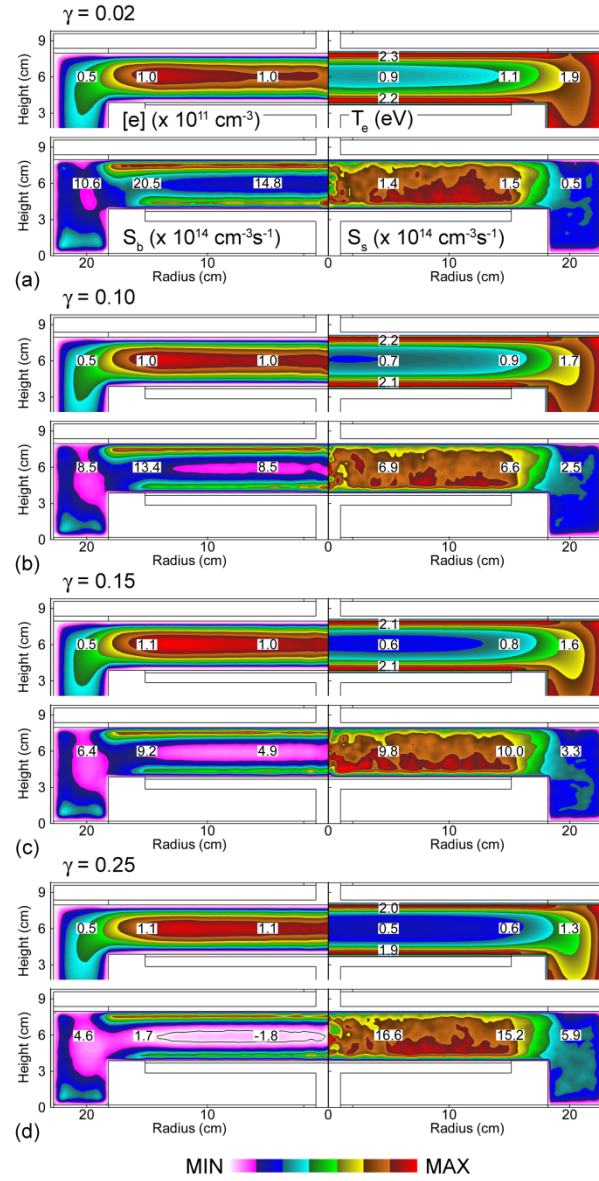


Fig. 5.6 Electron density, temperature, and electron ionization sources by bulk electron and secondary electrons in Ar/CF<sub>4</sub>/O<sub>2</sub>=75/20/5 for CW excitation with different secondary electron emission coefficients,  $\gamma$ . (a) 0.02, (b) 0.10, (c) 0.15, and (d) 0.25.

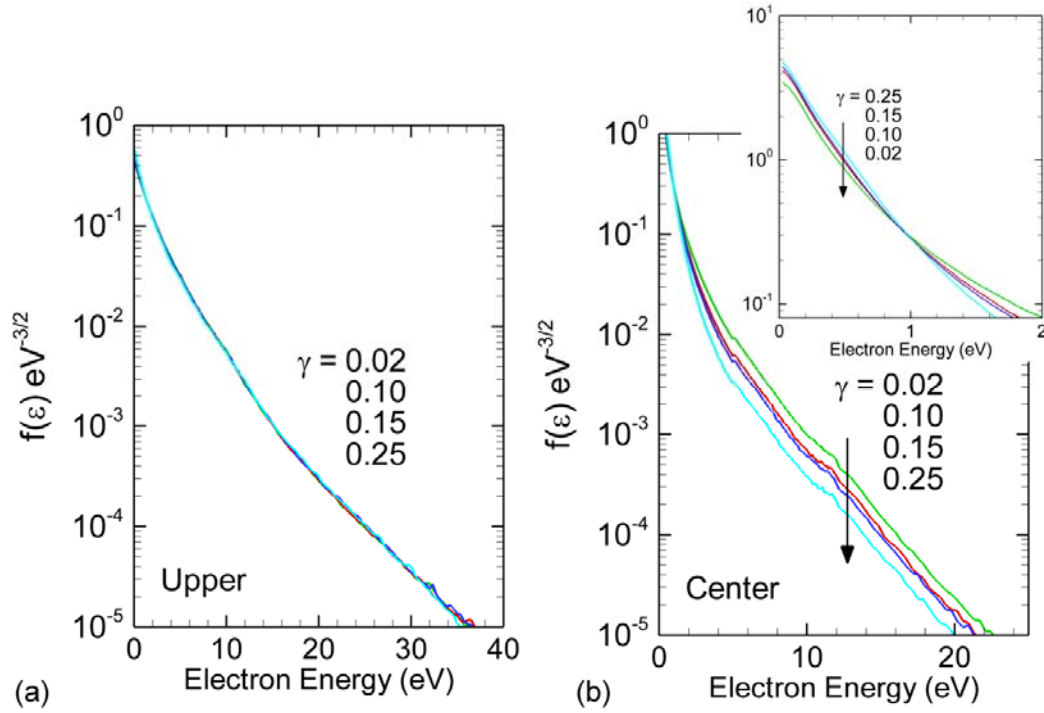


Fig. 5.7 Electron energy distributions in Ar/CF<sub>4</sub>/O<sub>2</sub>=75/20/5 with CW excitation for different secondary electron emission coefficients,  $\gamma$  for base case conditions. (a) Near the HF sheath and (b) at the center of the plasma. With increasing rates of ionization by secondary electrons with increasing  $\gamma$ , the tail of the  $f(\epsilon)$  decreases.

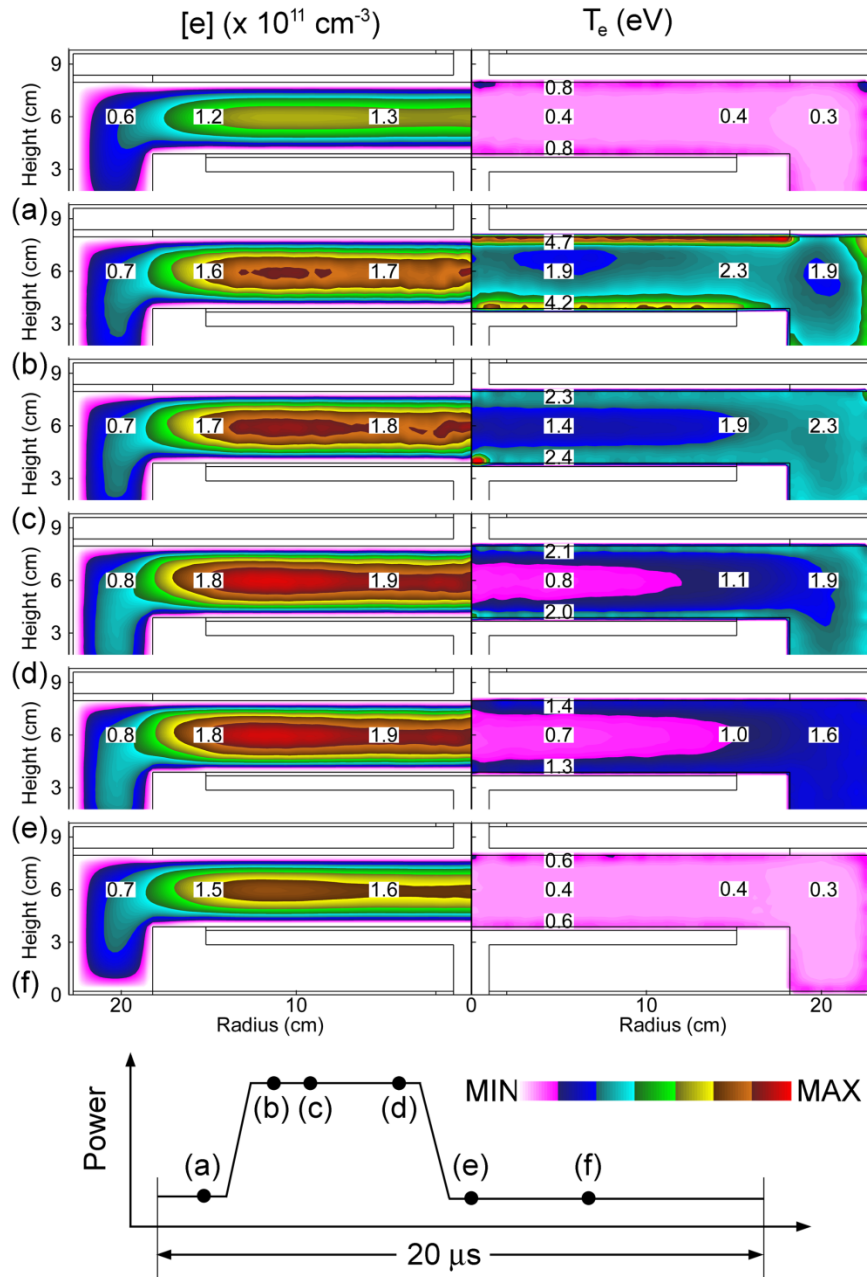


Fig. 5.8 Plasma properties with pulsed excitation in Ar/CF<sub>4</sub>/O<sub>2</sub>=75/20/5 – (left) Electron density and (right) electron temperature for the base case conditions (40 mTorr, 500 W at 10 MHz CW, and 500 W at 40 MHz in pulse mode – 50 kHz PRF with 25% duty cycle) at different times during the pulsed cycle (as indicated in the lower figure).

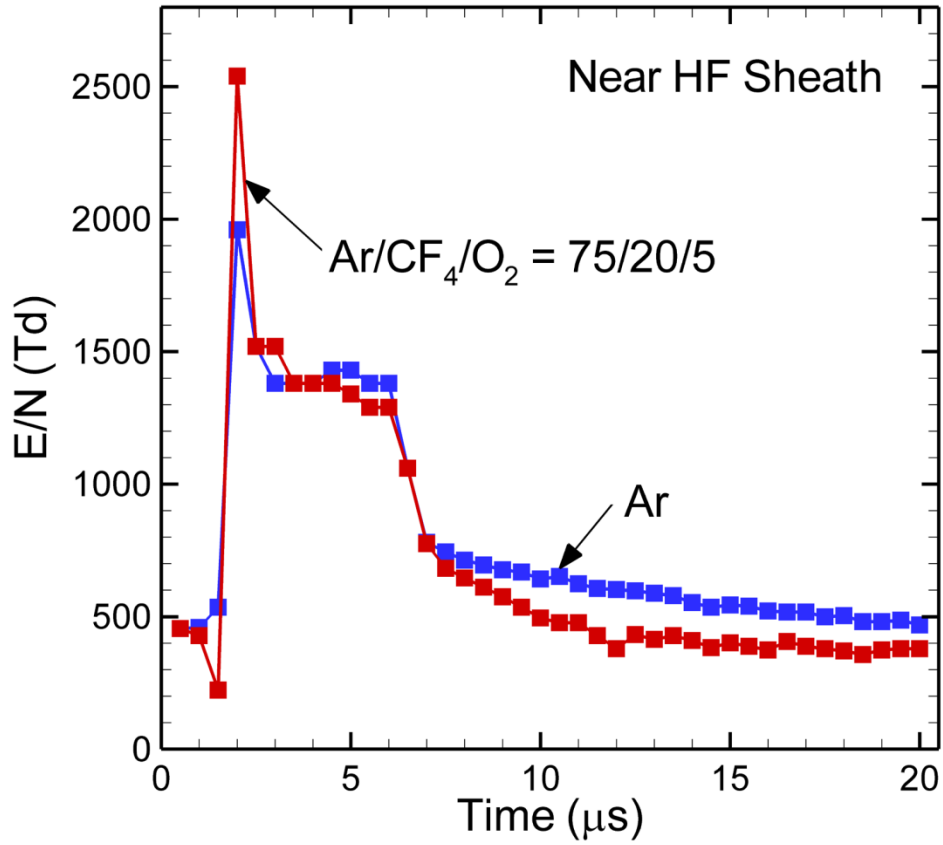


Fig. 5.9  $E/N$  over the pulsed cycle with Ar and Ar/CF<sub>4</sub>/O<sub>2</sub>=75/20/5 for base case conditions (40 mTorr, 500 W at 10 MHz CW, and 500 W at 40 MHz in pulse mode – 50 kHz PRF with 25% duty cycle). The overshoot is more severe in the Ar/CF<sub>4</sub>/O<sub>2</sub> mixture due to the lower electron density at the beginning of the pulse.

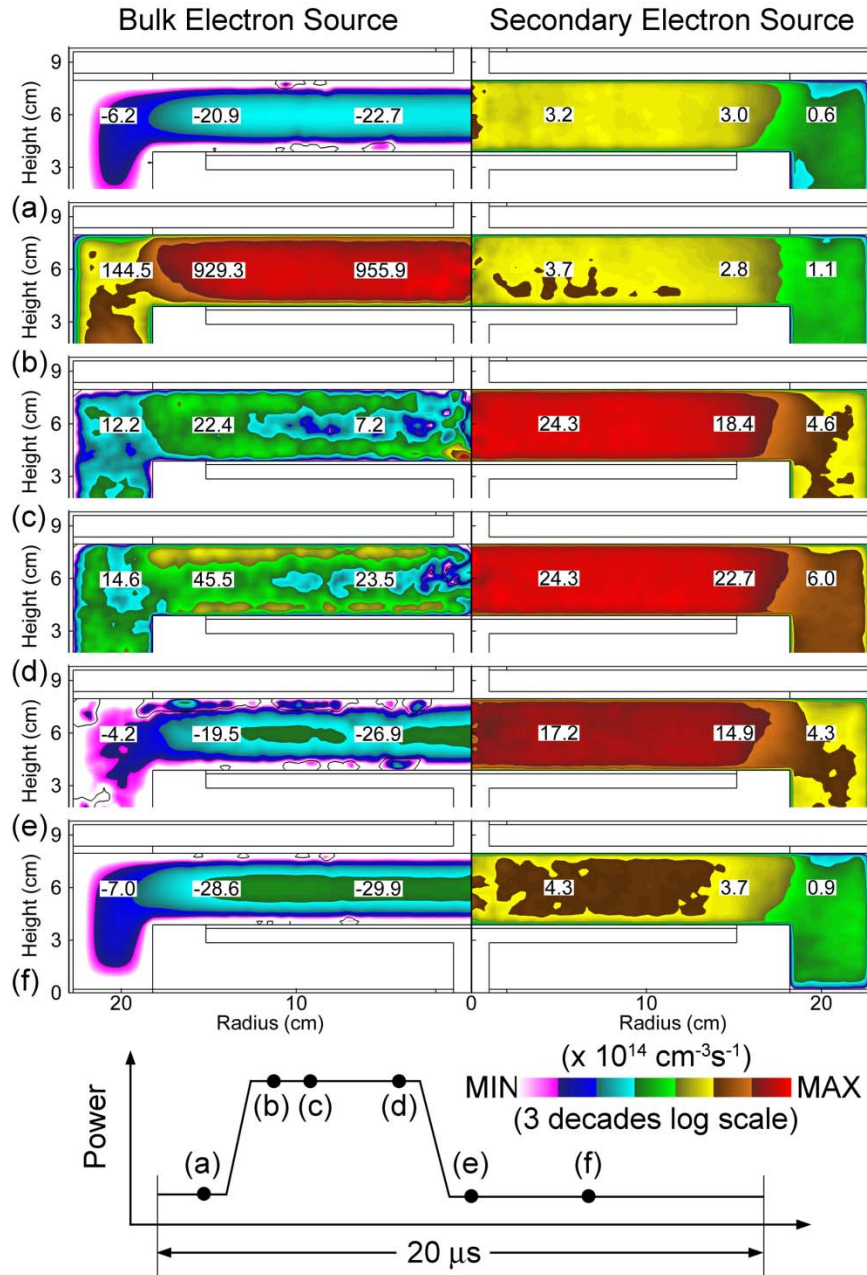


Fig. 5.10 Ionization source by (left) bulk electrons and (right) secondary electrons in  $\text{Ar}/\text{CF}_4/\text{O}_2=75/20/5$  for the base case conditions (40 mTorr, 500 W at 10 MHz CW, and 500 W at 40 MHz in pulse mode – 50 kHz PRF with 25% duty cycle) at different times during the pulsed cycle (as indicated in the lower figure). The ionization source by bulk electrons is largest at the beginning of the *power-ON* stage due to the expansion of the sheath with the application of voltage.

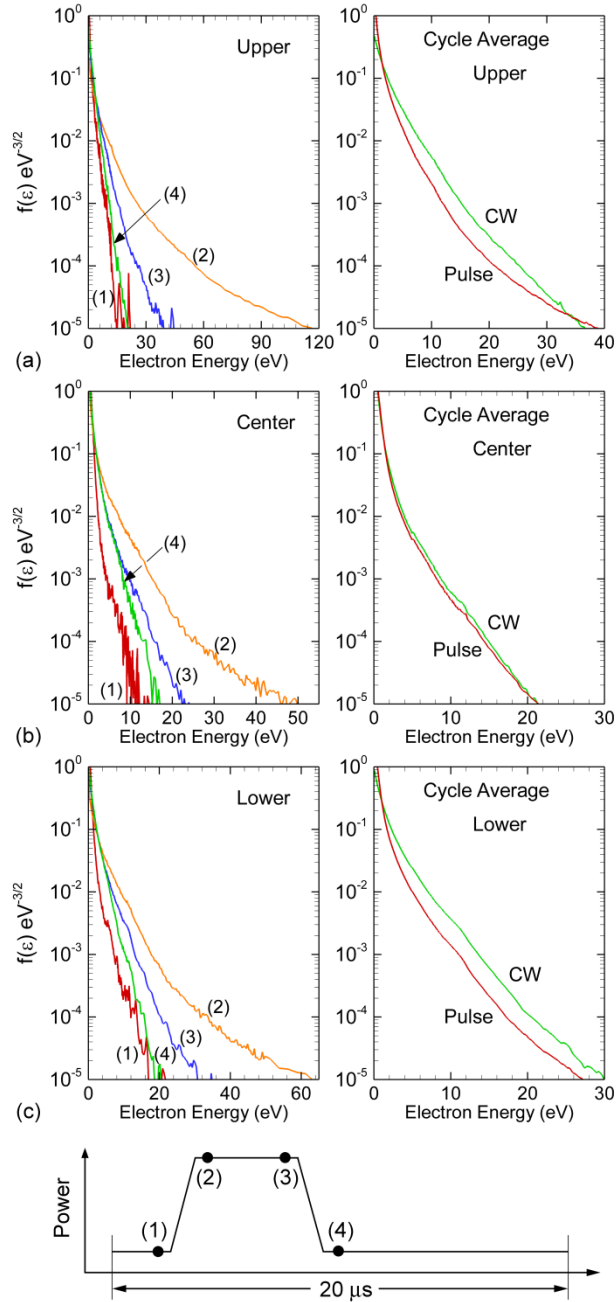


Fig. 5.11 Electron energy distribution functions in  $\text{Ar}/\text{CF}_4/\text{O}_2=75/20/5$  for the base case conditions (40 mTorr, 500 W at 10 MHz CW, and 500 W at 40 MHz in pulse mode – 50 kHz PRF with 25% duty cycle) at different times during the pulsed cycle (as indicated in the lower figure). (a) Near the *HF* sheath, (b) in the bulk plasma and (c) near the *LF* sheath (locations indicated in Fig. 5.1). Comparisons of  $f(\varepsilon)$  averaged over the pulse period and with CW excitation are in the right column.

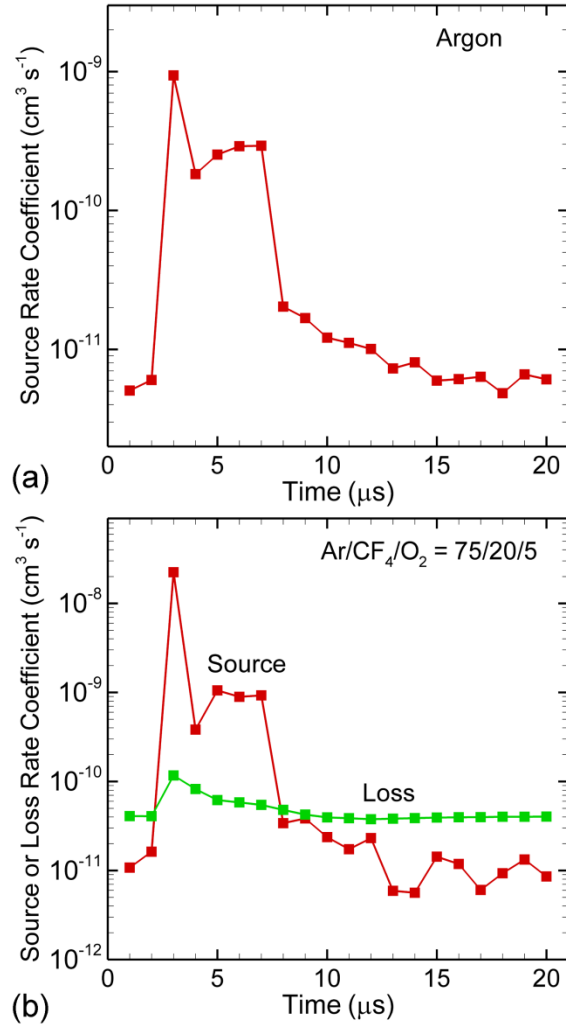


Fig. 5.12 Mole fraction weighted rate coefficients for electron impact ionization sources and electron impact loss reactions during the pulsed cycle for the base case conditions. (a) Ar and (b) Ar/CF<sub>4</sub>/O<sub>2</sub>=75/20/5. In Ar, the electron loss rate coefficient is negligible. Whereas in Ar/CF<sub>4</sub>/O<sub>2</sub> the loss rate coefficient is finite through the pulsed cycle.

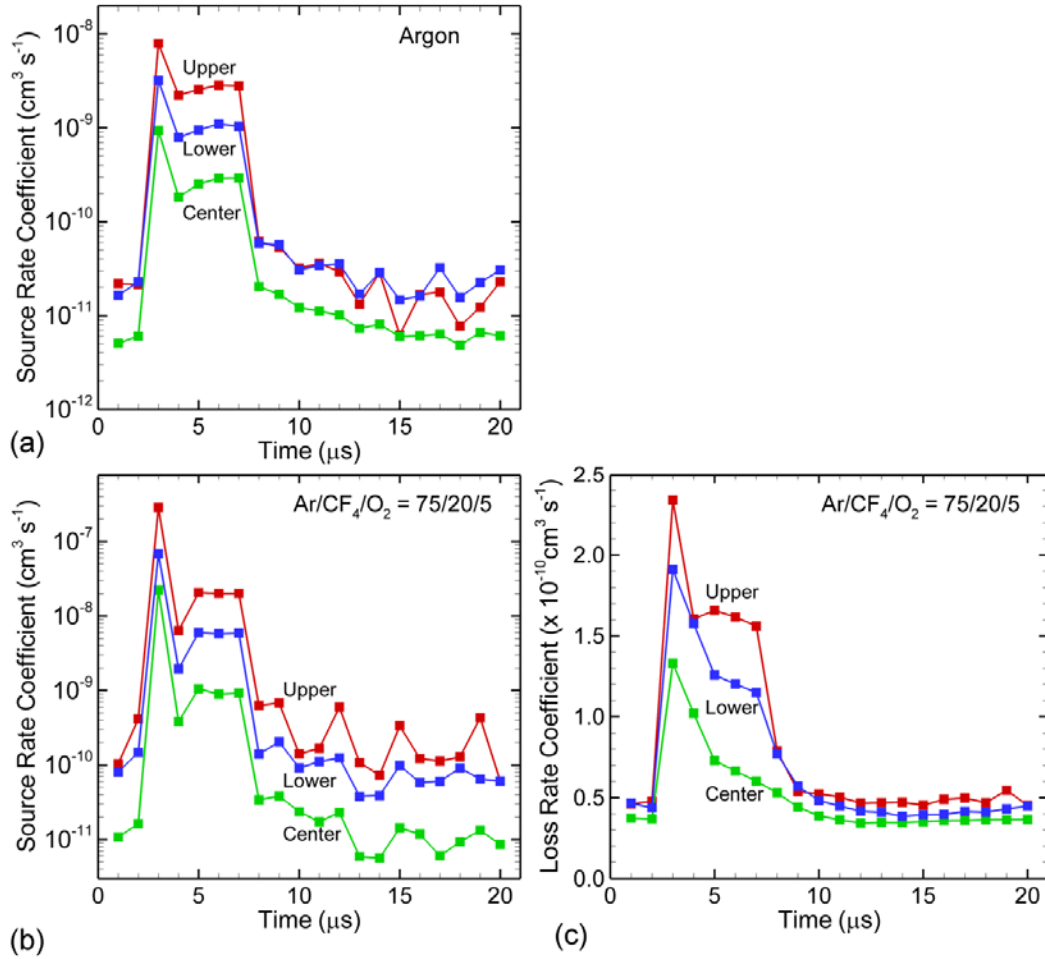


Fig. 5.13 Mole fraction weighted rate coefficients for the electron impact ionization sources and electron impact loss reactions during the pulsed cycle at different heights in the reactor for the base case conditions. (a) Ar ionization, sources, (b) Ar/CF<sub>4</sub>/O<sub>2</sub> ionization sources and (c) Ar/CF<sub>4</sub>/O<sub>2</sub> losses. The loss rate coefficients respond to the overshoot in  $E/N$  due to the resonant cross sections for attachment. The locations for heights are shown in Fig. 5.1.

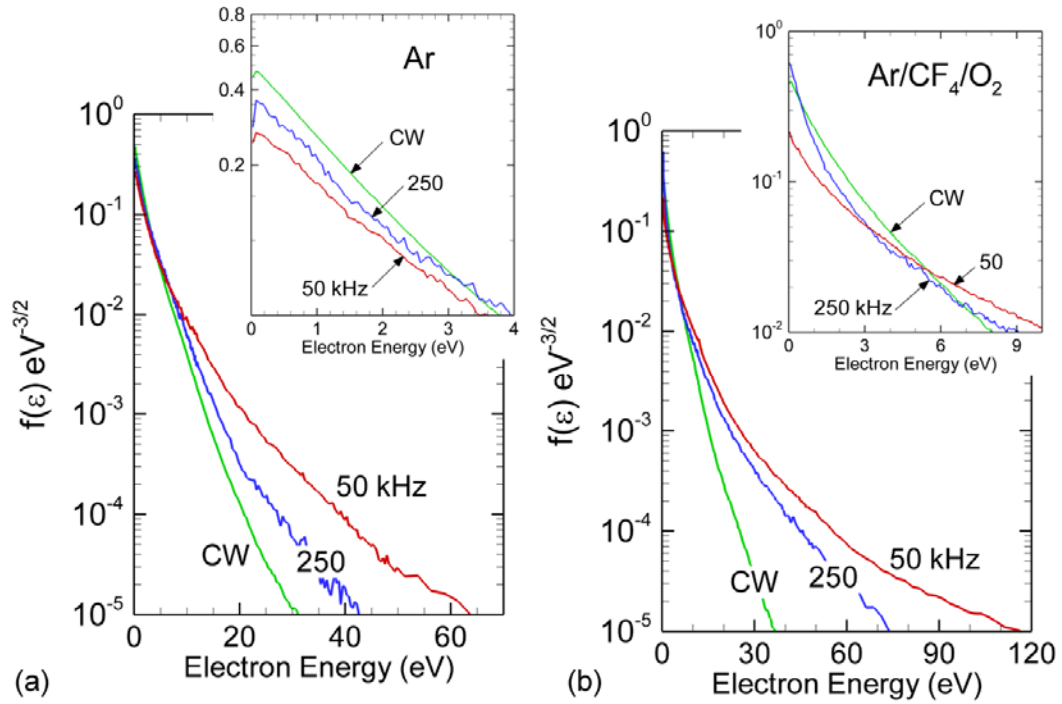


Fig. 5.14 Electron energy distribution functions near the *HF* sheath for the base case conditions (40 mTorr, 500 W at 10 MHz CW, 500 W at 40 MHz in pulse mode, 25% duty cycle) for different PRF. (a) Argon and (b) Ar/CF<sub>4</sub>/O<sub>2</sub>. Insets show enlargements of the low energy portion of  $f(\epsilon)$ .

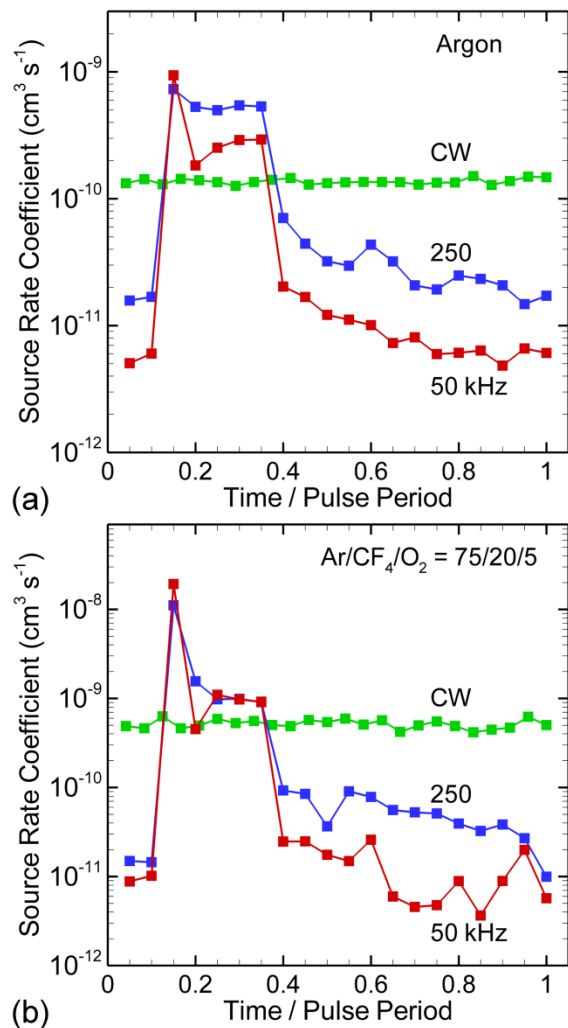


Fig. 5.15 Mole fraction weighted electron impact ionization rate coefficients in the middle of the gap with different PRFs (40 mTorr, 500 W at 10 MHz in *CW* mode, and 500 W at 40 MHz in pulse mode with 25% duty cycle). (a) Ar and (b) Ar/CF<sub>4</sub>/O<sub>2</sub>=75/20/5. The relative overshoot of the electron impact ionization rate coefficient is larger with smaller PRF.

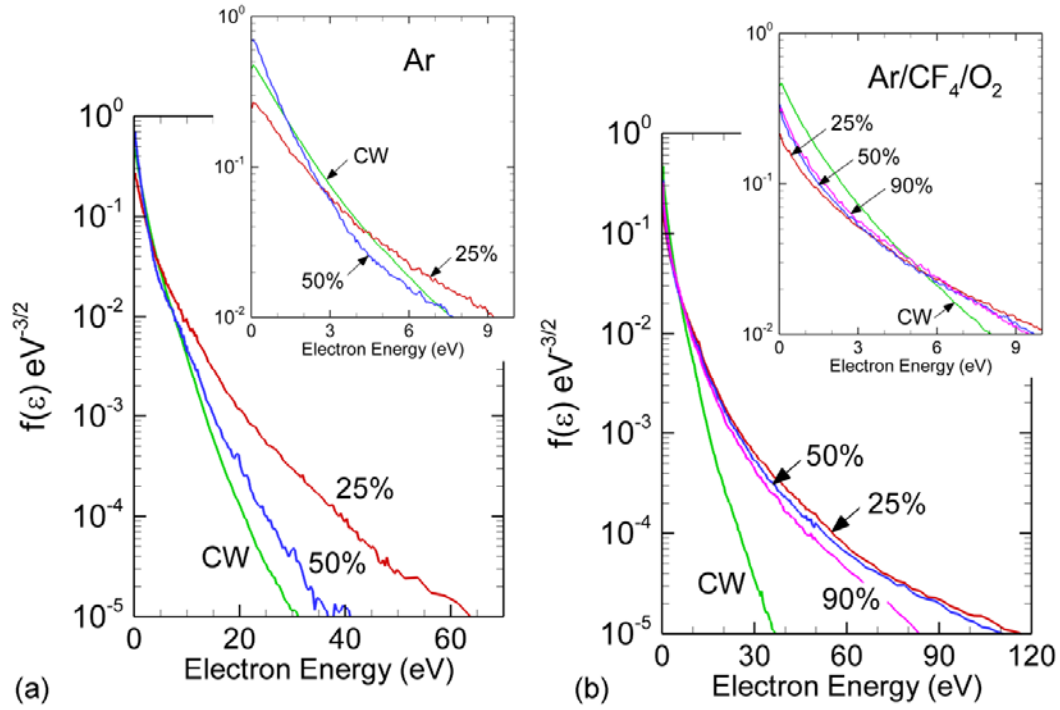


Fig. 5.16 Electron energy distribution functions near the *HF* sheath for the base case conditions (40 mTorr, 500 W at 10 MHz *CW*, 500 W at 40 MHz in pulse mode, 50 kHz) for different duty cycles. (a) Argon and (b) Ar/CF<sub>4</sub>/O<sub>2</sub>. Insets show enlargements of the low energy portion of  $f(\varepsilon)$ .

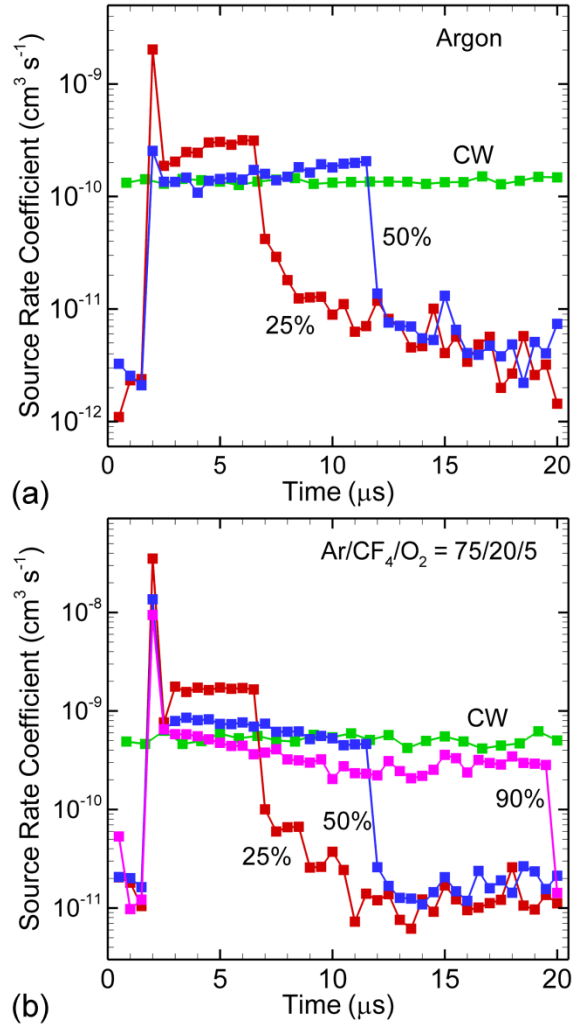


Fig. 5.17 Mole fraction weighted electron impact ionization rate coefficients in the middle of the gap with different duty cycles (40 mTorr, 500 W at 10 MHz in CW mode, and 500 W at 40 MHz in pulse mode, 50 kHz). (a) Ar and (b) Ar/CF<sub>4</sub>/O<sub>2</sub>=75/20/5. The relative overshoot of the electron impact ionization rate coefficient scales inversely with duty cycle.

## 5.8 References

1. A. Mareska, K. Orlov, and U. Kortshagen, "Experimental study of diffusive cooling of electrons in a pulse inductively coupled plasma", *Phys. Rev. E* **65**, 056405 (2002).
2. G. A. Hebner and C. B. Fleddermann, "Characterization of pulse-modulated inductively coupled plasmas in argon and chlorine", *J. Appl. Phys.* **82**, 2814 (1997).
3. S. Banna, A. Agarwal, K. Tokashiki, H. Cho, S. Rauf, V. Todorow, K. Ramaswamy, K. Collins, P. Stout, J.-Y. Lee, J. Yoon, K. Shin, S.-J. Choi, H.-S. Cho, H.-J. Kim, C. Lee, and D. Lymberopoulos, "Inductively Coupled Pulsed Plasmas in the Presence of Synchronous Pulsed Substrate Bias for Robust, Reliable, and Fine Conductor Etching", *IEEE Trans. Plasma Sci.* **37**, 1730 (2009).
4. V. Samara, M. D. Bowden, and N. St. J. Braithwaite, "Effect of power modulation on properties of pulsed capacitively coupled radiofrequency discharges", *J. Phys. D: Appl. Phys.* **43**, 124017 (2010).
5. M. J. Kushner, "Hybrid modeling of low temperature plasmas for fundamental investigations and equipment design", *J. Phys. D* **42**, 194013 (2009).
6. A. V. Vasenkov and M. J. Kushner, "Electron energy distributions and anomalous skin depth effects in high-plasma-density inductively coupled discharges," *Phys. Rev. E* **66**, 066411 (2002).
7. A. V. Vasenkov, X. Li, G. S. Oehrlein and M. J. Kushner, "Properties of  $C_4F_8$  inductively coupled plasmas. II. Plasma chemistry and reaction mechanism for modeling of Ar/c- $C_4F_8/O_2$  discharges", *J. Vac. Sci. Technol. A* **22**, 511 (2004).
8. E. Kawamura, M. A. Lieberman, and A. J. Lichtenberg, "Stochastic heating in single and dual frequency capacitive discharges", *Phys. Plasmas* **13**, 053506 (2006).
9. A. Agarwal, P. J. Stout, S. Banna, S. Rauf, and K. Collins, "Recouping etch rates in pulsed inductively coupled plasmas", *J. Vac. Sci. Technol. A* **29**, 011017 (2011).
10. R. A. Bonham, "Electron impact cross section data for carbon tetrafluoride", *Jpn. J. Appl. Phys.* **33**, 4157 (1994).
11. A. V. Phelps, "Tabulations of collision cross sections and calculated transport and reaction coefficients for electron collisions with  $O_2$ ", JILA Information Center Report no. 28, Sep. 1985.
12. R. J. Commisso, R. F. Fernsler, V. E. Scherrer, and I. M. Vitkovitsky, "Electron-beam controlled discharges", *IEEE Trans. Plasma Sci.* **PS-10**, 241 (1982).
13. M. J. W. Boness and R. E. Center, "High-pressure pulsed electrical CO laser", *J. Appl. Phys.* **48**, 2705 (1977).

14. D. H. Douglas-Hamilton, R. M. Feinberg, and R. S. Lowder, "Experimental and theoretical electron-beam-sustained CO<sub>2</sub> laser output at ~200 and ~300 °K", *J. Appl. Phys.* **46**, 3566 (1975).
15. F. A. Haas, A. Goodyear, and N. St. J. Braithwaite, "Tailoring of electron energy distributions in low temperature plasmas", *Plasma Sources Sci. Technol.* **7**, 471 (1998).
16. B. Ramamurthi and D. I. Economou, "Two-dimensional pulsed-plasma simulation of a chlorine discharge", *J. Vac. Sci. Technol. A* **20**, 467 (2002).

## Chapter 6 CONTROL OF ION ENERGY DISTRIBUTION USING PULSED POWER

### 6.1 Introduction

A common strategy for controlling IEDs is employing separate power supplies, typically called the source power and the bias power. The source power is intended to control electron kinetics in the plasma and so control the magnitude of ion and radical fluxes to the wafer. This power is typically applied inductively at many MHz frequencies, as microwave power; or in capacitively coupled plasmas (CCPs) as a high frequency bias (10s to 100s MHz). All of these means of applying the source power preferentially heat electrons compared to ions. The bias power is typically applied to the substrate on which the wafer sits in order to control the energy of ions incident onto the wafer, and typically has a lower radio frequency (*RF*), a few to 10 MHz. With an *RF* bias power on the substrate, a dc self-bias is often naturally generated in order to produce equal currents flowing into both sides of a series capacitance in the circuit. This series capacitance consists of the wafer, stray capacitance and a blocking capacitor in the circuit. The distribution of ion energies bombarding the wafer is then determined by the time variation in the plasma potential produced by the source power, the *RF* sheath potential generated by the bias power and the dc-bias on the series capacitance.

A number of strategies have been pursued to control the self-generated dc-bias on the *RF* driven electrode of CCPs, including variation of the pressure [1], use of a variable resistor in

series with the electrode [2], and manipulation of the *RF* bias power [3] or voltage [4]. Many of these prior works focused on the controlling the average ion energy. However, in many applications, such as HAR etching, the ability to control the shape of the IED rather than only the average ion energy is more likely to produce the desired etching profile. In this regard, Qin *et al.* investigated control of the peak energy of the IED and the separation of the peak energies in bimodal IEDs using non-sinusoidal bias waveforms [5]. They demonstrated the ability to predictably produce arbitrary IEDs at selected energies by tailoring the shape of the bias voltage waveform.

In continuous wave (*CW*) operation, the plasma must exactly balance the source of electrons and losses of electrons averaged over the *RF* period. In single frequency operation of CCPs, for a given set of operating conditions (pressure, gas mixture, flow rate power deposition, frequency), there is usually a single voltage amplitude that will satisfy this balance. For multi-frequency CCPs, there is additional latitude but not unlimited latitude. As a result, in *CW* operation, the ability to control of the IED is constrained by these balance requirements. One of the advantages of pulsed power operation is that the balance between electron sources and losses need only be obtained averaged over the pulsed cycle, which can be as long as many ms. As a result, additional control parameters are introduced, such as pulse repetition frequency (PRF) and duty-cycle. (PRF is the number of times per second the pulse power waveform is repeated and the duty-cycle is the fraction of the pulse period that the power is on.) Agarwal *et al* [6] investigated the temporal dynamics of charged species using pulse power in a multi-frequency CCP by varying PRF. In order to refine the control of ion fluxes to the substrate, they computed not only the plasma potential, but also the self-generated dc-bias across the blocking capacitor in the presence of pulse power on either one of the electrodes. They found that the dc-bias had time

variation during the pulse period that is delayed due to the charging of the blocking capacitor.

Maeshige *et al* [7] investigated the fluxes of charged species in a dual frequency capacitively coupled plasma (DF-CCP) with a 1 MHz *CW* bias and a pulsed 100 MHz source in a Ar/CF<sub>4</sub> = 95/5 mixture at 50 mTorr. They found that the self-bias oscillated during the pulse period (20 μs) where each of the electrodes is capacitively coupled through a blocking capacitor of 0.5 nF. They also demonstrated control of the incident fluxes of electrons as well as the positive and negative ions onto the wafer during the power on and off phases as a function of time. Experiments by Ohmori *et al* [8] showed similar trends, including negative ion generation during the afterglow.

In this chapter, we build on these prior works by discussing results from a computational investigation of ion energies produced in pulsed DF-CCPs sustained in a Ar/CF<sub>4</sub>/O<sub>2</sub> when varying the blocking capacitance. We found that ion energies averaged over the pulsed period extend to higher values when pulsing the high frequency (*HF*) power compared to pulsing the low frequency (*LF*). Depending on the size of the blocking capacitor (BC), the self-generated dc-bias voltage may be modulated during the pulse period. As a result, the IED incident onto the wafer may be a function of the size of BC during pulsed operation. Varying the size of BC then provides an additional means for controlling the IED.

The model used in this study is described in Sec. 6.2. The plasma properties in pulsed DF-CCP are discussed in Sec. 6.3 and the control of IED is discussed in Sec. 6.4. Our concluding remarks are in Sec. 6.5.

## 6.2 Description of the Model

The model used in this investigation is a two-dimensional fluid hydrodynamics simulation, the Hybrid Plasma Equipment Model (HPEM), which combines separate modules

which address different physical phenomena.[9] Using drift-diffusion fluxes derived using the Sharffeter-Gummel formulation [10], continuity equations are integrated for electrons. These equations are solved coincident with a semi-implicit solution of Poisson's equation. All electron transport coefficients and rate coefficients for electron impact collisions are provided by the EETM using the eMCS.[11] Since heavy species (charged and neutral) transport is obtained by solving fluid equations in the FKPM, the energy and angular distributions of these species are not directly available. These distributions incident onto the substrate are calculated using Monte-Carlo techniques in PCMCM.[12]

For *CW* excitation, the IEDs of particles striking the wafer are recorded after the last iteration of the HPEM. During pulsed operation, statistics are collected over many iterations during the last pulse period in order to resolve IEDs as a function of time during the pulse period. The ion energy and angular distributions (IEADs) are then averaged over the pulse period for display here.

For the DF-CCP investigated here, *HF* power is applied to the upper electrode and *LF* power is applied to the lower electrode on which the wafer sits. A pulse power waveform is specified by the voltage amplitude, PRF, and duty-cycle. It is common in actual operation of a plasma tool to specify the power and adjust the voltage to deliver that power. Unfortunately, doing so makes it difficult to make side-by-side comparisons of IEDs when varying other parameters. So in this investigation, the voltage is specified for each frequency. In order to resolve the *RF* cycle of both frequency, the fundamental time step is chosen to be less than 0.0025 of the period corresponding to the highest applied frequency ( $6.25 \times 10^{-11}$  s for 40 MHz). The time step may be further reduced to satisfy the Courant limit. A blocking capacitor is in series with the *LF* electrode and a time dependent dc-bias is obtained by a real time integration

of the collected current. The value of dc-bias is updated every *RF* cycle of the low frequency (0.1  $\mu$ s at 10 MHz).

We investigated IEDs and fluxes onto the wafer in pulsed DF-CCP using an Ar/CF<sub>4</sub>/O<sub>2</sub> = 75/20/5 gas mixture at 40 mTorr and 200 sccm. The species in the simulation are Ar, Ar<sup>+</sup>, Ar(4s) metastable, Ar(4s) radiative, Ar(4p, 5d), CF<sub>4</sub>, CF<sub>3</sub>, CF<sub>2</sub>, CF, C, F, F<sub>2</sub>, C<sub>2</sub>F<sub>4</sub>, C<sub>2</sub>F<sub>6</sub>, CF<sub>3</sub><sup>+</sup>, CF<sub>2</sub><sup>+</sup>, CF<sup>+</sup>, C<sup>+</sup>, F<sub>2</sub><sup>+</sup>, F<sup>+</sup>, CF<sub>3</sub><sup>-</sup>, F<sup>-</sup>, O<sub>2</sub>, O<sub>2</sub>(<sup>1</sup> $\Delta$ ), O<sub>2</sub><sup>+</sup>, O, O(<sup>1</sup>D), O<sup>+</sup>, O<sup>-</sup>, COF, COF<sub>2</sub>, CO<sub>2</sub>, FO, SiF<sub>4</sub>, SiF<sub>3</sub>, and SiF<sub>2</sub>. The reaction mechanism is discussed in Ref. [13]. For calculation of the IEDs, all 8 ions except for C<sup>+</sup> (negligible concentration) are included in the PCMCM.

### 6.3 Plasma Properties of Pulse Powered DF-CCP with Constant Voltage

The 2-dimensional, cylindrically symmetric reactor used in this investigation is schematically shown in Fig. 6.1a. The lower electrode serves as the substrate which is powered at a *LF* of 10 MHz. A conductive Si wafer ( $\epsilon/\epsilon_0 = 12.0$ ,  $\sigma = 0.01 \Omega^{-1} \text{ cm}^{-1}$ ), 30 cm in diameter, sits in electrical contact with the substrate. The upper electrode, 36 cm in diameter, is powered at a *HF* of 40 MHz. The *HF* electrode serves as the shower head through which gas is injected. Both electrodes are surrounded by a dielectric ( $\epsilon/\epsilon_0 = 8.0$ ,  $\sigma = 10^{-6} \Omega^{-1} \text{ cm}^{-1}$ ). All other surfaces in the reactor are grounded metal including the annular pump port. The gap between the two electrodes is 4 cm. All of the surfaces facing the plasma have the same secondary emission coefficient  $\gamma = 0.15$  for ion bombardment.[14] Both electrodes are powered at constant voltage.

A single blocking capacitor is used in the circuit whose value is varied from 10 nF to 1  $\mu$ F. The range of typical values of blocking capacitors in commercial plasma tools is from a few nF to several hundreds of nF depending on the system size and application. The BC is located between the *LF* electrode and the *LF* power supply source, as shown in Fig. 6.1b. The current

collected by the *LF* electrode is directed to the plasma facing plate of the BC. The current collected by all other metal surfaces in the reactor is directed through ground to the *LF* power supply facing plate of the BC. In practice, a control surface is placed at the edge of all metal surfaces. The average current over an *RF* cycle having period  $\tau$  through that control surface with surface normal  $\hat{n}$  to an electrode (or metal material) is then

$$\bar{I} = \frac{-1}{\tau} \int_0^\tau \left( \sum_i q_i \bar{\phi}_i (1 + \gamma_i) + \sum_i q_e \bar{\phi}_i \gamma_i + \varepsilon \frac{d\bar{E}}{dt} \right) \cdot \hat{n} dt, \quad (6.1)$$

where the first sum is over ions (and electrons) having charge  $q_i$ , incident flux  $\bar{\phi}_i$  and electron secondary electron emission coefficient  $\gamma_i$ , the second sum is for neutral particles and photons producing secondary electrons, and  $\varepsilon$  is the permittivity in the material adjacent to the metal surface (which may not be plasma).  $\hat{n}$  is the normal to the surface. Here, positive current for a given electrode is defined as positive charge flowing into the surface. The currents are collected over a single low frequency cycle and the dc bias is then incrementally updated. This results in discrete changes in the dc bias in the figures discussed below.

The base case operating conditions are 40 mTorr of an Ar/CF<sub>4</sub>/O<sub>2</sub> = 75/20/5 mixture with the amplitude of both the *LF* (10 MHz) and the *HF* (40 MHz) being 250 V. Either the *LF* or *HF* power can be delivered in a pulsed format. The rise (or decay) time of the *power-ON* (or *power-OFF*) period is 500 ns. The base case pulsing properties are 50 kHz PRF (pulse period 20  $\mu$ s) and 25% duty-cycle. For parametric investigations, the PRF was varied from 50 kHz to 250 kHz and the duty-cycle was varied from 25% to 75%. Since two frequencies are applied to separate electrodes, *CW* means that both *HF* and *LF* powers are applied in *CW* mode and *pulsed* means that one of these powers is operated in pulsed mode while the other remains in *CW* mode. In order to isolate the effects of pulsing the *LF* and *HF*, only one of the powers is pulsed at a time.

Electron density,  $n_e$ , and electron temperature,  $T_e$ , are shown in Fig. 6.2 at different times during the pulse period for the base case conditions of when pulsing the *HF* power.  $n_e$  and  $T_e$  are shown in Fig. 6.3 for pulsing the *LF* power. The modulation of  $n_e$  and  $T_e$  is greater when pulsing *HF* power than when pulsing the *LF* power, a consequence of the higher efficiency of electron heating at the higher frequency. When pulsing the *HF*, the maximum  $n_e$  increases from  $1.1 \times 10^{11} \text{ cm}^{-3}$  at the start of the *power-ON* period to  $1.6 \times 10^{11} \text{ cm}^{-3}$  at the end. The more efficient stochastic electron heating by the *HF* raises  $T_e$  to 2.9 eV in the bulk and to 5.1 eV in the *HF* sheath. Prior to applying the *HF* power,  $T_e$  in the bulk plasma is as low as 0.6 eV and only 1.3 eV adjacent to the sheaths. This value of  $T_e$  is enabled, in part, by the continuous background ionization by secondary electrons produced by the *LF* bias. When pulsing the *LF*,  $n_e$  remains at  $1.5 - 1.6 \times 10^{11} \text{ cm}^{-3}$  while  $T_e$  has only a nominal increase from 0.4 eV to 0.9 eV in the bulk and to 2.4 eV in the sheath.

Pulsing the *HF* produces a more uniform plasma, particularly during the *power-ON* phase. During the *HF power-OFF* period (when only the *LF* power is on),  $T_e$  adjacent to electrodes is about 1.3 eV, as shown in Fig. 6.2a. During *LF power-OFF* period (when only *HF* power is on),  $T_e$  adjacent to electrodes is about 1.9 eV, as shown in Fig. 6.3a. Due to the higher rate of stochastic heating by the *HF*, the  $T_e$  during the *power-OFF* cycle is larger when pulsing the *LF* (when the *HF* is on) than pulsing the *HF* (when the *LF* is on). For this reason, the electron density is larger during the *LF power-OFF* period.

At the start of the *power-ON* cycle,  $T_e$  momentarily increases (overshoots) its steady state value. This is due, in part, to the bulk electrons having drifted closer to the electrode during the power off period due to the reduction in the sheath thickness resulting from the lack of the applied voltage. Upon ramp up of the voltage at the start of the *power-ON* phase, these electrons

are heated by the progressively expanding sheath thickness. The amount of overshoot is larger with pulsing  $HF$  as the sheath velocity is higher.

#### **6.4 Control of the IED in Pulse Powered DF-CCP using Blocking Capacitance**

Due to the time varying current collected by the electrodes during the pulse period, the spatial variation of the current and the finite size of the BC, the self dc-bias may be modulated during the pulse period. The degree of modulation is determined in large part by the size of the BC. Larger BCs require longer periods to initially charge to a quasi-dc voltage, but then also require larger differential current to change that voltage. As a result, there is less modulation during the pulse period. Small BCs rapidly charge to their quasi-dc voltage, but that voltage is more sensitive to small changes in differential current. Since the differential current is a function of the pulse power waveform, the time dependence of the dc-bias will also be a function of the pulse power waveform for a given size of the BC.

For example, the plasma potential and voltage on the BC are shown in Fig. 6.4 when pulsing the  $HF$  for a PRF of 50 kHz and duty-cycle of 25%. Although difficult to discern in the figure due to plotting resolution, the plasma potential has oscillations at both the  $HF$  and  $LF$ . For  $CW$  excitation, the dc-bias is  $-48$  V. Upon application of  $HF$  power with a BC of 10 nF, the dc-bias spikes from  $-75$  V to  $5$  V, which accompanies an increase in the plasma potential to  $250$ - $275$  V. Upon termination of the  $HF$  power, the dc-bias falls to  $-200$  V before recovering to about  $-85$  V during the afterglow. Note that for this particular set of conditions and for this small value of BC, the dc-bias oscillates between  $-65$  V and  $-100$  V on a  $LF$  cycle to  $LF$  cycle basis during the  $HF$  afterglow. This is an effect that is magnified by the model which changes the dc-bias only on a  $RF$  cycle-by-cycle basis. The oscillation is nevertheless indicative of the sensitivity of the dc-bias to the size of the BC. Only the rf-cycle average dc-bias is plotted for clarity by omitting

the oscillation during the afterglow period. When the BC is increased to 1  $\mu\text{F}$ , the oscillation of the dc-bias during the pulse period is significantly reduced, in this case to only  $\pm 15$  V. This difference in behavior of the dc-bias is largely due to the different RC (resistance  $\times$  capacitance) constant of the circuit. This variation in dc-bias during a pulse period has been noted by Agarwal *et al.* [15].

The plasma potential and voltage on the BC are shown in Fig. 6.5 when pulsing the *LF* for a PRF of 50 kHz and duty-cycle of 25%. When pulsing the *LF*, the time averaged dc-bias is positive, which implies that the *CW HF* electrode is collecting more current. With the smaller BC (10 nF) the change in current at the onset of the *LF* pulse restores high current collection on the *LF* electrode and results in the dc-bias transitioning from +75 V to -55. (The RC time constant based on resistance of the plasma is about 0.3  $\mu\text{s}$ .) Upon cessation of the *LF* pulse, the dc-bias returns to positive values. With the larger BC (1  $\mu\text{F}$ ) and longer RC time constant (about 30  $\mu\text{s}$ ) the dc-bias has a smaller amplitude of oscillation. However the transient lasts almost the entire *LF* pulsed cycle. In either case, in spite of the dynamics of the dc-bias being different, the time averaged dc-bias is nearly independent of the value of the BC. The time averaged dc-bias is 44 V with 10 nF and 47 V with 1  $\mu\text{F}$ .

As a consequence of the different temporal dynamics of the dc-bias and so total bias voltage on the substrate, the IED to the substrate averaged over a pulsed cycle is a function of the value of the BC. If the value of the BC is large enough so that the RC time constant is much larger than a single *RF* period, the dc-bias should be constant and independent of the value of the BC. For example, time averaged IEDs for all ions (including  $\text{CF}_3^+$ ,  $\text{CF}_2^+$ ,  $\text{CF}^+$ ,  $\text{F}_2^+$ ,  $\text{F}^+$ ,  $\text{O}_2^+$ ,  $\text{O}^+$ , and  $\text{Ar}^+$ ) are shown in Fig. 6.6a for *CW* excitation with a BC of 10 nF and 1  $\mu\text{F}$ . The IED does not have the typical bi-modal appearance. This results from the IED being the sum of the

individual distributions for ions of different masses, the non-steady dc bias, ions responding to both frequencies and responding to the multi-frequency Fourier components resulting from pulsing. These shapes are discussed below. The IEDs are insensitive to the size of the BC in CW operation since the size of the BC only determines the initial charging time. (We note that it is possible that the dc-bias could vary during a single *RF* period if the value of the BC is small enough, however that is typically not the case in industrial practice.)

IEDs are shown in Fig. 6.6b and 6.6c for pulsing the *HF* and *LF* for a PRF of 50 kHz. When pulsing the *HF*, the IEDs extend to both higher and lower energy compared to the CW cases. The smaller BC produces a larger dynamic range of the IED, reaching a higher energy. Recall that the instantaneous sheath potential on the substrate is approximately  $V_S = V_P - V_{dc}$ , where  $V_P$  is the plasma potential and  $V_{dc}$  is the dc-bias. The change in IED behavior has at least two origins. The first is the increase in plasma potential during the *HF* pulse which increases  $V_S$ . The increase in plasma potential is both instantaneous and averaged over the *RF* cycle. The second is the transient in  $V_{dc}$  to more negative values which also increases  $V_S$ . The dynamic range of the dc-bias is larger with a smaller BC – the lowest dc-bias is -200 V with 10 nF and -100 V with 1  $\mu$ F. Nevertheless, the maximum ion energy with a BC of 10 nF is 280 eV which is only 20 eV larger than with 1  $\mu$ F in spite of the dc-bias being 100 V more negative. The dynamics of the plasma potential and dc-bias are such that the most negative dc-bias also occurs when the plasma potential is at its minimum value when only the *LF* is on. (See Fig. 6.4.) As a result,  $V_S = V_P - V_{dc}$  does not significantly increase during this time. On the other hand, when the *LF* power is pulsed, the opposite scenario occurs.

Pulsing *LF* power produces a sharp peak at low energy and a broad peak at high energy in the IED. These peaks are sensitive to the BC. The low energy peak results from ions

collected from that portion of the pulse period when the *LF* voltage is off and the plasma potential oscillates only at the *HF*. Since the *HF* is above the ion response frequency (ion plasma frequency is about 10 MHz for argon ions and 17 MHz for oxygen ions), a single low energy peak in the IED is produced. The high energy peak results from ions collected during that portion of the pulsed period when the *LF* voltage is on, the plasma potential is larger and the dc-bias is more negative (or less positive). The IED with the smaller BC (10 nF) extends to 250 eV, a consequence of the dc-bias cycling to more negative (or less positive) values, thereby producing a larger  $V_S$ . The IED with the larger BC (1  $\mu$ F) extends to only 180 eV, a consequence of the dc-bias having a smaller dynamic range thereby producing a smaller  $V_S$ . The location of the low energy peak is determined by the difference of the *HF* produced plasma potential and dc-bias after the *LF* pulse. Since the smaller BC responds more quickly to the change in plasma properties, the dc-bias is both more negative during the pulse and more positive after the pulse. Therefore  $V_S$  is smaller after the pulse and the IED peaks at lower energy.

Controlling the shape of IED can also be achieved by adjusting the pulse power parameters such as PRF and duty-cycle. The IEDs for all ions with different PRFs are shown in Fig. 6.7 for large and small BCs when pulsing the *HF* power. The corresponding dc-biases are shown in Fig. 6.8 as a function of the normalized time, which is time divided by the length of the pulse period. The width of the IED and its shape can be controlled for a given BC by changing PRF – or for a constant PRF, by varying BC. However, the relationship between PRF for a given BC and the maximum ion energy is non-monotonic. These trends depend on the details of the ions responses to the Fourier components of the bias that result from the pulsing. For a given PRF, the dc-bias changes over a larger dynamic range during the pulse period with the smaller

BC. The heavier ions tend to respond to the time averaged sheath potential and so do not reflect the full dynamic range of the dc-bias. As a result the IED tends to have a single major peak with smaller wings to higher and lower energy. With the larger BC, the dc-bias varies more slowly during the pulse cycle which enables the heavier ions to respond to the change in  $V_S$ , and so produce more structure to the IED.

For a given value of BC, the IEDs tend to have less structure with higher PRF since the heavier ions are not able to respond to the dynamics of the dc-bias during the shorter pulse period. With the smaller BC and smaller RC time constant, the dc-bias spikes at the leading edge of *HF power-ON*, as shown in Fig. 6.8a. This spike is suppressed at higher PRF due to the shorter inter-pulse period. With the higher PRF and shorter afterglow period, the dc-bias does not have enough time to recover back to what would be a *CW* value. The oscillation of dc-bias during the pulse period decreases as the BC increases due to the larger RC time constant. The magnitude of the oscillation also decreases with larger PRF due to the shorter inter-pulse period. It is natural to associate the IED obtained with high PRF with the IED obtained with *CW* excitation. While that is certainly true for very high PRF and large values of BC, the dynamics of the dc-bias with small values of BC make the IEDs even for a PRF of 250 kHz significantly different than those of *CW* excitation.

The IEDs for different ions ( $O^+$ ,  $Ar^+$  and  $CF_3^+$ ) are shown in Fig. 6.9 for small (10 nF) and large (1  $\mu$ F) BCs when pulsing the *HF* with a PRF of 50 kHz. Due to the different transit times through the sheath, there are differences in the IEDs between  $O^+$ ,  $Ar^+$  and  $CF_3^+$ . The  $O^+$  (16 amu) has a broader IED compared to  $CF_3^+$  (69 amu) as its lower mass makes it more sensitive to time dependent variations in the sheath potential. The IEDs for the heavier ions ( $Ar^+$  and  $CF_3^+$ ) track each more closely for a given BC. The IED for the lighter ion ( $O^+$ ) better

reflects the maximum and minimum in  $V_S$  during the pulse period. A portion of these differences in IEDs is likely due to the source functions of  $O^+$ ,  $Ar^+$  and  $CF_3^+$  being different during the pulse period. As a result, these different ions arrive at the sheath edge and are preferentially accelerated into the sheath when the dc-bias has different values.

When pulsing the *LF*, the general shapes of the IEDs are retained when changing PRF, as shown in Fig. 6.10. The dc-bias for these cases is shown in Fig. 6.11 as a function of the normalized time. The dynamic range of the oscillation in the dc-bias is from -40 to +80 V with the smaller BC (10 nF). The dynamic range with the larger BC (1  $\mu$ F) is at most +30 to +60 V. In both cases, the time dependence of the dc-bias is about the same between different PRFs. Consequently, the IEDs are relatively insensitive to the PRF for a given BC. The most significant variation in the IED occurs when changing the BC. The IEDs with the smaller BC extend to higher energy, reflecting the larger momentary  $V_S$  that occurs when the dc-bias cycles to more negative values during the *LF* pulse.

IEDs for  $O^+$ ,  $Ar^+$  and  $CF_3^+$  are shown in Fig. 6.12 for different BCs when pulsing the *LF* with a PRF of 50 kHz. Due to its smaller mass,  $O^+$  has a broader IED than  $Ar^+$  and  $CF_3^+$ . Counter to what one would expect based only on their masses, the IED for  $Ar^+$  is shifted towards lower energy in the tail of the IED compared to  $CF_3^+$ . This counter-intuitive trend is likely due to the source functions for different ions having different time dependencies during the pulse period and being formed at different distances from the sheath edge.

The IEDs for all ions with different duty-cycles are shown in Fig. 6.13 when pulsing the *HF* power with a PRF of 50 kHz and with BCs of 10 nF and 1  $\mu$ F. The dc-biases for these conditions are shown in Fig. 6.14. In all cases, with the onset of the *HF* pulse, the dc-bias increases to more positive values before settling to a more positive but still negative dc-bias. In

the case of the smaller BC, the dc-bias actually momentarily becomes positive. When the *HF* power is terminated, the dc-bias returns to its initially more negative value as would be expected for single *LF* operation. Although the range in energy of the IEDs does not significantly change when changing the duty-cycle, the shapes of the IEDs are sensitive to duty-cycle. The range in energies results from the maximum and minimum values of  $V_S = V_P - V_{dc}$ , which does not significantly vary with duty-cycle. The details of the structure of the IEDs depend on the time variation of  $V_S$ , which does depend on duty-cycle.

The IEDs for all ions are shown in Fig. 6.15 for different duty-cycles when pulsing the *LF* power for a PRF of 50 kHz and for BCs of 10 nF and 1  $\mu$ F. The dc-biases for these conditions are shown in Fig. 6.16. For these conditions, the dc-bias is positive when the *LF* is off (*CW HF*). When pulsing the *LF*, the dc-bias spikes to negative values. With the smaller BC, the dc-bias during the *LF power-ON* portion of the cycle is essentially the same as for *CW* operation and recovers back to positive values during the *LF power-OFF* portion of the cycle. With the smaller BC, the dc-bias is about the same value during the *LF power-ON* (-40 V) and *LF power-OFF* (80 V) portions of the cycle. As a result, the low energy and high energy portions of the IEDs have the same structure and ranges of energies for different duty-cycles. By changing the duty-cycle, the proportion of the IED in the low energy and high energy ranges can be controlled. For example, since the low energy range of the IED is produced during the *LF power-OFF* portion of the cycle, its magnitude increases with smaller duty-cycle (longer *power-OFF* period). Since the high energy range of the IED is produced during the *LF power-ON* portion of the cycle, its magnitude increases with larger duty-cycle (longer *power-ON* period).

When pulsing the *LF*, the IEDs are quite sensitive to duty-cycle when using the larger BC. The larger BC averages the time variations in the dc-bias obtained with the smaller BC. For

these conditions, the result is that the dc-bias appears to have a nearly constant value, varying by only 20-30 V, for each duty-cycle. The larger the duty-cycle, the more negative the dc-bias becomes, approaching the *CW* value. These trends are reflected in the IEDs, as shown in Fig. 6.15b. Larger duty-cycles produce IEDs which resemble those for *CW* excitation. Decreasing the duty-cycle produces a smaller  $V_S$  throughout the pulse period since the dc-bias is more positive, and this shifts the low energy peak of the IED to lower energies. The magnitude of the low energy peak increases with smaller duty-cycle. This trend results from the plasma potential being supported by only the *HF* during a larger fraction of the pulse period, and so  $V_S = V_P - V_{dc}$  is at its minimum value for a longer fraction of the period.

## 6.5 Concluding Remarks

The properties of IEDs in pulse powered DF-CCPs sustained in an Ar/CF<sub>4</sub>/O<sub>2</sub> mixture have been computationally investigated using results from a 2D plasma hydrodynamics model. We found that varying the size of the blocking capacitor (BC) is an additional variable which provides flexibility in controlling the shape of the IEDs. The maximum ion energy tends to increase with smaller BC as the dc-bias travels through a larger dynamic range over the pulse period when pulsing either the *LF* or *HF*. When pulsing the *LF*, lower ion energies are preferentially produced during the *power-OFF* period of the *LF* when only the *HF* is on regardless of the size of the BC. When pulsing the *HF*, higher ion energies are preferentially produced during the *power-ON* period of the *HF* regardless of the size of the BC. However, the dynamics and details of the shape of the IEDs depend on the value of the BC. The shape of the IED is further a function of the PRF and duty-cycle of the pulse period, and depends on whether the *LF* or *HF* is pulsed. When pulsing the *HF*, higher PRF and smaller duty-cycle tend to produce higher energy ions. When pulsing the *LF*, PRF does not have a large effect on the shape

of the IED, however duty-cycle does affect the shape of the IED, and more so with larger BC. The maximum values of ion energies are not necessarily monotonically dependent on, for example, PRF for a given BC since the IEDs depend on the details of the ion response to the Fourier components of the bias that result from the pulsing. These conclusions are based on the total IED for all ions – there is additional variation and control that depends on the individual masses of the ions. The individual spikes in the total IED can be correlated with the individual response of different ions to the Fourier components of the time variation in the dc-bias.

Our results also depend on the details of the matching networks used with the plasma tool. Our circuit model has purposely been chosen to be simple in order to make as direct connection between the change in the dc bias and the plasma properties. Having said that, commercial matching networks will attempt to compensate for the changing plasma impedance during the pulsed period, and part of that compensation may be to change the effective serial capacitance. To unambiguously control the IEDs, needs to be controlled, effective blocking capacitance, and this may compromise the ability to optimally match during pulsed operation.

## 6.6 Figures

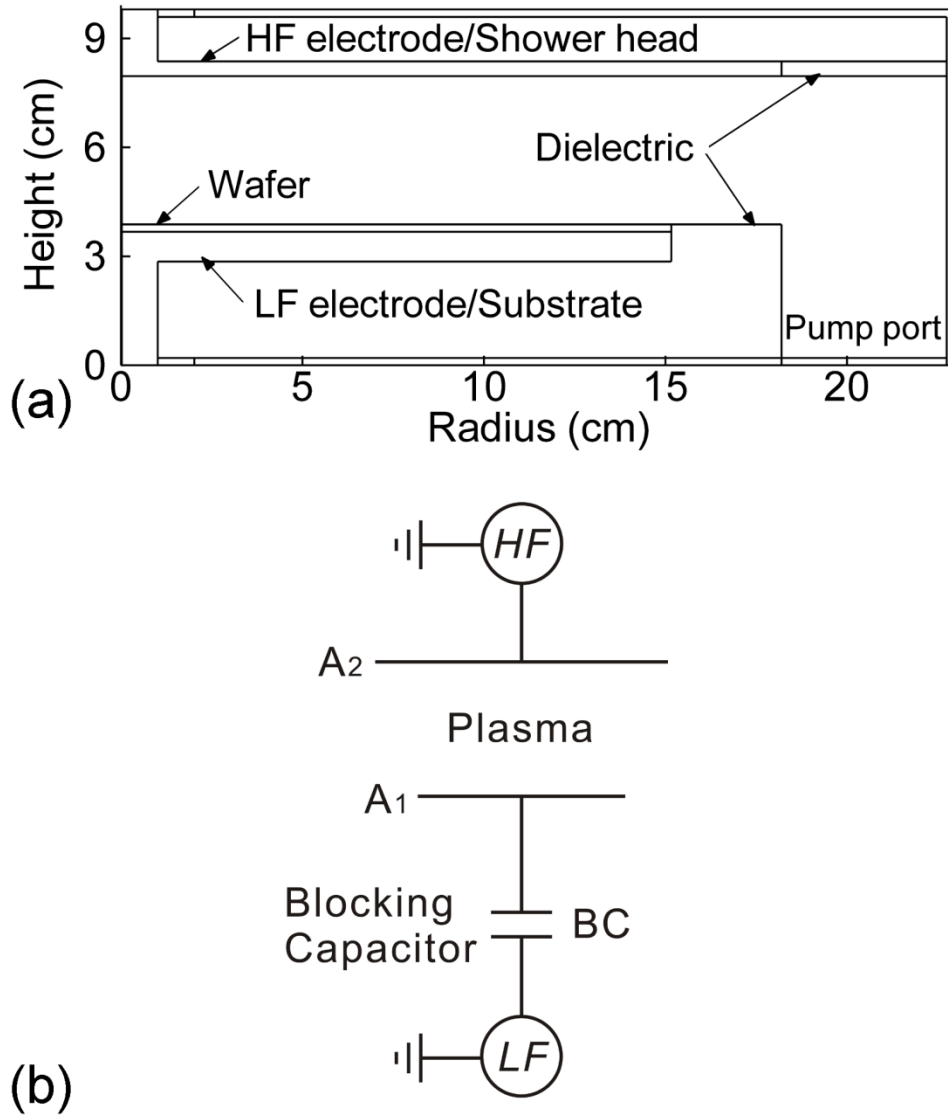


Fig. 6.1 Operating system for this investigation. (a) Geometry of the DF-CCP chamber. The *LF* (10 MHz) is applied on the lower electrode, and the *HF* (40 MHz) is applied on the upper electrode. One of the two frequencies is operated in pulse mode with a few tens of kHz PRF. (b) Electrical schematic for the DF-CCP system. The blocking capacitor (BC) is connected in series with the lower electrode.

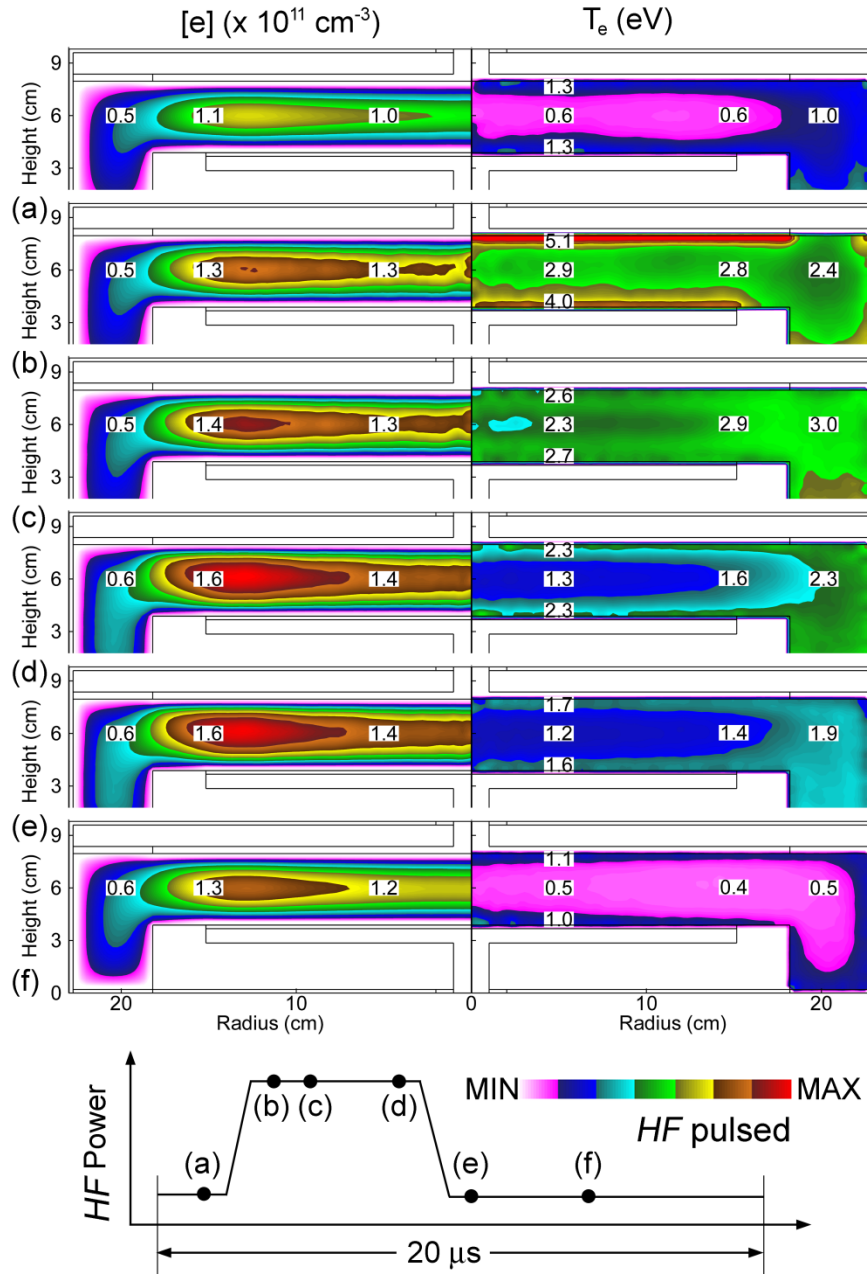


Fig. 6.2 Electron density (left) and temperature (right) when pulsing the  $HF$  power at different times during the pulsed cycle (as indicated in the lower figure). ( $\text{Ar}/\text{CF}_4/\text{O}_2 = 75/20/5$ , 40 mTorr, 200 sccm,  $LF = 250 \text{ V}$  at 10 MHz CW,  $HF = 250 \text{ V}$  at 40 MHz in pulse mode with  $BC = 1 \mu\text{F}$ ,  $\text{PRF} = 50 \text{ kHz}$  and duty-cycle = 25%) The electron density is modulated by about 30% during the pulse cycle while the electron temperature shows nearly instantaneous changes as the  $HF$  power toggles on and off, especially near the sheaths due to enhanced stochastic heating.

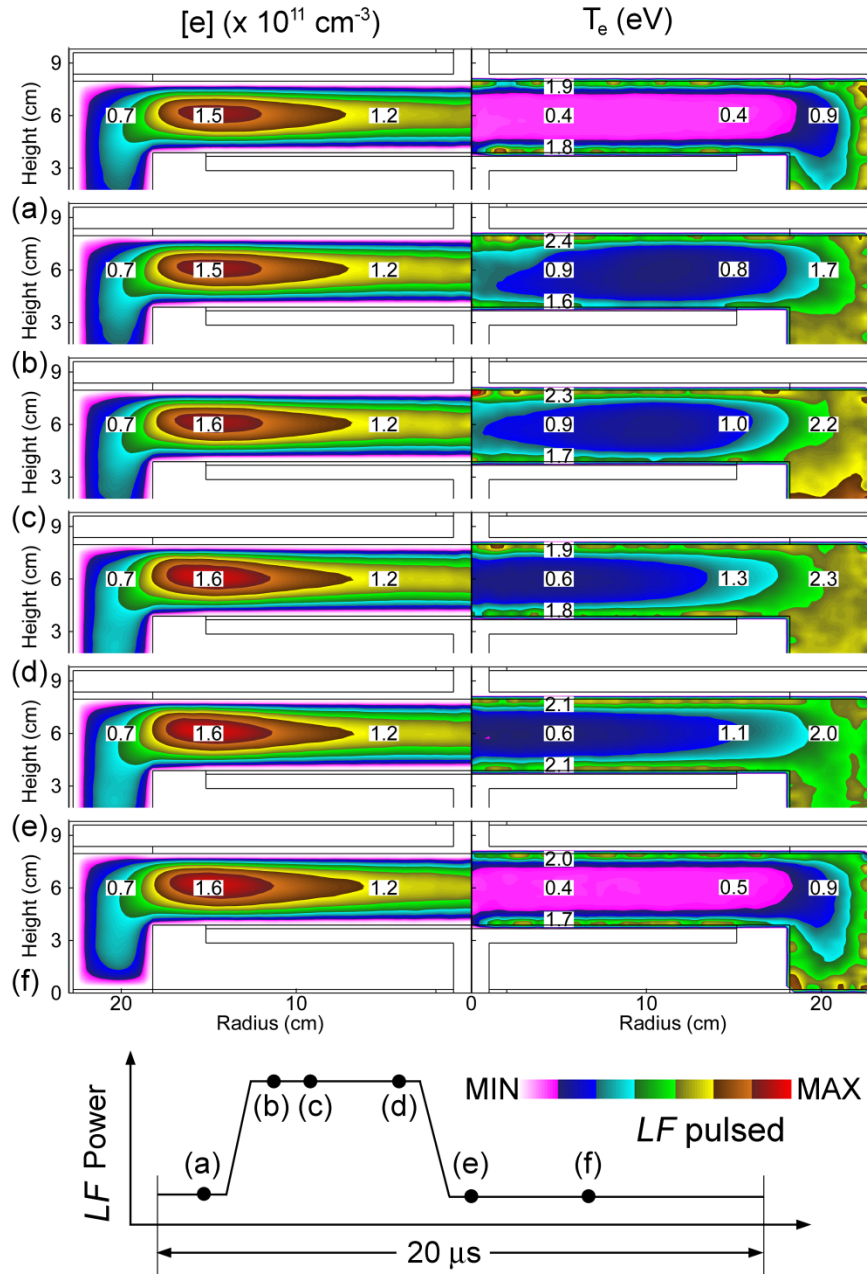


Fig. 6.3 Electron density and temperature when pulsing the  $LF$  power at different times during the pulsed cycle (as indicated in the lower figure). ( $\text{Ar}/\text{CF}_4/\text{O}_2 = 75/20/5$ , 40 mTorr, 200 sccm,  $LF = 250 \text{ V}$  at 10 MHz in pulse mode with  $BC = 1 \mu\text{F}$ ,  $\text{PRF} = 50 \text{ kHz}$  and duty-cycle = 25%,  $HF = 250 \text{ V}$  at 40 MHz CW). Pulsing the  $LF$  power produces nominal inter-cycle changes in electron density and temperature over the pulse period as the majority of the  $LF$  power is dissipated in ion acceleration.

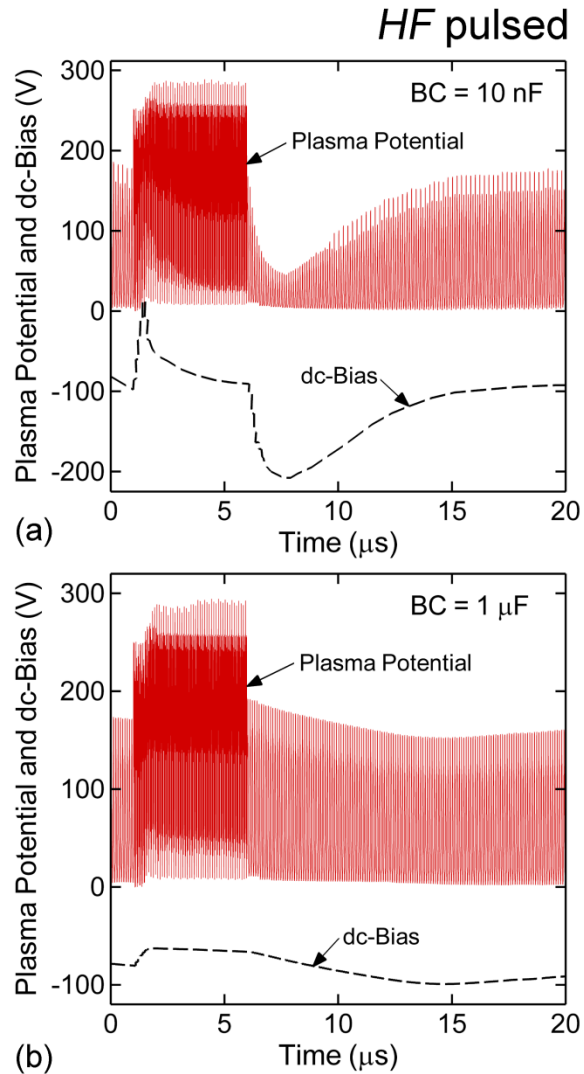


Fig. 6.4 Plasma potential,  $V_P$ , and dc-bias,  $V_{dc}$ , during one pulse period when pulsing the *HF* power (PRF = 50 kHz, 25% duty-cycle). (a)  $BC = 10 \text{ nF}$  and (b)  $BC = 1 \text{ } \mu\text{F}$ . The sheath potential is  $V_S = V_P - V_{dc}$ . The *LF* power is always on and the *HF* power is on only during the pulse window of 25%. Due to the smaller RC time constant with the small BC, the dc-bias responds more quickly. Since the voltage amplitude of the *LF* power rides on the dc-bias, the maximum envelope of the plasma potential has the same shape as the dc-bias.

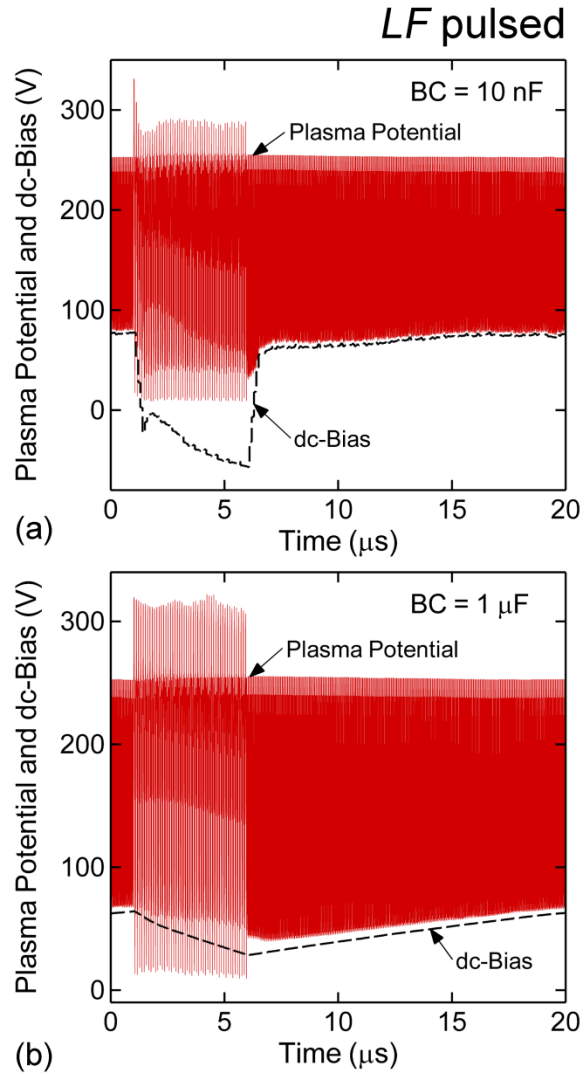


Fig. 6.5 Plasma potential,  $V_P$ , and dc-bias,  $V_{dc}$ , during one period when pulsing the *LF* power (PRF = 50 kHz, duty-cycle = 25%). (a)  $BC = 10 \text{ nF}$  and (b)  $BC = 1 \text{ } \mu\text{F}$ . The sheath potential is  $V_S = V_P - V_{dc}$ . The *HF* power is always on and the *LF* power is on only during the pulse window of 25%. The plasma potential is mainly determined throughout the pulse period by the voltage amplitude of the *CW HF* power. The dynamic range of dc-bias is larger with the smaller BC.

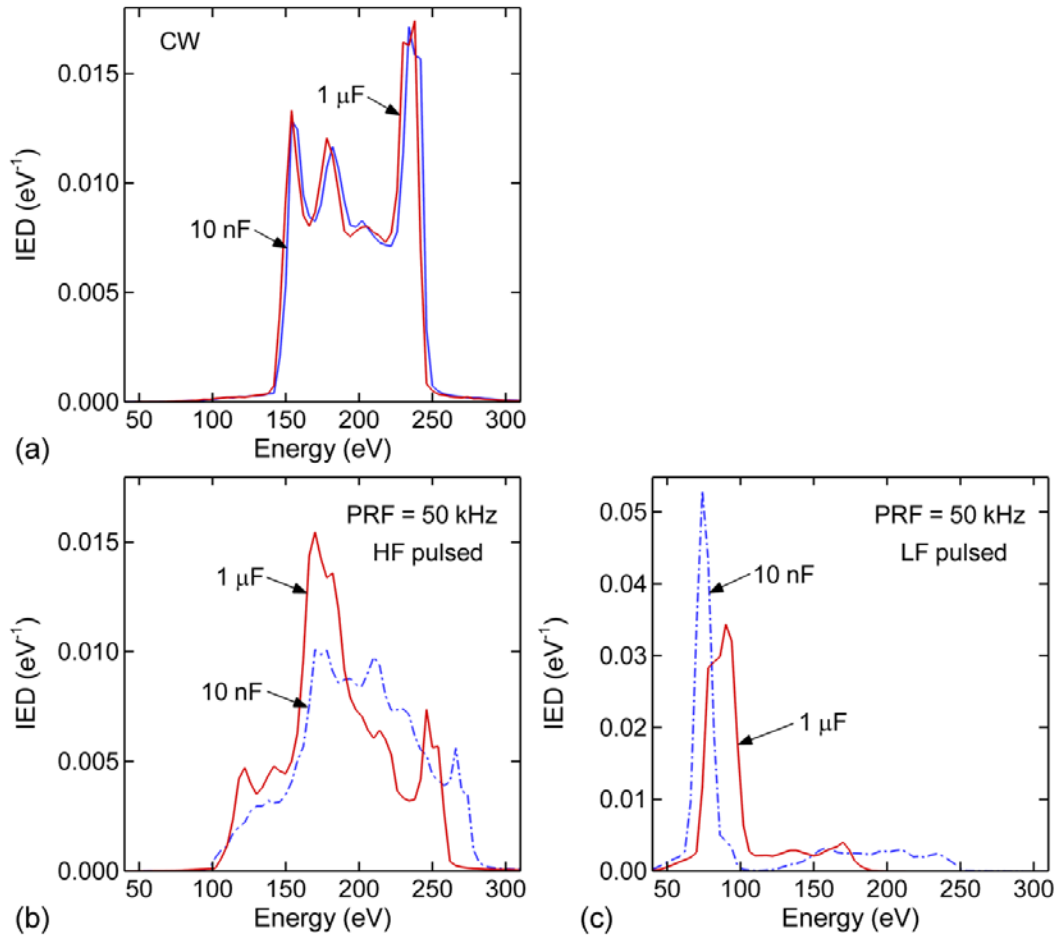


Fig. 6.6 Total IEDs for all ions with different sizes of the BC for the base case (40 mTorr, 250 V at 10 MHz, 250 V at 40 MHz). (a) *CW* operation, (b) pulsing *HF* power and (c) pulsing *LF* power. Pulsing has a PRF of 50 kHz and duty-cycle of 25%. The IED is insensitive to the size of BC with *CW* operation while its shape depends on the size of BC with pulsed operation.

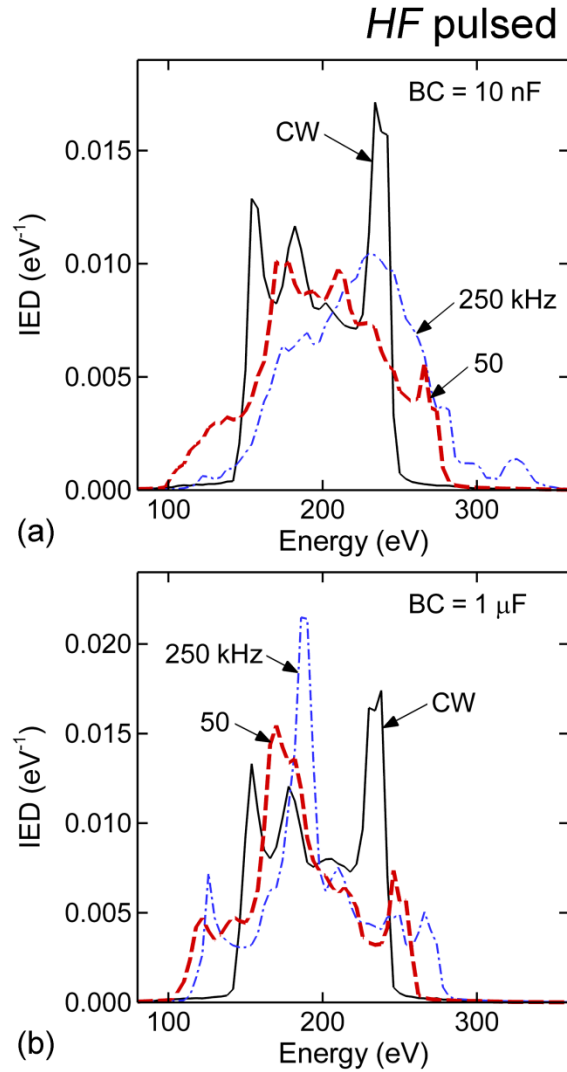


Fig. 6.7 Total IEDs for all ions for different PRFs when pulsing the *HF* power with duty-cycle of 25%. (a)  $BC = 10 \text{ nF}$  and (b)  $BC = 1 \mu\text{F}$ . The IED becomes single-peaked in appearance with the smaller BC while the IED maintains a multiple-peaked shape with the larger BC. The IEDs with larger PRFs extend to the higher energies.

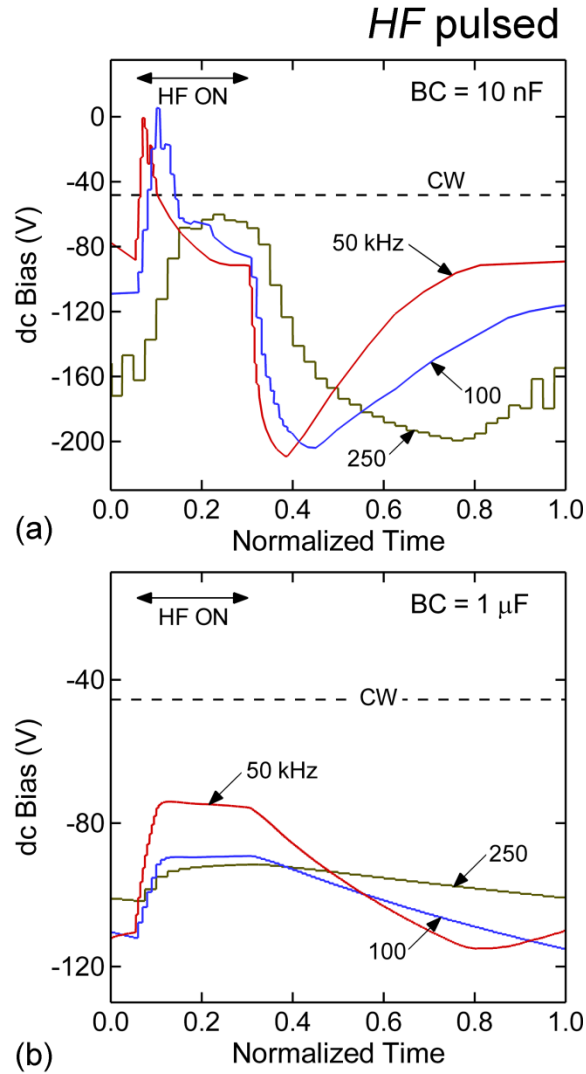


Fig. 6.8 The dc-bias as a function of normalized time (which is time divided by the length of each pulse period) with different PRFs when pulsing the *HF* power with a 25% duty-cycle. (a)  $BC = 10 \text{ nF}$  and (b)  $BC = 1 \text{ } \mu\text{F}$ . The *LF* power is *CW*. During *power-ON* period, the dc-bias becomes less negative with some overshoot with smaller PRFs.

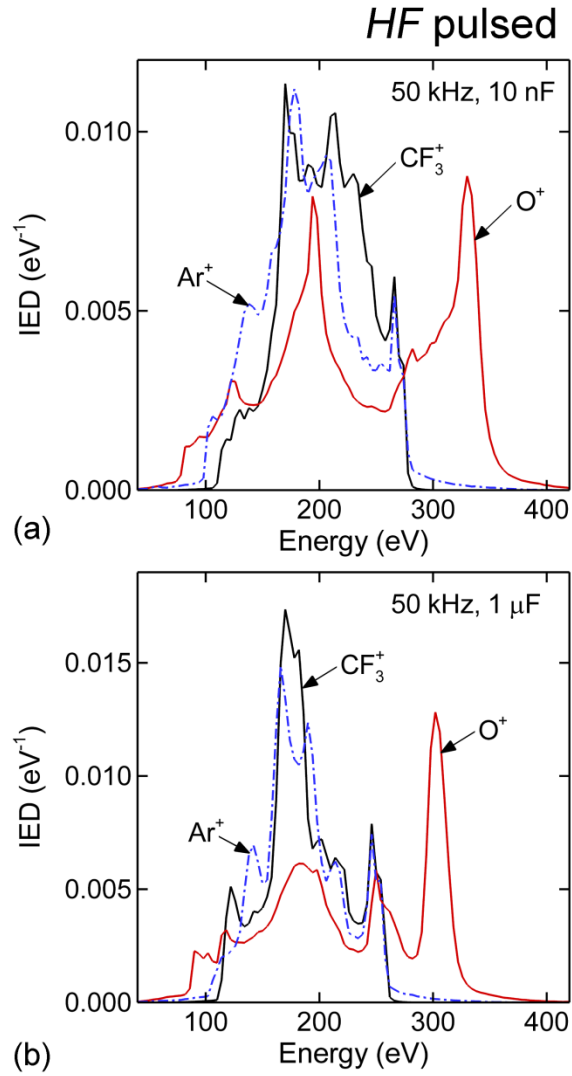


Fig. 6.9 Ion energy distributions for  $O^+$ ,  $Ar^+$  and  $CF_3^+$  when pulsing the *HF* power. (a)  $BC = 10$  nF and (b)  $BC = 1 \mu F$ .

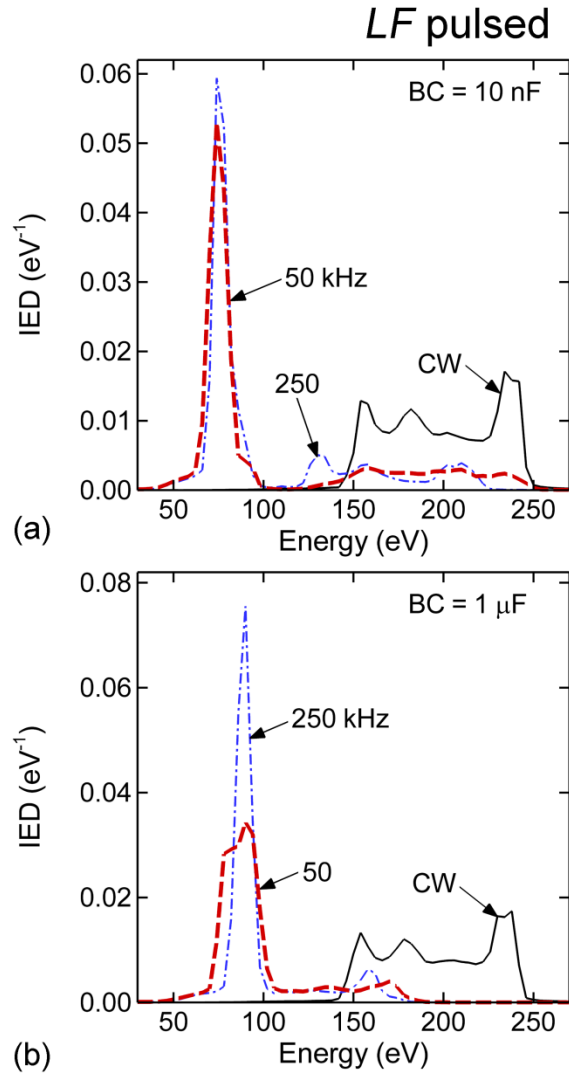


Fig. 6.10 Total IEDs for all ions for different PRFs when pulsing the *LF* power with duty-cycle of 25%. (a)  $BC = 10 \text{ nF}$  and (b)  $BC = 1 \mu\text{F}$ . The IED extends to higher energies with the smaller BC.

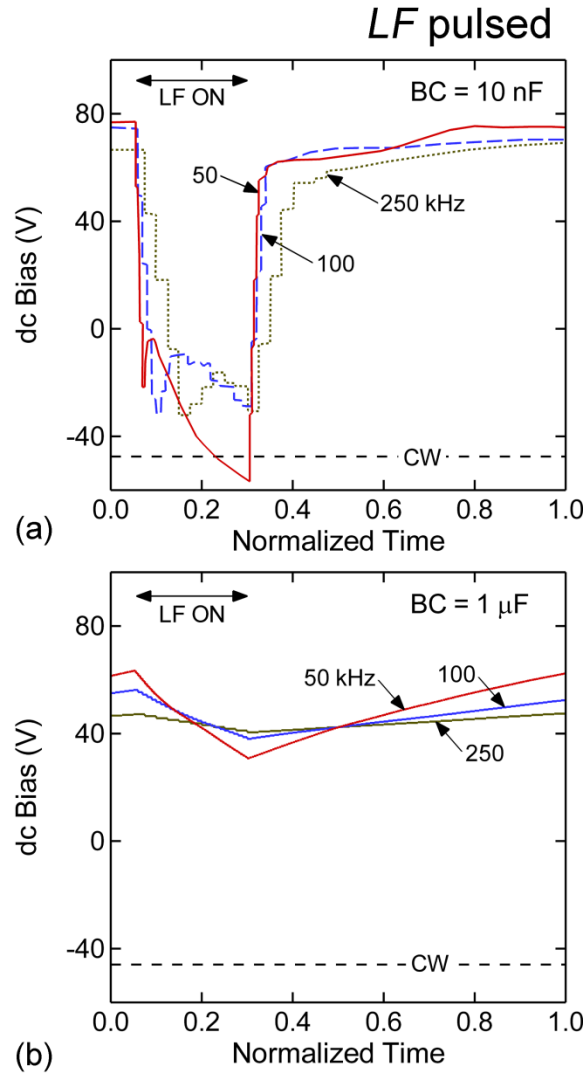


Fig. 6.11 The dc-bias as a function of the normalized time (which is time divided by the length of each pulse period) with different PRFs when pulsing the *LF* power with a 25% duty-cycle. (a)  $BC = 10 \text{ nF}$  and (b)  $BC = 1 \mu\text{F}$ . The *HF* power is *CW*. If the size of *BC* is small enough for the dc-bias to respond to the voltage on the electrode, the temporal behavior of dc-bias is similar for different PRFs.

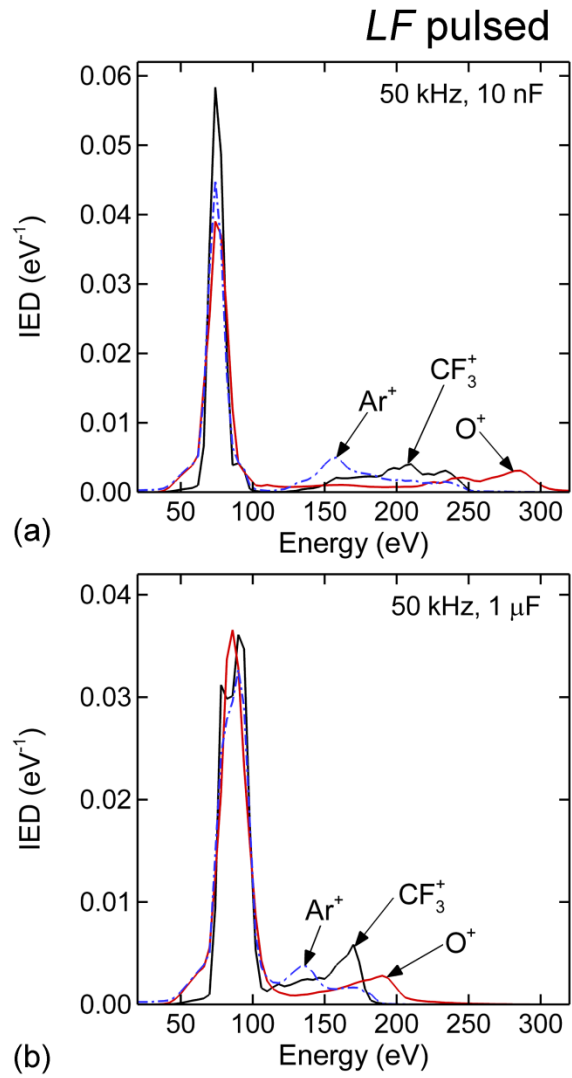


Fig. 6.12 IEDs for  $O^+$ ,  $Ar^+$  and  $CF_3^+$  when pulsing the  $LF$  power. (a)  $BC = 10$  nF and (b)  $BC = 1$   $\mu F$ .

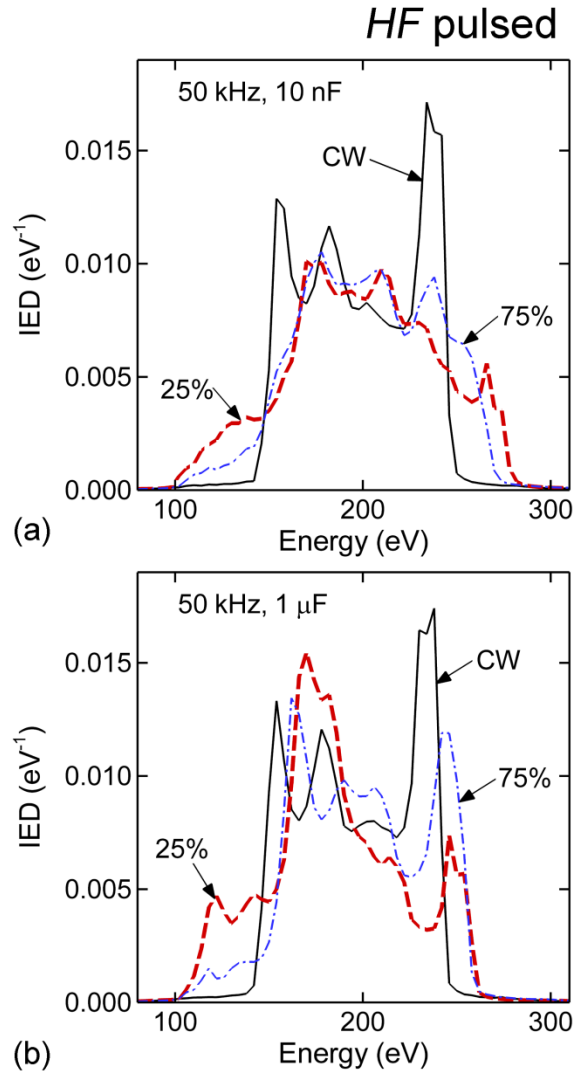


Fig. 6.13 Total IEDs for all ions for different duty-cycles when pulsing the *HF* power with a PRF of 50 kHz. (a) BC = 10 nF and (b) BC = 1 μF. The *LF* power is *CW*. The smaller duty-cycle tends to produce an extended energy range in the IED.

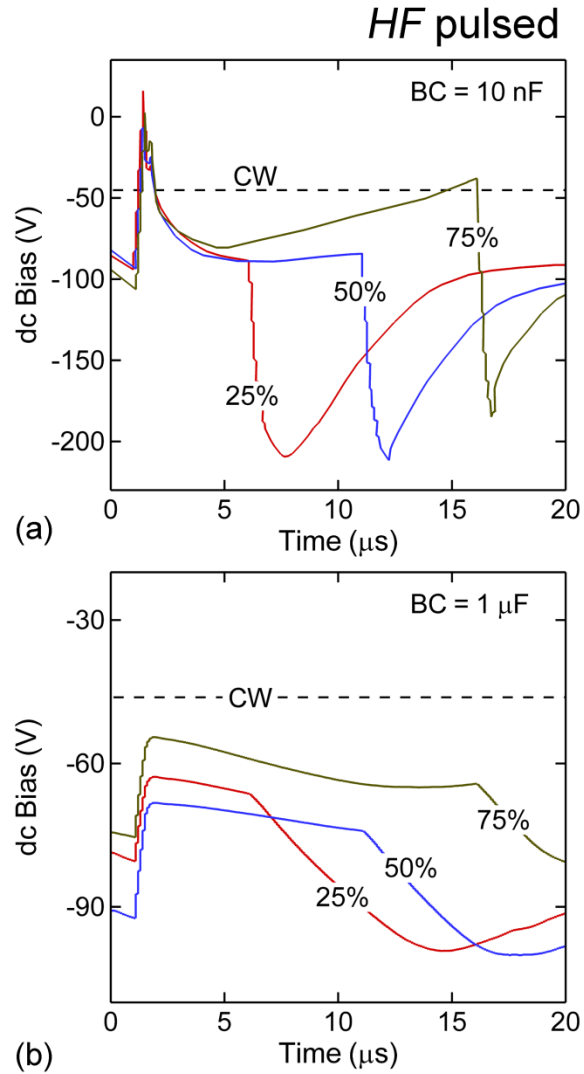


Fig. 6.14 The temporal behavior of dc-bias with different duty-cycles when pulsing the *HF* power with a PRF of 50 kHz. (a)  $BC = 10 \text{ nF}$  and (b)  $BC = 1 \mu\text{F}$ . The *LF* power is *CW*. The dynamic range of the dc-bias is from 0 V to -200 V with the smaller BC while the range is only from -60 to -90 V with larger BC.

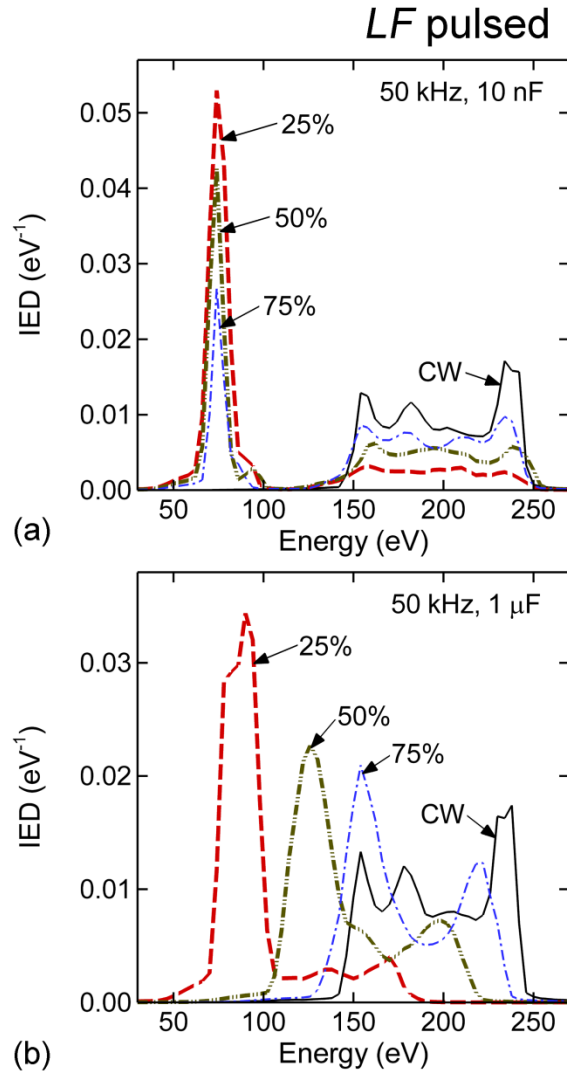


Fig. 6.15 Total IEDs for all ions for different duty-cycles when pulsing the *LF* power with a PRF of 50 kHz. (a) BC = 10 nF and (b) BC = 1  $\mu$ F. The *HF* power is *CW*. The amplitude of the low energy peak diminishes while the amplitude of the high energy peak increases as the duty-cycle increases. The IED becomes similar to that of the *CW* case with further increase of the duty-cycle.

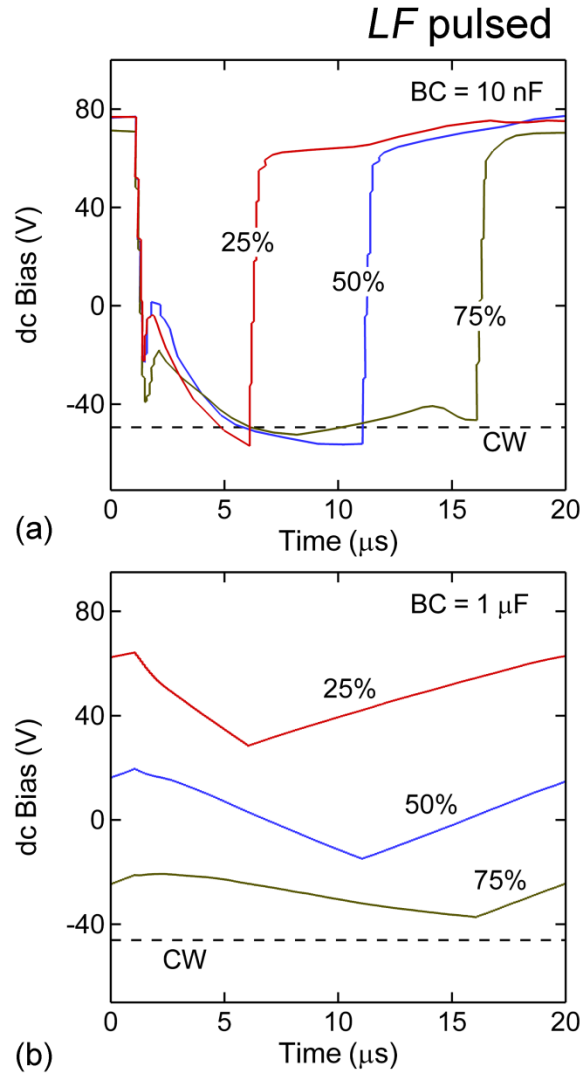


Fig. 6.16 The temporal behavior of dc-bias with different duty-cycles when pulsing the *LF* power with a 50 kHz PRF. (a)  $BC = 10 \text{ nF}$  and (b)  $BC = 1 \mu\text{F}$ . The *HF* power is *CW*. The dynamic range is from -40 to +80 V with the smaller BC while the range is at most  $\pm 15 \text{ V}$  at 25% duty-cycle with larger BC. Note that the range of oscillation the dc-bias is similar for different duty-cycles with the smaller BC while the range is shifted by duty-cycle with the larger BC.

## 6.7 References

1. R. Legtenberg, H. Jansen, M. de Boer, and M. Elwenspoek, "Anisotropic reactive ion etching of silicon using SF<sub>6</sub>/O<sub>2</sub>/CHF<sub>3</sub> gas mixtures", *J. Electrochem. Soc.* **142**, 2020 (1995).
2. H. M. Park, C. Garvin, D. S. Grimard, and J. W. Grizzle, "Control of Ion Energy in a Capacitively Coupled Reactive Ion Etcher", *J. Electrochem. Soc.* **145**, 4247 (1998).
3. A. C. Westerheim, A. H. Labun, J. H. Dubash, J. C. Arnold, H. H. Sawin, and V. Yu-Wang, "Substrate Bias Effects in High-aspect-ratio SiO<sub>2</sub> Contact Etching Using an Inductively Coupled Plasma Reactor", *J. Vac. Sci. Technol. A* **13**, 853 (1995).
4. G. S. Oehrlein, Y. Zhang, D. Vender, and O. Joubert, "Fluorocarbon High-density Plasmas. II. Silicon Dioxide and Silicon Etching Using CF<sub>4</sub> and CHF<sub>3</sub>", *J. Vac. Sci. Technol. A* **12**, 333 (1994).
5. X. V. Qin, Y.-H. Ting, and A. E. Wendt, "Tailored Ion Energy Distributions at an rf-biased plasma electrode", *Plasma Sources Sci. Technol.* **19**, 065014 (2010).
6. A. Agarwal, S. Rauf, and K. Collins, "Extraction of negative ions from pulsed electronegative capacitively coupled plasmas", *J. Appl. Phys.* **112**, 033303 (2012).
7. K. Maeshige, G. Washio, T. Yagisawa, and T. Makabe, "Functional design of a pulsed two-frequency capacitively coupled plasma in CF<sub>4</sub>/Ar for SiO<sub>2</sub> etching", *J. Appl. Phys.* **91**, 9494 (2002).
8. T. Ohmori, T. Goto, and T. Makabe, "Negative Charge Injection to a Wafer in a Pulsed Two-frequency Capacitively Coupled Plasma for Oxide Etching; Diagnostics by Emission-selected Computerized Tomography", *J. Phys. D: Appl. Phys.* **37**, 2223 (2004).
9. M. J. Kushner, "Hybrid Modeling of Low Temperature Plasmas for Fundamental Investigations and Equipment Design", *J. Phys. D* **42**, 194013 (2009).
10. D. L. Scharfetter and H. K. Gummel, "Large signal analysis of a silicon read diode", *IEEE Trans. Elec. Dev.* **16**, 64 (1969).
11. S. H. Song and M. J. Kushner, "Control of electron energy distributions and plasma characteristics of dual frequency, pulsed capacitively coupled plasmas sustained in Ar and Ar/CF<sub>4</sub>/O<sub>2</sub>", *Plasma Sources Sic. Technol.* **21**, 055028 (2012).
12. Y. Zhang, M. J. Kushner, N. Moore, P. Pribyl and W. Gekelman, "Space and phase resolved ion energy and angular distributions in single- and dual-frequency capacitively coupled plasmas", *J. Vac. Sci. Technol. A* **31**, 061311 (2013).
13. A. V. Vasenkov, X. Li, G. S. Oehrlein and M. J. Kushner, "Properties of C<sub>4</sub>F<sub>8</sub> Inductively Coupled Plasmas. II. Plasma Chemistry and Reaction Mechanism for Modeling of Ar/c-C<sub>4</sub>F<sub>8</sub>/O<sub>2</sub> discharges", *J. Vac. Sci. Technol. A* **22**, 511 (2004).

14. C. Bohm and J. Perrin, "Retarding-field analyzer for measurements of ion energy distributions and secondary electron emission coefficients in low pressure radio frequency discharges", *Rev. Sci. Instrum.* **64**, 31 (1993).
15. A. Agarwal, P. J. Stout, S. Banna, S. Rauf, and K. Collins, "Recouping etch rates in pulsed inductively coupled plasmas", *J. Vac. Sci. Technol. A* **29**, 011017 (2011).

## Chapter 7 CONTROL OF SiO<sub>2</sub> ETCH PROFILE IN PULSED CAPACITIVELY COUPLED PLASMAS SUSTAINED IN Ar/CF<sub>4</sub>/O<sub>2</sub>

### 7.1 Introduction

High aspect ratio (HAR) etching in microelectronics fabrication continues to face challenges to optimize plasma properties in order to maintain the desired critical dimensions (CD).[1] Maintaining the CD – such as a vertical angle of the sidewall during etching – requires optimizing the fluxes and energies of charged and neutral species incident onto the wafer from the plasma. A number of strategies have been developed to achieve these goals. For example, controlling etch profile and selectivity has been investigated by alternating deposition and etching steps [2], adjusting gas mixture [3–6], adjusting pressure [7], choosing different mask materials [8], tailoring the substrate bias voltage waveform [9], and employing pulsed source power [10–13] and bias power [14].

Plasma etching of dielectrics (e.g., SiO<sub>2</sub>, Si<sub>3</sub>N<sub>4</sub>) is typically performed using fluorocarbon gases such as CF<sub>4</sub> (carbon tetrafluoride), c-C<sub>4</sub>F<sub>8</sub> (octafluorocyclobutane), CHF<sub>3</sub> (trifluoromethane), CH<sub>2</sub>F<sub>2</sub> (methylene fluoride), CH<sub>3</sub>F (methyl fluoride), or C<sub>2</sub>F<sub>6</sub> (hexafluoroethane). The choice of gas can be used to tune the desired etch profile and selectivity. Oehrlein et al. explained etching behavior and selectivity of Si, SiO<sub>2</sub>, and Si<sub>3</sub>N<sub>4</sub> in fluorocarbon plasmas based on atomic fluorine and fluorocarbon (CF<sub>x</sub>, x=1 – 3) concentrations either in the

gas phase in polymer deposition.[15,16] The etch rate typically increases with higher F/C ratios, which can be achieved either by adding oxygen to react with carbon in the gas phase or by etching deposited polymer. The reduction in the thickness of the polymer layer aids in tuning the etch profile. The etch rate is decreased by lowering the F/C ratio, which can be achieved by adding H<sub>2</sub> to react with F in the gas phase, which also increases the rate of polymer deposition. For example, the selectivity of etching SiO<sub>2</sub> over resist and SiO<sub>2</sub> over Si is increased by lowering the F/C ratio of the feedstock gases, such as c-C<sub>4</sub>F<sub>8</sub>, c-C<sub>5</sub>F<sub>8</sub> (octafluorocyclopentene) and C<sub>4</sub>F<sub>6</sub> (hexafluoro-1,3-butadiene). Since the F/C ratio is a measure of the non-selective etch rate, an over-abundance of fluorine radicals typically pushes the etch profile toward being isotropic, and reduces the selectivity between photoresist (PR) and SiO<sub>2</sub>.

From the perspective of the plasma generation mechanism, a number of strategies have been attempted to control the flux and energy of electrons and ions to the wafer to produce desired etching properties. Plasmas used in etching processes are typically classified by the frequency of the power (microwave 2.45 GHz or radio-frequency 13.56 MHz) and coupling type (inductive or capacitive). Radio-frequency (*RF*) plasmas include inductively coupled plasmas (ICPs) and capacitively coupled plasmas (CCP). Typically, ICPs have a higher electron density and higher etch rate than CCPs for a given power deposition and so conductor etching that typically does not depend on deposition of passivation is performed using ICPs. Dielectric etching, which typically does depend on deposition of passivation, is performed by CCP. The distinction between ICP and CCP for dielectric etching is due to the inability to control fluxes of the polymerizing radicals in ICPs.

CCPs for etching are typically operated as single frequency or dual frequency systems, the former often called reactive-ion-etching (RIE) mode. Since the RF power in RIE mode is

applied to the lower electrode (substrate on which the wafer sits), a direct current (dc) “self-bias” voltage develops on the surface of the wafer with respect to the plasma potential. If the CCP is operated with two frequencies, the high frequency (*HF*) power is typically applied to the upper electrode and the low frequency (*LF*) power is applied to the lower electrode, though in some configuration, both *LF* and *HF* powers are applied to the same electrode.[17] Since the *LF* power produces the self-bias on the substrate, and since the *HF* power is mainly responsible for the electron kinetics, the *LF* power is often called bias power and the *HF* power is often called source power.

In order to increase the flexibility of controlling the energy and flux of energetic particles, time-modulated power has been investigated. Such studies have been performed in ICP [11], ECR discharge [12], and helicon plasmas [13]. In ECR discharge, Samukawa varied pulse repetition frequency (PRF) from 5 kHz to 50 kHz with a fixed duty cycle of 50% at 1 mTorr of Cl<sub>2</sub> and N<sub>2</sub>. He showed that IED becomes narrower as PRF increases, and that the selectivity between Si and SiO<sub>2</sub> increases with smaller PRF. He also reported that the CD is maintained with pulsed operation. Boswell et al. studied the etching selectivity of Si and SiO<sub>2</sub> in helicon plasma by varying PRFs from 0.02 kHz to 2 kHz with a constant duty cycle of 20% at 7mTorr of SF<sub>6</sub>, and reported that the selectivity increases by increasing PRF. Pulsing bias power is another strategy for controlling the etch profile. Schaepkens et al. [14] studied the RF bias pulsing effect on SiO<sub>2</sub> etch profile. The plasma system used in their investigation is ICP sustained in C<sub>2</sub>F<sub>6</sub> and CHF<sub>3</sub> at 6 mTorr. The RF bias frequency was kept constant at 3.4 MHz and the PRF of the bias power was also kept constant at 1 kHz. They varied the duty cycles from 29% to 99% and reported that the sidewall angle of the profile was reduced by lowering the duty cycle due to the increased deposition of fluorocarbon on the sidewall at a lower duty cycle. Time-modulated

power has also been applied to dual frequency CCP (DF-CCP) to study plasma properties computationally [18] and experimentally [19]. However, these studies mainly focused on the plasma properties instead of the etching profile of SiO<sub>2</sub>.

In this chapter, etch properties of SiO<sub>2</sub> used pulsed DF-CCPs sustained in Ar/CF<sub>4</sub>/O<sub>2</sub> will be discussed with results from a two-dimensional computational investigation. Previous studies have shown that the ion energy distribution (IED) can be manipulated by pulsing the *LF* and *HF* powers for a given size of the blocking capacitor (BC).[20] Since the IED is typically determined by the sheath potential on the *LF* electrode (the difference between the plasma potential the electrode potential), the IED is sensitive to pulsing both or either of the *LF* and *HF*, as the plasma potential is sensitive pulsing either power. Pulsing can occur in many formats – *LF* and *HF* simultaneously pulsed (synchronized), the *LF* pulsed while the *HF* is continuous or the *HF* pulsed while the *LF* is continuous. Control of etch profiles will be demonstrated based on the control of the IED using these different pulsing strategies. For example, bowing and undercut may occur in the CW operation while these effects are suppressed in the pulsed-mode operation.

The model used in this study is described in Sec. 7.2. The typical plasma properties in pulsed DF-CCP are discussed in Sec. 7.3, and the ion energies along with etch properties are in Sec. 7.4. Our concluding remarks are in Sec. 7.5.

## **7.2 Description of the Model**

The model used in this investigation is a two-dimensional fluid hydrodynamics simulation with combined separate modules that address different physical phenomena.[21] The modules used in this study are as follows. The Electron Monte Carlo Simulation (EMCS) is used to calculate the trajectory and temperature of electrons. The Fluid Kinetics-Poisson Module

(FKPM) solves continuity, momentum, and energy equations for heavy particle species (neutral and charged). The Plasma Chemistry Monte Carlo Module (PCMCM) is used to obtain the energy and angular distributions (EADs) of neutrals and charged species striking the wafer. The fluxes of reactant species and their EADs from PCMCM are then used as input to the MCFPM. The MCFPM resolves the surface of the wafer using a 2D rectilinear mesh. The probability of a surface reaction was determined by the number of dangling bonds in the species. The probability of reactions with photoresist (PR) was chosen to be small enough in order to eliminate the effect of PR mask erosion on the etch profile. The sputtering probability of the polymer by ion has been assumed to be 20%. We also considered polymer deposition on top of the polymer layer and the sputtering probability for this kind of polymer is assumed to be 25%, which is a little bit larger than that of a normal polymer. The sputtering probability for activated SiO<sub>2</sub> by ions is assumed to be 90%. The polymer deposition probability (sticking coefficient) has been taken into account by the number of dangling bonds of the species. For example, CF, CF<sub>2</sub> and CF<sub>3</sub> have 2%, 1%, and 0.3% polymer deposition probabilities on the chamber wall, respectively. The plasma equipment modeled in this investigation is a pulsed DF-CCP sustained in an Ar/CF<sub>4</sub>/O<sub>2</sub> = 75/20/5 gas mixture at 40 mTorr and 200 sccm. The fluxes of reactant species and their EADs from PCMCM are then used as input to the Monte Carlo Feature Profile Model (MCFPM). The species in the simulation are Ar, Ar<sup>+</sup>, Ar(4s) metastable, Ar(4s) radiative, Ar(4p, 5d), CF<sub>4</sub>, CF<sub>3</sub>, CF<sub>2</sub>, CF, C, F, F<sub>2</sub>, C<sub>2</sub>F<sub>4</sub>, C<sub>2</sub>F<sub>6</sub>, CF<sub>3</sub><sup>+</sup>, CF<sub>2</sub><sup>+</sup>, CF<sup>+</sup>, C<sup>+</sup>, F<sup>+</sup>, F<sub>2</sub><sup>+</sup>, CF<sub>3</sub><sup>-</sup>, F<sup>-</sup>, O<sub>2</sub>, O<sub>2</sub>(<sup>1</sup>Δ), O<sub>2</sub><sup>+</sup>, O, O(<sup>1</sup>D), O<sup>+</sup>, O<sup>-</sup>, COF, COF<sub>2</sub>, CO<sub>2</sub>, FO, SiF<sub>4</sub>, SiF<sub>3</sub>, and SiF<sub>2</sub>. [22]

The time step in the FKPM for an update of densities and between solutions of Poisson's equation is about 10<sup>-11</sup> s with consideration of the Courant limit and the resolution of the *RF* cycles. In the case of two-frequency excitation with the lower frequency being 10 MHz and the

higher frequency being 40 MHz, in order to resolve the *RF* cycle of both frequencies, the fundamental time step is chosen to be less than 0.0025 of the highest applied frequency ( $6.25 \times 10^{-11}$  s for 40 MHz). The time step may be further reduced to satisfy the Courant limit. The time step in the EMCS is similarly small by choosing the minimum of the following: a specified fraction of the *RF* cycle (0.0025 for 40 MHz), the time to cross half of the computational mesh in any direction, the time to the next collision, or the time for the particle to be decelerated to zero speed. To maintain the EMCS in lockstep with the FKPS, in this study trajectories are computed for 5 *LF RF* cycles for each call of the EMCS (which at 10 MHz is 0.5  $\mu$ s). Time steps in the PCMCM are dynamically chosen to resolve ion transport in the time-varying sheath. The time step is chosen to be no larger than a fraction of the *RF* cycle (typically 0.01) or the time to cross a fraction of a computational mesh cell (typically 0.5 far from the sheath and 0.02 in the sheath).

In pulsed operation, there are typically two times of interest during the pulse period – when the pulsed power is on and when the pulsed power is off. The fluxes and energies of the particles bombarding the wafer can be significantly different between these two portions of the pulsed period. Depending on the pulse repetition rate and duty cycle, the pulse-period average of the fluxes and EADs may not well represent the synergies that may occur when the fluxes and EADs are separately incident onto the wafer. In order to model these conditions, fluxes and EADs are separately recorded for when the pulse power is on (called the *power-ON* portion of the cycle) and when the pulse power is off (called the *power-OFF* portion of the cycle). These two sets of fluxes and EADs are then alternately used for calculating etch profile evolution in the MCFPM. The ratio of the integration time for set of fluxes and EADs is determined by the duty cycle of the pulse.

### 7.3 Plasma Properties of Pulse-Powered DF-CCP

The computational geometry for the DF-CCP used in this study is schematically shown in Fig. 7.1. The plasma is generated in the gap (4 cm) between two electrodes in a mixture of  $\text{Ar}/\text{CF}_4/\text{O}_2 = 70/25/5$  at 40 mTorr. Both electrodes are powered at a constant voltage (250 V) to more consistently maintain the energy of the ions incident on the electrodes while pulsing power. This results in a difference in power deposition as duty cycles and repetition rates are varied. As a result, etch rates are presented as power-normalized values. The lower electrode serves as the substrate that is powered at low frequency (*LF*), 10 MHz, through BC of 100 nF. A conductive Si wafer ( $\epsilon/\epsilon_0 = 12.0$ ,  $\sigma = 0.01 \Omega^{-1} \text{ cm}^{-1}$ ), 30 cm in diameter, sits in electrical contact with the substrate. The upper electrode, 36 cm in diameter, is powered at high frequency (*HF*), 40 MHz. The *HF* electrode serves as the shower head through which gas is injected at 200 sccm. Both the electrodes are surrounded by a dielectric focus ring ( $\epsilon/\epsilon_0 = 8.0$ ,  $\sigma = 10^{-6} \Omega^{-1} \text{ cm}^{-1}$ ). All the surfaces facing the plasma have the same secondary emission coefficient  $\gamma = 0.15$  for ion bombardment. All other surfaces in the reactor are grounded metal including the annular pump port. Either only one of the RF powers is pulsed or both the *LF* and *HF* powers are pulsed. Pulse operation was characterized by the pulse repetition frequency (PRF) that is how many times per second the waveform is repeated, and the duty cycle (DC) that is the fraction of the total time of the *power-ON* stage. The rise (or decay) time of the *power-ON* (or *-OFF*) period is 500 ns.

The base case operating conditions have PRF = 10 kHz (pulse period 100  $\mu\text{s}$ ) and DC = 25%. The duty cycle was varied from 25% to 75% with a PRF of 5 kHz and 10 kHz.

The electron density ( $n_e$ ) and electron temperature ( $T_e$ ) at the reference point (as indicated in Fig. 7.1) are shown as a function of the time for the case with PRF = 10 kHz and DC = 25%

(*power-ON* between 10  $\mu\text{s}$  and 35  $\mu\text{s}$ ) for *LF* pulsing in Fig. 7.2, *HF* pulsing in Fig. 7.3 and for pulsing both frequencies in Fig. 7.4. Two-dimensional snap shots of  $n_e$  and  $T_e$  are taken at 25  $\mu\text{s}$  (during the *power-ON*) and 85  $\mu\text{s}$  (during the *power-OFF*). When pulsing the *LF* power,  $n_e$  and  $T_e$  are moderately modulated between the *power-ON* and *power-OFF* cycles, as shown in Fig. 7.2a.  $n_e$  slowly increases up to  $1.7 \times 10^{11} \text{ cm}^{-3}$  from  $1.05 \times 10^{11} \text{ cm}^{-3}$ , while  $T_e$  rapidly increases from 0.46 eV to 1.57 eV. The electron temperature is low in the bulk plasma due to contributions to ionization by sheath accelerated beam electrons. The difference in  $T_e$  at different locations of the chamber results from the different mechanisms of electron heating. For example, electron heating in the boundary region is dominated by stochastic (collisionless) heating while the heating in the bulk of the plasma is dominated by Ohmic (collisional).[23] Stochastic power deposition increases with frequency and so  $T_e$  is higher near the top sheath. On the other hand, Ohmic heating is responsible for the electron heating in the bulk plasma. When the *RF* power is turned on,  $T_e$  increases above its afterglow value due to the *overshoot* phenomena that is common in the pulse mode operation. Overshoot for these conditions results from electrons that had diffused towards the unpowered electrode during the *power-OFF* period. When turning on the power, the sheath is re-established and electrons are accelerated out of the now thicker sheath. The overshoot of  $T_e$  is greater when pulsing the *HF* power than when pulsing the *LF* power due to the higher efficiency of electron heating at the higher frequency. The overshoot is even greater when pulsing both the *LF* and *HF* due to the collapse of the sheath when both powers are off. For example, when pulsing the *HF*,  $n_e$  gradually increases up to  $1.88 \times 10^{11} \text{ cm}^{-3}$  from  $0.46 \times 10^{11} \text{ cm}^{-3}$ , while  $T_e$  spikes up to 5.18 eV from 3.34 eV. When pulsing both the *LF* and *HF*,  $n_e$  increases up to  $1.87 \times 10^{11} \text{ cm}^{-3}$  from  $0.25 \times 10^{11} \text{ cm}^{-3}$ , while  $T_e$  spikes up to 6.2 eV from 0.17 eV. After the overshoot in  $T_e$  at the start of the pulse, moves towards a

steady state value until the pulsed power is turned off. During the *power-OFF* cycle,  $T_e$  tries to find another steady state value.

There is no significant difference in the plasma characteristics between different pulsing configurations during the *power-ON* portion of the cycle because both of the *RF* powers are turned on. However, during the *OFF* portion, the plasma characteristics are significantly differentiated because the plasma is sustained by the different *RF* powers in the *OFF* portion depending on the pulsing configurations. Typically, the steady state value of  $T_e$  during the *power-ON* portion of the cycle is higher than the value during the *power-OFF* portion of the cycle. The exception is the case with the *HF* pulsed where  $T_e$  increases late into the afterglow when only the *LF* is on. Since ionization is dominated by the *HF* power deposition, when the *HF* power is turned off, the plasma density decays rapidly. Stochastic heating is proportional to the sheath speed  $v_s$ . For a given frequency,  $v_s$  scales with sheath thickness,  $\lambda$  which in turn scales as  $n_e^{-1/2}$  ( $v_s \approx \omega\lambda$  for a given excitation frequency  $\omega$  that is 10 MHz for this case). So as  $n_e$  decreases during the afterglow of the *HF*, the rate of electron heating by the *LF* increases. At some point, the discharge re-establishes itself as a single-frequency CCP sustained by only the *LF*, as indicated by  $n_e$  and  $T_e$  coming to a new steady state. This phenomenon has been experimentally observed with substrate biases applied to pulsed inductively coupled plasmas sustained in chlorine.[24]

#### **7.4 Ion Energies and Etch Properties**

Energy fluxes to the wafer for different duty cycles and pulse configurations are shown in Fig. 7.5. The energy flux is calculated from the average total ion energy multiplied by the total ion flux on the wafer. A duty cycle of 100% corresponds to *CW*. Two values are shown –

averages over the *power-ON* portion of the cycle and average over the entire cycle. The overall trends of energy flux with various duty cycles are similar for different pulse configurations. There is an overshoot at the start of the pulse, and the amount of the overshoot is enhanced with the smaller duty cycle. The overshoot of the self-bias on the substrate results in producing higher-energy ions incident onto the wafer. Consequently, the ON-cycle average of the ion energy flux on the wafer are larger with the smaller duty cycle. However, the overall average values during the entire pulse cycle are reduced at the smaller duty cycle simply because of the reduced duration of the *power-ON* cycle in which the ion bombardment onto the wafer is active. In other words, the pulsed operation provides a larger impact of the ion energy flux during the *power-ON* cycle, but also provides a reduced impact of the ion energy flux in an average pulse cycle. Although the overall trends are similar for different configurations of the pulsing, the dynamic range is dependent on which of the *RF* powers is pulsed. For example, the dynamic range of the ON-cycle average of the ion energy flux with different duty cycles is largest when the *HF* is pulsed, and is lowest when the *LF* is pulsed alone. This is because the ion density during the *power-ON* cycle is larger when the *HF* is pulsed alone than when both the *LF* and *HF* are pulsed. The average ion energies during the *power-ON* cycle are all about 200 eV regardless of the pulsing configurations, but the *power-OFF* cycle average of the ion energy is 70 eV with the *LF* pulsed alone, 160 eV with the *HF* pulsed alone, and 26 eV with both the *LF* and *HF* pulsed. As a result, the total-cycle average of the ion energy fluxes with the *HF* pulsed shows the smallest changes by varying the duty cycle among the different pulsing configurations. The ion energy flux is determined not only by the ion flux but also the ion energy, and the ion energy is largely determined by the self-bias that originates from the *LF* power. Consequently, the modulation of ion energy is dominated by pulsing the *LF* power.

Since the self-bias induced on the substrate is modulated when the RF power is pulsed, the ion energy and angular distribution (IEAD) is significantly modified by pulsing not only in energy but also in angle, as shown in Fig. 7.6 and 7.7. Subject to small changes in the dc bias due to the pulsing, the IEAD for the *power-ON* period is the same for all cases since both the *LF* and *HF* are on. In principle, the IEAD during *power-ON* should closely resemble that for *CW* operation. However, differences in sheath thickness and dc bias due to the pulsing producing differences in the IEADs between *power-ON* and *CW*. The major differences in IEADs occur during *power-OFF* when only the *LF* or *HF* is on, or neither are on.

When pulsing the *LF* power while having the *HF* on, the IEDs consist of a high-energy distribution (*power-ON*) and a low-energy distribution (*power-OFF*). The high-energy component remains during the *power-ON* stage results from modulation of the plasma potential (and so sheath potential) by both the *LF* and *HF*. Since the sheath has both low frequency and high frequency components, there is breadth and structure to the IEDs. During the *power-OFF* cycle with only the *HF* on, the sheath has only high frequency components. Ions respond to only the average sheath potential because the oscillation of plasma potential generated from the *HF* power is faster than the ion response time.

When pulsing the *HF* power, there is less distinction between the IEDs produced during the *power-ON* and *power-OFF* portions of the cycle – both portions have high energy IEDs. Since the *LF* is continuously on, the self-bias remains negative and large during the *HF power-OFF* portion of the cycle while the sheath retains its low frequency components. The average energy and width of the IED during the *power-ON* and *power-OFF* portions of the cycle are similar. The exception is a shift of the IED to higher energy when pulsing the *HF* due to the increase in the plasma potential. When pulsing both the *HF* and the *LF*, the plasma potential and

sheath potential decay to only a few volts during the inter-pulse period. As a result, the IED during the *power-OFF* portion of the cycle consists of largely thermal ions having a broad angular distribution.

The relative magnitudes of the low-energy and high-energy components of the IEDs can be controlled by the DC and PRF, as shown in Figs. 7.9–7.11. For example, the low energy portion of the IED generated during the *power-OFF* cycle is enhanced by decreasing the duty cycle and PRF, while the high energy portion of the IED generated during the *power-ON* cycle is enhanced by increasing the duty cycle and PRF. For the range of PRFs examined, the IEDs are most sensitive to DC. For example, IEDs are shown in Fig. 7.9 when pulsing the *LF* for different DCs. The relative proportion of the ion flux in the low energy and high energy portions of the IEDs scale linearly with DC. The low energy component already does not have much structure and so its shape does not change with DC. The shape of the high energy component of the IED is sensitive to DC. As the duty cycle increases and the *CW* state is approached, the structure appears in the IED that results from the residence time of ions in the presheath and sheath. As the DC increases, the residence time increases and so begins to resemble the *CW* IED that allows for the maximum residence time. When changing the PRF, a similar trend is seen. There is more structure in the IED with the smaller PRF which translates to a longer *power-ON* cycle for a given DC. The longer *power-ON* cycle allows for longer residence time in the presheath and sheath.

Although the ion energies change significantly during the pulse-period, the neutral fluxes to the substrate are not particularly sensitive to the pulse-period. The residence time for neutral fluxes are long enough for these PRFs that there is little modulation of their fluxes during the pulse period. In the Ar/CF<sub>4</sub>/O<sub>2</sub> gas mixture, polymerizing fluxes consist dominantly of CF<sub>x</sub>

( $x=1-3$ ). Once deposited, high energy ions are required to sputter the polymer and initiate etching of the underlying  $\text{SiO}_2$ . Therefore, during the *power-OFF* cycle, the likelihood for net-deposition increases whereas during the *power-ON* cycle, the likelihood for etching increases. The proportion of the cycle that dominated by deposition phase is therefore controlled by the fraction of the cycle that dominantly has a low-energy IED. Thus, the amount of deposition and etching on the wafer can be controlled through customizing the IEAD by adjusting the DC.

To demonstrate these trends, high aspect ratio (HAR) etching of  $\text{SiO}_2$  over Si was simulated in MCFPM using the fluxes and energy distributions from PCMCM, as discussed in Chapter 2.2. The width of opening of the hard mask is 22 nm and the thickness of  $\text{SiO}_2$  is 350 nm. Profiles are compared while varying DC. Since power may change while changing DC, profiles are compared for the same 100% over-etch. That is, etching continues for double the time required to reach the bottom of the feature. Recall that both etching and deposition simultaneously occur during dielectric etching.[25] The balance between deposition and etching is largely determined by the IEDs. Since the direction of ion bombardment is perpendicular to the wafer surface, the sidewall protected by a passivation layer (polymer deposition). Polymers deposited on the sidewalls of an HAR feature generally prevent the profile from bowing. In fact, an excess of polymerization leads to tapering of the profile. So to some degree the sidewall slope can be controlled by the rate of deposition compared to etching – or the likelihood to sputter polymer.

Etch profiles and the width of the profile for different duty cycles are shown for pulsing the *LF* in Fig. 7.12, *HF* in Fig. 7.13 and both the *LF* and *HF* in Fig. 7.14. The general trend is that the feature transitions from being tapered at low DC to having bowing and undercut with high DC (or *CW*). When pulsing the *LF*, there is a significant degradation in the energy of the

IED during the *power-OFF*, that then allows more polymer deposition to occur. This higher rate of deposition leads to tapering of the profile. When increasing DC, less cycle averaged deposition occurs, which produces less tapering, until with *CW* operating, there is bowing due to the lack of sufficient polymerization. For these conditions a DC = 75% produces the straightest sidewalls.

When pulsing both the *HF* and *LF*, the same general trends are observed – more tapered profile at low DC due to there being a larger fraction of the pulsed cycled with net deposition. The details of how the sidewall slow transitions from tapered to bowed due differ as individual reaction rates depend on the details of the IEDs. When pulsing the *HF*, we see the least variation in the sidewall slope since there is the least variation in the IEDs. With the *LF* always on, the IED does not have a significant low-energy phase where deposition dominates.

In general, an intermediate duty cycle produces a better sidewall profile depending on the particular pulsing configuration. However, it is difficult to avoid reduced etch rate with pulsing simply because of the reduced *power-ON* period. For a fair comparison of the etch rate with different duty cycles with pulsed operation should be made on a power-normalized basis. In this regard, power-normalized etch rates are compared as a function of DC for different pulsing configurations in Fig. 7.15.

## 7.5 Concluding Remarks

The plasma properties, fluxes of reactive species, ion energies, and SiO<sub>2</sub> etch properties in the pulsed DF-CCP with different pulsing configurations have been investigated using the results from the HPEM and the MCFPM. The investigation has been parameterized with various duty cycles at the PRF of 5 kHz and 10 kHz that are typically used in the industry. The electron densities gradually increase and reach the maximum density during the *power-ON* cycle, and

gradually decrease down to the minimum value during the *power-OFF* cycle. The electron temperatures instantaneously increase and decrease at the start and cessation of the pulsed power, and then approach the steady state value at each stage of *power-ON* and *-OFF* after experiencing the transition. The dynamic range of the electron density and temperature during the pulse period is largest when the *HF* is pulsed because the electron heating is more efficient at the higher-frequency *RF*-power. We found that the ion energy flux can be manipulated by DC. The IED is also significantly modified by pulsing the *RF* powers. The amplitude of the peaks in the distribution can be controlled by the duty cycle, as well. The low-energy component in the IED is produced during the *power-OFF* period, and consequently the amplitude of the low-energy peak becomes larger with the smaller duty cycle. The minimum ion energy is lowest with pulsing both the *LF* and *HF*, and is largest with pulsing the *HF* power alone. The range of the high-energy component in the IED is similar between different DCs, but the amplitude of the high-energy peak becomes larger with the higher DC. As a result, different etch profiles are obtained with various DCs. Typically, with the larger duty cycle, the etch rate is faster but the sidewall bowing is observed. The sidewall bowing can be suppressed by pulsing and also can be adjusted by changing DC.

## 7.6 Figures

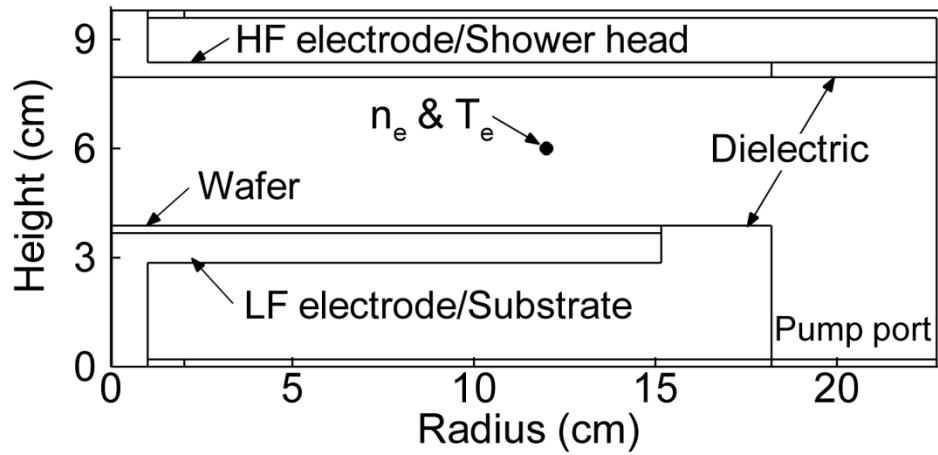


Fig. 7.1 Operating conditions for this investigation. (a) Geometry of the DF-CCP chamber. The *LF* (10 MHz) is applied on the lower electrode, and the *HF* (40 MHz) is applied on the upper electrode. One or both of the two frequencies are operated in pulse mode with 5 and 10 kHz PRF. Electron density ( $n_e$ ) and temperature ( $T_e$ ) are traced at the reference point indicated in the chamber.

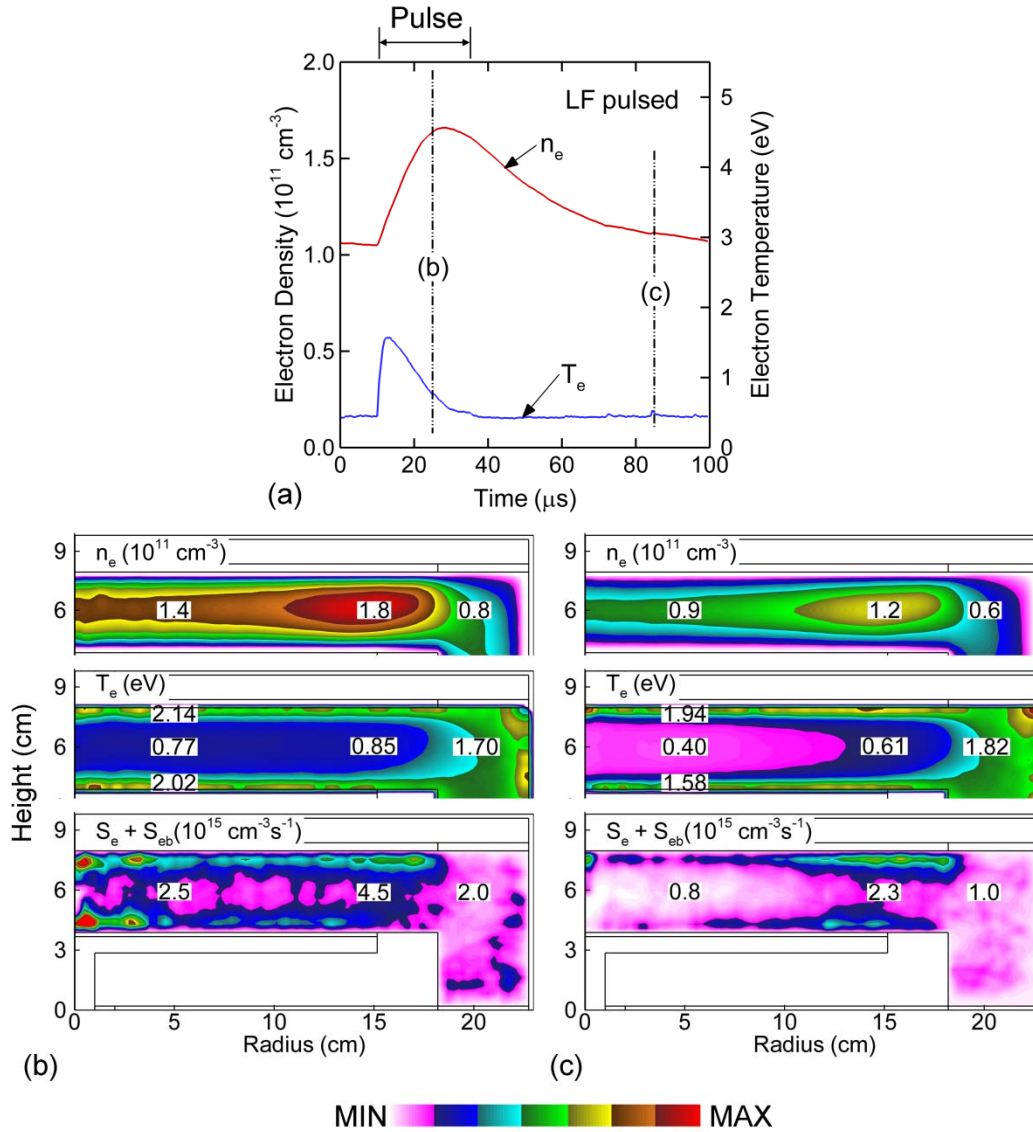


Fig. 7.2 Electron density, temperature, and source rates for the conditions of pulsing the *LF* power (the *HF* in *CW*). The *LF* power-ON period is from 10  $\mu\text{s}$  to 35  $\mu\text{s}$ . (a)  $n_e$  and  $T_e$  as a function of time at the reference point (indicated in Fig. 7.1). (b) The spatial distribution of  $n_e$ ,  $T_e$ , and electron sources in the chamber at 25  $\mu\text{s}$  (15  $\mu\text{s}$  after the *LF* power ON). (c) The spatial distribution of  $n_e$ ,  $T_e$ , and electron sources in the chamber at 85  $\mu\text{s}$  (50  $\mu\text{s}$  after the *LF* power OFF).

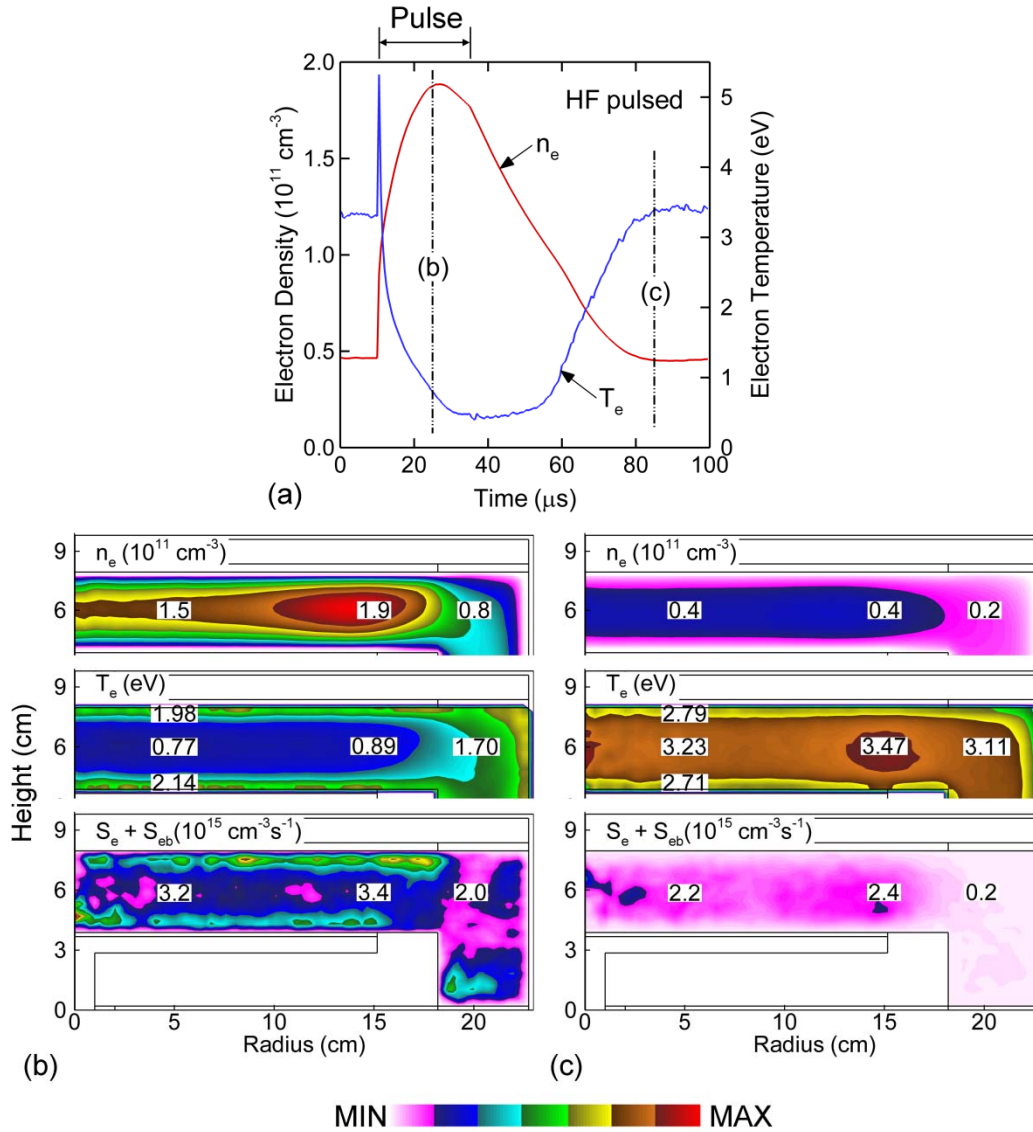


Fig. 7.3 Electron density, temperature, and source rates for the conditions of pulsing the *HF* power (the *LF* in *CW*). The *HF* power-ON period is from 10  $\mu\text{s}$  to 35  $\mu\text{s}$ . (a)  $n_e$  and  $T_e$  as a function of time at the reference point (indicated in Fig. 7.1). (b) The spatial distributions of  $n_e$ ,  $T_e$ , and electron sources in the chamber at 25  $\mu\text{s}$  (15  $\mu\text{s}$  after the *HF* power ON). (c) The spatial distributions of  $n_e$ ,  $T_e$ , and electron sources in the chamber at 85  $\mu\text{s}$  (50  $\mu\text{s}$  after the *HF* power OFF).

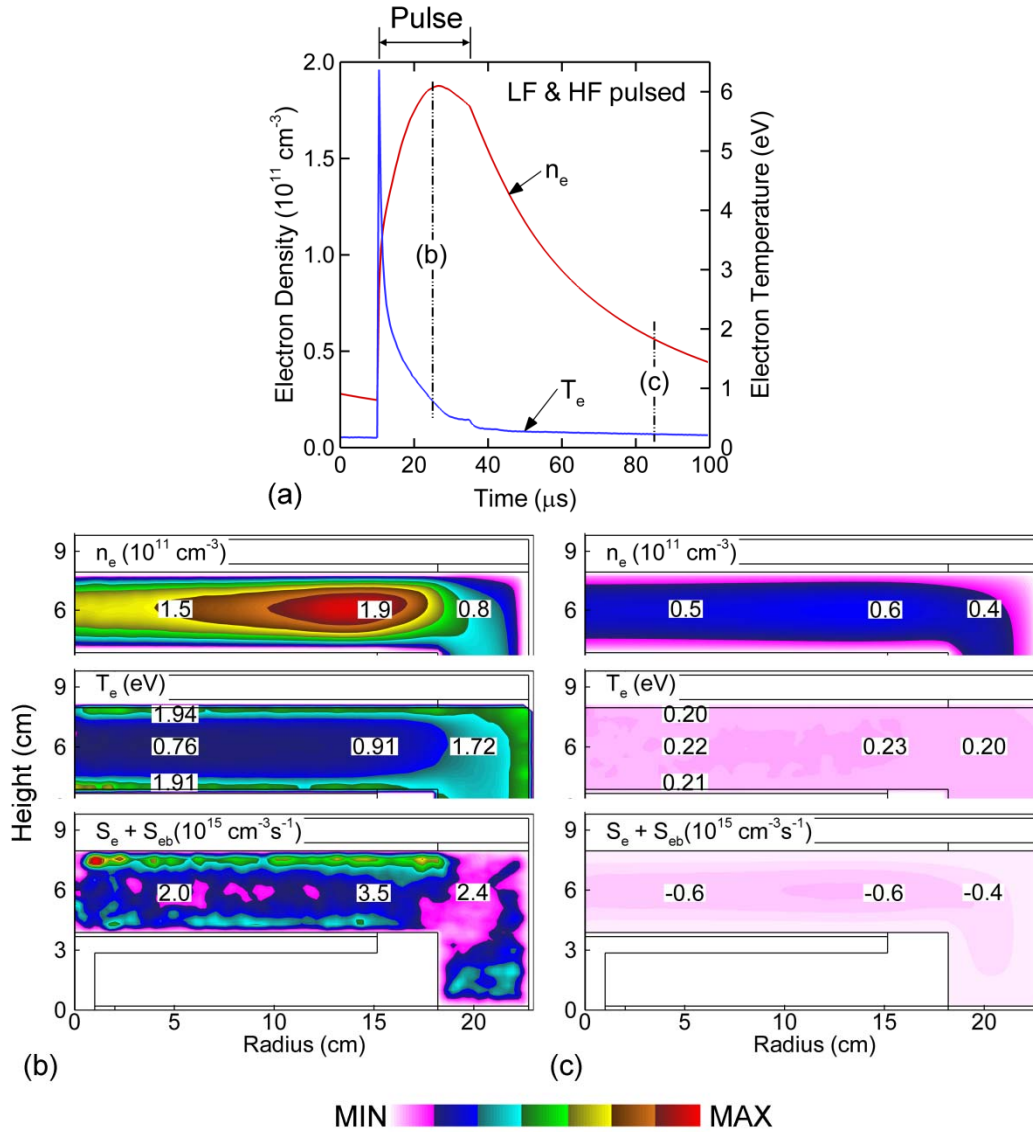
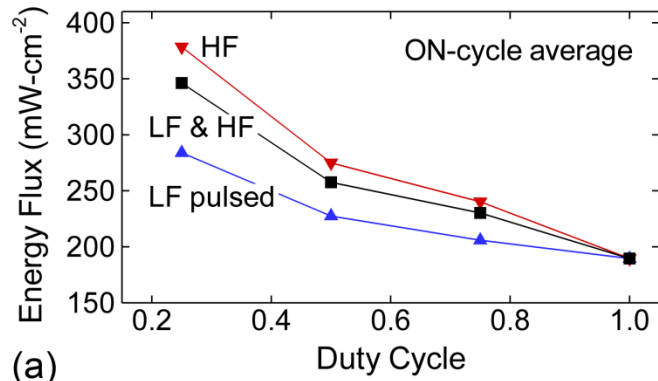
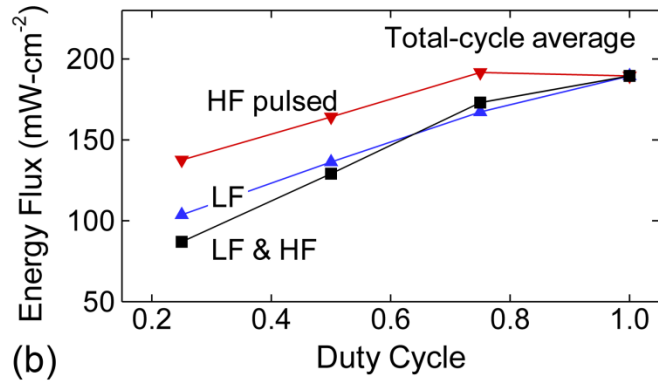


Fig. 7.4 Electron density, temperature, and source rates for the conditions of pulsing the *LF* and *HF* power. The *power-ON* period is from 10  $\mu\text{s}$  to 35  $\mu\text{s}$ . (a)  $n_e$  and  $T_e$  as a function of time at the reference point (indicated in Fig. 7.1). (b) The spatial distributions of  $n_e$ ,  $T_e$ , and electron sources in the chamber at 25  $\mu\text{s}$  (15  $\mu\text{s}$  after the powers ON). (c) The spatial distributions of  $n_e$ ,  $T_e$ , and electron sources in the chamber at 85  $\mu\text{s}$  (50  $\mu\text{s}$  after the powers OFF).



(a)



(b)

Fig. 7.5 Energy flux with various duty cycles. (a) Average energy flux during ON-cycle. (b) Average energy flux over the total pulse period.

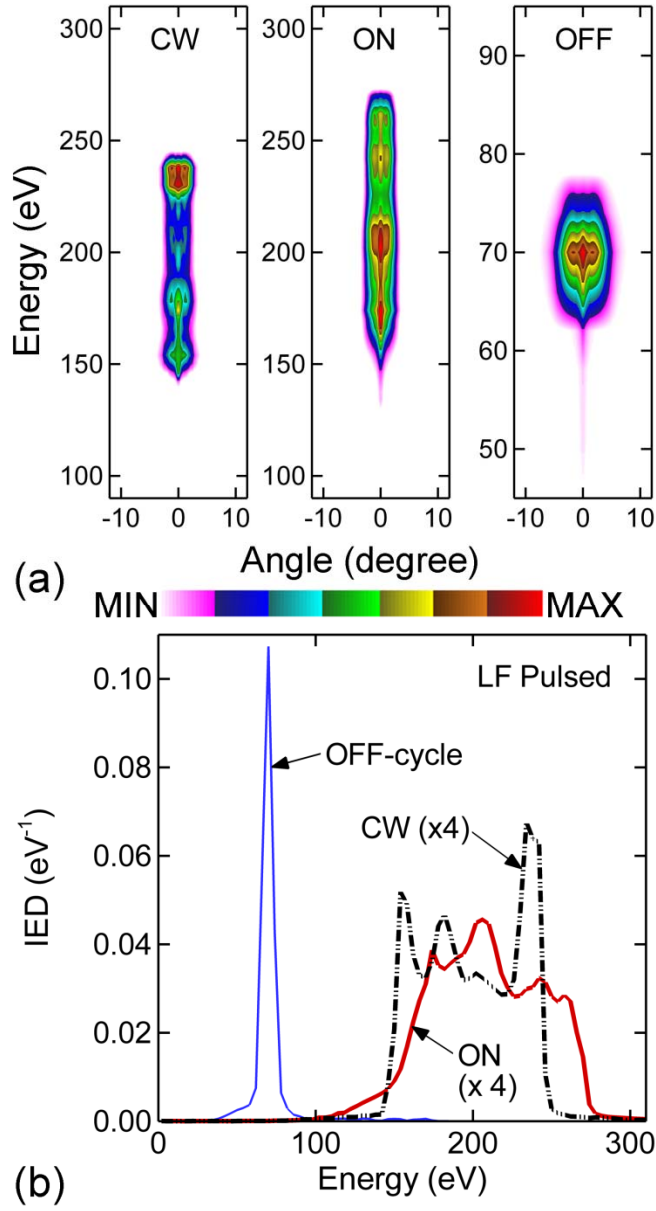


Fig. 7.6 Ion energy and angular distribution when pulsing the *LF* with a 25% of duty cycle and a 10 kHz of PRF. (a) IEAD for the ON and OFF periods compared to CW. (b) IED.

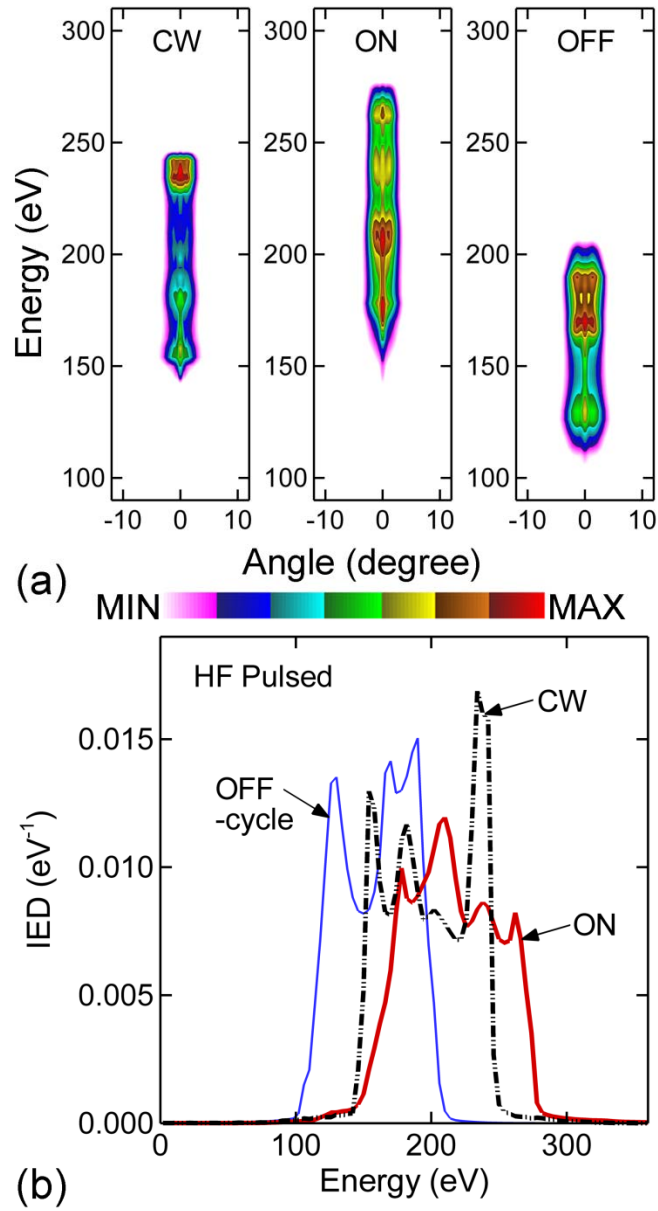


Fig. 7.7 Ion energy and angular distribution when pulsing the *HF* with a 25% of duty cycle and a 10 kHz of PRF. (a) IEAD for the ON and OFF periods compared to CW. (b) IED.

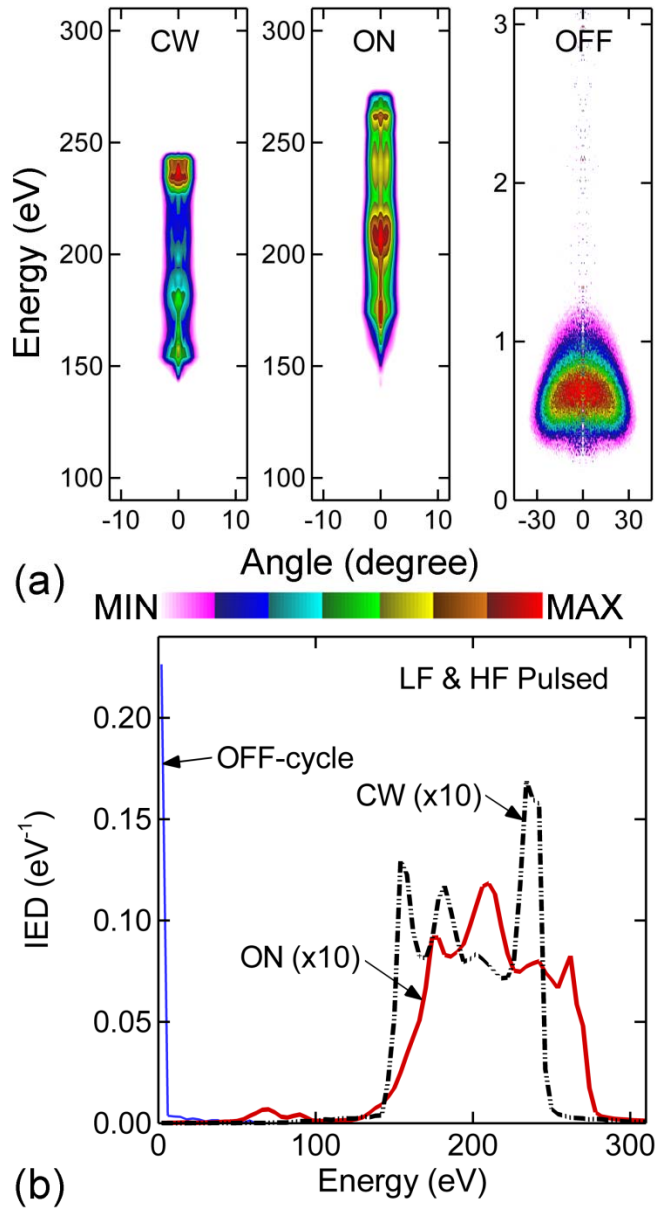


Fig. 7.8 Ion energy and angular distribution when pulsing the *LF & HF* with 25% duty and 10 kHz PRF. (a) IEAD for the ON and OFF periods compared to CW. (b) IED. The ion energy during the OFF cycle appears only at about zero because the sheath collapses during the afterglow.

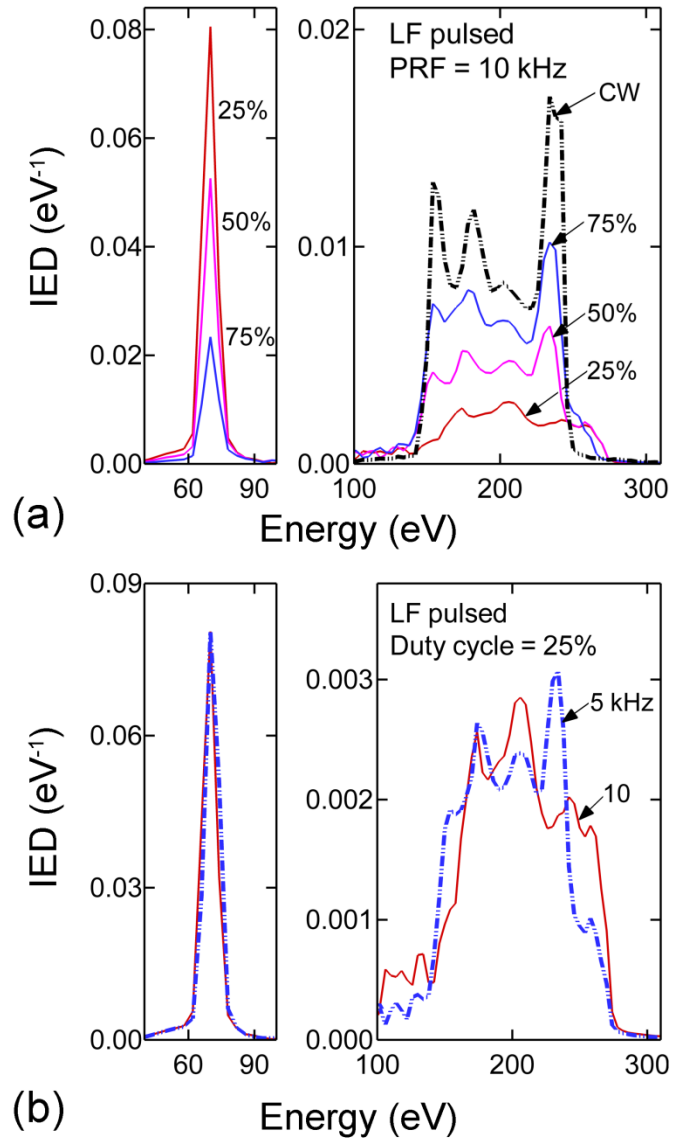


Fig. 7.9 IEDs when pulsing the *LF* power. (a) IEDs with different duty cycles at 10 kHz of PRF. (b) IEDs with different PRFs at 25% of duty cycle.

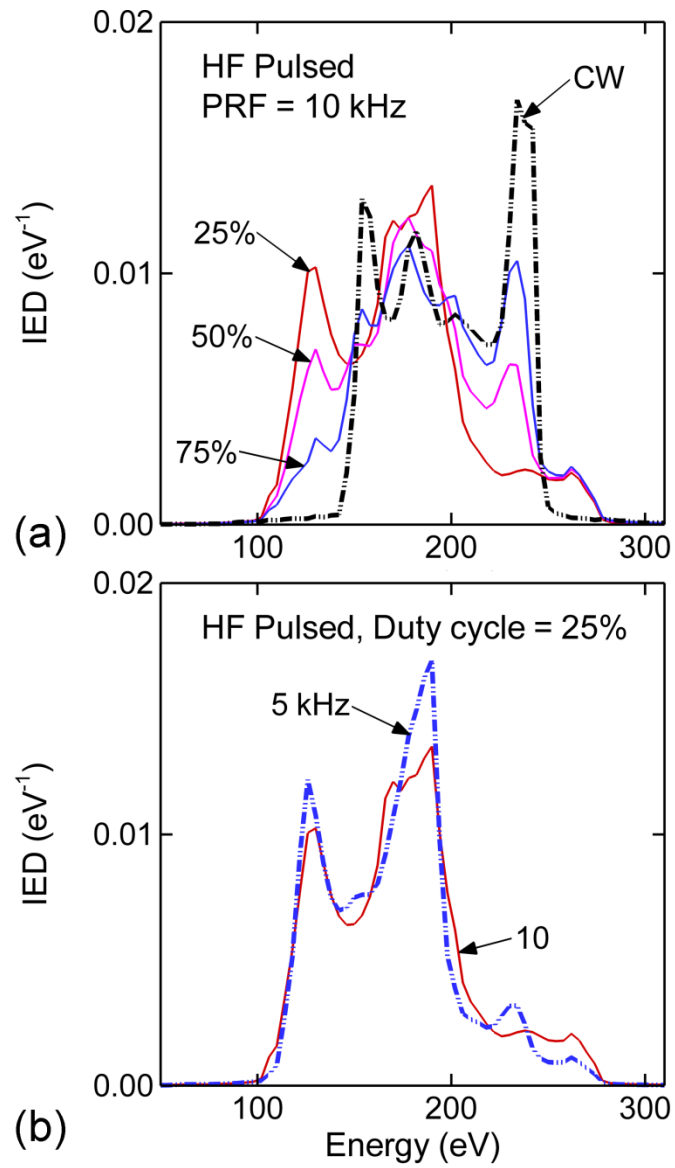


Fig. 7.10 IEDs when pulsing the *HF* power. (a) IEDs with different duty cycles at 10 kHz of PRF. (b) IEDs with different PRFs at 25% of duty cycle.

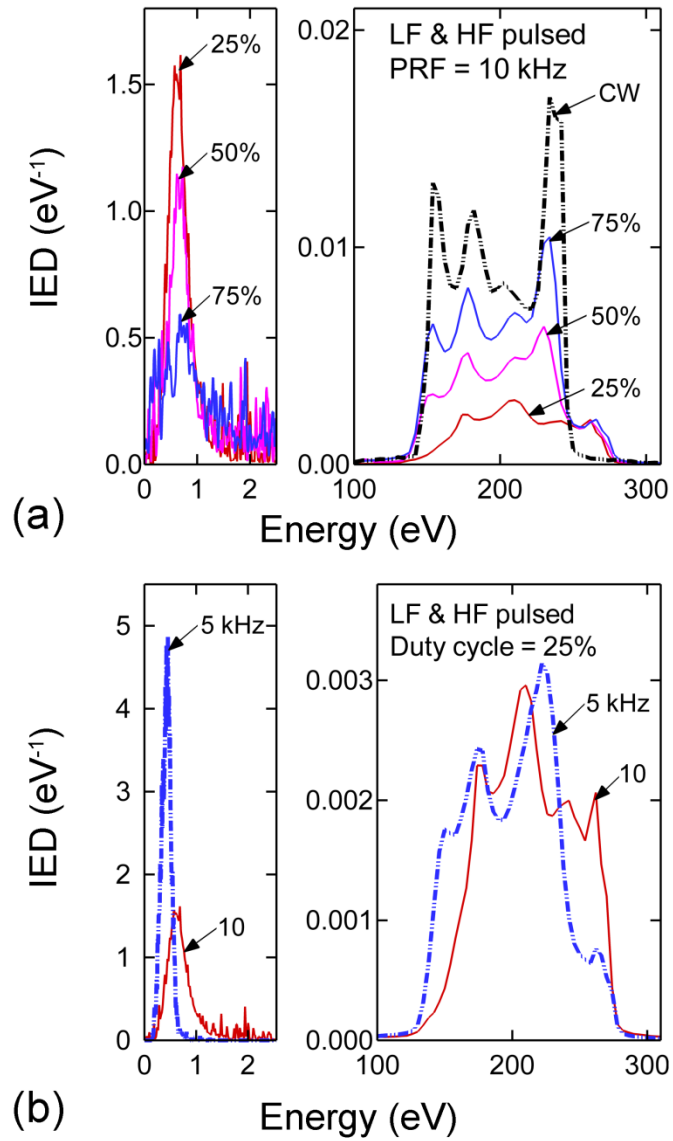


Fig. 7.11 IEDs when pulsing the *LF* & *HF* powers. (a) IEDs with different duty cycles at 10 kHz of PRF. (b) IEDs with different PRFs at 25% of duty cycle.

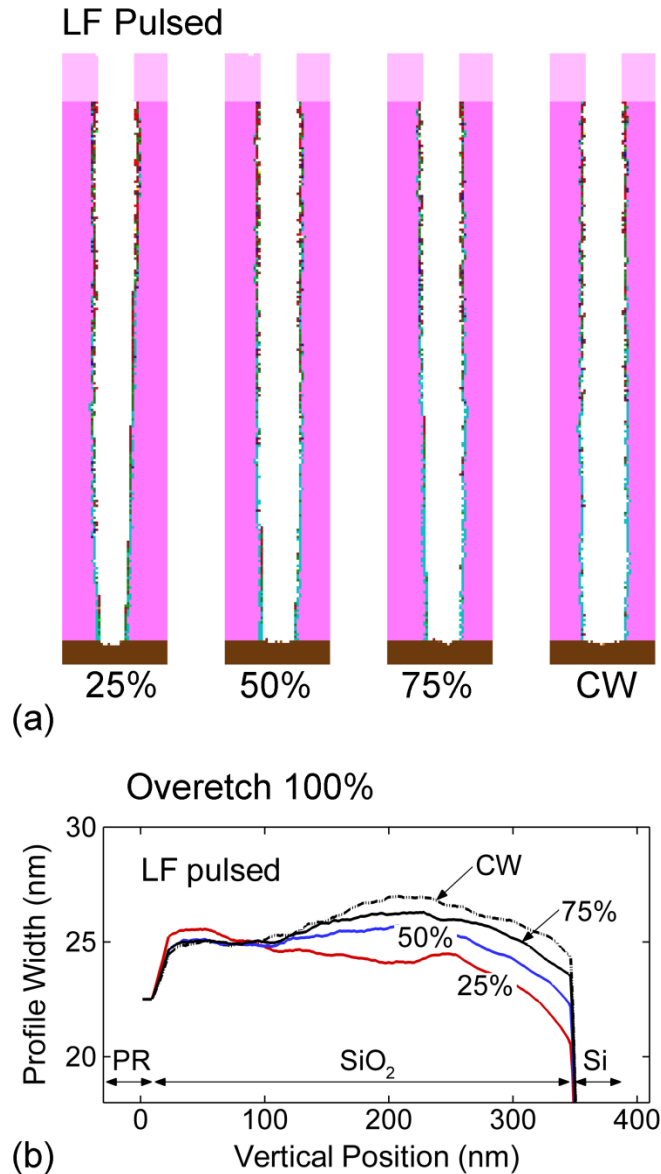


Fig. 7.12 Etch profile when pulsing the *LF* power at 10 kHz. (a) Etch profile after overetch 100%. (b) Profile width as a function of height with 100% of overetching. At 100% overetching, the sidewall bowing with *CW* mode started at about 100 nm in the depth but this is suppressed by pulsed operation.

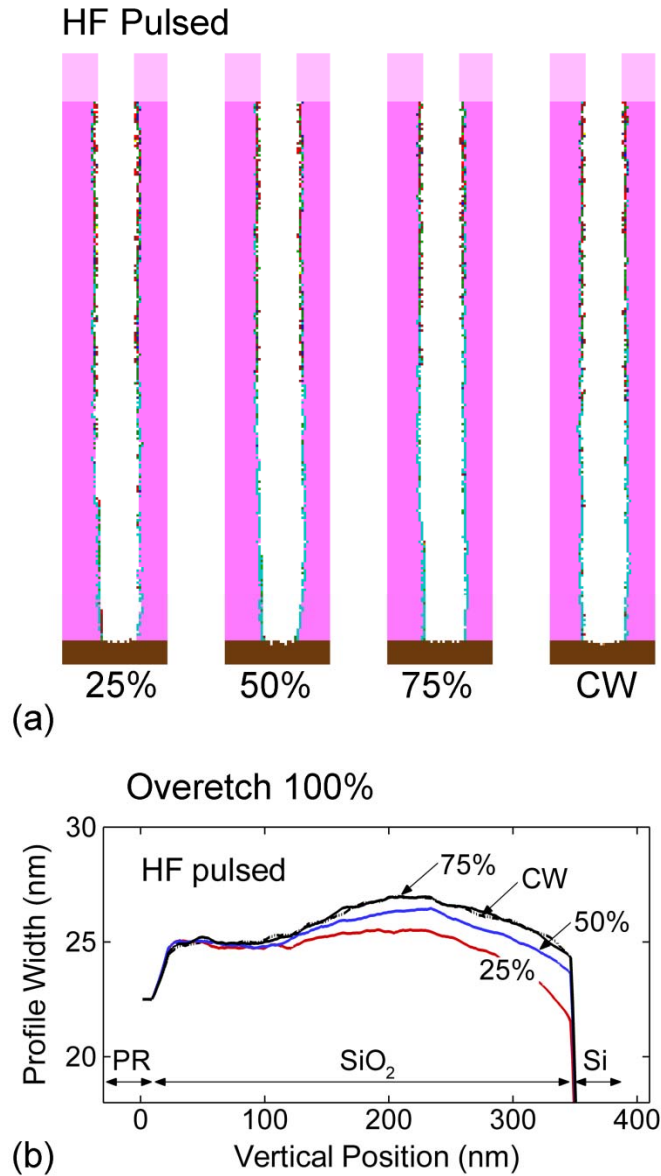


Fig. 7.13 Etch profile when pulsing the *HF* power at 10 kHz. (a) Etch profile after Overetch 100%. (b) Profile width as a function of height with 100% of overetching.

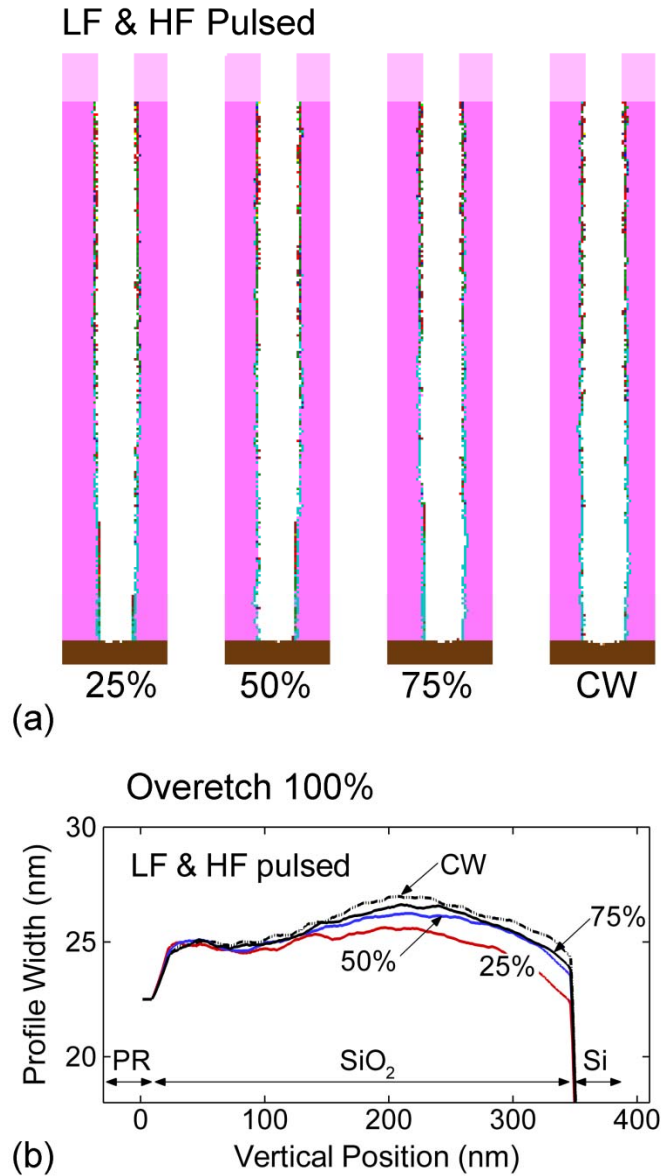
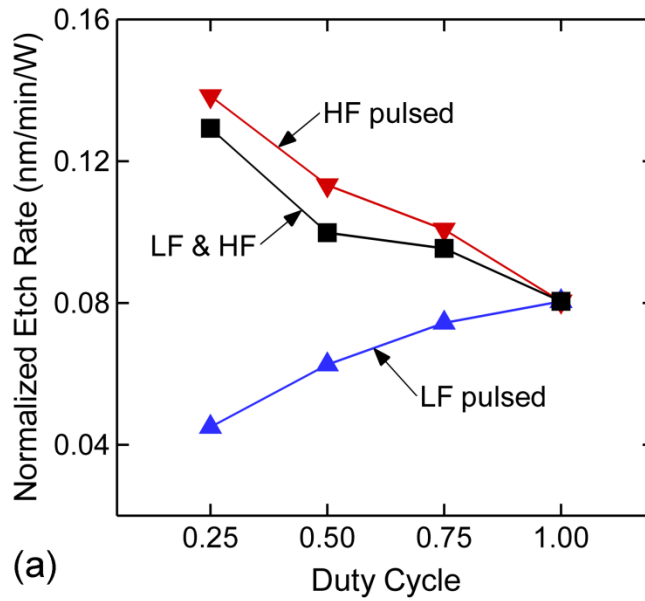
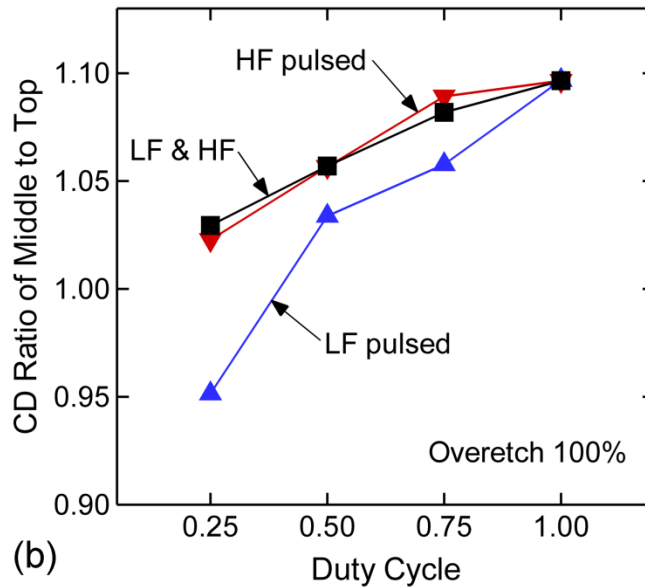


Fig. 7.14 Etch profile when pulsing the *LF* & *HF* powers at 10 kHz. (a) Etch profile after overetch 100%. (b) Profile width as a function of height with 100% of overetching.



(a)



(b)

Fig. 7.15 Etch rate and CD ratio as a function of duty cycle for different configurations of pulsing. (a) Power normalized etch rate. (b) CD ratio of middle to top. The normalized etch rate is higher with pulsed operation than *CW* mode except for the *LF* pulsed. An intermediate duty cycle produces a better sidewall profile.

## 7.7 References

1. D. Koehler and D. Fischer, "Challenges of high aspect ratio oxide etching", *ECS Trans.* **13**, 47 (2008).
2. J.-K. Lee, I.-Y. Jang, S.-H. Lee, C.-K. Kim, and S. H. Moon, "Cyclic deposition/etching process to etch a bowing-free SiO<sub>2</sub> contact hole", *J. Electrochem. Soc.* **156**, D269 (2009).
3. R. Chatterjee, S. Karecki, R. Reif, V. Vartanian, and T. Sparks, "The use of unsaturated fluorocarbons for dielectric etch applications", *J. Electrochem. Soc.* **149**, G276 (2002).
4. J. Ding, J.-S. Jenq, G.-H. Kim, H. L. Maynard, J. S. Hamers, N. Hershkowitz, and J. W. Taylor, "Etching rate characterization of SiO<sub>2</sub> and Si using ion energy flux and atomic fluorine density in a CF<sub>4</sub>/O<sub>2</sub>/Ar electron cyclotron resonance plasma", *J. Vac. Sci. Technol. A* **11**, 1283 (1993).
5. X. Li, X. Hua, L. Ling, G. S. Oehrlein, M. Barela, and H. M. Anderson, "Fluorocarbon-based plasma etching of SiO<sub>2</sub>: Comparison of C<sub>4</sub>F<sub>6</sub>/Ar and C<sub>4</sub>F<sub>8</sub>/Ar discharges", *J. Vac. Sci. Technol. A* **20**, 2052 (2002).
6. H.-K. Ryu, Y.-W. Kim, K. Lee, C. Shin, C.-K. Kim, "A comparative study on a high aspect ratio contact hole etching in UFC- and PFC-containing plasmas", *Microelectr. J.* **38**, 125 (2007).
7. H. Jansen, M. de Boer, R. Legtenberg, and M. Elwenspoek, "The black silicon method: a universal method for determining the parameter setting of a fluorine-based reactive ion etcher in deep silicon trench etching with profile control", *J. Micromech. Microeng.* **5**, 115 (1995).
8. H. Jansen, M. de Boer, J. Burger, R. Legtenberg, and M. Elwenspoek, "The black silicon method II: the effect of mask material and loading on the reactive ion etching of deep silicon trenches", *Microelectron. Eng.* **27**, 475 (1995).
9. R. Silapunt, A. E. Wendt, and K. H. R. Kirmse, "Ion energy control at substrates during plasma etching of patterned structures", *J. Vac. Sci. Technol. B* **25**, 1882 (2007).
10. S. Banna, A. Agarwal, G. Cunge, M. Darnon, E. Pargon, and O. Joubert, "Pulsed high-density plasmas for advanced dry etching processes", *J. Vac. Sci. Technol. A* **30**, 040801 (2012).
11. C. J. Choi, O. S. Kwon, and Y. S. Seol, "Negative ion formation in SiO<sub>2</sub> etching using a pulsed inductively coupled plasma", *Jpn. J. Appl. Phys.* **37**, 6894 (1998).
12. S. Samukawa, "Pulse-time-modulated Electron Cyclotron Resonance Plasma Etching for Highly Selective, Highly Anisotropic, and Notch-free Polycrystalline Silicon Patterning", *Appl. Phys. Lett.* **64**, 3398 (1994).
13. R. W. Boswell and D. Henry, "Pulsed High Rate Plasma Etching with Variable Si/SiO<sub>2</sub> selectivity and Variable Si Etch Profiles", *Appl. Phys. Lett.* **47**, 1095 (1985).

14. M. Schaepkens, G. S. Oehrlein, and J. M. Cook, "Effects of radio frequency bias frequency and radio frequency bias pulsing on SiO<sub>2</sub> feature etching in inductively coupled fluorocarbon plasmas", *J. Vac. Sci. Technol. B* **18**, 856 (2000).
15. T. E. F. M. Standaert, M. Schaepkens, N. R. Rueger, P. G. M. Sebel, J. M. Cook, and G. S. Oehrlein, "High density fluorocarbon etching of silicon in an inductively coupled plasma: Mechanism of etching through a thick steady state fluorocarbon layer", *J. Vac. Sci. Technol. A* **16**, 239 (1998).
16. M. Schaepkens, T. E. F. M. Standaert, N. R. Rueger, P. G. M. Sebel, J. M. Cook, and G. S. Oehrlein, "Study of the SiO<sub>2</sub>-to-Si<sub>3</sub>N<sub>4</sub> etch selectivity mechanism in inductively coupled fluorocarbon plasmas and comparison with the SiO<sub>2</sub>-to-Si mechanism", *J. Vac. Sci. Technol. A* **17**, 26 (1999).
17. E. Semmler, P. Awakowicz, and A. von Keudell, "Heating of a dual frequency capacitively coupled plasma via the plasma series resonance", *Plasma Sources Sci. Technol.* **16**, 839 (2007).
18. K. Maeshige, G. Washio, T. Yagisawa, and T. Makabe, "Functional design of a pulsed two-frequency capacitively coupled plasma in CF<sub>4</sub>/Ar for SiO<sub>2</sub> etching", *J. Appl. Phys.* **91**, 9494 (2002).
19. T. Ohmori, T. Goto, and T. Makabe, "Negative charge injection to a wafer in a pulsed two-frequency capacitively coupled plasma for oxide etching; diagnostics by emission-selected computerized tomography", *J. Phys. D: Appl. Phys.* **37**, 2223 (2004).
20. S. H. Song and M. J. Kushner, "Role of the blocking capacitor in control of ion energy distributions in pulsed capacitively coupled plasmas sustained in Ar/CF<sub>4</sub>/O<sub>2</sub>", *J. Vac. Sci. Technol. A* **32**, 021306 (2014).
21. M. J. Kushner, "Hybrid Modeling of Low Temperature Plasmas for Fundamental Investigations and Equipment Design", *J. Phys. D* **42**, 194013 (2009).
22. A. V. Vasenkov, X. Li, G. S. Oehrlein and M. J. Kushner, "Properties of C<sub>4</sub>F<sub>8</sub> Inductively Coupled Plasmas. II. Plasma Chemistry and Reaction Mechanism for Modeling of Ar/c-C<sub>4</sub>F<sub>8</sub>/O<sub>2</sub> discharges", *J. Vac. Sci. Technol. A* **22**, 511 (2004).
23. M. A. Lieberman and A. J. Lichtenberg, *Principles of plasma discharges and materials processing* (Wiley, New York, 2005), p. 99.
24. M. V. Malyshev and V. M. Donnelly, "Dynamics of inductively-coupled pulsed chlorine plasmas in the presence of continuous substrate bias", *Plasma Sources Sci. Technol.* **9**, 353 (2000).
25. S. Tinck, A. Bogaerts, and D. Shamiryan, "Simultaneous etching and deposition processes during the etching of silicon with a Cl<sub>2</sub>/O<sub>2</sub>/Ar inductively coupled plasma", *Plasma Process. Polym.* **8**, 490 (2011).

## Chapter 8 CONCLUSION AND FUTURE WORK

### 8.1 Overview of Research

In this dissertation, advanced techniques for controlling energy distributions of electrons and ions were presented with results from a 2D hybrid plasma model. The techniques include use of magnetic fields, electron beams and a pulsed power source. The outcome of this fundamental study was then applied to optimizing etching for microelectronics fabrication.

The addition of an external magnetic field changed the electron kinetics from *nonlocal* to *local* depending on the pressure and power, and also modified the power deposition to be deeper than the conventional skin depth. At a lower pressure, the EEDs at different radial positions were similar to each other without the magnetic field due to the longer energy relaxation distance,  $\lambda_e$ . The EEDs varied with radial positions at higher pressure due to the shorter  $\lambda_e$ . With the magnetic field, the EEDs were significantly modified with respect to the radial position due to the magnetic confinement of electrons. By applying an external magnetic field in the test ICP system, the classical diffusion coefficient was reduced from  $10^6 \text{ cm}^2\text{s}^{-1}$  to  $10^4 \text{ cm}^2\text{s}^{-1}$  due to the larger cyclotron frequency ( $\approx 10^8 \text{ Hz}$ ) compared to the collision frequency ( $\approx 10^6 \text{ Hz}$ ). At pressures high enough to make the collision frequency commensurate with the cyclotron frequency, the confinement effect diminished. Although the applied power does not directly affect electron transport, the gas temperature increased with power in the presence of the

magnetic field. The electron collision frequency was then reduced by the increased power due to the rarefied gas density at higher temperature.

High energy secondary electrons are produced from surfaces by the bombardment of energetic particles including ions, photons, and electrons. The beam-like secondary electrons produced by acceleration in the sheath collide with low energy electrons in the bulk plasma, delivering energy to the bulk electrons and depleting the beam electrons. Beam-like secondary electrons deliver a power density ( $\approx 10 \text{ mW/cm}^3$ ) to the bulk electrons, while traversing back and forth between two parallel electrodes. On average, secondary electrons bounce back and forth 7-8 times between electrodes, making one collision in the bulk of the plasma per one reflection at the sheath boundary. Although the beam electrons collide mostly with the background gas, collisions of beam electrons with bulk electrons do occur. These interactions were spatially dependent due to the inverse energy dependence of  $e-e$  collisions, and so are most prominent near the sheaths. This interaction between beam electron and bulk electrons modified the EED of the bulk electrons, to produce shapes that are not otherwise attainable in self-sustained  $RF$  equilibrium plasmas. For example, an EED was produced that has a raised high energy tail component due to the energy transferred from the high energy electrons in the beam to the low energy bulk electrons.

Control of EEDs was also investigated in pulsed DF-CCPs with various PRFs and duty cycles as control variables. The PRF and duty cycle provide possibilities to control EEDs due to there being transients in  $E/N$  above the steady state and different lengths of the afterglow period during which thermalization occurs. Smaller PRF and duty cycle produced a higher overshoot of  $E/N$  and a more raised tail of EED at the rising edge of the pulse. Electrons quickly thermalized during the power OFF stage. As a result, on average, an EED was produced that has both a high

energy tail and a large thermal component. These EEDs will produce different dissociation patterns in the feedstock gases. The choice of duty cycle and PRF were important to the time average EED as these determine the relative role of thermalization.

The IED onto the substrate was varied by the choice of duty cycle and blocking capacitor size through the dynamics of the dc-bias that results. Larger capacitance resulted in the delayed response of the dc-bias. By pulsing, low energy ions were generated during the OFF stage of the pulse, while the high energy portion of the IED produced during the ON stage is still maintained which resembles that produced with *CW* power. The high energy component of the IED was extended towards higher energies due to the transition of the pulsing, though the maximum energy is not a simple function of duty cycle and the capacitance. However, the amplitudes of the low and high energy peaks in the distribution were linear with the duty cycle. As a result, the desired etch profile was obtained by adjusting the duty cycle. Pulsed power can adjust the etch profile width in dielectric etch by 4-5% by changing duty cycle. The sidewall profile can be effectively controlled by the pulse duty cycle with less than 90% duty cycle when pulsing LF, less than 75% duty cycle when pulsing HF, and less than 50% duty cycle when pulsing LF & HF.

## **8.2 Validation and Impact**

Comparison between model and experimental results is an important task. The computational model is sensitive to the accuracy of the fundamental parameters used in the solutions (e.g. cross sections, surface reaction probabilities). A discussion of the robustness of the databases, and the accuracy of the algorithms and their solutions used in this model can be found elsewhere. Having said that, this thesis is more focused on predicting plasma properties and understanding the physics behind the phenomena rather than more detailed examination of isolated cases for comparison with experiments. This approach is motivated by plasma

simulations being a cost saving tool in microelectronics fabrication. For example, prediction of wafer charge damage saves on the number of Charm wafers used (\$6,800 each), modelling chemistry changes can save \$170,000 on development of new process methods, and developing a new tool with 98% design by simulation will save over \$420,000 in the tool development cycle.[1]

### 8.3 Future Work

This dissertation has presented a number of techniques to control fundamental plasma properties. The following is an overview of future work that would provide further insights into the areas of plasma kinetics control and plasma material processing.

- 1) **Investigation of the pulsed magnetic field.** A preliminary investigation of pulsing the magnetic field in ICP has been initiated in this dissertation. A possibility of using pulsed magnetic fields to control the EED has been observed. However, a more detailed study would help to understand the physics behind the phenomena with respect to the power dissipation, induced plasma current and external antenna coil current.
- 2) **Investigation of pulsed DF-CCP with lower PRF.** Number of ions incident into the etched trench hole per *power-ON* cycle is

$$N_{hole} = A \cdot \phi \cdot \Delta t = \frac{A \cdot \phi \cdot d}{f}, \quad (8.1)$$

where  $A$  is an area of feature,  $\phi$  is an ion flux,  $d$  is a duty cycle,  $\Delta t$  is a sub-cycle period, and  $f$  is a PRF. As the feature size shrinks, the number of ions entering into the feature decreases. When pulsing with 50% duty cycle, the number of ions per feature is plotted as a function of the feature size in Fig. 8.1 for various PRFs. For the side-by-side comparison, the

ion current onto the feature is assumed to be constant with  $0.5 \text{ mA/cm}^2$ . In order to get a statistically relevant number of ions into the feature during the sub-cycle, PRF is required to be less than 1 kHz for sub-20 nm feature.

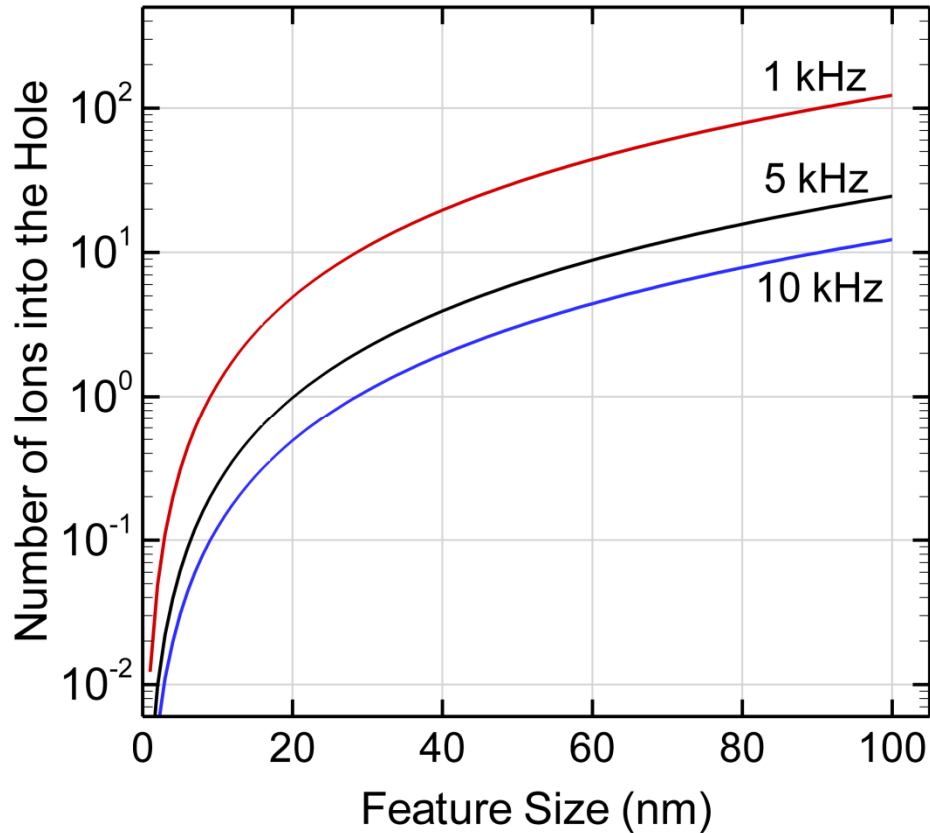


Fig. 8.1 Number of ions into the feature as a function of the feature size with the ion current of  $0.5 \text{ mA/cm}^2$  and duty cycle of 50%. For 20 nm feature size, only one single ion gets into the feature during the *power-ON* period with 5 kHz of PRF.

**3) Development of a circuit model that is altered dynamically based on feedback from the pulsed plasma.** In the CCP, the blocking capacitor connected to the substrate was included in the model. In reality, the circuit in the plasma system is more complicated including the matching network. Especially in the pulse mode operation, the circuit in the matching box would have been dynamically adjusted to deliver the maximum power. In order to simulate the pulse powered plasma having an active circuit system, a dedicated circuit model that

responses dynamically to the transition of the plasma would be helpful in the investigation of the time transient phenomena. This would also allow one to formulate real time control strategies for pulsed plasma etching systems.

- 4) Including charging effect in the profile simulation.** One of the advantages of using pulsed plasmas for the material processing is the generation of negative ions during the afterglow. Electrons decay fast during the afterglow but ions are left over, so that the charge balance is made between the negative and positive ions (ion-ion plasmas). Typically, the charging on the feature alters the direction of the ion incident onto the wafer, which could result in the potential defects such as damage on the sidewall, undercut, and micro-trenching. However, the negative ions may neutralize the surface charge on the feature to reduce the potential defects. Therefore, some of the unknown statistical phenomena would be captured by including the charging effect in the feature profile simulation.

## 8.4 References

1. Quantemol, <http://www.quantemol.com/about/oem-page/>

## **AUTHOR'S BIOGRAPHY**

Sang Heon Song was born in Busan, Korea, in 1980. He received his B.S. degree in Nuclear Engineering from Seoul National University in 2003. He obtained his M.S. in 2005 where he worked on experiments of atmospheric pressure plasmas under guidance of Prof. Gon-Ho Kim at Seoul National University. With his Master's degree, he worked with Samsung Electronics as a research engineer from 2005 to 2009. He joined University of Michigan in 2009 as a Ph.D. student in the group of Prof. Mark J. Kushner and has been working on modeling of low-temperature plasmas. His work has resulted in 3 refereed journal publications and 11 conference presentations. He will also receive a graduate certificate in Plasma Science and Engineering (PSE) from Michigan Institute for Plasma Science and Engineering (MIPSE). Upon graduation in June 2014 with his Ph.D. from University of Michigan, he will work as a senior process engineer at Tokyo Electron Ltd. (TEL) technology center in Albany, NY.

He was awarded graduate fellowship from MIPSE in 2011 and also awarded for a distinguished academic achievement from College of Engineering, University of Michigan in 2014. He is a member of the following honor societies: Phi Kappa Phi, Tau Beta Pi, Alpha Nu Sigma, and Sigma Xi.